

MODELING AND CONTROL OF HYBRID  
WIND/PHOTOVOLTAIC/FUEL CELL DISTRIBUTED GENERATION SYSTEMS

by  
Caisheng Wang

A dissertation submitted in partial fulfillment  
of the requirement for the degree

of  
Doctor of Philosophy

in  
Engineering

MONTANA STATE UNIVERSITY  
Bozeman, Montana

July 2006

©COPYRIGHT

by

Caisheng Wang

2006

All Rights Reserved

APPROVAL

of a dissertation submitted by

Caisheng Wang

This dissertation has been read by each member of the thesis committee and has been found to be satisfactory regarding content, English usage, format, citations, bibliographic style, and consistency, and is ready for submission to the Division of Graduate Education.

Dr. M. Hashem Nehrir

Approved for the Department of Electrical and Computer Engineering

Dr. James N. Peterson

Approved for the Division of Graduate Education

Dr. Joseph J. Fedock

## STATEMENT OF PERMISSION TO USE

In presenting this dissertation in partial fulfillment of the requirements for a doctoral degree at Montana State University, I agree that the Library shall make it available to borrowers under rules of the Library. I further agree that copying of this dissertation is allowable only for scholarly purposes, consistent with "fair use" as prescribed in the U.S. Copyright Law. Requests for extensive copying or reproduction of this dissertation should be referred to ProQuest Information and Learning, 300 North Zeeb Road, Ann Arbor, Michigan 48106, to whom I have granted "the exclusive right to reproduce and distribute my dissertation in and from microform along with the non-exclusive right to reproduce and distribute my abstract in any format in whole or in part."

Caisheng Wang

July 2006

## ACKNOWLEDGEMENTS

I am grateful to acknowledge and thank all of those who assisted me in my graduate program at Montana State University. First, I would like to thank Dr. Hashem Nehrir, my academic advisor here at MSU. His guidance, support, patience and personal time throughout my years as a graduate student have been truly appreciated. Special thanks are given to my other graduate committee members, Dr. Steven Shaw, Dr. Don Pierre, Dr. Hongwei Gao, Dr. Robert Gunderson, and Dr. Gary Bogar. Special thanks also go to Dr. Hong Mao for his time and clarifying conversations on design and control of power electronic devices. Mr. Sreedhar Guda's help in the model developing for wind energy conversion systems and Mr. Marc Keppler's help in setting up the experimental circuit for PEM fuel cell model validation are acknowledged. Most importantly, I would like to thank my family and friends for their support throughout all the years.

## TABLE OF CONTENTS

LIST OF FIGURES .....	xii
LIST OF TABLES .....	xi
Abstract .....	xii
1. INTRODUCTION .....	1
World Energy Demands.....	1
World and U.S. Electricity Demands & Generation.....	2
Conventional Thermal Electric Power Generation .....	6
Coal .....	6
Natural Gas.....	6
Oil.....	7
Nuclear Power.....	9
Hydroelectric Power .....	9
Why Alternative/Renewable Energy? .....	10
Recent Progress in Alternative/Renewable Energy Technologies.....	14
Wind Energy .....	14
Photovoltaic Energy.....	16
Fuel Cells .....	18
Other Renewable Energy Sources .....	20
Distributed Generation Applications.....	23
Need for the Research .....	26
Scope of the Study.....	28
Organization of the Dissertation.....	28
REFERENCES .....	30
2. FUNDAMENTALS OF ALTERNATIVE ENERGY SYSTEMS .....	33
Energy Forms .....	33
Definition of Energy .....	33
Mechanical Energy .....	34
Chemical Energy.....	35
Electrical and Electromagnetic Energy.....	35
Thermal Energy .....	36
Nuclear Energy .....	37
Fundamentals of Thermodynamics .....	37
The First Law of Thermodynamics.....	37
The Heat Engine and Carnot Cycle .....	39
The Second Law of Thermodynamics .....	41

## TABLE OF CONTENTS - CONTINUED

Heat Transfer.....	42
Heat Transfer by Conduction .....	42
Heat Transfer by Convection.....	42
Heat Transfer by Radiation.....	43
Fundamentals of Electrochemical Processes.....	43
The Gibbs Free Energy .....	43
Energy Balance in Chemical Reactions.....	44
The Nernst Equation .....	47
Fundamentals of Alternative Energy Systems.....	48
Wind Energy System.....	49
Energy in Wind.....	49
Power Extracted from Wind.....	49
Tip Speed Ratio.....	51
Wind Energy Conversion System.....	52
Constant Speed and Variable Speed Wind Energy Conversion Systems.....	53
Wind Turbine Output Power vs. Wind Speed.....	54
Photovoltaic Energy System.....	57
Fuel Cells .....	59
PEMFC.....	61
SOFC.....	63
MCFC.....	65
Electrolyzer.....	66
Summary .....	69
REFERENCES .....	70
<b>3. MULTI-SOURCE ALTERNATIVE ENERGY DISTRIBUTED GENERATION SYSTEM.....</b>	<b>72</b>
Introduction .....	72
AC Coupling vs. DC Coupling.....	75
Stand-alone vs. Grid-connected Systems .....	79
The Proposed System Configuration.....	79
System Unit Sizing.....	80
REFERENCES .....	85
<b>4. COMPONENT MODELING FOR THE HYBRID ALTERNATIVE ENERGY SYSTEM .....</b>	<b>89</b>
Dynamic Models and Model Validation for PEMFC .....	89
Introduction.....	89
Dynamic Model Development.....	91

## TABLE OF CONTENTS - CONTINUED

Gas Diffusion in the Electrodes.....	92
Material Conservation Equations .....	96
Fuel Cell Output Voltage .....	97
Double-Layer Charging Effect.....	101
Energy Balance of the Thermodynamics .....	102
Dynamic Model Built in Matlab/Simulink .....	104
Equivalent Electrical Model in Pspice.....	105
Internal Potential E.....	106
Circuit for Activation Loss.....	107
Circuits for Ohmic and Concentration Voltage Drops .....	108
Equivalent Capacitor of Double-layer Charging Effect .....	109
Thermodynamic Block.....	109
Model Validation.....	110
Experimental Setup .....	111
Steady-State Characteristics .....	113
Temperature Response.....	115
Transient Performance.....	116
Dynamic Models for SOFC.....	118
Introduction.....	118
Dynamic Model Development.....	119
Effective Partial Pressures.....	120
Material Conservation Equations .....	124
Fuel Cell Output Voltage .....	126
Energy Balance of the Thermodynamics .....	131
Dynamic SOFC Model Implementation.....	135
Model Responses under Constant Fuel Flow Operation.....	137
Steady-State Characteristics .....	137
Dynamic Response .....	140
Constant Fuel Utilization Operation .....	144
Steady-state Characteristics.....	145
Dynamic Responses .....	147
Wind Energy Conversion System.....	150
Introduction.....	150
System Configuration.....	151
Dynamic Model for Variable Speed Wind Turbine.....	152
Wind Turbine Characteristics .....	152
Pitch Angle Controller.....	155
Variable-speed Wind Turbine Model.....	157
Dynamic Model for SEIG.....	157
Steady-state Model .....	157
Self-excitation Process .....	160
Dynamic Model of SEIG in $dq$ Representations .....	161

Responses of the Model for the Variable Speed WECS .....	165
Wind Turbine Output Power Characteristic .....	165
Process of Self-excitation in SEIG .....	166
Model Responses under Wind Speed Changes .....	169
Solar Energy Conversion System.....	172
Modeling for PV Cell/Module .....	172
Light Current .....	173
Saturation Current .....	174
Calculation of $\alpha$ .....	174
Series Resistance .....	175
Thermal Model of PV.....	175
PV Model Development in MATLAB/Simulink .....	176
Model Performance .....	177
Temperature Effect on the Model Performance .....	179
Maximum Power Point Tracking Control.....	180
Current-Based Maximum Power Point Tracking .....	180
Control Scheme .....	182
Simulation Results.....	183
Electrolyzer .....	185
<i>U-I</i> Characteristic .....	185
Hydrogen Production Rate.....	186
Thermal Model.....	187
Electrolyzer Model Implementation in MATLAB/Simulink.....	189
Electrolyzer Model Performance .....	191
Power Electronic Interfacing Circuits .....	193
AC/DC Rectifiers.....	193
Simplified Model for Controllable Rectifiers .....	197
DC/DC Converters.....	200
Circuit Topologies .....	200
State-space Models Based on the State-space Averaging Technique .....	202
Averaged Models for DC/DC Converters .....	205
DC/AC Inverters .....	208
Circuit Topology.....	208
State-Space Model.....	208
<i>dq</i> Representation of the State-Space Model.....	212
Ideal Model for Three-phase VSI.....	214
Battery Model.....	217
Models for Accessories .....	218
Gas Compressor .....	218
High Pressure H <sub>2</sub> Storage Tank.....	219
Gas Pressure Regulator .....	220
Summary .....	223

## TABLE OF CONTENTS - CONTINUED

REFERENCES .....	224
5. CONTROL OF GRID-CONNECTED FUEL CELL POWER GENERATION SYSTEMS .....	231
Introduction .....	231
System Description.....	232
Controller Designs for Power Electronic Devices .....	238
Controller Design for the Boost DC/DC Converter.....	238
Controller Design for the 3-Phase VSI .....	241
Current Control Loop .....	241
Voltage Control Loop .....	245
Control of Power Flow .....	247
Overall Power Control System for the Inverter.....	249
Simulation Results.....	250
Desired P and Q Delivered to the Grid: Heavy Loading .....	251
PEMFC DG .....	251
SOFC DG .....	254
Desired P Delivered to the Grid, Q Consumed from the Grid: Light Loading.....	256
PEMFC DG .....	256
SOFC DG .....	258
Load-Following Analysis.....	260
Fixed Grid Power .....	260
Fixed FC Power.....	261
Fault Analysis.....	263
Summary .....	266
REFERENCES .....	268
6. CONTROL OF STAND-ALONE FUEL CELL POWER GENERATION SYSTEMS.....	271
Introduction .....	271
System Description and Control Strategy .....	272
Load Mitigation Control .....	272
Battery Charging/Discharging Controller.....	276
Filter Design.....	277
Simulation Results.....	279
Load Transients.....	279
DC Load Transients.....	280
AC Load Transients.....	280
Load mitigation .....	282

## TABLE OF CONTENTS - CONTINUED

PEMFC System .....	282
SOFC System .....	286
Battery Charging/Discharging .....	289
Summary .....	292
REFERENCES .....	293
<b>7. CONTROL SCHEMES AND SIMULATION RESULTS FOR THE PROPOSED HYBRID WIND/PV/FC SYSTEM .....</b>	<b>295</b>
Introduction .....	295
System Control Strategy .....	295
Overall Power Management Strategy .....	296
AC Bus Voltage Regulator .....	299
Electrolyzer Controller .....	300
Simulation Results under Different Scenarios .....	301
Winter Scenario .....	303
Weather Data .....	303
Simulation Results .....	305
Summer Scenario .....	314
Weather Data .....	314
Simulation Results .....	316
Summary .....	330
REFERENCES .....	331
<b>8. OPTIMAL PLACEMENT OF DISTRIBUTED GENERATION SOURCES IN POWER SYSTEMS .....</b>	<b>332</b>
Introduction .....	332
Optimal Placement of DG on a Radial Feeder .....	333
Theoretical Analysis .....	334
Procedure to Find the Optimal Location of DG on a Radial Feeder .....	336
Case Studies with Time Invariant Loads and DGs .....	338
Case Study with Time Varying Load and DG .....	340
Optimal Placement of DG in Networked Systems .....	341
Simulation Results .....	345
Radial Feeder with Time Invariant Loads and DG .....	346
Radial Feeder with Time Varying Loads and DG .....	348
Networked Systems .....	351
Summary .....	358

## TABLE OF CONTENTS - CONTINUED

REFERENCES .....	359
9. CONCLUSIONS.....	361
APPENDICES .....	364
APPENDIX A: <i>abc-dq0</i> TRANSFORMATION .....	365
<i>abc-dq0</i> Transformation.....	366
<i>dq0-abc</i> Transformation.....	367
APPENDIX B: SIMULATION DIAGRAMS OF THE HYBRID ENERGY SYSTEM.....	368
APPENDIX C: MATLAB PROGRAMS FOR DG OPTIMAL PLACEMENT .....	373
DG Optimal Program for the IEEE 6-Bus system.....	374
DG Optimal Program for the IEEE 30-Bus system.....	375

## LIST OF FIGURES

Figure	Page
1.1. World Energy Consumption 1970-2025 .....	2
1.2. World and US Electricity Demands, 1980-2025.....	4
1.3. World Electricity Generating Capacity 1980-2025.....	5
1.4. The world and US net electricity generation by type in 2002 .....	5
1.5. Fuel shares of world electricity generation, 2002-2025.....	8
1.6. U.S. electricity generation by fuel types.....	8
1.7. World crude oil prices 1978-2006.....	13
1.8. The world and the U.S. wind power cumulative capacity .....	16
1.9. Cumulative Installed PV capacity in IEA PVPS countries.....	18
1.10. Cumulative installed FC units world-wide, 1990-2005.....	19
2.1. Block diagram of an ideal heat engine.....	39
2.2. Carnot cycle. (a) P-V (pressure-volume) diagram.....	40
(b) T-S (temperature-entropy) diagram.....	40
2.3. Theoretical rotor efficiency vs. $v_0/v$ ratio.....	51
2.4. Block diagram of a typical wind energy conversion system.....	52
2.5. Constant and variable speed wind energy conversion systems .....	55
2.6. Typical curves for a constant speed stall controlled (dotted) and variable speed pitch controlled (solid) wind turbine.....	56
2.7. Schematic block diagram of a PV cell.....	58
2.8. PV Cell, module and array.....	59
2.9. Schematic diagram of a PEMFC.....	61
2.10. $V-I$ characteristic of a 500W PEMFC stack .....	62
2.11. Schematic diagram of a SOFC.....	63
2.12. $V-I$ characteristic of a 5kW SOFC stack.....	64
2.13. Schematic diagram of a MCFC.....	65
2.14. Progress in generic performance of MCFCs on reformat gas and air.....	66
2.15. Schematic diagram of an alkaline electrolyzer.....	68
3.1. Hybrid energy system integration: DC coupling.....	75

Figure	Page
3.2. Hybrid energy system integration: (a) PFAC coupling; (b) HFAC coupling.....	76
3.3. System configuration of the proposed multi-source alternative hybrid energy system (coupling inductors are not shown in the figure).....	81
3.4. Hourly average demand of a typical residence in the Pacific Northwest area. ....	82
4.1. Schematic diagram of a PEMFC and voltage drops across it.....	93
4.2. Equivalent circuit of the double-layer charging effect inside a PEMFC. ....	101
4.3. Diagram of building a dynamic model of PEMFC in SIMULINK. ....	105
4.4. Diagram of building an electrical model of PEMFC in Pspice. ....	106
4.5. Electrical circuit for internal potential E.....	107
4.6. Electrical circuit for activation loss. ....	107
4.7. Electrical circuit for ohmic voltage drop. ....	108
4.8. Electrical circuit for concentration voltage drop. ....	109
4.9. Equivalent circuit of thermodynamic property inside PEMFC. ....	110
4.10. Experimental configuration on the SR-12 PEMFC stack. ....	112
4.11. V-I characteristics of SR-12 and models.....	114
4.12. P-I characteristics of SR-12 and models. ....	114
4.13. Temperature responses of the SR 12 stack and models. ....	115
4.14. Transient responses of the models in short time range. ....	117
4.15. Transient responses of the models in long time range. ....	117
4.16. Schematic diagram of a solid oxide fuel cell. ....	121
4.17. Equivalent electrical circuit of the double-layer charging effect inside a SOFC	130
4.18. Heat transfer inside a tubular solid oxide fuel cell. ....	132
4.19. Diagram of building a dynamic model of SOFC in SIMULINK. ....	137
4.20. V-I characteristics of the SOFC model at different temperatures.....	138
4.21. Three voltage drops at different temperatures. ....	139
4.22. P-I characteristics of the SOFC model at different temperatures. ....	140
4.23. Model dynamic responses with different equivalent capacitance values for double-layer charging effect in small time scale. ....	141

Figure	Page
4.24. Model dynamic responses under different operating pressures in medium time scale. ....	142
4.25. Model dynamic responses under different inlet temperatures in large time scale. ....	143
4.26. Model temperature responses. ....	144
4.27. Constant utilization control. ....	145
4.28. V-I and P-I characteristics of the SOFC model under constant fuel utilization and constant fuel flow operating modes. ....	146
4.29. H <sub>2</sub> input for the constant utilization and constant flow operating modes. ....	147
4.30. Model dynamic responses under different operating pressures in medium time scale with constant utilization operating mode. ....	149
4.31. System block diagram of the WECS. ....	152
4.32. $C_p$ - $\lambda$ characteristics at different pitch angles ( $\theta$ ). ....	154
4.33. Variable speed pitch controlled wind turbine operation regions. ....	155
4.34. Pitch angle controller. ....	156
4.35. Simulation model of the variable speed pitch-regulated wind turbine. ....	156
4.36. Equivalent T circuit of self-excited induction generator with R-L Load. ....	159
4.37. Determination of stable operation of SEIG. ....	161
4.38. $dq$ representation of a SEIG (All values are referred to stator). ....	162
4.39. Wind turbine output power characteristic. ....	166
4.40. A successful self excitation process. ....	167
4.41. Voltage fails to build up. ....	167
4.42. Variation of magnetizing current, $I_m$ . ....	168
4.43. Variation of magnetizing inductance, $L_m$ . ....	168
4.44. Wind speed variations used for simulation study. ....	169
4.45. Output power of the WECS model under wind speed changes. ....	169
4.46. Wind turbine rotor speed. ....	170
4.47. Pitch angle controller response to the wind changes. ....	171
4.48. Variation of power coefficient $C_p$ . ....	171

Figure	Page
4.49. One-diode equivalent circuit model for a PV cell. (a) Five parameters model; (b) Simplified four parameters model.....	172
4.50. Block diagram of the PV model built in MATLAB/Simulink. ....	176
4.51. $I-U$ characteristic curves of the PV model under different irradiances.....	178
4.52. $P-U$ characteristic curves of the PV model under different irradiances. ....	178
4.53. $I-U$ characteristic curves of the PV model under different temperatures. ....	179
4.54. $P-U$ characteristic curves of the PV model under different temperatures. ....	179
4.55. Linear relationship between $I_{sc}$ and $I_{mp}$ under different solar irradiances.....	181
4.56. $U_{mp}$ vs. $U_{oc}$ curve under different solar irradiances. ....	181
4.57. CMPPT control scheme. ....	182
4.58. $I_{mp}$ and $I_{pv}$ curves under the CMPPT control.....	183
4.59. PV output power and the maximum power curves. ....	184
4.60. Block diagram of the electrolyzer model built in MATLAB/Simulink. ....	189
4.61. $U-I$ characteristics of the electrolyzer model under different temperatures.....	191
4.62. Temperature response of the model. ....	192
4.63. Three-phase full diode bridge rectifier.....	194
4.64. Three-phase 12-diode bridge rectifier with a Y-Y and a Y- $\Delta$ transformer. ....	195
4.65. A 6-pulse thyristor rectifier. ....	197
4.66. Block diagram of the simplified model for 3-phase controllable rectifiers. ....	198
4.67. DC output voltages of the different rectifier models. ....	199
4.68. AC side phase current of the different rectifier models. ....	199
4.69. Boost DC/DC converter. ....	201
4.70. Buck DC/DC converter. ....	201
4.71. Averaged model for boost DC/DC converters. ....	205
4.72. Simulation result of the averaged model for boost DC/DC converter. ....	206
4.73. Simulation result of the detailed model for boost DC/DC converter.....	206
4.74. Averaged model for buck DC/DC converters. ....	207
4.75. Simulation result of the averaged model for buck DC/DC converter. ....	207
4.76. Simulation result of the detailed model for buck DC/DC converter.....	208

Figure	Page
4.77. 3-phase DC/AC voltage source inverter. ....	209
4.78. Ideal model for three-phase VSI. ....	215
4.79. AC phase output voltages of the ideal VSI model and the switched VSI model. ....	216
4.80. Output power of the ideal VSI model and the switched VSI model. ....	216
4.81. Equivalent circuit model for battery reported in [4.81]. ....	217
4.82. Simplified circuit model for lead-acid batteries. ....	218
4.83. Pressured H <sub>2</sub> storage tank. ....	219
4.84. Gas pressure regulator. ....	221
4.85. Performance of the model for gas pressure regulators. ....	222
5.1. Block diagram of a fuel cell distributed generation system. ....	233
5.2. Block diagram of the control loop for the boost DC/DC converter. ....	239
5.3. Bode plot of the control loop of the boost DC/DC converter. ....	240
5.4. Block diagram of the current control loop of the inverter. ....	242
5.5. Bode plot of the current control loop. ....	244
5.6. Unit step response of the current control loop and its approximation. ....	245
5.7. Block diagram of the voltage control loop of the inverter. ....	245
5.8. Bode plot of the voltage control loop. ....	247
5.9. Power flow between a voltage source and utility grid. ....	247
5.10. Block diagram of the overall power control system of the inverter. ....	249
5.11. PEMFC DG: P and Q delivered to the grid under heavy loading. ....	252
5.12. PEMFC DG: dq values of the inverter output voltage under heavy load. ....	252
5.13. PEMFC DG: Output voltage and current of each fuel cell array under heavy load. ....	253
5.14. PEMFC DG: DC bus voltage waveform under heavy load. ....	254
5.15. SOFC DG: P and Q delivered to the grid under heavy loading. ....	254
5.16. SOFC DG: Output voltage and current of each FC array under heavy load. ....	255
5.17. SOFC DG: DC bus voltage under heavy loading. ....	255
5.18. PEMFC DG: P and Q delivered to the grid: light loading. ....	257
5.19. PEMFC DG: Output voltage and current of	

Figure	Page
each fuel cell array under light loading.....	257
5.20. SOFC DG: P and Q delivered to the grid under light loading.....	259
5.21. SOFC DG: Output voltage and current of each fuel cell array under light load	259
5.22. System for the PEMFC DG load-following study.....	261
5.23. Power curves of the load-following study with fixed grid power.....	262
5.24. System for the PEMFC DG load-following study.....	262
5.25. Power curves of the load-following study with fixed FC power.....	263
5.26. Faulted fuel cell DG system.....	264
5.27. Faulted PEMFC DG: Power flow of the transmission line.....	265
5.28. Faulted PEMFC DG: Fuel cell output powers for the fault studies.....	266
6.1. Schematic diagram of a FC-battery hybrid system with load transient mitigation control.....	274
6.2. Schematic diagram of the battery charging/discharging controller.....	275
6.3. Example of the responses of different filters to a load transient.....	278
6.4. Load transient of starting a 2.5HP and a 5kW 220V DC motor.....	280
6.5. AC load transient used on PEMFC-battery system.....	282
6.6. Reference signal ( $I_{ref}$ ) for the current controller, battery current ( $i_b$ ), and converter output current ( $i_{dd\_out}$ ) under the load transient for PEMFC shown in Figure 6.4.....	284
6.7. The PEMFC output current and voltage responses to the DC load transient shown in Figure 6.4.....	284
6.8. PEMFC: The control reference signal ( $I_{ref}$ ) and battery current ( $i_b$ ) under the AC load transient shown in Figure 6.5.....	285
6.9. The PEMFC output current and voltage responses to the AC load transient shown in Figure 6.5.....	286
6.10. Reference signal ( $I_{ref}$ ) for the current controller, the battery current ( $i_b$ ) and the converter output current ( $i_{dd\_out}$ ) under the load transient for SOFC shown in Figure 6.4.....	287
6.11. SOFC output current and voltage responses	

Figure	Page
to the DC load transient shown in Figure 6.4. ....	287
6.12. Control reference signal ( $I_{ref}$ ) and battery current ( $i_b$ ) under the AC load transient.....	288
6.13. The SOFC output current and voltage responses to the AC load transient.....	288
6.14. Battery voltage and extra current reference ( $I_{ref2}$ ) curves when the battery is being charged.....	290
6.15. The load transient, the overall current control reference signal ( $I_{ref}$ ), the low-pass filter output signal ( $I_{ref1}$ ) and the corresponding converter output current ( $i_{dd\_out}$ ) when the battery is being charged. ....	291
7.1. Simulation model for the proposed hybrid alternative energy system in MATLAB/Simulink. ....	297
7.2. Block diagram of the overall control scheme for the proposed hybrid alternative energy system.....	298
7.3. Block diagram of the AC voltage regulator. ....	299
7.4. Block diagram of the electrolyzer controller. ....	300
7.5. Load demand profile over 24 hours for the system simulation study.....	302
7.6. Wind speed data for the winter scenario simulation study.....	303
7.7. Solar irradiance data for the winter scenario simulation study.....	304
7.8. Air temperature data for the winter scenario simulation study.....	304
7.9. Wind power of the winter scenario study.....	305
7.10. Pitch angle of the wind turbine of the winter scenario study.....	306
7.11. Rotor speed of the induction generator of the winter scenario study.....	306
7.12. PV power for the winter scenario. ....	308
7.13. Current difference between the actual output current and the reference current for the maximum power point of the winter scenario.....	308
7.14. The PV temperature response over the simulation period for the winter scenario. ....	309
7.15. Power available for H <sub>2</sub> generation of the winter scenario.....	309
7.16. H <sub>2</sub> generation rate of the winter scenario study.....	310

Figure	Page
7.17. Electrolyzer voltage and current for the winter scenario study.....	310
7.18. Power shortage over the simulation period of the winter scenario study. ....	311
7.19. Power supplied by the FC of the winter scenario study.....	312
7.20. H2 consumption rate of the winter scenario study.....	312
7.21. The pressure tank over the 24 hour of the winter scenario study.....	313
7.22. The battery power over the simulation period for the winter scenario. ....	314
7.23. Corrected wind speed data for the summer scenario simulation study. ....	315
7.24. Irradiance data for the summer scenario simulation study.....	315
7.25. Air temperature data for the summer scenario simulation study. ....	316
7.26. Wind power generated for the summer scenario study.....	317
7.27. Rotor speed of the induction generator for the summer scenario study.....	317
7.28. PV power generated for the winter scenario study. ....	318
7.29. The PV and air temperature over the simulation period for the winter scenario study.....	319
7.30. Power available for H2 generation for the summer scenario study. ....	320
7.31. H2 generation rate for the summer scenario study.....	320
7.32. Electrolyzer voltage and current for the summer scenario study.....	321
7.33. Power shortage over the simulation period for the summer scenario study. ....	322
7.34. Power supplied by the FC over the simulation period for the summer scenario study. ....	322
7.35. H2 consumption rate for the summer scenario study.....	323
7.36. The H <sub>2</sub> tank pressure over the 24 hour for the summer scenario study. ....	323
7.37. The battery power over the simulation period for the summer scenario. ....	324
7.38. Wind speed data for the simulation study with continuous weather data and load demand. ....	325
7.39. Solar irradiance data for the simulation study with continuous weather data and load demand. ....	325
7.40. Air temperature for the simulation study with continuous weather data and load demand. ....	326

Figure	Page
7.41. Wind power for the continuous weather data and load demand scenario.....	327
7.42. PV power for the continuous weather data and load demand scenario. ....	327
7.43. Power available for H <sub>2</sub> generation for the continuous weather data and load demand scenario. ....	328
7.44. FC output power for the continuous weather data and load demand scenario. ..	328
7.45. Battery power for the continuous weather data and load demand scenario.....	329
8.1. A feeder with distributed loads along the line. ....	334
8.2. Procedure for finding optimal place for a DG source in a radial feeder. ....	338
8.3. A networked power system. ....	342
8.4. Flow chart of The theoretical procedure to find the optimal bus to place DG in a networked system.....	346
8.5. A radial feeder with uniformly distributed loads. ....	347
8.6. Annual daily average output power profile of a 1-MW wind-DG. ....	349
8.7. Daily average demand of a typical house. ....	350
8.8. Power losses of the radial feeder with the wind-DG at different buses. ....	350
8.9. 6-bus networked power system studied. ....	351
8.10. Power losses of the system in Figure. 8.9 with a 5MW DG. ....	352
8.11. Values of the objective function of the system in Figure. 8.9. ....	353
8.12. IEEE 30-bus test system. ....	354
8.13. Power losses of the IEEE 30-bus test system with a 15MW DG. ....	354
8.14. Values of the objective function of the IEEE 30-bus system. ....	355
8.15. Power losses of the subset system in Figure 8.12 with a 5MW DG. ....	356
8.16. Values of the objective function of the subset system in Figure 8.12. ....	356
B.1. Simulink model for the wind energy conversion system. ....	369
B.2. Simulink model for the solar energy conversion system. ....	370
B.3. Simulink model for the fuel cell and the gas pressure regulation system. ....	371
B.4. Simulink model for the electrolyzer and the gas compression system. ....	372

## LIST OF TABLES

Table	Page
1.1. Current Status and the DOE Targets for PEMFC Stack in Stationary Applications .....	21
1.2. Current status and the SECA targets for 3-10 kW SOFC module in stationary applications .....	22
1.3. Technologies for Distributed Generation Systems .....	25
2.1. Standard thermodynamic properties (enthalpy, entropy and Gibbs energy).....	46
3.1. Comparison among Different Integration Schemes.....	78
3.2. Component Parameters of the Proposed Hybrid Energy System .....	84
4.1. Analogies between Thermodynamic and Electrical Quantities .....	110
4.2. Specifications of SR-12 .....	111
4.3. Electrical Model Parameter Values for SR-12 Stack .....	112
4.4. Operating Conditions for the Model Dynamic Response Studies .....	141
4.5. Parameter values for C1-C5.....	153
4.6. SEIG Model Parameters .....	165
4.7. The PV Model Parameters .....	177
4.8. The Electrolyzer Model Parameters.....	190
4.9. Constants of Beattie-Bridgeman Equation of State for H <sub>2</sub> .....	220
5.1. Configuration Parameters of the Proposed System .....	236
5.2. System Parameters of the Boost DC/DC Converter .....	240
5.3. Parameters of the Current Control Loop the Inverter .....	243
5.4. Parameters of the Voltage Control Loop the Inverter .....	246
6.1. Parameters of the DC/DC Converter .....	275
6.2. Parameters of the Battery Model .....	276
7.1. Weather Station information at Deer Lodge, Montana AgriMet Station (DRLM) .....	302
8.1. Theoretical Analysis Results of Case Studies with Time Invariant Loads and DGs .....	339
8.2. Parameters of the System in Figure 8.5 .....	347

8.3. Simulation Results of Case Studies with Time Invariant Loads and DG .....	348
8.4. Parameters of the System in Figure 8.9 .....	352
8.5. Bus Data of the IEEE 30-Bus Test System .....	357

## Abstract

Due to ever increasing energy consumption, rising public awareness of environmental protection, and steady progress in power deregulation, alternative (i.e., renewable and fuel cell based) distributed generation (DG) systems have attracted increased interest. Wind and photovoltaic (PV) power generation are two of the most promising renewable energy technologies. Fuel cell (FC) systems also show great potential in DG applications of the future due to their fast technology development and many merits they have, such as high efficiency, zero or low emission (of pollutant gases) and flexible modular structure.

The modeling and control of a hybrid wind/PV/FC DG system is addressed in this dissertation. Different energy sources in the system are integrated through an AC bus. Dynamic models for the main system components, namely, wind energy conversion system (WECS), PV energy conversion system (PVECS), fuel cell, electrolyzer, power electronic interfacing circuits, battery, hydrogen storage tank, gas compressor and gas pressure regulator, are developed. Two types of fuel cells have been modeled in this dissertation: proton exchange membrane fuel cell (PEMFC) and solid oxide fuel cell (SOFC). Power control of a grid-connected FC system as well as load mitigation control of a stand-alone FC system are investigated. The pitch angle control for WECS, the maximum power point tracking (MPPT) control for PVECS, and the control for electrolyzer and power electronic devices, are also addressed in the dissertation.

Based on the dynamic component models, a simulation model for the proposed hybrid energy system has been developed using MATLAB/Simulink. The overall power management strategy for coordinating the power flows among the different energy sources is presented in the dissertation. Simulation studies have been carried out to verify the system performance under different scenarios using a practical load profile and real weather data. The results show that the overall power management strategy is effective and the power flows among the different energy sources and the load demand is balanced successfully.

The DG's impacts on the existing power system are also investigated in this dissertation. Analytical methods for finding optimal sites to deploy DG sources in power systems are presented and verified with simulation studies.

## CHAPTER 1

### INTRODUCTION

Energy is essential to everyone's life no matter when and where they are. This is especially true in this new century, where people keep pursuing higher quality of life. Among different types of energy, electric energy is one of the most important that people need everyday. In this chapter, an overview is given on the world energy demand, electricity consumption and their development trend in the near future. The electric power generation technologies based on different energy sources are also reviewed in the chapter. Finally, the need for this research work is addressed and the scope of the research is also defined.

#### World Energy Demands

The world energy consumption is expected to grow about 57% in the next two decades [1.1]. Figure 1.1 shows the strong growth of the global energy demand in the past three decades and its projection over the next two decades. The world energy consumption by fuel type in 2002 is also shown in the figure. It is clear that a large part of the total energy is provided by fossil fuels (about 86% in 2002). The future of the global economy growth is highly dependent on whether the ever-increasing energy demand can be met.

Fossil fuels are not evenly distributed around the world, and regional or global conflicts may arise from energy crisis if our economy is still heavily dependent on them. Moreover, during the process of generating and using electrical energy with today's

conventional technologies, the global environment has already been significantly affected and the environment of some regions has been damaged severely. Therefore, it is a big challenge for the whole world to figure out how to generate the needed amount of energy and the types of energy sources.

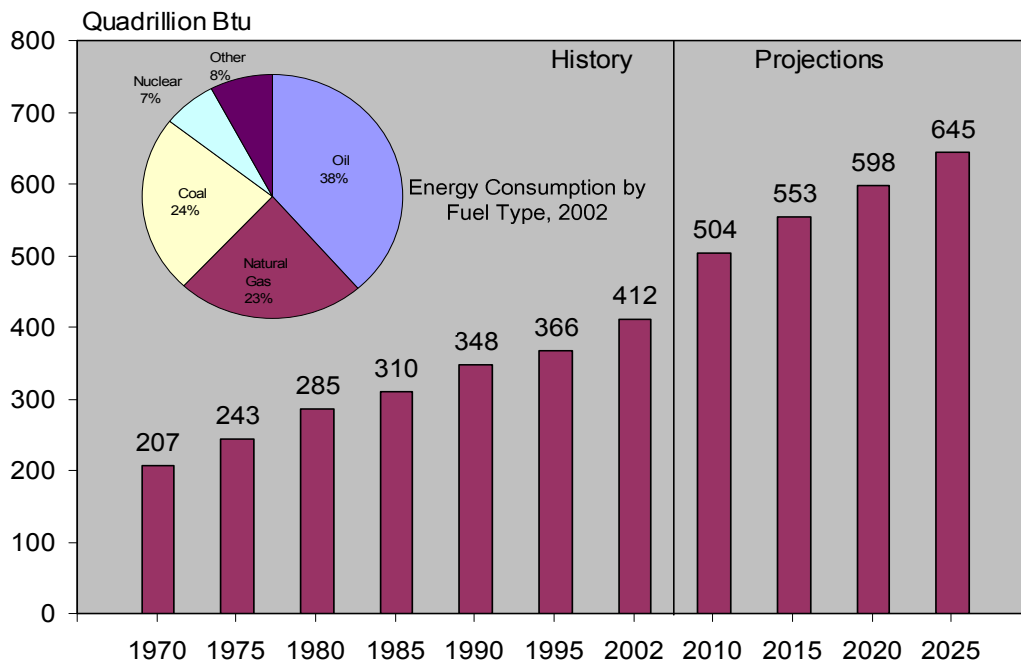


Figure 1.1. World Energy Consumption 1970-2025 [1.1]-[1.3]

### World and U.S. Electricity Demands & Generation

The world electric energy consumption is expected to increase by more than 50% by 2025 [1.1]-[1.3], shown in Figure 1.2. About 24% of the world total electricity demand in 2003 is consumed by U.S. (Figure 1.2), and it is anticipated to grow 44% in the first quarter of the new century [1.1]-[1.3]. Moreover, the electricity demand from emerging economic regions such as China and India is increasing even faster.

To meet the future global electricity demand, an extensive expansion of installed generating capacity is necessary. Worldwide installed electricity generating capacity is expected to increase from 3,626 GW (gigawatts) in 2003 to 5,495 GW in 2025 (Figure 1.3) at a 2.2-percent average annual growth rate [1.1]-[1.4].

The percentage of U.S. electricity generating capacity over the total world generating capacity is declining. It drops from around 25% in 2003 to about 20% in 2025 (Figure 1.3) according to the estimation of Energy Information Administration (EIA). Nevertheless, the electricity generation capacity of U.S. is still expected to grow about 38% from 2000 to 2025 [1.1]. By comparing the electricity consumption data in Figure 1.2 and the generation capacity data in Figure 1.3, it is noted that the U.S. electricity consumption is growing faster than the generation capacity. If this trend is not reversed, it is expected that the U.S. would have to import more electric power in the near future. Otherwise, the reserve margin of the whole power system in the U.S. will shrink, which will compromise system stability and power delivery reliability.

Electricity can be generated in many ways from various energy sources. Electric power can be generated by conventional thermal power plants (using fossil fuels, or nuclear energy), hydropower stations, and other alternative power generating units (such as wind turbine generators, photovoltaic arrays, fuel cells, biomass power plants, geothermal power stations, etc.). Fossil fuels (including coal, oil and natural gas) and nuclear energy are not renewable, and their resources are limited. On the other hand, renewable energy resources (wind and solar energy for example) can self-renew and sustain for future use. Figure 1.4 shows the world and US net electricity generation by type in 2002. It is clear from this figure that more than 80% of the world and US

electricity generation are still contributed by the conventional fossil-fuel thermal power plants and nuclear power plants [1.1], [1.4]. Except for the hydroelectric power, the portion of the electricity generated from other renewable/alternative sources is very small. In the following of this section, an overview will be given on the current status and the future development trend of different types of electricity generation.

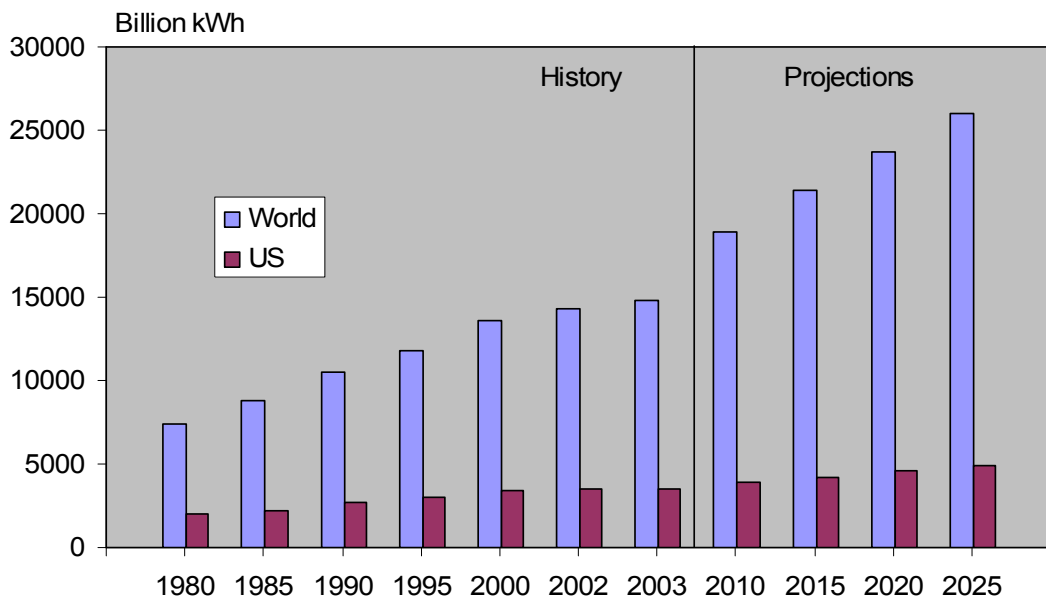


Figure 1.2. World and US Electricity Demands, 1980-2025 [1.1]-[1.3].

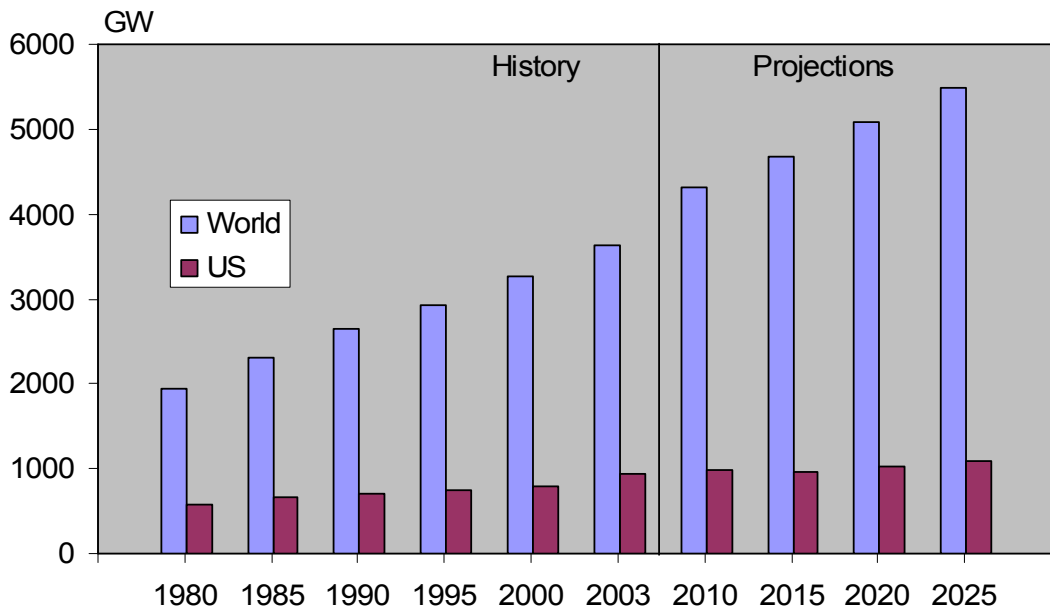


Figure 1.3. World Electricity Generating Capacity 1980-2025 [1.1], [1.4]

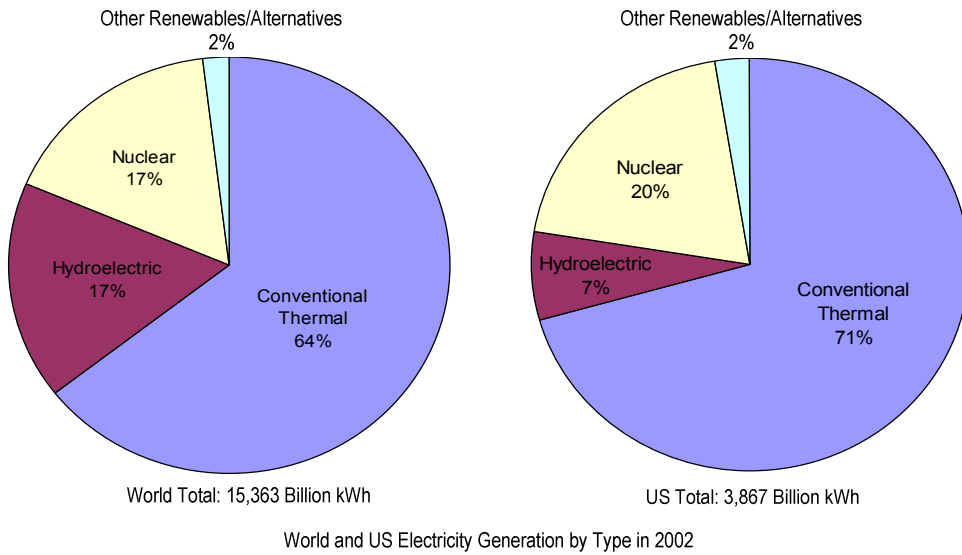


Figure 1.4. The world and US net electricity generation by type in 2002 [1.1], [1.4].

### Conventional Thermal Electric Power Generation

Conventional thermal power plants generate electric power using fossil fuels, namely, coal, oil and natural gas. In a fossil-fired thermal power plant, water passes through a boiler, heated by burning fossil fuels, to produce high temperature and high pressure steam. The steam then enters a multi-stage steam turbine which operates a generator to produce electricity.

Coal. Due to its low price and relative abundant reserves, coal is, and should continue to be, the dominant fuel for electricity generation of the world and the U.S., shown in Figures 1.5 and 1.6. The United States and China currently are the leaders in terms of installed coal-fired capacity. Both countries have large amount of coal reserves. Even under the pressure of Kyoto Protocol for reducing greenhouse gas and other air pollutant emissions, coal-fired electricity generation capacity is still expected to grow by 1.5 percent per year, and coal is expected to fuel 38% (Figure 1.5) of the electricity generation of the entire world by 2025 [1.3]. However, this trend could be changed if higher pressure is applied to implement environment protection policies, such as the Kyoto Protocol and the Clean Air Act in the U.S.

Natural Gas. Natural-gas-fired power generation technology is an attractive option for new power plants because of its fuel efficiency, operating flexibility, rapid deployment, and lower installation costs compared to other conventional generation technologies. Regulatory policies to reduce carbon dioxide emissions could accelerate the switch from coal to gas. However, the amount of natural gas reserve is not as plentiful as

coal. In the U.S., the amount of dry natural gas reserves was 192,513 billion cubic feet in 2004 [1.4]. In the same year, the total natural gas consumption in the U.S. was 22,430.3 billion cubic feet. And about a quarter of this consumption was for electricity generation. If dry natural gas was the only means of reserving and the amount of reserves would not change, then that amount could only supply the U.S. natural gas needs for less than 10 years at the consumption rate of 2004 [1.4].

Oil. On the world average, oil is not and will not be a major source for electric power. The main reason is that the major petroleum products are produced for transportation purposes, such as automobile gasoline, jet fuel, etc, but not for electricity generation. The first problem with oil is that the whole world is short of its reserves while the demand for oil keeps increasing. The oil demand is expected to grow at about 2.5% per year [1.5]. The amount of proven crude oil reserves in the world in 2005 is 1277 billion barrels<sup>1</sup>. The world oil consumption in 2002 was 78.2 million barrels per day [1.5]. If we could keep this consuming rate unchanged, then the whole world oil reserves could only sustain for less than 45 years. Even if the more optimistic data, 2947 billion barrels (including reserve growth and the estimated undiscovered oil reserves) of the oil reserves are used, the world will still run out of oil in about one hundred years and forty years under the same consumption rate. Greenhouse gas and air pollutant emission is another big problem with using oil. Moreover, there are many other problems associated with oil, such as high oil price and the instability of some oil production regions.

---

<sup>1</sup> 1 barrel = 42 U.S. gallons.

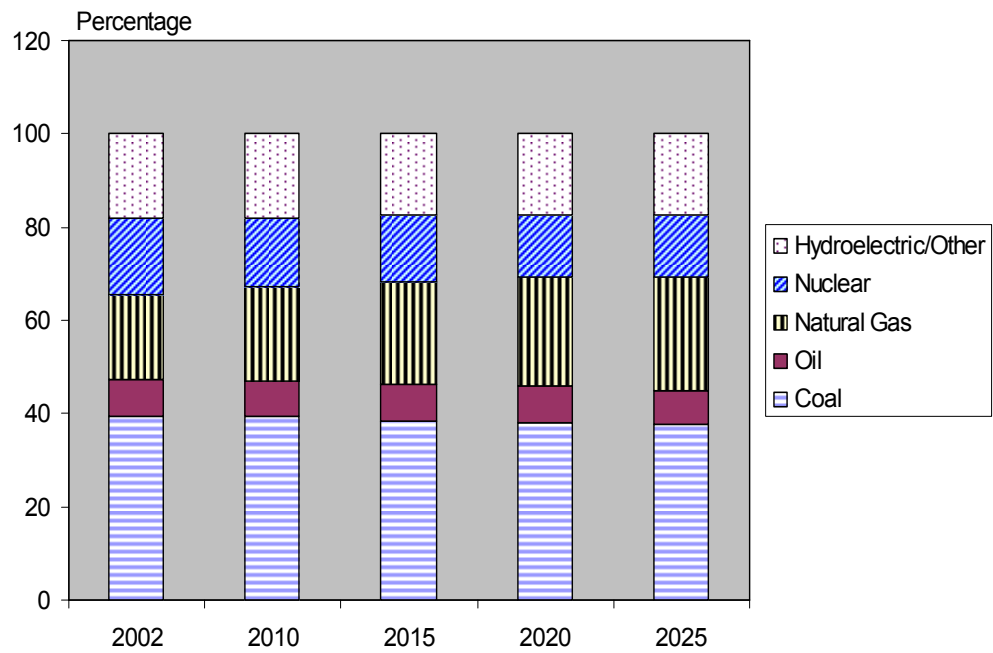


Figure 1.5. Fuel shares of world electricity generation, 2002-2025 [1.1], [1.2].

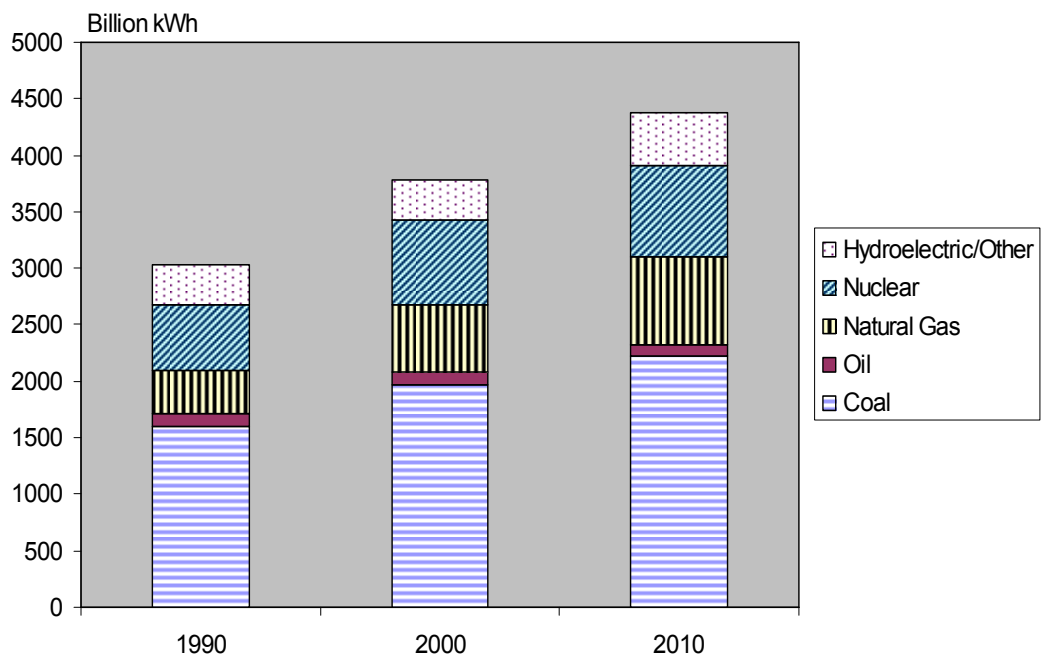


Figure 1.6. U.S. electricity generation by fuel types [1.4].

### Nuclear Power

Nuclear energy is an important source for electricity generation in many countries. In 2003, 19 countries depended on nuclear power for at least 20 percent of their electricity generation [1.6]. France is the country which has the highest portion (78.1%) of the electricity generated by nuclear power [1.6]. Though the percentage of nuclear electric power over the total national electricity generation is not very high (about 20%), the U.S. is still the world's largest producer of electric power using nuclear fuels. Higher fossil fuel prices and the entry into force of the Kyoto Protocol could result in more electricity generated by nuclear power. In the emerging economic regions, such as China and India, nuclear power capacity is expected to grow [1.1]. However, nuclear power trends can be difficult or even be reversed due to a variety of reasons. The safety of a nuclear power plant is still the biggest concern. And how to deposit nuclear wastes can always be a discussion topic for environmentalists. Moreover, the nuclear fuel (Uranium) is not renewable. The U.S. Uranium reserves are 1414 million pounds at the end of 2003 [1.6]. This amount of reserve can supply the U.S. for about 270 years at the Uranium annual consumption rate of 2,407.2 metric tons (2002 statistical data).

### Hydroelectric Power

Today, hydropower is still the largest renewable source for electricity generation in the world. In 2002, more than 18% of the world electricity was supplied by renewable sources, most of which comes from hydropower, shown in Figure 1.5 [1.1], [1.2]. The world hydroelectric capacity is expected to grow slightly due to large hydroelectric projects in the regions with emerging economies. The Three Gorges hydropower project

in China is now the biggest hydropower project ever carried out in the world. Upon the completion of the Three Gorges project in 2009, it will have a generating capacity of 18.2 GW (26 units total and 700MW for each unit) [1.7].

Although the hydropower is clean and renewable, there are still some problems associated with it. First, the big dams and reservoirs cause a lot of environmental concerns and social disputes. Second, the relocation of reservoir populations can be a big problem. For example, over a million people will be relocated for the Three Gorges project [1.8]. Moreover, hydropower is not as abundant as desired. In the U.S., for example, the available hydropower sources (except in Alaska) have almost been explored. All these factors determine that hydropower can not play a major role in the future new electricity supply in the world.

### Why Alternative/Renewable Energy?

The term “alternative energy” is referred to the energy produced in an environmentally friendly way (different from conventional means, i.e., through fossil-fuel power plants, nuclear power plants and hydropower plants). Alternative energy considered in this dissertation is either renewable or with high energy conversion efficiency. There is a broad range of energy sources that can be classified as alternative energy such as solar, wind, hydrogen (fuel cell), biomass, and geothermal energy.

Nevertheless, as mentioned in the previous section, at the present the majority of the world electricity is still generated by fossil fuels, nuclear power and hydropower. However, due to the following problems/concerns for conventional energy technologies, the renewable/alternative energy sources will play important roles in electricity

generation. And, sooner or later, today's alternatives will become tomorrow's main sources for electricity.

1) Conventional energy sources are not renewable: As discussed in the above section, both the fossil fuels (coal, and oil and natural gas) and nuclear fuels are not renewable. The reserves of these fuels will run out some day in the future. A long term energy development strategy is therefore important for sustainable and continuous economy growth.

2) Conventional generation technologies are not environmentally friendly: Although there have been substantial improvements in the technologies (such as desulfurization) for reducing emissions, conventional thermal power plants still produce a large amount of pollutant gases, such as sulfur oxide and nitrogen oxide [1.9]. The radioactive waste of nuclear power plants is always a big concern to the environment. The dams and reservoirs of hydropower can change the ecological systems of the original rivers and the regions of the reservoirs substantially [1.10].

3) The cost of using fossil and nuclear fuels will go higher and higher: Since these fuel sources are not renewable, while the world energy demand is steadily increasing, it is obvious that the price of these fuels will go higher. Taking world crude oil price for example, the price has been increased by 57% in the last year [1.11]. Compared to natural gas and petroleum, coal is cheap for electricity generation. However, if the cost for reducing emissions is taken into account, the actual price of generating electricity from coal would be much higher. The growing cost of using conventional technologies will make alternative power generation more competitive and will justify the switchover from conventional to alternative ways for electric power generation.

4) Hydropower sources are not enough and the sites are normally far away from load centers: Hydropower is good because it is clean and renewable. However, as mentioned in the previous section, the total amount of hydropower that can be explored is not enough. And, in many developed countries, the hydropower has been almost explored fully. Moreover, hydroelectric sites normally are in remote areas. Long transmission lines add more difficulties and cost in exploring hydropower since the permission of the right-of-way for transmission lines is much more difficult to obtain than before.

5) Political and social concerns on safety are pushing nuclear power away: In general, government energy strategy guides the development of nuclear power. There are almost no cases that corporations or utilities make the decisions to build nuclear power plants based on their economic considerations. Accidents at the Three Mile Island nuclear power plant in the United States in 1979 and Chernobyl in the Soviet Union in 1986 fed people full of fears. No body wants to be a neighbor of a nuclear power plant or facility. This changes the government energy policy substantially. In the U.S., there is no new order for nuclear units in the near future [1.6]. In Europe, several countries, including Italy, Austria, Belgium, Germany, and Sweden stepped out from nuclear power even before the Chernobyl disaster [1.1].

On the other hand, compared with conventional electricity generation technologies, alternative/renewable power have the following advantages:

1) Renewable energy resources are not only renewable, but also abundant: For example, according to the data of 2000, the U.S. wind resources can produce more electricity than the entire nation would use [1.12]. The total solar energy from sun in a day at the earth surface is about 1000 times more than the all fossil fuels consumption

[1.9].

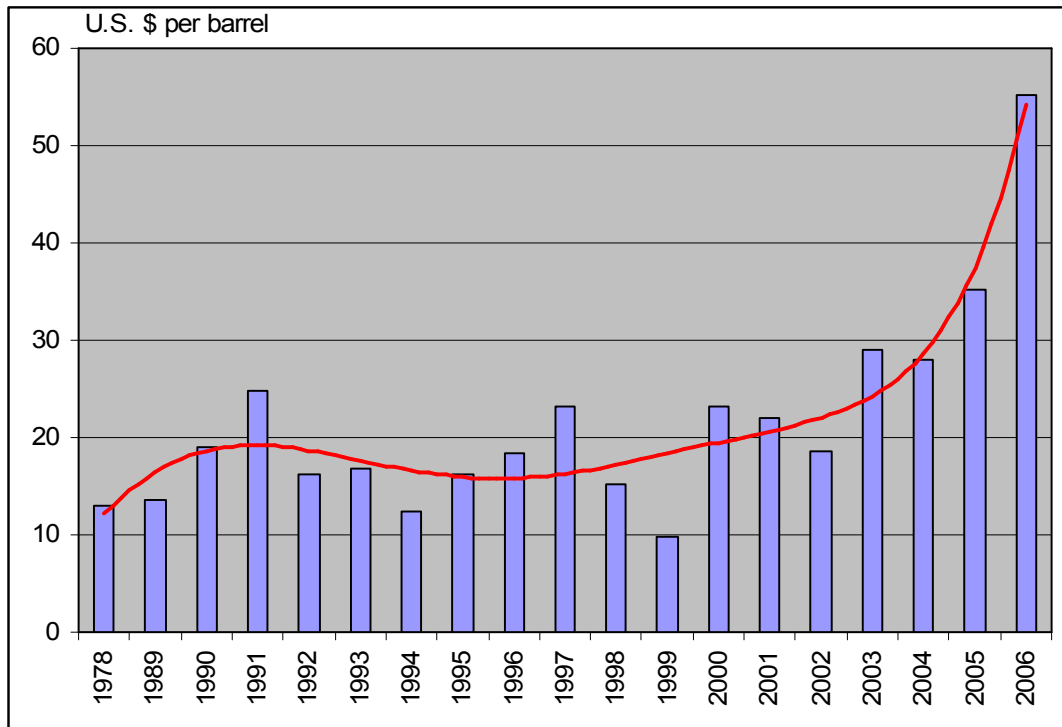


Figure 1.7. World crude oil prices 1978-2006 [1.11].

(Note: The price is based on the first week data of January in each year.)

2) Fuel cell systems have high energy efficiency: The efficiency of low temperature proton exchange membrane (PEM) fuel cells is around 35-45% [1.13]. High temperature solid oxide fuel cells (SOFC) can have efficiency as high as 65% [1.14]. The overall efficiency of an SOFC based combined-cycle system can even reach 70% [1.14].

3) Renewable energy and fuel cell systems are environmentally friendly: From these systems, there is zero or low emission (of pollutant gases) that cause acid rain, urban smog and other health problems; and, therefore, there is no environmental cleanup or waste disposal cost associated with them [1.9].

4) Different renewable energy sources can complement each other: Though renewable

energy resources are not evenly distributed throughout the world, every region has some kinds of renewable energy resources. At least, sunlight reaches every corner in the world. And different energy resources (such as solar and wind energy) can complement each other. This is important to improve energy security for a nation like the U.S. which is currently dependent on the foreign energy sources.

5) These renewable/alternative power generation systems normally have modular structure and can be installed close to load centers as distributed generation sources (except large wind and PV farms). Therefore, no high voltage transmission lines are needed for them to supply electricity.

In general, due to the ever increasing energy consumption, the rising public awareness for environmental protection, the exhausting density of fossil-fuel, and the intensive political and social concerns upon the nuclear power safety, alternative (i.e., renewable and fuel cell based) power generation systems have attracted increased interest.

### Recent Progress in Alternative/Renewable Energy Technologies

In the following section, the recent progress in wind power, solar power, fuel cells, and other renewable energy technologies will be reviewed. An overview on their applications as distributed generation will also be given.

#### Wind Energy

Wind energy is one of world's fastest-growing energy technologies. Both the global and U.S. wind energy experienced a record year in 2005. According to the figures

released by the Global Wind Energy Council (GWEC), in 2005 there was a 43.4% increase in annual additions to the global market and a 564.2% increase in the annual addition to the U.S. wind power generation capacity. Last year was just one of the record years. In the past 11 years, the global wind energy capacity has increased more than 17 times — from 3.5 GW in 1994 to almost 60 GW by the end of 2005 (Figure 1.8). In the United States, wind power capacity has increased more than 3 times in only 5 years (from 2554 MW in 2000 to 9149 MW by the end of 2005), also shown in Figure 1.8. The future prospects of the global wind industry are also very promising even based on a conservative projection that the total global wind power installed could reach 160 GW by 2012. A spread of new countries across the world will participate in the global wind energy market in the next ten years [1.15].

The phenomenal worldwide growth of the wind industry during the past decade can be attributed to supportive government policies and the fast development in innovative cost-reducing technologies. In the U.S., the work conducted under the Wind Energy Program's Next Generation Wind Turbine (1994 – 2003) and WindPACT (1999 – 2004) projects under the Department of Energy (DOE) resulted in innovative designs, high power ratings, and increased efficiencies [1.16]. All these technological advances have led to dramatic reductions in cost of electricity (COE) — from \$0.8/kWh in the early 1980s to about \$0.04/kWh today for utility-scale (normally  $\geq 750$  kW) turbines [1.16], [1.9]. Although this drop in COE has been impressive, more research work is still needed to make wind power more competitive. Development in aerodynamic efficiency, structural strength of wind turbine blades, larger turbine blades and higher towers, variable speed generators, and power controllers will help to reduce the COE further. The

DOE goal is to reduce the COE produced by land-based utility-scale turbines located in Class 4 wind resource areas (areas with 5.8 m/s wind speed at a 10-m height) to \$0.03/kWh by 2012 [1.16].

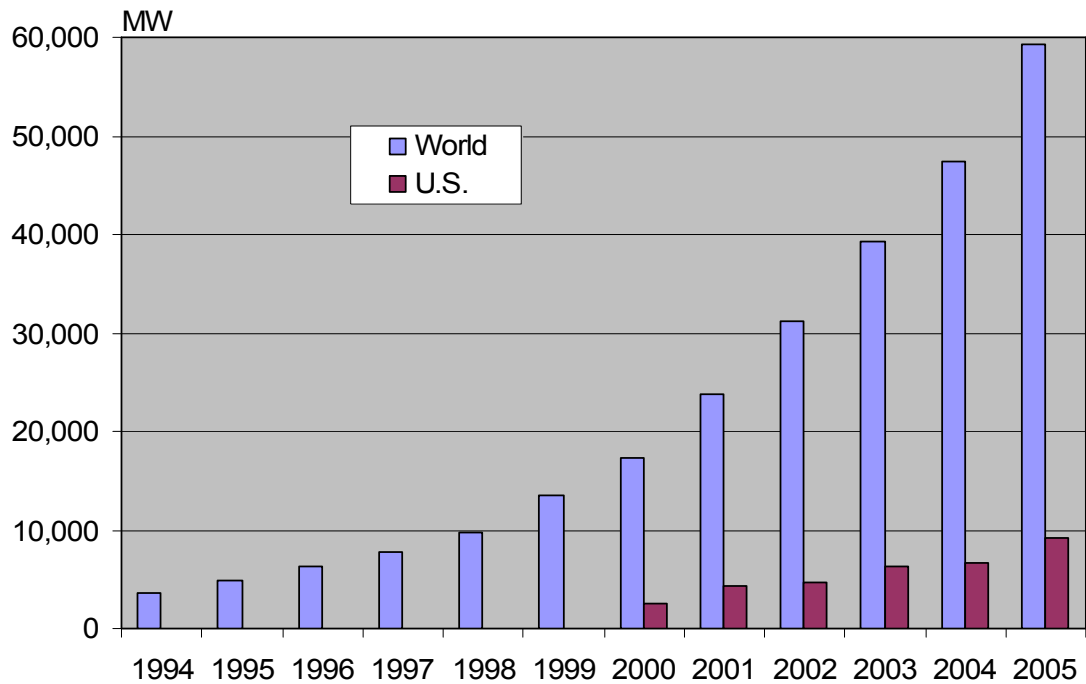


Figure 1.8. The world and the U.S. wind power cumulative capacity [1.15], [1.16].

### Photovoltaic Energy

Solar energy basically is the ultimate source for all kinds of energy resources on the earth with only a few exceptions such as geothermal energy. There are normally two ways to generate electricity from sunlight: through photovoltaic (PV) and solar thermal systems. In this section and this dissertation, only photovoltaic energy and system will be discussed.

Just like the growth of wind energy, PV energy is another fast growing renewable energy technology. Though the absolute size of global solar power generation capacity is

much smaller than wind power, it has been increased even faster than wind power during the past dozen years (from 1992-2004) [1.17]. In terms of the market for PV power applications in the IEA-PVPS<sup>2</sup> (International Energy Agency – Photovoltaic Power Systems Programme) countries, the total installed PV capacity has been increased more than 23 times – from the 110 MW in 1992 to 2596 MW in 2004 (Figure 1.9) [1.17].

Due to improvements in semiconductor materials, device designs and product quality, and the expansion of production capacity, capital costs for PV panels have been decreased significantly, from more than \$50/W in the early of 1980s [1.9] to about 3.5\$ to 4.5\$ per watt in 2004 [1.17]. The cost of electricity produced by PV systems continues to drop. It has declined from \$0.90/kWh in 1980 to about 0.20\$/kWh today [1.9]. In the U.S., the DOE goal is to reduce the COE of PV to \$0.06/kWh by 2020 [1.19]. However, PV energy is still usually more expensive than energy from the local utility. Currently, the initial investment of a PV system is also higher than that of an engine generator. Nevertheless, there are many applications for which a PV system is the most cost-effective long-term option, especially in remote areas, such as power for remote telecommunications, remote lighting and signs, remote homes and recreational vehicles.

---

<sup>2</sup> There are 19 countries participating in the IEA PVPS program. They are Australia, Austria, Canada, Denmark, France, Germany, Israel, Italy, Japan, Korea, Mexico, the Netherlands, Norway, Portugal, Spain, Sweden, Switzerland, U.K., and U.S.A. Over 90% of the world total PV capacity is installed in the IEA-PVPS countries. The top three PV countries, Japan, Germany, and the U.S., are all the members of the organization.

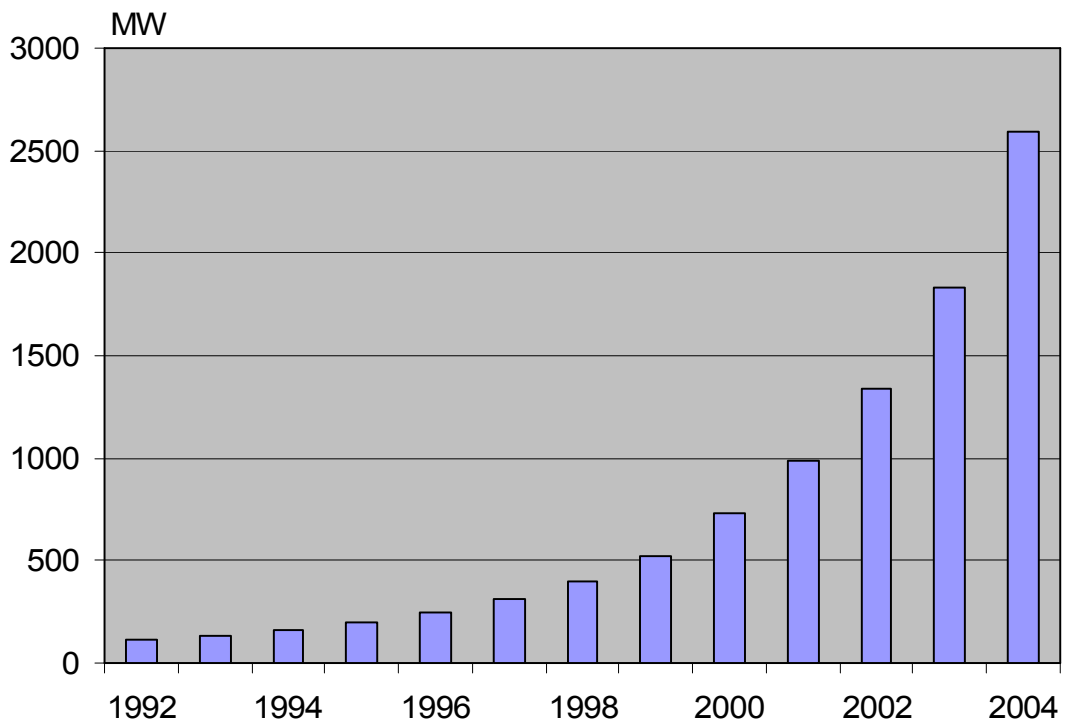


Figure 1.9. Cumulative Installed PV capacity in IEA PVPS countries [1.17].

### Fuel Cells

Fuel cells (FCs) are static energy conversion devices that convert the chemical energy of fuel directly into DC electrical energy. Fuel cells have a wide variety of potential applications including micro-power, auxiliary power, transportation power, stationary power for buildings and other distributed generation applications, and central power.

Since entering the new century, fuel cell technologies have experienced exponential growth, shown in Figure 1.10 [1.20]. The total number of fuel cell applications reached 14,500 in 2005 [1.20]. Government policies, public opinion, and technology advance in fuel cells, all contributed to this phenomenal growth.

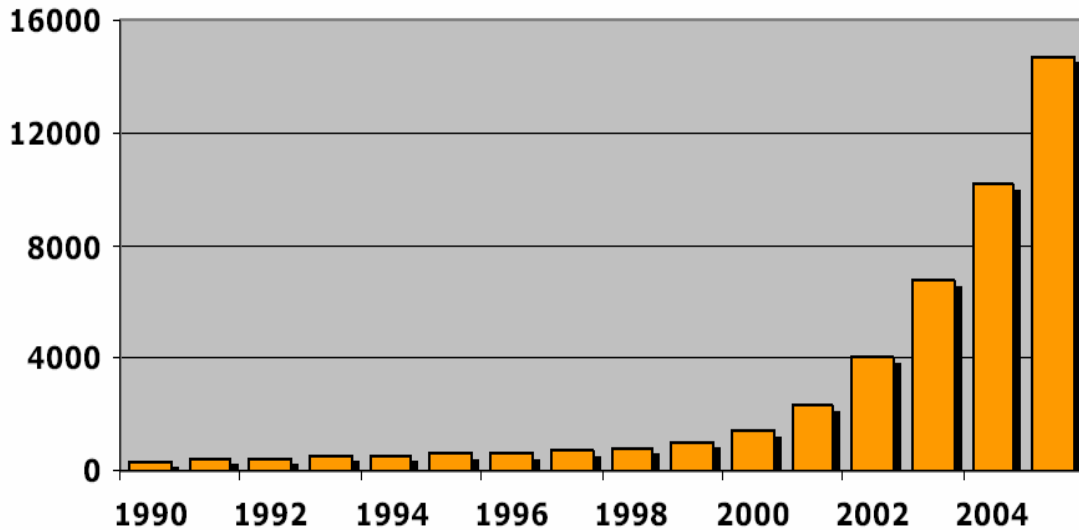


Figure 1.10. Cumulative installed FC units world-wide, 1990-2005 [1.20].

Among different types of fuel cells, polymer electrolyte membrane fuel cells (PEMFC) and solid oxide fuel cells (SOFC) both show great potentials in transportation and DG applications<sup>3</sup> [1.13], [1.20]. Compared with conventional power plants, these fuel cell DG systems have many advantages such as high efficiency, zero or low emission (of pollutant gases) and flexible modular structure. Fuel cell DGs can be strategically placed at any site in a power system (normally at the distribution level) for grid reinforcement, deferring or eliminating the need for system upgrades, and improving system integrity, reliability and efficiency. Moreover, as a byproduct, high-temperature fuel cells also generate heat that makes them suitable for residential, commercial, or industrial applications, where electricity and heat are needed simultaneously [1.13], [1.21].

<sup>3</sup> Vehicle application is still the main market for PEMFC though it also has high potential for stationary power generation. For SOFCs, stationary power generation is their main application. But they do have a foothold in the transport market as well with new planar design.

The DOE recently updated its “Hydrogen, Fuel Cells and Infrastructure Technologies Program’s Multi-Year Research, Development and Demonstration Plan”, written in 2003 [1.22]. In the Plan, it lays out industry targets for key fuel cell performance indices such as cost, durability and power density. In 1999, the Solid State Energy Conversion Alliance (SECA) was founded for bringing together government, industry, and the scientific community to promote the development of SOFC. Through these years collaborative work among the government, industry, national labs and universities, great advances in fuel cell technologies have been achieved in many aspects. These address FCs a bright future although extensive work is still needed to be done before they can really play main roles in energy market. Table 1.1 gives the current status and the DOE goals for PEMFC [1.22], [1.23]. Table 1.2 summaries the current development stage of SOFC and SECA targets [1.24]-[1.26]. It is noted from the two tables that the possibility of reaching the ultimate DOE and SECA goals is high.

#### Other Renewable Energy Sources

In addition to PV and wind energy, there are many other renewable energy resources, such as biomass, geothermal energy, solar thermal energy, and tidal power. These energy resources can all be utilized to generate electricity. Among them, biomass and geothermal energy technologies have the leading generation capacity in the U.S [1.9].

TABLE 1.1. CURRENT STATUS AND THE DOE TARGETS <sup>A</sup> FOR  
PEMFC STACK <sup>B</sup> IN STATIONARY APPLICATIONS

Characteristics	Units	Current Status	2010 Goal
Stack power density	W/L	1330	2000
Stack specific power	W/kg	1260	2000
Stack efficiency @ 25% of rated power	%	65	65
Stack efficiency @ rated power	%	55	55
Precious metal loading	g/kW	1.3	0.3
Cost	\$/kWe	75	30
Durability with cycling	hours	2200 <sup>C</sup>	5000
Transient response (time for 10% to 90% of rated power)	sec	1	1
Cold startup time to 90% of rated power @ -20 °C ambient temperature	sec	100 <sup>C</sup>	30
Survivability	°C	-40	-40

A: Based on the technical targets reported in [1.22] for 80-kWe (net) transportation fuel cell stacks operating on direct Hydrogen

B: Excludes hydrogen storage and fuel cell ancillaries: thermal, water, air management systems

C: Based on the performance data reported by Ballard in 2005 [1.23].

Biomass can be burned directly, co-fired with coal, or gasified first and then used to generate electricity. It can also be used to generate bio-fuels, such as ethanol. Most of today's U.S. biomass power plants use direct-combustion method. In 2004, the total

generation capacity of biomass reached 9709 MW, about 1% of the total U.S. electric capacity [1.27].

TABLE 1.2. CURRENT STATUS AND THE SECA TARGETS FOR  
3-10 kW SOFC MODULE IN STATIONARY APPLICATIONS

Phase	I <sup>A</sup>	Current Status	II	III (By 2010)
Cost	800\$/kW	724\$/kW <sup>B</sup>	*	\$400/kW
Efficiency	35-55%	41% <sup>b</sup>	40-60%	40-60%
Steady State				
Test Hours	1,500	1,500	1,500	1,500
Availability	80%	90% <sup>B</sup>	85%	95%
Power Degradation per 500 hours	≤2%	1.3% <sup>C</sup>	≤1%	≤0.1%
Transient Test				
Cycles	10	n/a	50	100
Power Degradation after Cycle Test	≤1%	n/a	≤0.5%	≤0.1%
Power Density	0.3W/cm <sup>2</sup>	0.575W/cm <sup>2D</sup>	0.6W/cm <sup>2</sup>	0.6W/cm <sup>2</sup>
Operating Temperature	800 °C	700-750 °C <sup>C</sup>	700 °C	700 °C

\*: Evaluate the potential to achieve \$400/kW [1.24]

A: The goals of Phase I have been achieved. GE is the first of six SECA industry teams to complete phase I of the program [1.25].

B: Based on the data reported by GE

C: Based on the data reported by FuelCell Energy [1.26]

D: Based on the data reported by Delphi [1.25]

Geothermal energy can be converted into electricity by three technologies: dry steam, flash and binary cycle. The most common type of geothermal plants is flash power plant while the world largest geothermal plant is of the dry steam type [1.28]. The dry stream geothermal power plant at The Geysers in California is the largest geothermal power plant in the world, with a capacity of 2000 MW [1.9]. However, due to the limited amount of available geothermal heat resources, one will not expect to see any considerable growth in this area. Actually the geothermal generation capacity in the U.S. declined from 2793MW in 2000 to 2133 MW in 2004 [1.27]. Nevertheless, it can be an important energy source in remote areas where geothermal resources are available and abundant.

#### Distributed Generation Applications

The ever-increasing need for electrical power generation, steady progress in the power deregulation and utility restructuring, and tight constraints over the construction of new transmission lines for long distance power transmission have created increased interest in distributed power generation. DG sources are normally placed close to consumption centers and are added mostly at the distribution level. They are relatively small in size (relative to the power capacity of the system in which they are placed; and normally less than 10 MW) and modular in structure. These DG devices can be strategically placed in power systems for grid reinforcement, reducing power losses and on-peak operating costs, improving voltage profiles and load factors, deferring or eliminating the need for system upgrades, and improving system integrity, reliability and efficiency [1.33].

The technology advances in renewable energy sources, fuel cells and small generation techniques provide a diverse portfolio for DG applications. Table 1.3 shows the candidate technologies for DG systems. The DOE proposed a strategic plan for distributed energy sources in 2000 [1.29]. The energy market with DG sources in 2020 was envisioned in the plan as *“The United States will have the cleanest and most efficient and reliable energy system in the world by maximizing the use of affordable distributed energy resources”* [1.29]. To achieve this ultimate goal, the DOE also set sub-goals for DG development. The long-term goal by 2020 is *“to make the nation’s energy generation and delivery system the cleanest and most efficient, reliable, and affordable in the world by maximizing the use of cost efficient distributed energy resources.”* The mid-term by 2010 is to reduce costs, to increase the efficiency and reliability of distributed generation technologies, and to add 20% of new electric capacity. By the end of 1999, about 22GW distributed energy systems with 18 GW backup units were installed across the US [1.31]. According to EIA, U.S. generation capacity history and forecast data, 198 GW of new capacity is needed during the period between 2000 and 2010 [1.4]. Based on the mid-term goal, 20% (39.6 GW) of the new addition should come from DG systems. This means about 4.4% annual growth rate in DG capacity.

TABLE 1.3. TECHNOLOGIES FOR DISTRIBUTED GENERATION SYSTEMS [1.30]

Technology	Size	Fuel	Electrical Efficiency (% LHV)
Combustion Turbine Combined Cycle	50-500 MW	Natural gas, liquid fuels	50-60
Industrial Combustion Turbine	1-50 MW	Natural gas, liquid fuels	25-40
Internal Combustion Turbine/(Reciprocating Engine)	1kW – 10 MW	Natural gas, diesel, oil, propane, gasoline, etc	25-38
Mircroturbine	27-400 kW	Landfill gas, propane, natural gas and other fuels	22-30
Stirling Engine	1.1-5.0kW	Any	18-25
Fuel Cells	1kW	Natural gas, H <sub>2</sub> , other H <sub>2</sub> -rich fuels	35-60
Photovoltaic	1W – 10MW	Renewable	5-15 <sup>A</sup>
Wind Turbine	0.2kW – 5MW	Renewable	< 40
Biomass <sup>B</sup>	Several kW – 20 MW	Renewable	~ 20

A: PV cell energy conversion efficiency

B: Based on the data reported in [1.9]

### Need for the Research

The ever increasing energy consumption, rapid progress in wind, PV and fuel cell power generation technologies, and the rising public awareness for environmental protection have turned alternative energy and distributed generation as promising research areas. Due to natural intermittent properties of wind and solar irradiation, stand-alone wind/PV renewable energy systems normally require energy storage devices or some other generation sources to form a hybrid system. Because some of renewable energy sources can complement each other (section 1.3), multi-source alternative energy systems (with proper control) have great potential to provide higher quality and more reliable power to customers than a system based on a single resource. However, the issues on optimal system configuration, proper power electronic interfaces and power management among different energy sources are not resolved yet. Therefore, more research work is needed on new alternative energy systems and their corresponding control strategies.

Fuel cells are good energy sources to provide reliable power at steady state, but they cannot respond to electrical load transients as fast as desired. This problem is mainly due to their slow internal electrochemical and thermodynamic responses [1.32]. The transient properties of fuel cells need to be studied and analyzed under different situations, such as electrical faults on the fuel cell terminals, motor starting and electric vehicle starting and acceleration. Therefore, dynamic fuel cell models are needed to study those transient phenomena and to develop controllers to solve or mitigate the problem.

Fuel cells normally work along with power electronic devices. One problem is that there is not adequate information exchange between fuel cell manufacturers and power electronic interface designers. Without adequate knowledge about the area of each other, the fuel cell manufacturers normally model the power electronic interface as an equivalent impedance while the power electronic circuit designers take the fuel cell as a constant voltage source with some series resistance. These inaccurate approaches may cause undesired results when fuel cells and their power electronic interfaces are connected together. It is important and necessary to get a better understanding of the impact of power electronic interface on fuel cell's performance and of the fuel cell's impact on power electronic interfacing circuits. Dynamic model development for fuel cells using electrical circuits can be a solution so that the researchers in both areas can understand each other. Moreover, it will provide a more efficient way to integrate the fuel cells and power electronic devices together.

Distributed generation devices can pose both positive and negative impacts on the existing power systems [1.33]. These new issues have led DG operation to be an important research area. Research on optimal placement (including size) of DGs can help obtain maximum potential benefits from DGs.

### Scope of the Study

Although there are many types of alternative/renewable resources, the alternative sources in this dissertation are confined to wind, PV and fuel cells for the research on the proposed hybrid alternative energy systems. The main focus is given to modeling, validation and control for fuel cells, and fuel cell based stand-alone and grid-connected systems. Two types of fuel cells will be modeled and used in the dissertation, PEMFC and SOFC. The ultimate goal of this dissertation is to model a multi-source alternative DG system consisting of wind turbine(s), PV arrays, fuel cells and electrolyzers, and to manage the power flows among the different energy resources in the system. The optimal placement of DG sources in power systems is also investigated on system operation level.

### Organization of the Dissertation

After the introduction conducted and the reason for the research explained in this chapter, Chapter 2 reviews the fundamentals of electrochemistry, thermodynamics, power electronics, and the alternative energy technologies including wind, PV and fuel cells. Chapter 3 introduces hybrid energy systems, gives possible ways of system integration and presents a proposed hybrid wind/PV/FC energy system. Chapter 4 describes the models for the components in the proposed system, discussed in Chapter 3. Power electronic interfacing circuits with appropriate controllers are discussed in Chapter 4 as well.

Chapters 5 and 6 focus on control for fuel cell based systems. Control for grid-connected fuel cell systems is discussed in Chapter 5. In Chapter 6, load mitigation control for stand-alone fuel cell systems is investigated.

The overall control scheme development for the proposed multi-source alternative system is given in Chapter 7. Simulation results under different scenarios are given and discussed in the chapter. The optimal placement of DG sources in power systems (both radial feeders and networked systems) is investigated in Chapter 8.

## REFERENCES

- [1.1] International Energy Outlook 2005, Energy Information Administration (EIA), <http://www.eia.doe.gov/iea>.
- [1.2] International Energy Annual 2003, EIA, <http://www.eia.doe.gov/iea>.
- [1.3] System for the Analysis of Global Energy Markets 2005, EIA, <http://www.eia.doe.gov/iea>.
- [1.4] Annual Energy Outlook 2006 (Early Release), EIA, <http://www.eia.doe.gov/>.
- [1.5] World Oil Market, International Energy outlook - International Petroleum (Oil) Reserves and Resources, EIA, <http://www.eia.doe.gov/iea>.
- [1.6] U.S. Nuclear Generation of Electricity, EIA, <http://www.eia.doe.gov/iea>
- [1.7] Online, [http:// www.3g.gov.cn](http://www.3g.gov.cn).
- [1.8] Million Relocates of Unprecedented Scale, <http://www.3g.gov.cn/shuniu/ymsgc/200305170065.htm>.
- [1.9] S.R. Bull, "Renewable Energy Today and Tomorrow," *Proceedings of IEEE*, Vol. 89, No. 8, pp.1216-1221, August 2001.
- [1.10] F.A. Farret and M.G. Simões, *Integration of Alternative Sources of Energy*, John Wiley & Sons, Inc., 2006.
- [1.11] World Crude Oil Prices, EIA, [http://tonto.eia.doe.gov/dnav/pet/pet\\_pri\\_wco\\_k\\_w.htm](http://tonto.eia.doe.gov/dnav/pet/pet_pri_wco_k_w.htm).
- [1.12] M. R. Patel, *Wind and Solar Power Systems*, CRC Press LLC, 1999.
- [1.13] *Fuel Cell Handbook (Sixth Edition)*, EG&G Services, Inc., Science Applications International Corporation, DOE, Office of Fossil Energy, National Energy Technology Lab, Nov. 2002.
- [1.14] O. Yamamoto, "Solid oxide fuel cells: fundamental aspects and prospects," *Electrochimica Acta*, Vol. 45, No. (15-16), pp. 2423-2435, 2000.
- [1.15] Global Power Source, Global Wind Energy Council, <http://www.gwec.net/>
- [1.16] Wind Power Today – Federal Wind Program Highlights, NREL, DOE/GO-102005-2115, April 2005.

- [1.17] Trends in photovoltaic applications: Survey report of selected IEA countries between 1992 and 2004, International Energy Agency Photovoltaics Power Systems Programme (IEA PVPS), September 2005.
- [1.18] Online, [http://www.nrel.gov/analysis/newsletters/2006\\_january.html](http://www.nrel.gov/analysis/newsletters/2006_january.html)
- [1.19] National Status Report 2004 –USA, IEA-PVPS, <http://www.oja-services.nl/iea-pvps/nsr04/usa2.htm>.
- [1.20] Fuel Cell Today 2005 Worldwide Survey, <http://www.fuelcelltoday.com>.
- [1.21] James Larminie and Andrew Dicks, *Fuel Cell Systems Explained, 2<sup>nd</sup> Edition*, John Wiley & Sons, Ltd., 2003.
- [1.22] The Hydrogen, Fuel Cells & Infrastructure Technologies Program Multi-Year Research, Development and Demonstration Plan, February 2005 Version.
- [1.23] Technology "Road Map" –Ballard Power Systems Inc., [http://www.ballard.com/be\\_informed/fuel\\_cell\\_technology/roadmap](http://www.ballard.com/be_informed/fuel_cell_technology/roadmap).
- [1.24] SECA Program Plan, DOE Office of Fossil Energy: The DOE National Energy Technology Laboratory (NETL) and the Pacific Northwest National Laboratory, Jan. 2002.
- [1.25] Significant Milestone Achieved in SECA Fuel Cell Development Program, [http://www.netl.doe.gov/publications/TechNews/tn\\_ge\\_seca.html](http://www.netl.doe.gov/publications/TechNews/tn_ge_seca.html), Jan. 2006.
- [1.26] *Thermally Integrated High Power Density SOFC Generator*, FuelCell Energy Inc., FY 2004 Progress Report.
- [1.27] Renewables and Alternate Fuels, Energy Information Administration (EIA), <http://www.eia.doe.gov/fuelrenewable.html>.
- [1.28] Online, <http://www.eere.energy.gov/geothermal/powerplants.html#flashsteam>.
- [1.29] Strategic Plan for Distributed Energy Resources — Office of Energy Efficiency and Renewable Energy, U.S. Department of Energy, September 2000.
- [1.30] DER Technologies, Electric Power Research Institute (EPRI), October 2002.
- [1.31] Establishing a Goal for Distributed Energy Resources, Distributed Energy Resources: The Power to Choose, on November 28, 2001, by Paul Lemar [http://www.distributed-generation.com/Library/paul\\_lemar.pdf](http://www.distributed-generation.com/Library/paul_lemar.pdf).
- [1.32] C. Wang, M.H. Nehrir, and S.R. Shaw, "Dynamic Models and Model Validation for PEM Fuel Cells Using Electrical Circuits," *IEEE Transactions on Energy Conversion*, vol. 20, no. 2, pp.442-451, June 2005.

- [1.33] C. Wang and M.H. Nehrir, "Analytical Approaches for Optimal Placement of Distributed Generation Sources in Power Systems," *IEEE Transactions on Power Systems*, vol. 19, no. 4, pp. 2068-2076, Nov. 2004.

## CHAPTER 2

## FUNDAMENTALS OF ALTERNATIVE ENERGY SYSTEMS

This chapter reviews the fundamental concepts and principles of energy systems and energy conversion. The overview of the fundamentals of electrochemistry, thermodynamics and alternative energy systems is a good introduction for understanding and modeling of the proposed multi-source alternative energy system discussed in the following chapters.

Energy FormsDefinition of Energy

Energy is defined as the amount of work a physical system is capable of doing. Energy is a fundamental quantity that every physical system possesses. In a broad sense, energy, can neither be created nor consumed or destroyed. However, it may be converted or transferred from one form to other. Generally speaking, there are two fundamental types of energy: transitional energy and stored energy [2.1]. Transitional energy is energy in motion, also called kinetic energy, such as mechanical kinetic energy. Stored energy is energy that exists as mass, position in a force field (such as gravity and electromagnetic fields), etc, which is also called potential energy. More specifically, energy can exist in the following five basic forms:

- (1) Mechanical energy
- (2) Chemical energy
- (3) Electrical and electromagnetic energy

(4) Thermal energy

(5) Nuclear energy

### Mechanical Energy

Mechanical energy is the type of energy associated with moving objects, or objects that have potential to move themselves or others. It can be defined as work used to raise a weight [2.1]. The mechanical kinetic energy of a translating object ( $E_{mt}$ ) with a mass  $m$  at speed  $v$  is:

$$E_{mt} = \frac{1}{2}mv^2 \quad (2.1)$$

For a rotating body with moment of inertia (rotational inertia)  $I$  at angular speed  $\omega$ , its kinetic mechanical energy ( $E_{mr}$ ) is defined as:

$$E_{mr} = \frac{1}{2}I\omega^2 \quad (2.2)$$

Mechanical potential energy is the energy that a given system possesses as a result of its status in a mechanical force field [2.1]. For example, in a gravity field  $g$ , the potential mechanical energy of a body with mass  $m$  at height  $h$  is given as:

$$E_{mpg} = mgh \quad (2.3)$$

As another example, the potential energy of an elastic spring with the spring constant  $k$  at the displacement  $x$  is:

$$E_{mps} = \frac{1}{2}kx^2 \quad (2.4)$$

### Chemical Energy

Chemical energy is the energy held in the chemical bonds between atoms and molecules [2.2]. Every bond has a certain amount of energy. Chemical energy exists as a stored energy form, which can be converted to other energy forms through reactions. First, energy is required to break the bonds - called *endothermic*. Then, energy will be released (called *exothermic*) when these broken bonds combine together to create more stable molecules. If the total energy released is more than the energy taken in, then the whole reaction is called *exothermic*. Otherwise, the reaction is called *endothermic*. The burning of fossil fuels (combustion) is one of the most important *exothermic* reactions for producing energy. Photosynthesis is a good example for *endothermic* reaction since plants use energy from sun to make the reaction happen.

### Electrical and Electromagnetic Energy

Electrical and electromagnetic energy is the energy associated with electrical, magnetic and/or electromagnetic fields. It is normally expressed in terms of electrical and/or electromagnetic parameters. For example, the electro-static energy stored in a capacitor is:

$$E_c = \frac{1}{2} \frac{q^2}{C} \quad (2.5)$$

where  $C$  is the capacitance of the capacitor and  $q$  is the total charge stored.

The magnetic energy stored in an inductor with inductance  $L$  at current  $i$  is:

$$E_m = \frac{1}{2} Li^2 \quad (2.6)$$

Another expression used to represent magnetic energy is [2.3]:

$$E_m = \frac{1}{2} \int_V \mu H^2 dV \quad (2.7)$$

where  $\mu$  is the material permeability,  $H$  is the magnetic field intensity and  $V$  is the object volume under consideration. This expression is especially useful in calculating hysteresis losses inside power transformers.

Radiation energy is one of the forms of electromagnetic energy. The radiation energy only exists in transitional form, and it is given by [2.1]:

$$E_R = h \cdot f \quad (2.8)$$

where  $h$  is the Planck's constant ( $6.626 \times 10^{-34}$  Js), and  $f$  is the frequency of the radiation.

### Thermal Energy

From a macroscopic observation, thermal energy, or heat, can be defined as energy transferred between two systems due to temperature difference [2.4]. From a micro-level point of view, thermal energy is associated with atomic and molecular vibration [2.1]. All other forms of energy can be converted into thermal energy while the opposite conversion is limited by the second law of thermodynamics (which will be explained briefly in section 2.2). Based on this fact, thermal energy can be considered the most basic form of energy [2.1].

### Nuclear Energy

Nuclear energy is a topic irrelevant to this dissertation. But for the completion of the discussion on energy forms, a very brief overview on nuclear energy is also included here. Similar to chemical energy, nuclear energy is also a type of stored energy. The energy will be released as a result of nuclear reaction (normally fission reaction) to produce a more stable configuration. Take the uranium-235 nucleus as an example. When it captures a neutron, it will split into two lighter atoms and throws off two or three new neutrons. The new atoms then emit gamma radiation as they settle into their new more stable states. An incredible amount of energy is released in the form of heat and gamma radiation during the above process. The mass of fission products and the neutrons together is less than the original U-235 atom mass. The mass defect is governed by the famous Einstein's mass-energy equation [2.1]:

$$E = mc^2 \quad (2.9)$$

where  $m$  is the material mass and  $c$  is the speed of light in vacuum ( $\approx 2.998 \times 10^8$  m/s).

### Fundamentals of Thermodynamics

Thermodynamic analysis of energy conversion processes is important for modeling and control of hybrid energy systems. Therefore, in this section, a brief overview of the fundamental concepts and principles of thermodynamics is given.

#### The First Law of Thermodynamics

According to the first law of thermodynamics, the energy of a system is conserved. Energy here is in the form of either of heat or work. This law describes that energy can

neither be created or destroyed but it can be converted from one type to another. The change in the system energy  $dE$  is contributed by the heat entering ( $dQ$ ) the system and the work done by the system ( $dW$ ) to the outside [2.5], [2.6].

$$dE = dQ - dW \quad (2.10)$$

Note that the work in the above equation is the work leaving the system. The system here is an idealized object, which is used to limit our study scope. A system can be isolated from “everything else” in the sense that changes in everything else need not affect its state [2.5]. The external “everything else” is considered to be the environment of the system. Of particular interest is one type of system, called a *simple system* that is not affected by capillarity, distortion of solid phase, external force fields (electromagnetic and gravitational), or internal adiabatic walls [2.5]. For a simple system, the total system energy is equal to the total system internal energy, denoted by symbol  $U$  [2.5]. In this dissertation, we only consider simple systems.

$$E = U \quad (2.11)$$

For a *control volume* or open system (any prescribed and identifiable volume in space), usually there is expansion when heat is absorbed by the system at constant pressure. Part of the heat goes into internal energy and causes temperature to rise. And the rest of the heat is used to expand against the pressure  $P$ . A property of the system, called *enthalpy* ( $H$ ), is used to represent the system state under certain condition.

$$H = U + PV \quad (2.12)$$

where  $V$  is the system volume. Enthalpy is a state parameter which is independent of which way the system reaches that condition. Equation (2.11) now can be represented as:

$$dH = dQ - dW \quad (2.13)$$

### The Heat Engine and Carnot Cycle

The heat engine is designed to convert heat to work. Figure 2.1 shows the block diagram of an idealized heat engine. If we want the heat engine to work continuously, then the *system* (the working substance in the figure) is subjected to a cyclic process. A cyclic process is one in which the system returns to its original state after a cycle. For a practical heat engine, there are many processes undergoing. And it is also complicated and difficult to analyze all of them. In 1842, a French scientist named Sadi Carnot presented a way to analyze cyclic thermal processes and discovered the maximum possible heat efficiency of a heat engine.

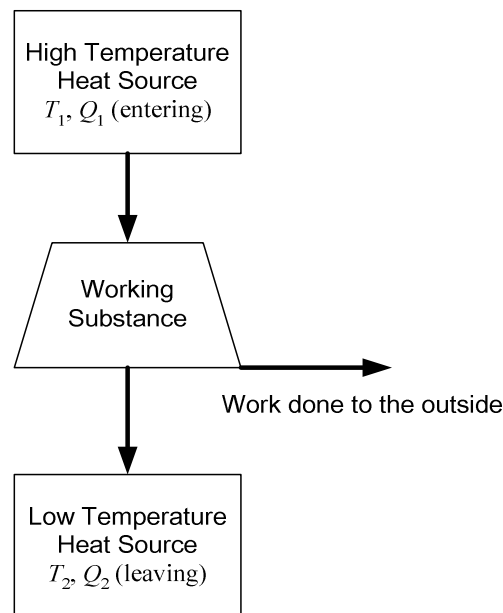


Figure 2.1. Block diagram of an ideal heat engine.

The Carnot cycle is shown in Figure 2.2. The cycle consists of two isothermal processes and two adiabatic processes. Figure 2.2 (a) shows the  $P$ - $V$  diagram of the

Carnot cycle [2.6]. The heat  $Q_1$  enters the system at  $T_1$ , and  $Q_2$  leaves system at  $T_2$ . Since this process is cyclic, the system energy remains the same after any cycle. According to the First Law of Thermodynamics (Equation 2.10), it can be shown that

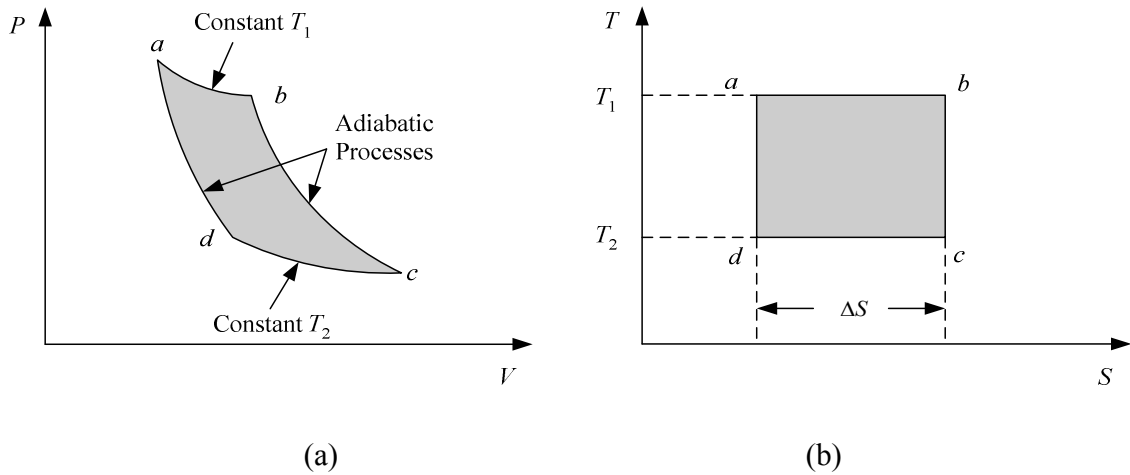


Figure 2.2. Carnot cycle. (a) P-V (pressure-volume) diagram. (b) T-S (temperature-entropy) diagram.

$$W = Q_1 - Q_2 \quad (2.14)$$

$W$  is the work done by the system to the outside, which can also be represented by the area  $abcd$  in Figure 2.2 (a). For the Carnot cycle, it has been proved that

$$\frac{Q_1}{T_1} = \frac{Q_2}{T_2} \quad (2.15)$$

The efficiency of the system then is

$$\eta_c = \frac{W}{Q_1} = \frac{Q_1 - Q_2}{Q_1} = 1 - \frac{T_2}{T_1} \quad (2.16)$$

It is clear from (2.16) that in order to get a higher efficiency the temperature difference should be larger.

Another contribution from Carnot is that  $Q/T$  can be a state property of the system by

showing the equivalence of  $Q_1/T_1$  and  $Q_2/T_2$  [see (2.15)]. Based on Carnot's idea, Clausius developed the concept of entropy and presented the Second Law of Thermodynamics.

### The Second Law of Thermodynamics

The concept is introduced to indicate to what extent of disorder a system is at. If the system is undergoing an infinitesimal reversible process with  $dQ$  heat entering the system at temperature  $T$ , then the infinitesimal change in its entropy is defined as [2.5]-[2.8]:

$$dS = \frac{dQ}{T} \Big|_{rev} \quad (2.17)$$

A reversible process is a process that can be reversed without leaving any traces to its environment. If a cyclic process only consists of reversible processes, then there is no entropy change ( $\Delta S = 0$ ) after a cycle. On the other hand, if the cycle contains an irreversible process, then a change of entropy will be generated. Entropy is an important system property. It is also very useful in describing a thermodynamic process. Figure 2.2 (b) shows the  $T$ - $S$  diagram of a Carnot Cycle. The area  $abcd$  also represents the work done to the system environment.

The Second Law of Thermodynamics is described by the Clausius inequality [2.5], [2.8]. For any cyclic process, we have

$$\oint \frac{dQ}{T} \leq 0 \quad (2.18)$$

The equality sign only applies to a reversible cyclic process. The above inequality can be expressed in an infinitesimal form as:

$$dS \geq \frac{dQ}{T} \quad (2.19)$$

The equality sign applies to a reversible cyclic process and the inequality sign applies to an irreversible process. That is to say, for any irreversible process, it occurs in a direction to which the change of entropy is greater than  $dQ/T$ . This means that heat cannot be transferred from a low temperature to a higher temperature without a need of work from outside. The Second Law also reveals that no real heat engine efficiency can reach 100% due to the increase of entropy. For an isolated system, the change of entropy will always be greater than or equal to zero.

### Heat Transfer

In this section, the equations governing different ways of heat transfer are reviewed.

Heat Transfer by Conduction. For isotropic solids (whose properties and constitution in the neighborhood of any two points are the same at any direction), heat transfer by conduction is governed by *Fourier* heat-conduction equation [2.4]:

$$Q_{cond} = kA \frac{T_2 - T_1}{d} \quad (2.20)$$

where  $Q_{cond}$  is the heat transferred,  $A$  is the face area of the element normal to the heat flow,  $k$  is the effective thermal conductivity,  $d$  is the distance between the two points of interest and  $(T_2 - T_1)$  is the temperature difference.

Heat Transfer by Convection. Heat transfer by convection is the heat exchange between a flowing fluid (natural or forced) and a solid surface. The convective heat transfer is given as [2.4]:

$$Q_{conv} = hA(T_f - T_s) \quad (2.21)$$

where  $h$  is the effective convection heat transfer coefficient,  $A$  is the solid area contacting the fluid,  $T_f$  is the bulk temperature of the fluid and  $T_s$  is the temperature of the solid. This equation is also called *Newton's* law of cooling.

Heat Transfer by Radiation. Based on (2.8), the radiation heat exchange rate between two objects at different temperatures is [2.4]:

$$\dot{Q}_{rad} = \varepsilon\sigma A(T_1^4 - T_2^4) \quad (2.22)$$

where  $Q_{rad}$  is the radiation heat (J),  $\varepsilon$  is the effective emissivity of the system,  $\sigma$  is Stefan-Boltzmann Constant ( $5.6703 \times 10^{-8} \text{ W}\cdot\text{m}^{-2}\cdot\text{K}^{-4}$ ).

### Fundamentals of Electrochemical Processes

#### The Gibbs Free Energy

The Gibbs Free Energy, also called the Gibbs Energy or “free enthalpy”, is defined as [2.5], [2.8]:

$$G = H - TS = U + PV - TS \quad (2.23)$$

Chemical reactions proceed towards the direction that minimizes the Gibbs Energy.

Differentiating the above equation we can obtain

$$dG = dH - (TdS + SdT) = dU + PdV + VdP - (TdS + SdT) \quad (2.24)$$

$dG$  is negative as a chemical reaction approaches its equilibrium point, and it will be zero at the equilibrium point. According to the First Law of Thermodynamics (2.10), for a simple system, the above equation can be rewritten as

$$dG = dH - (TdS + SdT) = dQ - dW + PdV + VdP - (TdS + SdT) \quad (2.25)$$

If the system is restricted to performing only expansion-type of work ( $dW = PdV$ ) and the process is reversible ( $dQ = TdS$ ), then four terms on the right side of (2.25) will be cancelled out, resulting in:

$$dG = VdP - SdT \quad (2.26)$$

At a given temperature  $T$ , Gibbs energy under any pressure can be calculated based on the above equation for that given temperature.

$$G(T) = G^0(T) + nRT \ln\left(\frac{P}{P^0}\right) \quad (2.27)$$

where  $G^0(T)$  is the standard ( $P^0 = 1 \text{ atm}$ ) Gibbs energy at temperature  $T$ .

For an electrochemical reaction, the maximum work (electricity) is determined by the change in the Gibbs Energy as the reactants change to products. It can be shown that the maximum work is equal to the change in the Gibbs energy [2.8].

$$W_e = -\Delta G \quad (2.28)$$

### Energy Balance in Chemical Reactions

In a chemical reaction, the change in enthalpy due to the reaction is [2.8]

$$\Delta H = H_P - H_R = \sum_{P_i} N_{P_i} H_{P_i} - \sum_{R_j} N_{R_j} H_{R_j} \quad (2.29)$$

where  $H_P$  is the total enthalpy of the products and  $H_R$  is the total enthalpy of the reactants.  $N_{P_i}$  is the amount of moles of the  $i$ th species in the products and  $N_{R_j}$  is the amount of moles of the  $j$ th species in the reactants. Accordingly,  $H_{P_i}$  ( $H_{R_j}$ ) is the molar enthalpy of the corresponding species, which can be represented as:

$$H_{P_i} = (H_f^0 + H - H^0)_{P_i} \quad (2.30)$$

where  $H_f^0$  is the standard molar enthalpy of formation (J/mol) and  $(H-H_0)$  is the sensible enthalpy due to the temperature difference.

The change of entropy due to the reaction is [2.8]

$$\Delta S = S_P - S_R = \sum_{P_i} N_{P_i} S_{P_i} - \sum_{R_j} N_{R_j} S_{R_j} \quad (2.31)$$

where  $S_P$  is the total entropy of the products and  $S_R$  is the total entropy of the reactants.  $S_{P_i}$  ( $S_{R_j}$ ) is the molar entropy of the corresponding species.

The change of the Gibbs free energy due to the reaction then can be obtained from (2.23) as:

$$\Delta G = \Delta G_P - \Delta G_R = \Delta H - T\Delta S \quad (2.32)$$

Two example reactions [(2.33) and (2.34)] are given to show how to calculate the change of Gibbs energy in a reaction. The enthalpy and entropy values for water, hydrogen and oxygen are given in Table 2.1. The reactions are assumed to happen under standard conditions (1 atm and 25 °C).



where subscript “g” represents that the reaction product is in gas form and subscript “l” is used to indicate that the reaction product is in liquid form.

TABLE 2.1. STANDARD THERMODYNAMIC PROPERTIES  
(ENTHALPY, ENTROPY AND GIBBS ENERGY) [2.9]

Name	$H_f$ (kJ/mol)	S (J/mol/K)
H <sub>2</sub> O(g)	-241.8	188.7
H <sub>2</sub> O(l)	-285.8	69.9
H <sub>2</sub>	0	130.6
O <sub>2</sub>	0	205

For the reaction given in (2.33), we have

$$\Delta H = H_p - H_R = (-241.8 - 0 - 0) = -241.8 \quad (\text{kJ/mol})$$

$$\Delta S = S_p - S_R = (188.7 - 130.6 - 0.5 \times 205) = -44.4 \quad (\text{J/mol/K})$$

Therefore, the change in the Gibbs energy of the reaction given in (2.33) is

$$\Delta G = \Delta H - T\Delta S = -241.8 - 298 \times (-44.4 \times 10^{-3}) = \mathbf{-228.57} \text{ kJ/mol}$$

For the reaction given in (2.34), we have

$$\Delta H = H_p - H_R = (-285.8 - 0 - 0) = -285.8 \quad (\text{kJ/mol})$$

$$\Delta S = S_p - S_R = (69.9 - 130.6 - 0.5 \times 205) = -163.2 \quad (\text{J/mol/K})$$

Therefore, the change in the Gibbs energy of the reaction given in (2.34) is

$$\Delta G = \Delta H - T\Delta S = -285.8 - 298 \times (-163.2 \times 10^{-3}) = \mathbf{-237.16} \text{ kJ/mol}$$

From the above examples, we can see that more work can be done if the product (H<sub>2</sub>O) is in liquid form.

### The Nernst Equation

Consider an electrochemical reaction under constant temperature and pressure that the reactants  $X$  and  $Y$  form products  $M$  and  $N$ , given by (2.35).



where  $a$ ,  $b$ ,  $c$  and  $d$  are stoichiometric coefficients.

According to (2.32), the change of the Gibbs energy of the reaction is [2.8]:

$$\Delta G = G_p - G_R = cG_M + dG_N - aG_X - bG_Y$$

In terms of the change of the standard Gibbs energy,  $\Delta G$  can also be expressed as [see (2.27)]:

$$\Delta G = \Delta G^0 + RT \ln \left( \frac{P_M^c P_N^d}{P_X^a P_Y^b} \right) \quad (2.36)$$

where  $\Delta G^0 = cG_M^0 + dG_N^0 - aG_X^0 - bG_Y^0$ .

In an electrochemical reaction, the work can be considered as the electrical energy delivered by the reaction. The electrochemical work is

$$W_e = n_e FE \quad (2.37)$$

where  $n_e$  is number of participating electrons,  $F$  is Faraday constant (96487 C/mol) and  $E$  is the voltage difference across the electrodes.

According to (2.28), the change in Gibbs energy is the negative value of the work done by the reaction.

$$\Delta G = -W_e = -n_e FE \quad (2.38)$$

Under standard condition, the above equation turns out to be

$$\Delta G^0 = -W_e^0 = -n_e F E^0 \quad (2.39)$$

where  $E^0$  is the standard reference potential.

From (2.38) we can calculate the electrode voltage  $E$  as

$$E = -\frac{\Delta G}{n_e F} = -\frac{\Delta G^0}{n_e F} - \frac{RT}{n_e F} \ln\left(\frac{P_M^C P_N^d}{P_X^a P_Y^b}\right) \quad (2.40)$$

Writing the above in terms of standard reference potential  $E^0$ , we get the well-known electrochemical formula: *Nernst equation* [2.8], [2.10].

$$E = E^0 - \frac{RT}{n_e F} \ln\left(\frac{P_M^C P_N^d}{P_X^a P_Y^b}\right) = E^0 + \frac{RT}{n_e F} \ln\left(\frac{P_X^a P_Y^b}{P_M^C P_N^d}\right) \quad (2.41)$$

For a fuel cell with an overall reaction as given by (2.33), then the voltage across the fuel cell electrodes (or the internal potential of the fuel cell) is

$$E = E^0 + \frac{RT}{2F} \ln\left(\frac{P_{H_2} P_{O_2}^{0.5}}{P_{H_2O}}\right) \quad (2.42)$$

If the product ( $H_2O$ ) is in liquid form, given by (2.34), then the fuel cell internal potential is

$$E = E^0 + \frac{RT}{2F} \ln(P_{H_2} P_{O_2}^{0.5}) \quad (2.43)$$

### Fundamentals of Alternative Energy Systems

In this section, the fundamentals of wind energy generation system, PV cells, fuel cells, and electrolyzers are reviewed.

### Wind Energy System

Energy in Wind. Wind energy systems harness the kinetic energy of wind and convert it into electrical energy or use it to do other work, such as pump water, grind grains, etc. The kinetic energy of air of mass  $m$  moving at speed  $v$  can be expressed as

[2.11]

$$E_k = \frac{1}{2}mv^2 \quad (2.44)$$

During a time period  $t$ , the mass ( $m$ ) of air passing through a given area  $A$  at speed  $v$  is:

$$m = \rho Avt \quad (2.45)$$

where  $\rho$  is the density of air ( $\text{kg/m}^3$ ).

Based on the above two equations, the wind power is

$$P = \frac{1}{2} \rho Av^3 \quad (2.46)$$

The specific power or power density of a wind site is given as

$$P_{den} = \frac{P}{A} = \frac{1}{2} \rho v^3 \quad (2.47)$$

It is noted that the specific power of a wind site is proportional to the cube of the wind speed.

Power Extracted from Wind. The actual power extracted by the rotor blades from wind is the difference between the upstream and the down stream wind powers

$$P = \frac{1}{2} k_m (v^2 - v_0^2) \quad (2.48)$$

where  $v$  is the upstream wind velocity at the entrance of the rotor blades,  $v_0$  is the downstream wind velocity at the exit of the rotor blades.  $k_m$  is the mass flow rate, which can be expressed as

$$k_m = \rho A \frac{v + v_0}{2} \quad (2.49)$$

where  $A$  is the area swept by the rotor blades.

From (2.48) and (2.49), the mechanical power extracted by the rotor is given by:

$$P = \frac{1}{2} \left[ \rho A \frac{v + v_0}{2} \right] (v^2 - v_0^2) \quad (2.50)$$

Let  $C_p = \frac{1}{2} \left( 1 + \frac{v_0}{v} \right) \left[ 1 - \left( 1 - \frac{v_0}{v} \right)^2 \right]$  and rearrange the terms in (2.50), we have:

$$P = \frac{1}{2} \rho A v^3 C_p \quad (2.51)$$

$C_p$  is called the power coefficient of the rotor or the rotor efficiency. It is the fraction of the upstream wind power, which is captured by the rotor blades and has a theoretical maximum value of 0.59, shown in Figure 2.3. In practical designs, maximum achievable  $C_p$  is between 0.4 and 0.5 for high-speed, two-blade turbines and between 0.2 and 0.4 for low-speed turbines with more blades [2.11].

It is noted from (2.51) that the output power of a turbine is determined by the effective area of the rotor blades ( $A$ ), wind speed ( $v$ ), and wind flow conditions at the rotor ( $C_p$ ). Thus, the output power of the turbine can be varied by changing the effective area and/or by changing the flow conditions at the rotor system. Control of these quantities forms the basis of control of wind energy systems.

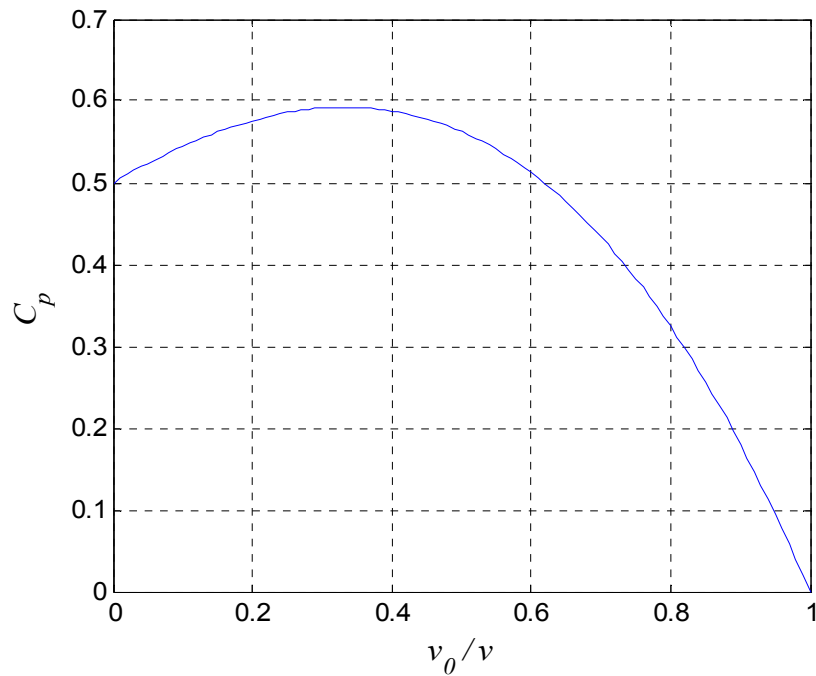


Figure 2.3. Theoretical rotor efficiency vs.  $v_0/v$  ratio.

Tip Speed Ratio. The tip speed ratio  $\lambda$  (TSR), defined as the ratio of the linear speed at the tip of the blade to the free stream wind speed, is given as follows [2.11]:

$$\lambda = \frac{\omega R}{v} \quad (2.52)$$

where  $R$  is the rotor blade radius and  $\omega$  is the rotor angular speed.

TSR is related to the wind turbine operating point for extracting maximum power. The maximum rotor efficiency  $C_p$  is achieved at a particular TSR, which is specific to the aerodynamic design of a given wind turbine. For variable TSR turbines, the rotor speed will change as wind speed changes to keep TSR at some optimum level. Variable TSR turbines can produce more power than fixed TSR turbines [2.12].

Wind Energy Conversion System. The block diagram of a typical wind energy conversion system is shown in Figure 2.4.

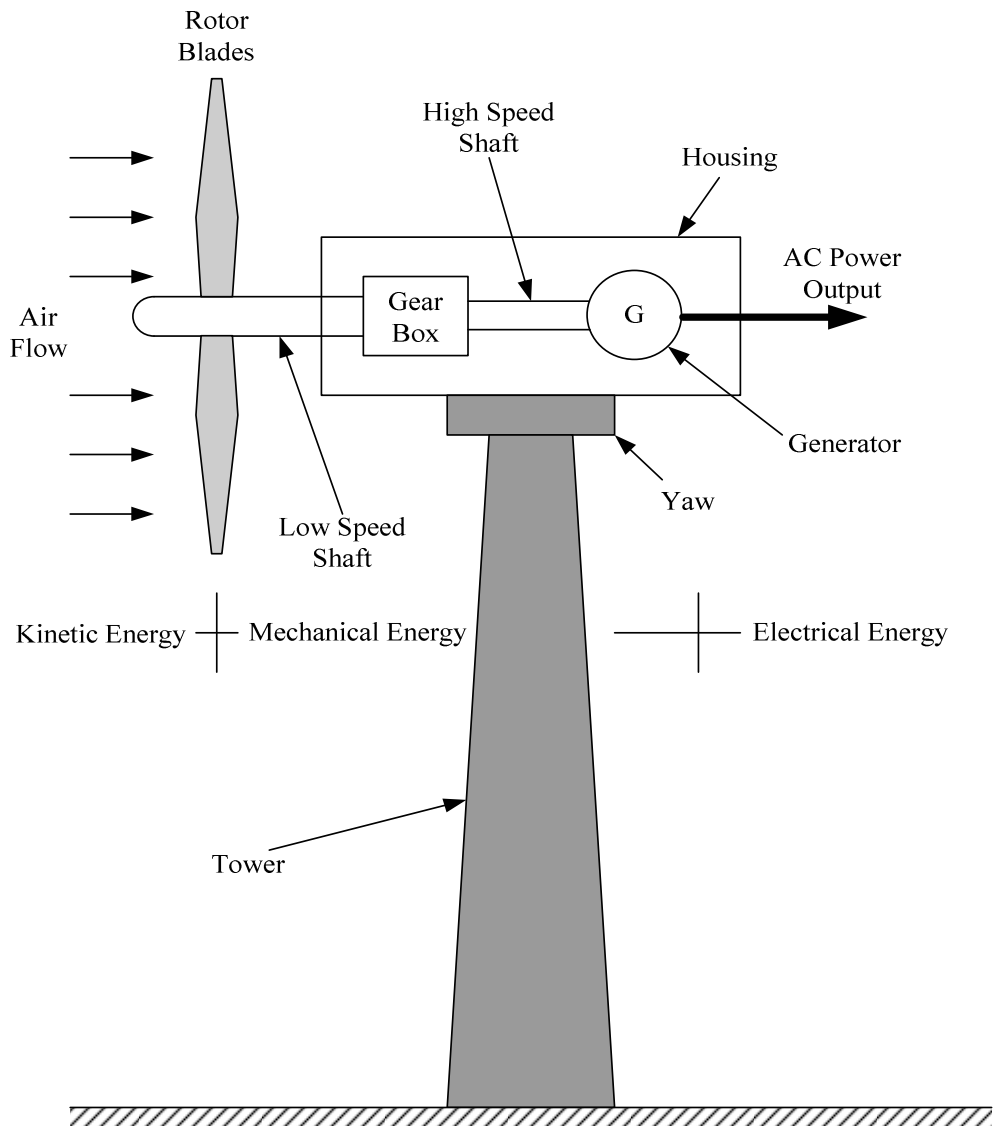


Figure 2.4. Block diagram of a typical wind energy conversion system.

The principle components of a modern wind turbine are the tower, the yaw, the rotor and the nacelle, which accommodates the gear box and the generator. The tower holds the

main part of the wind turbine and keeps the rotating blades at a height to capture sufficient wind power. The yaw mechanism is used to turn the wind turbine rotor blades against the wind. Wind turbine captures the wind's kinetic energy in the rotor consisting of two or more blades. The gearbox transforms the slower rotational speeds of the wind turbine to higher rotational speeds on the electrical generator side. Electrical generator will generate electricity when its shaft is driven by the wind turbine, whose output is maintained as per specifications, by employing suitable control and supervising techniques. In addition to monitoring the output, these control systems also include protection equipment to protect the overall system [2.11].

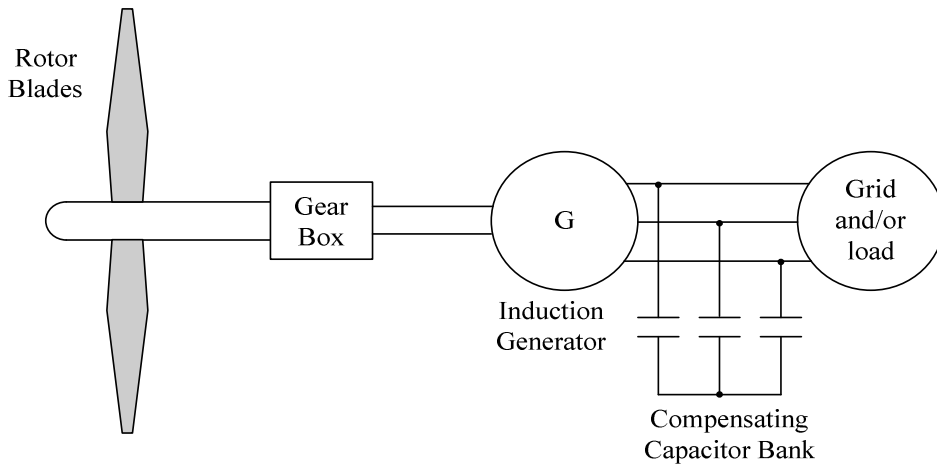
Two distinctly different design configurations are available for a wind turbine, the horizontal axis configuration and the vertical axis configuration. The vertical axis machine has the shape like an egg beater (also called the Darrieus rotor after its inventor). However, most modern turbines use horizontal axis design [2.11].

#### Constant Speed and Variable Speed Wind Energy Conversion Systems (WECS).

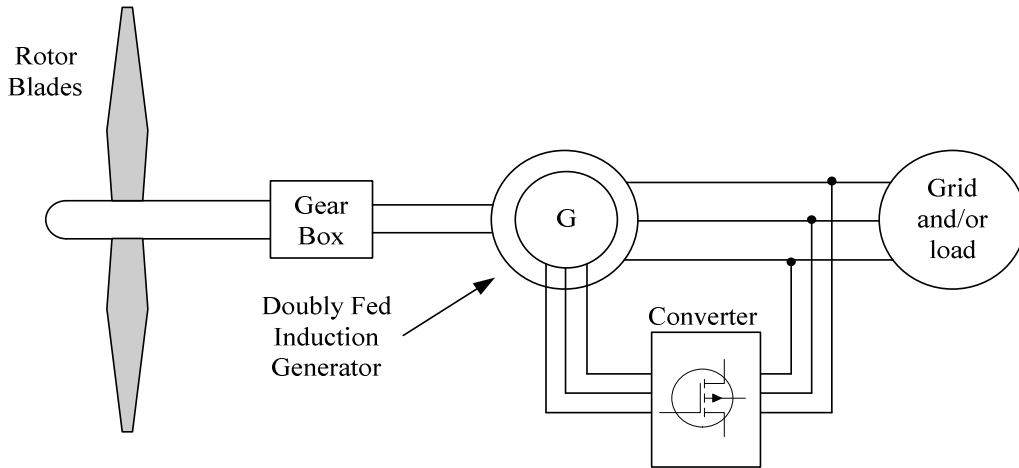
Generally, there are two types of wind energy conversion systems: *constant speed* and *variable speed systems*, shown in Figure 2.5 [2.12]. In Figure 2.5 (a), the generator normally is a squirrel cage induction generator which is connected to a utility grid or load directly. Since the generator is directly coupled, the wind turbine rotates at a constant speed governed by the frequency of the utility grid (50 or 60 Hz) and the number of poles of the generator. The other two wind power generation systems, shown in Figure 2.5 (b) and (c), are variable speed systems. In Figure 2.5 (b), the generator is a doubly-fed induction generator (wound rotor). The rotor of the generator is fed by a back-to-back

converter voltage source converter. The stator of the generator is directly connected to load or grid. Through proper control on the converter for the rotor, the mechanical speed of the rotor can be variable while the frequency of output AC from the stator can be kept constant. Figure 2.5 (c) shows a variable speed system which is completely decoupled from load or grid through a power electronic interfacing circuit. The generator can either be a synchronous generator (with excitation winding or permanent magnet), or an induction generator. In this dissertation, a variable speed WECS, similar to the one shown in Figure 2.5 (c), is used for the hybrid energy system study. The generator used in the study is a self-excited induction generator.

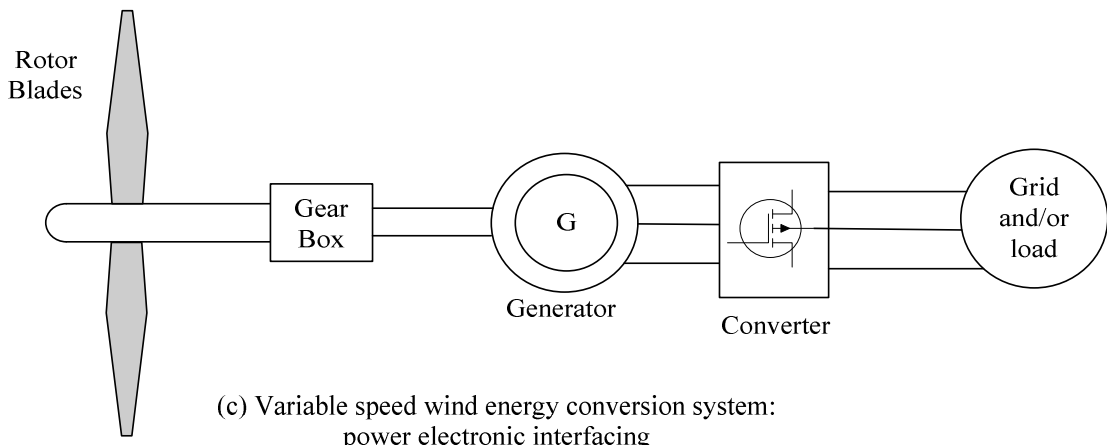
Wind Turbine Output Power vs. Wind Speed. A typical power vs. wind speed curve is shown in Figure 2.6 [2.12], [2.15]. When the wind speed is less than the cut-in speed (normally 3-5 m/s) [2.12], there is no power output. Between the cut-in speed and the rated or nominal wind speed (normally 11-16 m/s) [2.12], the wind turbine output power is directly related to the cubic of wind speed as given in (2.51). When the wind speed is over the nominal value, the output power needs to be limited to a certain value so that the generator and the corresponding power electronic devices (if any) will not be damaged. In other words, when the wind speed is greater than the rated value, the power coefficient  $C_p$  needs to be reduced [see (2.51)]. When the wind speed is higher than the cut-out speed (normally 17-30 m/s) [2.12], the system will be taken out of operation for protection of its components.



(a) Constant speed wind energy conversion system



(b) Variable speed wind energy conversion system:  
doubly fed generator



(c) Variable speed wind energy conversion system:  
power electronic interfacing

Figure 2.5. Constant and variable speed wind energy conversion systems [2.12].

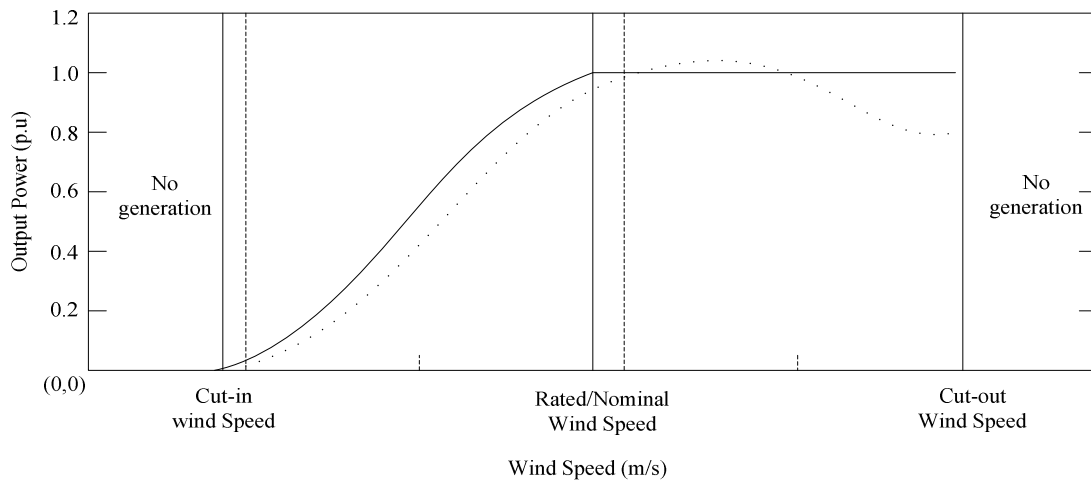


Figure 2.6. Typical curves for a constant speed stall controlled (dotted) and variable speed pitch controlled (solid) wind turbine [2.12], [2.15].

There are several ways to control the wind turbine output power. The two common ways to achieve this goal are: *stall control* and *pitch control* [2.11]-[2.15].

For a stall controlled wind turbine, there is no active control applied to it. The output power is regulated through a specifically designed rotor blades. The design ensures that when the wind speed is too high, it creates turbulences on the side of the rotor blades. The turbulences will decrease the aerodynamic efficiency of the wind turbine as a result.

Pitch control is an active method which is used to reduce the aerodynamic efficiency by changing pitch angle (turning the rotor blades out of wind) of the rotor blades. It should be noted that the pitch angle can change at a finite rate, which may be quite low due to the size of the rotor blades. The maximum rate of change of the pitch angle is in the order of 3 to 10 degrees/second [2.15].

It is noted from Figure 2.6 that a variable speed system normally has lower cut-in speed. The rated speed is also normally lower than a constant speed system. For wind

speeds between the cut-in and the nominal speed, there will be 20-30% increase in the energy capture with variable speed compared to the fixed-speed operation [2.11]-[2.15], shown in Figure 2.6. For a pitch controlled wind system, the power for wind speeds over the nominal value can be held constant precisely. On the other hand, for a stall controlled constant speed system, the output power will reach its peak value somewhat higher than its rated value and then decreases as wind speed grows.

### Photovoltaic Energy System

#### *Terminology:*

*Solar radiation:* Also called insolation, consists of the radiation that comes directly from the sun (beam radiation) as well as the radiation that comes indirectly (diffusion and albedo radiation) [2.16].

*Solar constant:* The solar radiation that falls on a unit area above the atmosphere at a vertical angle is called solar constant. It has a value of  $1367 \text{ W/m}^2$  [2.16].

*Air mass:* A convenient lumped parameter used for the amount of sunlight absorbed in the atmosphere. The amount of beam solar radiation absorbed in the atmosphere in a direct vertical path to sea level is designated as one *air mass* (AM1). In general, air mass is proportional to the secant of the zenith angle [2.16].

*Irradiance:* A measure of power density of sunlight, it has a unit of  $\text{W/m}^2$ .

*Irradiation:* A measure of energy density ( $\text{J/m}^2$ ), it is the integral of irradiance over time.

Photovoltaic effect is a basic physical process through which solar energy is converted into electrical energy directly. The physics of a PV cell, or solar cell, is similar

to the classical  $p-n$  junction diode, shown in Figure 2.7 [2.11]. At night, a PV cell can basically be considered as a diode. When the cell is illuminated, the energy of photons is transferred to the semiconductor material, resulting in the creation of electron-hole pairs. The electric field created by the  $p-n$  junction causes the photon-generated electron-hole pairs to separate. The electrons are accelerated to  $n$ -region (N-type material), and the holes are dragged into  $p$ -region (P-type material), shown in Figure 2.7. The electrons from  $n$ -region flow through the external circuit and provide the electrical power to the load at the same time.

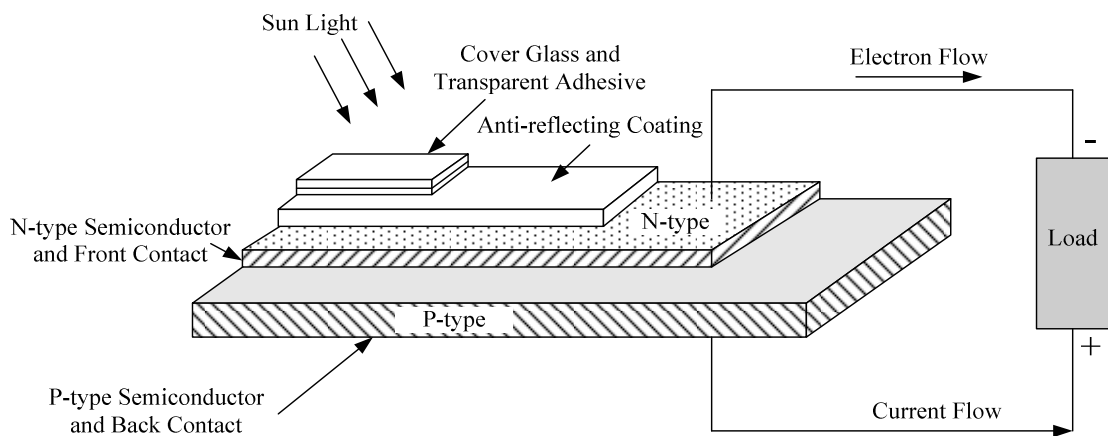


Figure 2.7. Schematic block diagram of a PV cell.

The PV cell shown in Figure 2.7 is the basic component of a PV energy system. Since a typical PV cell produces less than 2 W at approximately 0.5 V DC, it is necessary to connect PV cells in series-parallel configurations to produce desired power and voltage ratings. Figure 2.8 shows how single PV cells are grouped to form modules and how modules are connected to build arrays. There is no fixed definition on the size of a module and neither for an array. A module may have a power output from a few watts to

hundreds of watts. And the power rating of an array can vary from hundreds of watts to megawatts [2.11], [2.16].

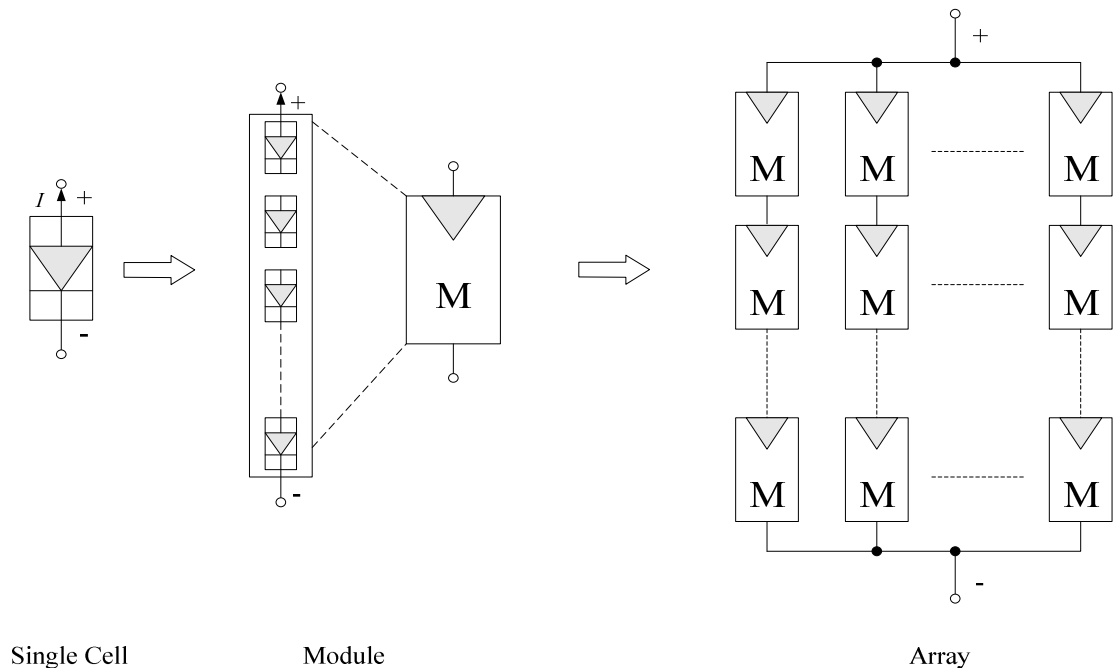


Figure 2.8. PV Cell, module and array.

### Fuel Cells

Fuel cells (FCs) are static energy conversion devices that convert the chemical energy of fuel directly into DC electrical energy [2.17]-[2.18]. The basic physical structure of a fuel cell consists of two porous electrodes (anode and cathode) and an electrolyte layer in the middle. Figure 2.9 shows a schematic diagram of a polymer electrolyte membrane fuel cell (PEMFC). The electrolyte layer is a good conductor for ions (positive or negative charged), but not for electrons. The electrolyte can either be solid, such as PEMFC and solid oxide fuel cells (SOFC) or liquid, such as molten carbonate fuel cells (MCFC). The type and chemical properties of the electrolyte used in fuel cells are very

important to their operating characteristics, such as their operating temperatures.

The polarity of an ion and its transport direction can differ for different fuel cells, determining the site of water production and removal. If the working ion is positive, like in a PEMFC, shown in Figure 2.9, then water is produced at the cathode. On the other hand, if the working ion is negative, like SOFC and MCFC, shown in Figures 2.11 and 2.13, water is formed at the anode. In both cases electrons have to pass through an external circuit and produce electric current.

In a typical fuel cell, fuel is fed continuously to the anode and oxidant is fed continuously to the cathode. The electrochemical reactions take place at the electrodes to convert chemical energy into electricity. Note that anode is the electrode from which electrons leave (negative) and cathode is the electrode to which the electrons are coming (positive). The most common used fuel for fuel cells is hydrogen, and the oxidant is usually oxygen or air. Nevertheless, theoretically, any substance capable of chemical oxidation that can be supplied continuously (as a fluid) can be used as fuel at the anode of a fuel cell. Similarly, the oxidant can be any fluid that can be reduced at a sufficient rate [2.19].

Among different types of fuel cells, SOFC, PEMFC and MCFC are most likely to be used for distributed generation (DG) applications [2.17]-[2.18], [2.20]-[2.24]. Compared with conventional power plants, these FCDG systems have many advantages such as high efficiency, zero or low emission (of pollutant gases) and flexible modular structure. In the following, an overview is given on the operating principles of the above three types of fuel cells. Though MCFC is out of the scope of this dissertation, it is also included here as a potential candidate for fuel cell DG applications.

PEMFC. PEMFC has a sandwich like structure, as shown in Figure 2.9 [2.17], [2.18], [2.20]. Between two porous electrodes is a Teflon-like membrane, which is an excellent conductor of protons and an insulator of electrons [2.17], [2.18]. The hydrogen molecules are broken into electrons and hydrogen protons at the anode with the help of platinum catalyst. The hydrogen protons pass through the membrane (electrolyte), reach the cathode surface and combine with the electrons, which travel from anode to cathode through the external load, to produce water. The reactions at the anode and cathode side and the overall reaction are given in Figure 2.9.

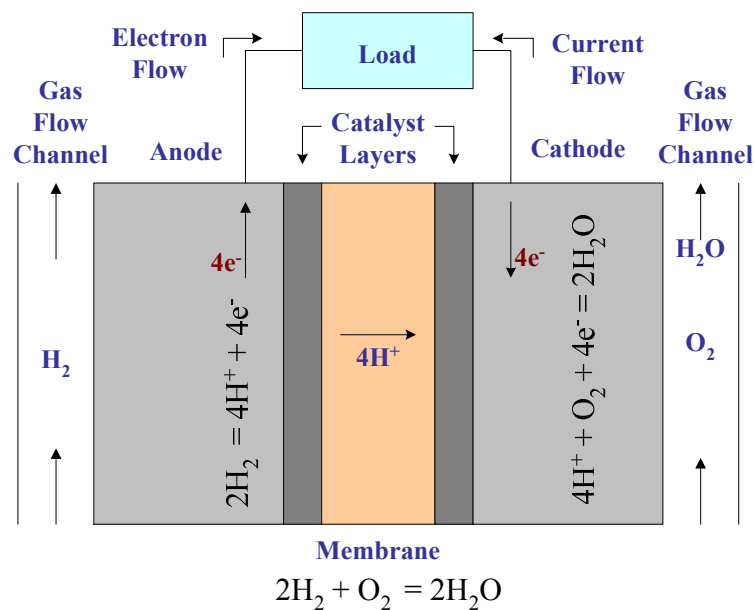


Figure 2.9. Schematic diagram of a PEMFC.

One of the advantages of the PEMFC is its high power density and high efficiency (40-45%). This makes the technology competitive in transportation and stationary applications. Another benefit is its lower operating temperature (between 60°C and 80°C),

and because of this, the PEMFC has a quick start, which is beneficial in automotive applications where quick start is necessary.

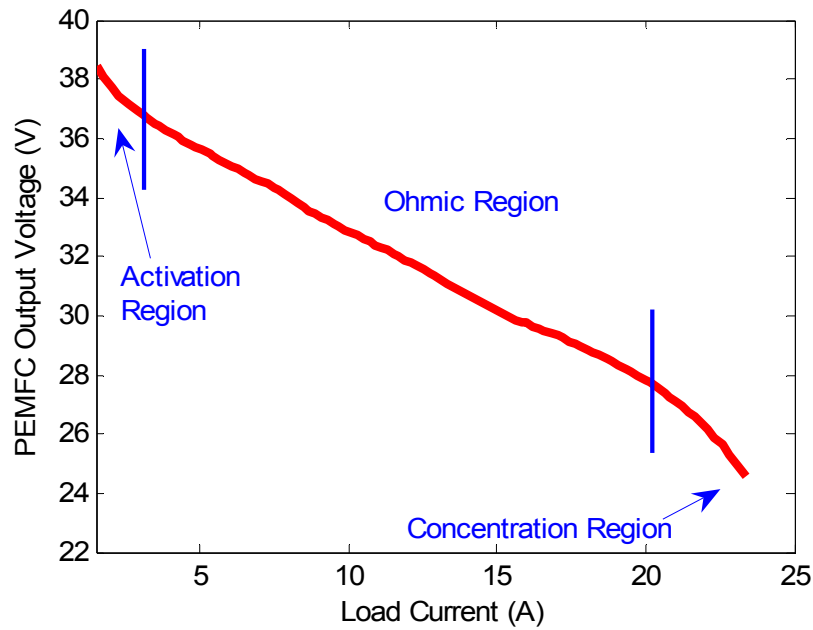


Figure 2.10.  $V$ - $I$  characteristic of a 500W PEMFC stack [2.20].

Figure 2.10 shows the output voltage vs. load current ( $V$ - $I$ ) characteristic curve of a 500W PEMFC stack [2.20]. This characteristic curve, which is typical of other fuel cells, can be divided into three regions. The voltage drop across the fuel cell associated with low currents is due to the activation loss inside the fuel cell; the voltage drop in the middle of the curve (which is approximately linear) is due to the ohmic loss in the fuel cell stack; and as a result of the concentration loss, the output voltage at the end of the curve will drop sharply as the load current increases [2.17], [2.18].

SOFC. SOFC is a high temperature fuel cell technology with a promising future. Based on a negative-ion conductive electrolyte, SOFCs operate between 600 °C and 1000 °C, and convert chemical energy into electricity at high efficiency, which can reach up to 65% [2.21]. The overall efficiency of an integrated SOFC-combustion turbine system can even reach 70% [2.21]. Despite slow start-up and more thermal stresses due to the high operating temperature, SOFC allows for internal reforming of gaseous fuel inside the fuel cell, which gives multi-fuel capability to SOFCs [2.17], [2.18]. Moreover, their solid nature simplifies system designs, where the corrosion and management problems related to liquid electrolyte are eliminated [2.17]. These merits give SOFC a bright future to be used in stationary applications. Figure 2.11 shows a block diagram of a SOFC. The reactions at the anode and cathode are also given in the figure.

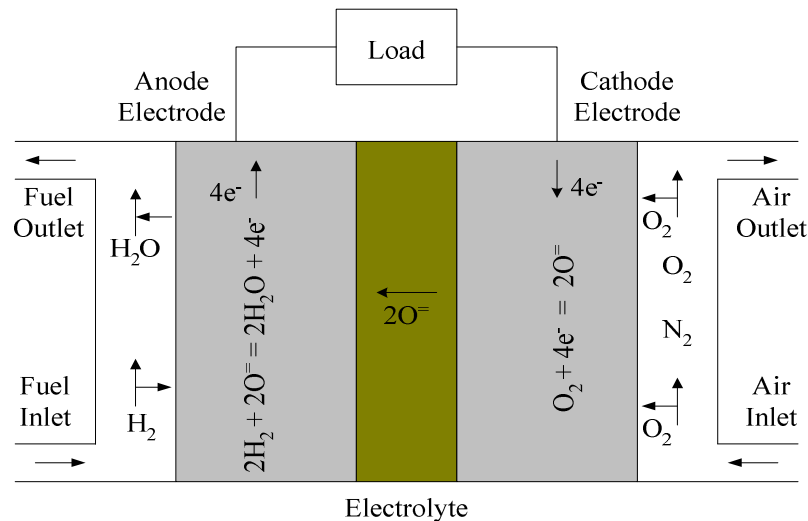


Figure 2.11. Schematic diagram of a SOFC.

The steady-state terminal  $V-I$  curves of a 5kW SOFC model (which will be discussed in detail in Chapter 4) at different temperatures, which are typical of SOFCs, are shown in Figure 2.12 [2.23]. The activation voltage drop dominates the voltage drop in the low-current region. As load current increases, the ohmic voltage drop increases fast and becomes the main contribution to the SOFC voltage drop. When load current exceeds a certain value, fuel cell output voltage will drop sharply due to the concentration voltage drop inside SOFC. Figure 2.12 also shows the effect of temperature on SOFC V-I characteristic curve. SOFC output voltage is higher at lower temperature in the low current zone while the voltage is higher at higher temperature in the high current region.

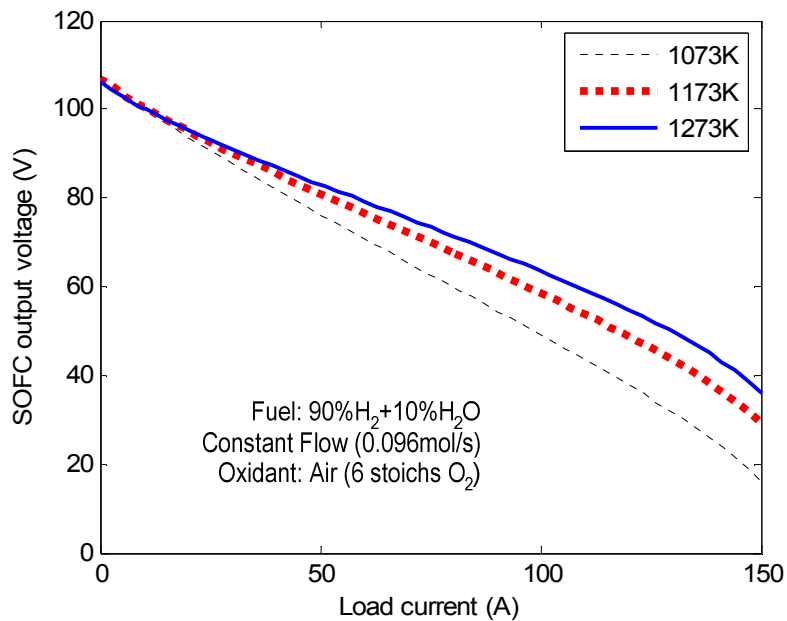


Figure. 2.12. V-I characteristic of a 5kW SOFC stack [2.23].

MCFC. MCFCs use a molten mixture of alkali metal carbonate as their electrolyte [2.17], [2.18]. At high temperatures ( $600^{\circ}\text{C} - 700^{\circ}\text{C}$ ), the salt mixture is in liquid phase and is an excellent conductor of  $\text{CO}_3^{2-}$  ions. At the cathode, the oxygen and carbon oxide combine with the electrons flowing through the external circuit to produce carbonate ions ( $\text{CO}_3^{2-}$ ). At the anode,  $\text{CO}_3^{2-}$  ions are deoxidized by hydrogen, and electrons are released at the same time. These electrons will have to go through the external circuit and then reach the cathode surface. Figure 2.13 shows the schematic diagram of a MCFC. The reactions at the anode and cathode side are given in the figure.

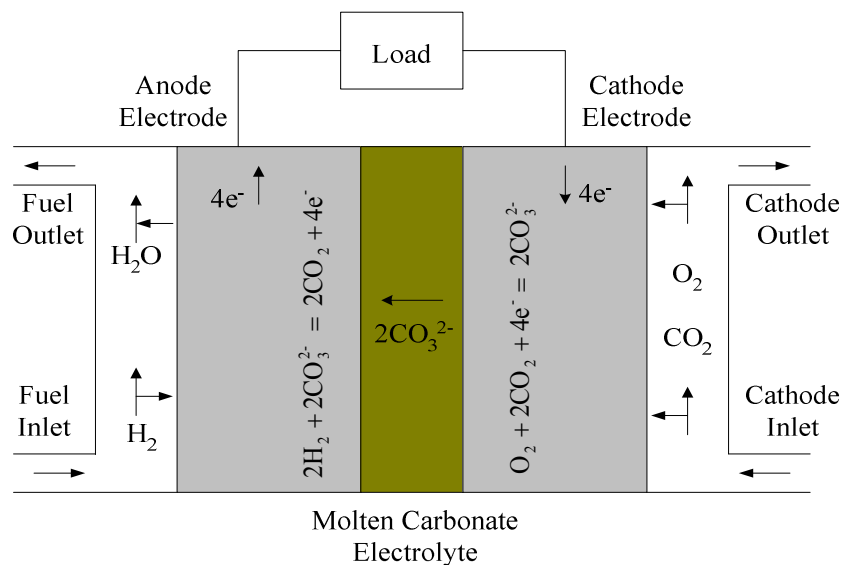


Figure 2.13. Schematic diagram of a MCFC.

Figure 2.14 shows the V-I performance progress for MCFCs from 1967 to 2002, [2.17]. During the 1980s, the performance of MCFC stacks made dramatic improvements. It is noted from this figure that MCFCs normally operate in the range of  $100\text{-}200 \text{ mA/cm}^2$  at  $750\text{-}850 \text{ mV}$  for a single cell [2.17]. MCFs have achieved

efficiencies in the range of 50-60% before heat recovery, and with heat recovery their efficiency could exceed 70% [2.24].

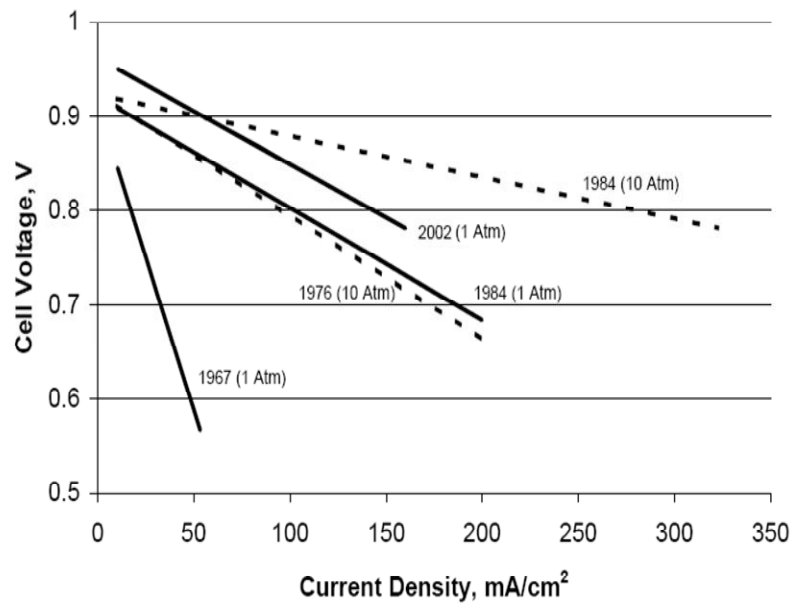


Figure 2.14. Progress in generic performance of MCFCs on reformat gas and air.

### Electrolyzer

An electrolyzer is a device that produces hydrogen and oxygen from water. Water electrolysis can be considered a reverse process of a hydrogen fueled fuel cell. Opposite to the electrochemical reaction occurring in fuel cell, an electrolyzer converts the DC electrical energy into chemical energy stored in hydrogen.

Water electrolysis is a long-established process, which started in the early part of nineteenth century [2.25]. Nicholson and Carlisle, English chemists, first discovered the phenomenon of electrolytic decomposition in acid water in 1800. However, alkaline medium is preferred in today's industrial electrolysis plants. Currently, there are three principal types of electrolyzer available in the market: alkaline, PEM, and solid oxide.

The alkaline and PEM electrolyzers are well established devices with thousands of units in operation, while the solid-oxide electrolyzer is as yet unproven [2.26]. Alkaline water electrolysis is the dominating technology today. In this section, the principle of alkaline water electrolysis is reviewed.

An alkaline electrolyzer uses potassium hydroxide (KOH) as electrolyte solution for transferring hydroxyl ions. Figure 2.15 shows the schematic diagram of an alkaline electrolyzer. At the cathode, two water molecules are reduced electrochemically (by the two electrons from the cathode) to one molecule of  $H_2$  and two hydroxyl ions ( $OH^-$ ). The reaction at the cathode can be expressed as:



Under the external electric field, the hydroxyl ions are forced to move towards the anode through the porous diaphragm. At the anode, the two molecule hydroxyl ions, losing two electrons to the anode, are discharged into  $1/2$  molecule of  $O_2$  and one molecule of water. The chemical reaction at the cathode is



By combining the above two equations, the overall chemical reaction inside an electrolyzer is



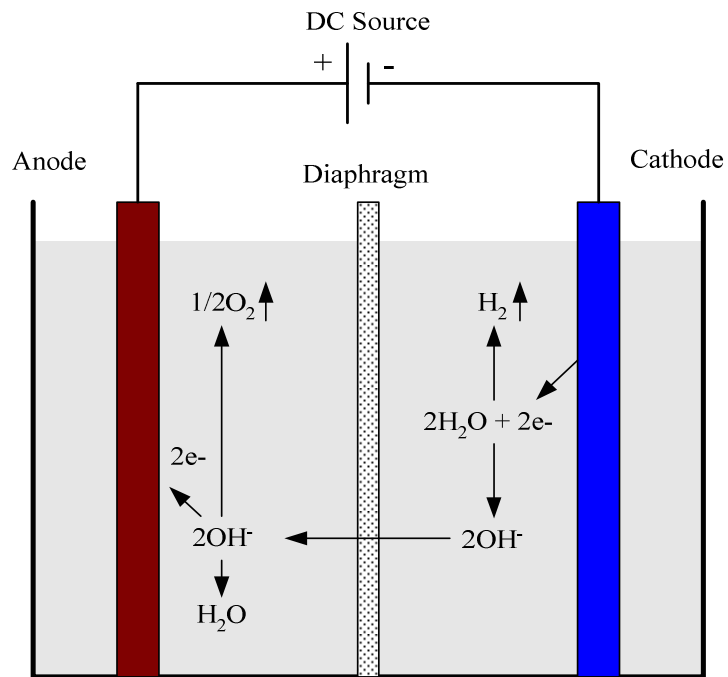


Figure 2.15. Schematic diagram of an alkaline electrolyzer.

The current density of alkaline electrolyzers is normally less than  $0.4 \text{ A/cm}^2$ . The energy conversion efficiencies can range from 60-90%. Without auxiliary purification equipment, purities of 99.8% for  $\text{H}_2$  can be achieved. Alkaline electrolysis technology can be implemented at a variety of scales from less than 1 kW to large industrial electrolyzer plant over 100 MW as long as there is a proper DC electricity supply [2.27].

### Summary

In this chapter, the fundamental concepts and principles of energy systems and energy conversion are reviewed. The chapter begins with the introduction of the basic energy forms, and then reviews the fundamentals of thermodynamics and electrochemistry. The First and Second Law of Thermodynamics, the maximum conversion efficiency of a conventional heat engine, heat transfer, the concepts of enthalpy, entropy and the Gibbs energy, and the well-known Nernst equation are briefly explained. The fundamentals of wind energy conversion systems, photovoltaic systems, fuel cells and electrolyzers are also reviewed. The principles reviewed in this chapter are the fundamentals needed for modeling the proposed multi-source alternative energy system discussed in the following chapters.

REFERENCES

- [2.1] Archie W. Culp, Jr., *Principles of Energy Conversion*, McGraw-Hill Book Company, 1979.
- [2.2] Steven S. Zumdahl, *Chemical Principles, 2<sup>nd</sup> Edition*, DC Heath and Company, Toronto, 1995.
- [2.3] F.T. Ulaby, *Fundamentals of Applied Electromagnetics*, Prentice-Hall, Inc., 1999.
- [2.4] E.R.G. Eckert and R. M. Drake, Jr., *Analysis of Heat and Mass Transfer*, McGraw-Hill Book Company, 1972.
- [2.5] George N. Hatsopoulos and Joseph H. Keenan, *Principles of General Thermodynamics*, John Wiley & Sons, Inc., 1965.
- [2.6] E. L. Harder, *Fundamentals of Energy Production*, John Wiley & Sons, 1982.
- [2.7] F.A. Farret and M.G. Simões, *Integration of Alternative Sources of Energy*, John Wiley & Sons, Inc., 2006.
- [2.8] G. Hoogers, *Fuel Cell Technology Handbook*, CRC Press LLC, 2003
- [2.9] JANAF Thermochemical Tables, 2<sup>nd</sup> Edition, NSRDS-NBS 37, 1971.
- [2.10] G. Kortum, *Treatise on Electrochemistry (2nd Edition)*, Elsevier Publishing Company, 1965.
- [2.11] M. R. Patel, *Wind and Solar Power Systems*, CRC Press LLC, 1999.
- [2.12] J.G. Sloopweg, “Wind power: modeling and impact on power system dynamics,” PhD dissertation, Dept. Elect. Eng., Delft University of Technology, Delft, Netherlands, 2003.
- [2.13] J.F. Manwell, J.G. McGowan and A.L. Rogers, *Wind energy Explained – Theory, Design and Application*, John Wiley& Sons, 2002.
- [2.14] Tony Burton, David sharpe, Nick Jenkins and Ervin Bossanyi, *Wind Energy Handbook*, John Wiley& Sons, 2001.
- [2.15] S.R. Guda, “Modeling and power management of a hybrid wind-microturbine power generation system,” MS thesis, Montana State University, 2005.

- [2.16] R. Messenger and J. Ventre, *Photovoltaic Systems Engineering*, CRC Press LLC, 2000.
- [2.17] *Fuel Cell Handbook (Sixth Edition)*, EG&G Services, Inc., Science Applications International Corporation, DOE, Office of Fossil Energy, National Energy Technology Lab, Nov. 2002.
- [2.18] James Larminie and Andrew Dicks, *Fuel Cell Systems Explained, 2<sup>nd</sup> Edition*, John Wiley & Sons, Ltd., 2003.
- [2.19] A.J. Appleby, F.R. Foulkes, *Fuel Cell Handbook*, Van Nostrand Reinhold, New York, NY, 1989.
- [2.20] C. Wang, M.H. Nehrir, and S.R. Shaw, "Dynamic Models and Model Validation for PEM Fuel Cells Using Electrical Circuits," *IEEE Transactions on Energy Conversion*, Vol. 20, No. 2, pp.442-451, June 2005.
- [2.21] O. Yamamoto, "Solid oxide fuel cells: fundamental aspects and prospects," *Electrochimica Acta*, Vol. 45, No. (15-16), pp. 2423-2435, 2000.
- [2.22] J. Padullés, G.W. Ault, and J. R. McDonald, "An integrated SOFC plant dynamic model for power system simulation," *J. Power Sources*, pp.495–500, 2000.
- [2.23] C. Wang and M.H. Nehrir, "A Dynamic SOFC Model for Distributed Power Generation Applications," *Proceedings*, 2005 Fuel Cell Seminar, Palm Springs, CA, Nov. 14-18, 2005.
- [2.24] M.D. Lukas, K.Y. Lee, H. Ghezeli-Ayagh, "An Explicit Dynamic Model for Direct Reforming Carbonate Fuel Cell Stack," *IEEE Transactions on Energy Conversion*, Vol. 16, No. 3, pp. 289-295, Sept. 2000.
- [2.25] W. Kreuter and H. Hofmann, "Electrolysis: The Important Energy Transformer in a World of Sustainable Energy," *Int. J. Hydrogen Energy*, Vol. 23, No.8, pp. 661-666, 1998.
- [2.26] M. Newborough, "A Report on Electrolysers, Future Markets and the Prospects for ITM Power Ltd's Electrolyser Technology," Online, <http://www.h2fc.com/Newsletter/>.
- [2.27] A.F.G. Smith and M. Newborough, "Low-Cost Polymer Electrolysers and Electrolyser Implementation Scenarios for Carbon Abatement," *Report to the Carbon Trust and ITM-Power PLC*, Nov. 2004.

## CHAPTER 3

## MULTI-SOURCE ALTERNATIVE ENERGY

## DISTRIBUTED GENERATION SYSTEM

Introduction

The ever increasing energy consumption, the soaring cost and the exhaustible nature of fossil fuel, and the worsening global environment have created booming interest in green (renewable energy source or fuel cell based) power generation systems. Compared to the conventional centralized power plants, these systems are sustainable, smaller in size and (some) can be installed closer to load centers. The power is delivered to customers by many distributed generation (DG) systems other than the conventional way that power is transmitted from centralized power plants to load centers over transmission lines and then through distribution systems. Due to steady progress in power deregulation and utility restructuring, and tight constraints imposed on the construction of new transmission lines for long distance power transmission, DG applications are expected to increase in the future.

Wind and solar power generation are two of the most promising renewable power generation technologies. The growth of wind and photovoltaic (PV) power generation systems has exceeded the most optimistic estimation. Fuel cells also show great potential to be green power sources of the future because of many merits they have (such as high efficiency, zero or low emission of pollutant gases, and flexible modular structure) and

the rapid progress in fuel cell technologies. However, none of these technologies is perfect now. Wind and solar power are highly dependent on climate while fuel cells need hydrogen-rich fuel and the cost for fuel cells is still very high at current stage. Nevertheless, because different renewable energy sources can complement each other, multi-source hybrid alternative energy systems (with proper control) have great potential to provide higher quality and more reliable power to customers than a system based on a single resource. And because of this, hybrid energy systems have caught worldwide research attention [3.1]-[3.34].

There are many combinations of different alternative energy sources and storage devices to build a hybrid system. The following lists some of the stand-alone or grid-connected hybrid systems that have been reported in the literature.

- 1) Wind/PV/FC/electrolyzer/battery system [3.1]-[3.3].
- 2) Micro-turbine/FC system [3.4]-[3.5].
- 3) Microturbine/wind system [3.6].
- 4) Gas-turbine/FC system [3.7]-[3.9].
- 5) Diesel/FC system [3.10]-[3.11].
- 6) PV/battery [3.12].
- 7) PV/FC/electrolyzer [3.13]-[3.15].
- 8) PV/FC/electrolyzer/battery system [3.16]-[3.18].
- 9) FC/battery, or super-capacitor system [3.19]-[3.20].
- 10) Wind/FC system [3.21].
- 11) Wind/diesel system [3.22].
- 12) Wind/PV/battery system [3.23]-[3.25].

- 13) PV/diesel system [3.26].
- 14) Diesel/wind/PV system [3.27].
- 15) PV/FC/ Super-conducting Magnetic Energy Storage (SMES) system [3.28].

From the above listed hybrid energy systems, it is noted that the main renewable energy sources are wind and photovoltaic power. Due to natural intermittent properties of wind and photovoltaic power, stand-alone wind and/or PV renewable energy systems normally require energy storage devices or some other generation sources to form a hybrid system. The storage device can be a battery bank, super-capacitor bank, SMES, or a FC-electrolyzer system.

In this study, a multi-source hybrid alternative distributed generation system consisting of wind, PV, fuel cell, electrolyzer and battery is proposed. Wind and photovoltaic are the primary power sources of the system to take full advantage of renewable energy around us. The FC/electrolyzer combination is used as a backup and long term storage system. For a stand-alone application, a battery is also used in the system as short term energy storage to supply fast transient and ripple power. In the proposed system, the different energy sources are integrated through an AC link bus (discussed later in this chapter). An overall power management controller is designed for the system to coordinate the power flows among the different energy sources. The details of the system configuration are discussed in this chapter. The system component modeling will be discussed in Chapter 4. The system control scheme and simulation results under different scenarios will be given in Chapter 7.

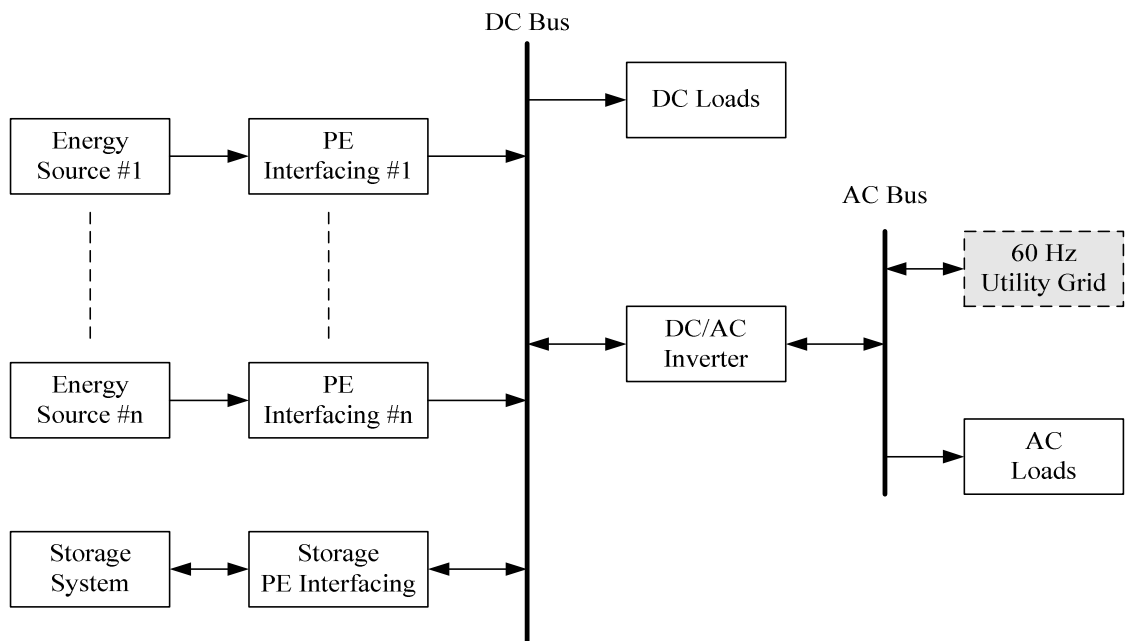


Figure 3.1. Hybrid energy system integration: DC coupling.

### AC Coupling vs. DC Coupling

There are several ways to integrate different alternative energy sources to form a hybrid system. The methods can be generally classified into two categories: DC coupling and AC coupling. AC coupling can be classified further into power frequency AC (PFAC) coupling and high frequency AC (HFAC) coupling. In a DC coupling configuration, shown in Figure 3.1, different alternative energy sources are connected to a DC bus through appropriate power electronic interfacing circuits. Then the DC energy is converted into 60 Hz (or 50 Hz) AC through a DC/AC converter (inverter) which can be bi-directional.

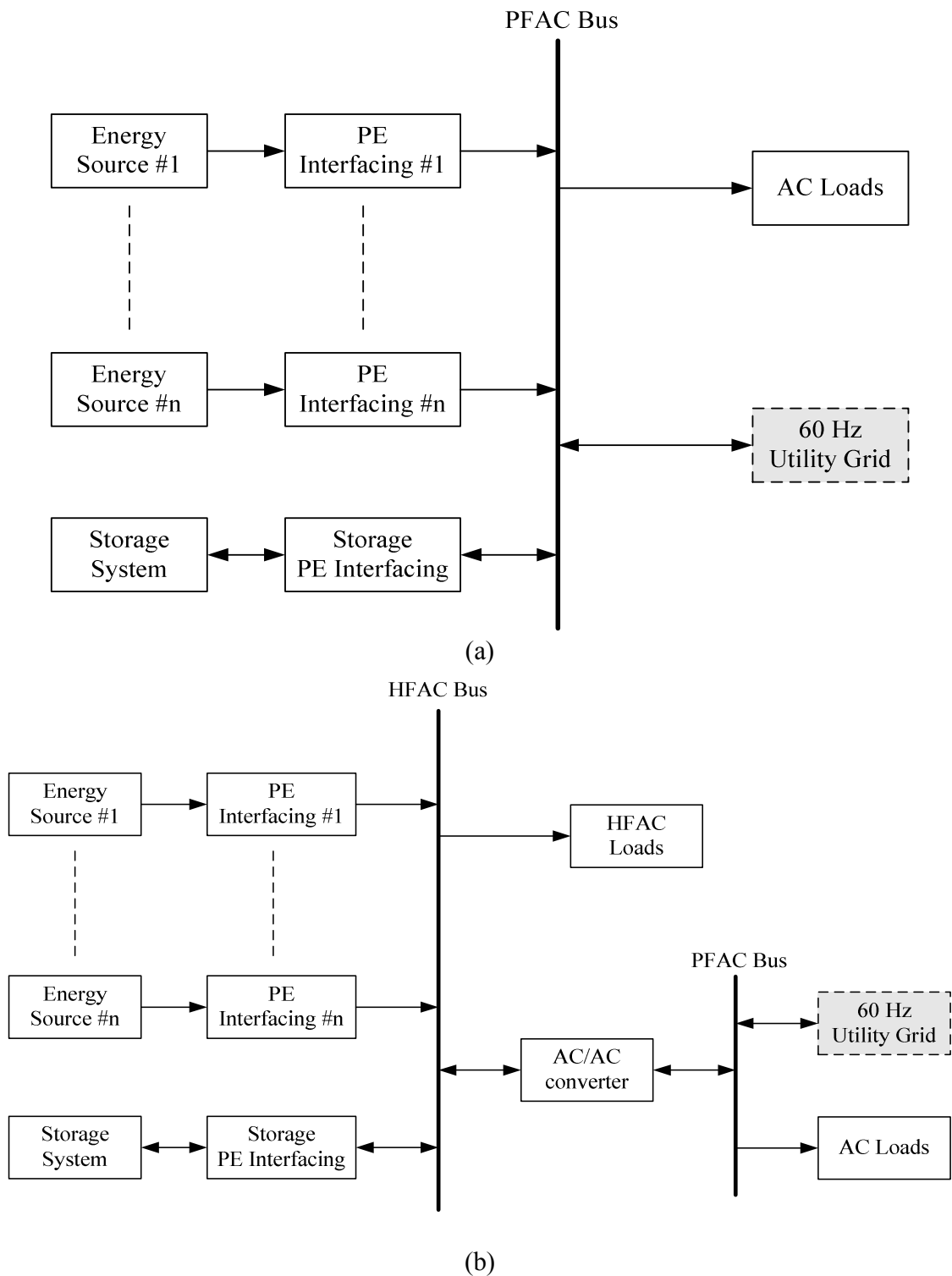


Figure 3.2. Hybrid energy system integration: (a) PFAC coupling; (b) HFAC coupling.

In a PFAC coupling scheme, shown in Figure 3.2 (a), different energy sources are integrated through proper power electronic interfacing circuits to a power frequency AC bus. Coupling inductors may also be needed to achieve desired power flow management. In a HFAC link scheme, shown in Figure 3.2 (b), different alternative energy sources are coupled to a HFAC bus. HFAC loads are connected directly to the HFAC bus. The HFAC can also be converted into PFAC through an AC/AC converter so that regular AC loads can be connected to the PFAC bus. HFAC link is originally developed for supplying power to HFAC loads. This configuration has been used mostly in applications with HFAC (e.g., 400 Hz) loads, such as airplanes, vessels, submarines and space station applications [3.29].

Different coupling schemes find their own appropriate applications. DC coupling is the simplest and the oldest type of integration. PFAC link is more modular than DC scheme and is ready for grid connection. HFAC coupling is more complicated and is more suitable for the applications with HFAC loads. Table 3.1 summarizes the advantages and disadvantages of each coupling scheme.

TABLE 3.1. COMPARISON AMONG DIFFERENT INTEGRATION SCHEMES

Coupling Scheme	Advantage	Disadvantage
DC [3.1]-[3.2], [3.12], [3.29]-[3.30]	<ol style="list-style-type: none"> <li>1. Synchronism not needed.</li> <li>2. Suitable for long distance transmission; it has less transmission losses.</li> <li>3. Single-wired connection</li> </ol>	<ol style="list-style-type: none"> <li>1. Concerns on the voltage compatibility</li> <li>2. Corrosion concerns with the DC electrodes.</li> <li>3. Non-standard connection requires high costs in installing and maintenance.</li> <li>4. If the DC/AC inverter is out of service, the whole system fails to supply AC power.</li> </ol>
PFAC [3.29], [3.31]-[3.32]	<ol style="list-style-type: none"> <li>1. High reliability. If one of the energy sources is out of service, it can be isolated from the system easily.</li> <li>2. Ready for grid connection.</li> <li>3. Standard interfacing and modular structure.</li> <li>3. Easy multi-voltage and multi-terminal matching.</li> <li>4. Well established scale economy.</li> </ol>	<ol style="list-style-type: none"> <li>1. Synchronism required.</li> <li>2. The need for power factor and harmonic distortion correction.</li> <li>3. Not suitable for long distance transmission.</li> </ol>
HFAC [3.29], [3.33]-[3.34]	<ol style="list-style-type: none"> <li>1. Higher order harmonics can be easily filtered out.</li> <li>2. Suitable for applications with HFAC loads with improved efficiency.</li> <li>3. Size of high frequency transformers, harmonic filters and other passive components are smaller.</li> </ol>	<ol style="list-style-type: none"> <li>1. Complex control</li> <li>2. Higher component and maintenance costs due to high frequency.</li> <li>3. The dependence on future advances of power electronics.</li> <li>4. Concerns about electromagnetic compatibility.</li> <li>5. Extremely limited capability of long distance transmission.</li> </ol>

### Stand-alone vs. Grid-connected Systems

A hybrid alternative energy system can either be stand-alone or grid-connected if utility grid is available. For a stand-alone application, the system needs to have sufficient storage capacity to handle the power variations from the alternative energy sources involved. A system of this type can be considered as a micro-grid, which has its own generation sources and loads [3.35]. For a grid-connected application, the alternative energy sources in the micro-grid can supply power both to the local loads and the utility grid. In addition to real power, these DG sources can also be used to give reactive power and voltage support to the utility grid. The capacity of the storage device for these systems can be smaller if they are grid-connected since the grid can be used as system backup. However, when connected to a utility grid, important operation and performance requirements, such as voltage, frequency and harmonic regulations, are imposed on the system [3.36]. Both grid-connected and stand-alone applications will be discussed in the later chapters. The optimal placement of DG sources in power systems will also be discussed in Chapter 8.

### The Proposed System Configuration

Figure 3.3 shows the system configuration for the proposed hybrid alternative energy system. In the system, the renewable wind and solar power are taken as the primary source while fuel cell/electrolyzer combination is used as a backup and storage system. This system can be considered as a complete “green” power generation system because the main energy sources and storage system are all environmentally friendly, and it can be

stand-alone or grid-connected. When there is excess wind and/or solar generation available, the electrolyzer turns on to begin producing hydrogen, which is delivered to the hydrogen storage tanks. If the H<sub>2</sub> storage tanks become full, the excess power will be diverted to other dump loads which are not shown in Figure 3.3. When there is a deficit in power generation, the fuel cell stack will begin to produce energy using hydrogen from the reservoir tanks, or in case they are empty, from the backup H<sub>2</sub> tanks. A battery bank is used to supply transient power to fast load transients, ripples and spikes in stand-alone applications. For grid-connected applications, the battery bank can be taken out from the system; the utility grid will take care of transient power. Different energy sources are connected to a 60 Hz AC bus through appropriate power electronic interfacing circuits. The system can be easily expanded; i.e., other energy sources can be integrated into the system when they are available as shown in Figure 3.3. The main system components and their sizes are discussed in the following section.

### System Unit Sizing

The unit sizing procedure discussed in this section is assumed for a stand-alone hybrid system with the proposed structure (Figure 3.3) for residential electricity supply in southwestern part of Montana. The hybrid system is designed to supply power for five homes. A typical load demand for each home reported in [3.37] in the Pacific Northwest regions is used in this simulation study. The total load demand of the five homes is shown in Figure 3.4. A 50 kW wind turbine is assumed to be available already for the hybrid system. The following unit sizing procedure is used to determine the size of PV arrays, fuel cells, the electrolyzer and the battery.

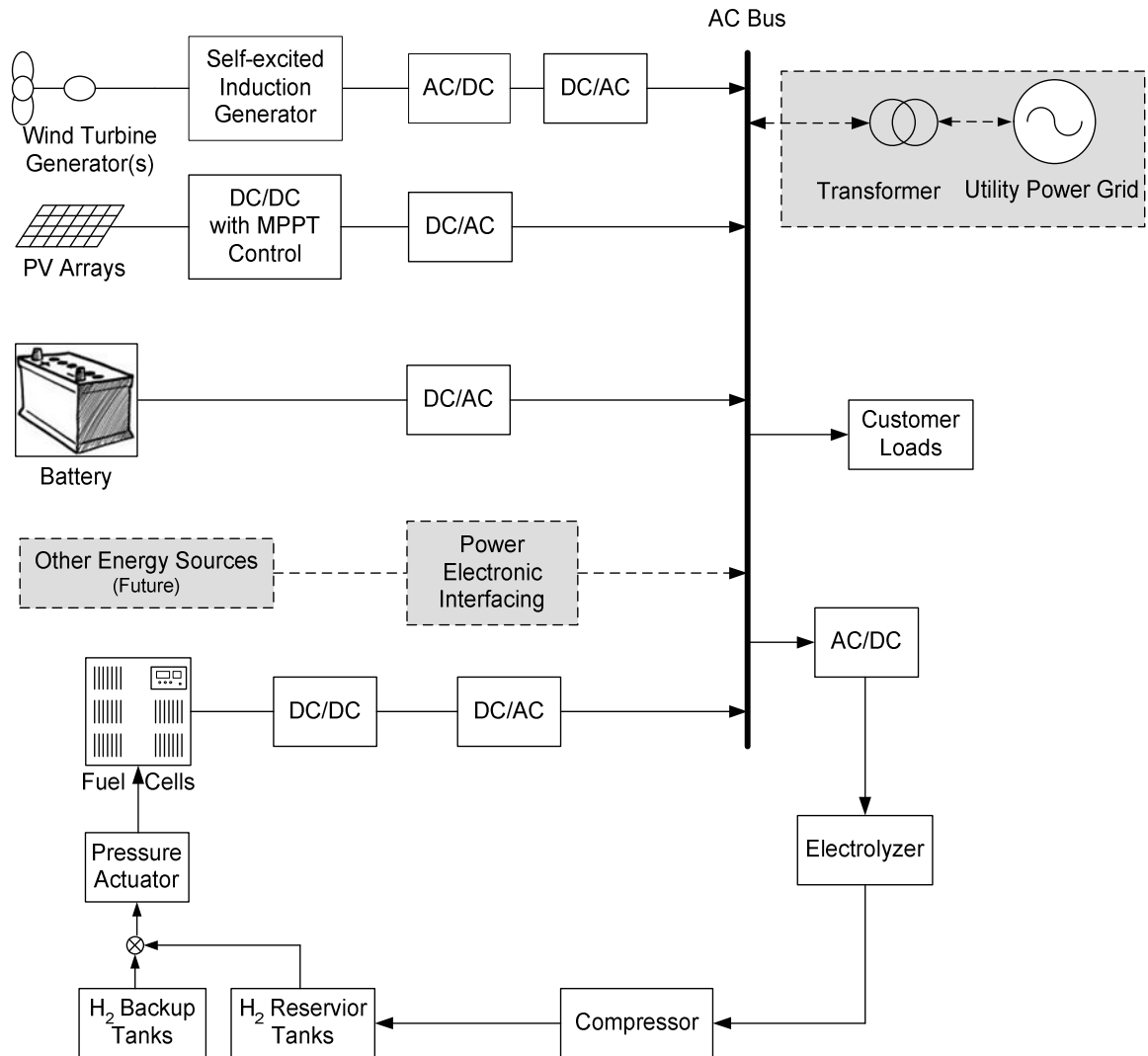


Figure 3.3. System configuration of the proposed multi-source alternative hybrid energy system (coupling inductors are not shown in the figure).

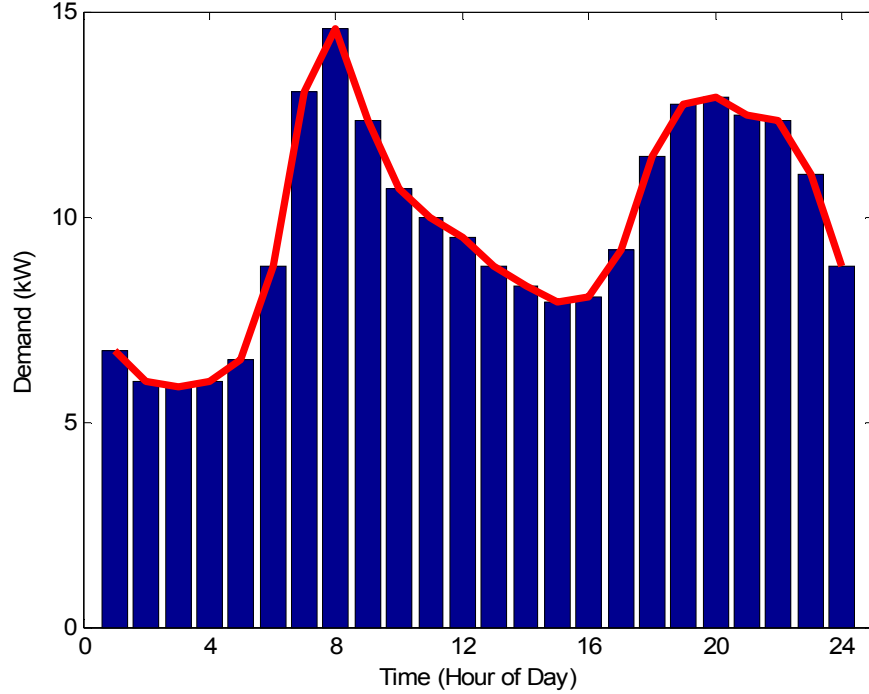


Figure 3.4. Hourly average demand of a typical residence in the Pacific Northwest area.

Before the discussion of unit sizing, the following concept is applied for indicating the overall efficiency and availability of a renewable energy source.

Capacity factor of a renewable energy,  $k_{cf}$ , is defined as:

$$k_{cf} = \frac{\text{Actual average output power over a period of time } T}{\text{Nominal power rating of the renewable energy source}} \quad (3.1)$$

For the wind and solar data reported in [3.3], [3.24], the capacity factor of the wind turbine ( $k_{cf\_wtg}$ ) and the PV ( $k_{cf\_pv}$ ) array used in the proposed hybrid system for the southwestern part of Montana are taken as 13% and 10%, respectively.

The purpose of unit sizing is to minimize the difference between the generated power ( $\bar{P}_{gen}$ ) from the renewable energy source and the demand ( $\bar{P}_{dem}$ ) over a period of time  $T$ .  $T$  is taken as one year in this study.

$$\Delta P = \bar{P}_{gen} - \bar{P}_{dem} = k_{eff\_wtg} \times P_{wtg,rated} + k_{eff\_pv} \times P_{pv,rated} - \bar{P}_{dem} \quad (3.2)$$

where  $P_{wtg,rated}$  is the power rating of the wind turbine generator and  $P_{wtg,pv}$  is the power rating the PV array.

To balance the generation and the demand, the rated power for the PV arrays is:

$$P_{pv,rated} = (\bar{P}_{dem} - k_{eff\_wtg} \times P_{wtg,rated}) / k_{eff\_pv} \quad (3.3)$$

From Figure 3.4, the average load demand is 9.76 kW. Then according to (3.3), the size of the PV array is calculated to be 32.6 kW.

The FC/electrolyzer combination is taken as the storage for the system. The fuel cell needs to supply the peak load demand when there is no wind and solar power. Therefore, the size of fuel cell is 14.6 kW (Figure 3.4). To leave some safe margin, an 18 kW fuel cell stack array is used.

The electrolyzer should be able to handle the excess power from the wind and solar power source. The maximum possible excess power is:

$$(P_{gen} - P_{dem})_{max} = 76.6 \text{ kW} \quad (3.4)$$

However, the possibility that both the wind and solar power reach their maximum points while the load demand is at its lowest value is very small. According to the data reported in [3.30], the excess available power normally is less than half of the maximum possible value. And electrolyzer is also very expensive. Therefore, a 50 kW electrolyzer [over 60% of the maximum available given in (3.4)] is used in this study.

Battery capacity can be determined based on the transient power at the load site. In this study, a 10 kWh battery bank is used.

The details of the system component parameters are listed in Table 3.2.

TABLE 3.2. COMPONENT PARAMETERS OF THE PROPOSED HYBRID ENERGY SYSTEM

<b>Wind turbine</b>	
Rated power	50 kW
Cut in speed (Cut out speed)	3 m/s (25 m/s)
Rated speed	14 m/s
Blade diameter	15 m
Gear box ratio	7.5
<b>Induction generator</b>	
Rated power	50 kW
Rated voltage	670 V
Rated frequency	60 Hz
<b>PV array</b>	
Module unit	153 cells, 173 W @1 kW/m <sup>2</sup> , 25 °C
Module number	16×12 = 192
Power rating	192×173 ≈ 33 kW
<b>Fuel cell array</b>	
PEMFC stack	500 W
PEMFC array	6×6 = 36
PEMFC array power rating	36×0.5 = 18 kW
Or, SOFC stack	5 kW
SOFC array	2×2 = 4
SOFC array power rating	4×5 kW = 20 kW
<b>Electrolyzer</b>	
Rated power	50 kW
Number of cells	40 (in series)
Operating voltage	60 - 80 V
<b>Battery</b>	
Capacity	10 kWh
Rated voltage	400 V

REFERENCES

- [3.1] K. Agbossou, M. Kolhe, J. Hamelin and T.K. Bose, "Performance of a stand-alone renewable energy system based on energy storage as hydrogen," *IEEE Transactions on Energy Conversion*, Vol. 19, No. 3, pp. 633 – 640, Sept. 2004.
- [3.2] K. Agbossou, R. Chahine, J. Hamelin, F.Laurencelle, A. Anourar, J.-M. St-Arnaud and T.K. Bose, "Renewable energy systems based on hydrogen for remote applications," *Journal of Power Sources*, Vol. 96, pp.168-172, 2001.
- [3.3] D.B. Nelson, M.H. Nehrir and C. Wang, "Unit Sizing and Cost Analysis of Stand-Alone Hybrid Win/PV/Fuel Cell Systems", *Renewable Energy* (accepted).
- [3.4] R. Lasseter, "Dynamic models for micro-turbines and fuel cells," *Proceedings*, 2001 PES Summer Meeting, Vol. 2, pp. 761-766, 2001.
- [3.5] Y. Zhu and K. Tomsovic, "Development of models for analyzing the load-following performance of microturbines and fuel cells," *Journal of Electric Power Systems Research*, pp. 1-11, Vol. 62, 2002.
- [3.6] S.R. Guda, C. Wang, and M.H. Nehrir, "Modeling of Microturbine Power Generation Systems," *Journal of Power Components & Systems* (accepted).
- [3.7] K. Sedghisigarchi and A. Feliachi, "Dynamic and Transient Analysis of Power Distribution Systems with Fuel Cells—Part I: Fuel-Cell Dynamic Model," *IEEE Transactions on Energy Conversion*, Vol. 19, No. 2, pp.423-428, June 2004.
- [3.8] K. Sedghisigarchi and A. Feliachi, "Dynamic and Transient Analysis of Power Distribution Systems with Fuel Cells—Part II: Control and Stability Enhancement," *IEEE Transactions on Energy Conversion*, Vol. 19, No. 2, pp.429-434, June 2004.
- [3.9] S.H. Chan, H.K. Ho and Y. Tian, "Multi-level modeling of SOFC-gas turbine hybrid system," *International Journal of Hydrogen Energy*, Vol. 28, No. 8, pp. 889-900, Aug. 2003.
- [3.10] Z. Miao, M. A. Choudhry, R. L. Klein and L. Fan, "Study of A Fuel Cell Power Plant in Power Distribution System – Part I: Dynamic Model," *Proceedings*, IEEE PES General Meeting, June 2004, Denver, CO.
- [3.11] Z. Miao, M. A. Choudhry, R. L. Klein and L. Fan, "Study of A Fuel Cell Power Plant in Power Distribution System – Part II: Stability Control," *Proceedings*, IEEE PES General Meeting, June 2004, Denver, CO.

- [3.12] H. Dehbonei, "Power conditioning for distributed renewable energy generation," Ph.D. Dissertation, Curtin University of Technology, Perth, Western Australia, 2003.
- [3.13] P. A. Lehman, C.E. Chamberlin, G. Pauletto, M.A. Rocheleau, "Operating Experience with a photovoltaic-hydrogen energy system," *Proceedings, Hydrogen'94: The 10<sup>th</sup> World Hydrogen Energy Conference*, Cocoa Beach, FL, June 1994.
- [3.14] A. Arkin and J .J. Duffy, "Modeling of PV, Electrolyzer, and Gas Storage in a Stand-Alone Solar-Fuel Cell System," *Proceedings, the 2001 National Solar Energy Conference, Annual Meeting, American Solar Energy Society*, 2001.
- [3.15] L. A Torres, F. J. Rodriguez and P.J. Sebastian, "Simulation of a solar-hydrogen-fuel cell system: results for different locations in Mexico," *International Journal of Hydrogen Energy*, Vol. 23, No. 11, pp. 1005-1010, Nov. 1998.
- [3.16] S. R. Vosen and J.O. Keller, "Hybrid energy storage systems for stand-alone electric power systems: optimization of system performance and cost through control strategies," *International Journal of Hydrogen Energy*, Vol. 24, No. 12, pp. 1139-56, Dec. 1999.
- [3.17] Th. F. El-Shatter, M. N. Eskandar and M.T. El-Hagry, "Hybrid PV/fuel cell system design and simulation," *Renewable Energy*, Vol. 27, No. 3, pp.479-485, Nov. 2002.
- [3.18] Ø. Ulleberg and S. O. MØRNER, "TRNSYS simulation models for solar-hydrogen systems," *Solar Energy*, Vol. 59, No. 4-6, pp. 271-279, 1997.
- [3.19] J. C. Amphlett, E.H. de Oliveira, R.F. Mann, P.R. Roberge and Aida Rodrigues, "Dynamic Interaction of a Proton Exchange Membrane Fuel Cell and a Lead-acid Battery," *Journal of Power Sources*, Vol. 65, pp. 173-178, 1997.
- [3.20] D. Candusso, L. Valero and A. Walter, "Modelling, control and simulation of a fuel cell based power supply system with energy management," *Proceedings, 28<sup>th</sup> Annual Conference of the IEEE Industrial Electronics Society (IECON 2002)*, Vol. 2, pp.1294-1299, 2002.
- [3.21] M. T. Iqbal, "Modeling and control of a wind fuel cell hybrid energy system," *Renewable Energy*, Vol. 28, No. 2, pp. 223-237, Feb. 2003.
- [3.22] H. Sharma, S. Islam and T. Pryor, "Dynamic modeling and simulation of a hybrid wind diesel remote area power system," *International Journal of Renewable Energy Engineering*, Vol. 2, No.1, April 2000.

- [3.23] R. Chedid, H. Akiki and S. Rahman, "A decision support technique for the design of hybrid solar-wind power systems," *IEEE Transactions on Energy Conversion*, Vol. 13, No. 1, pp. 76-83, March 1998.
- [3.24] W. D. Kellogg, M. H. Nehrir, G. Venkataramanan, and V. Gerez, "Generation unit sizing and cost analysis for stand-alone wind, photovoltaic, and hybrid wind/PV systems," *IEEE Transactions on Energy Conversion*, Vol. 13, No. 1, pp. 70-75, March 1998.
- [3.25] F. Giraud and Z. M. Salameh, "Steady-state performance of a grid-connected rooftop hybrid wind-photovoltaic power system with battery storage," *IEEE Transactions on Energy Conversion*, Vol. 16, No. 1, pp. 1 – 7, March 2001.
- [3.26] E. S. Abdin, A .M. Osheiba and M.M Khater, "Modeling and optimal controllers design for a stand-alone photovoltaic-diesel generating unit," *IEEE Transactions on Energy Conversion*, Vol. 14, No. 3, pp. 560-565, Sept. 1999.
- [3.27] F. Bonanno, A. Consoli, A. Raciti, B. Morgana and U. Nocera, "Transient analysis of integrated diesel-wind-photovoltaic generation systems," *IEEE Transactions on Energy Conversion*, Vol. 14, No. 2, pp. 232-238, June 1999.
- [3.28] T. Monai, I. Takano, H. Nishikawa and Sawada, "Response characteristics and operating methods of new type dispersed power supply system using photovoltaic fuel cell and SMES," *2002 IEEE PES Summer Meeting*, Vol. 2, pp. 874-879, 2002.
- [3.29] F. A. Farret and M. G. Simões, *Integration of Alternative Sources of Energy*, John Wiley & Sons, Inc., 2006.
- [3.30] Øystein Ulleberg, "Stand-Alone Power Systems for the Future: Optimal Design, Operation & Control of Solar-Hydrogen Energy Systems," Ph.D. Dissertation, Norwegian University of Science and Technology, Trondheim, 1998.
- [3.31] P. Strauss, A. Engler, "AC coupled PV hybrid systems and microgrids-state of the art and future trends," *Proceedings*, 3rd World Conference on Photovoltaic Energy Conversion, Vol. 3, No. 12-16, pp. 2129 – 2134, May 2003.
- [3.32] G. Hegde, P. Pullammanappallil, C. Nayar, "Modular AC coupled hybrid power systems for the emerging GHG mitigation products market," *Proceedings*, Conference on Convergent Technologies for Asia-Pacific Region, Vol. 3, No.15-17, pp. 971 – 975, Oct. 2003.
- [3.33] S.K Sul, I. Alan and T.A. Lipo, "Performance testing of a high frequency link converter for space station power distribution system," *Proceedings*, the 24th Intersociety: Energy Conversion Engineering Conference (IECEC-89), Vol. 1, No. 6-11, pp. 617 – 623, Aug. 1989.

- [3.34] H. J. Cha and P. N. Enjeti, "A three-phase AC/AC high-frequency link matrix converter for VSCF applications," *Proceedings, IEEE 34th Annual Power Electronics Specialist Conference 2003 (PESC '03)*, Vol. 4, No. 15-19, pp. 1971 – 1976, June 2003.
- [3.35] R. H. Lasseter, "MicroGrids," *Proceedings, 2002 IEEE PES Winter Meeting*, Vol. 1, pp. 305-308, 2002.
- [3.36] IEEE Std 1547, *IEEE Standard for Interconnecting Distributed Resources with Electric Power Systems*, 2003.
- [3.37] J. Cahill, K. Ritland, W. Kelly, "Description of Electric Energy Use in Single Family Residences in the Pacific Northwest 1986-1992," Office of Energy Resources, Bonneville Power Administration, December 1992, Portland, OR.

## CHAPTER 4

## COMPONENT MODELING FOR THE HYBRID

## ALTERNATIVE ENERGY SYSTEM

In this chapter, the models for the main components of the proposed hybrid alternative energy system, given in Chapter 3, are developed. Namely, they are fuel cells, wind energy conversion system, PV energy conversion system, electrolyzer, battery, power electronic interfacing circuits and accessory devices.

Two types of fuel cells are modeled and their applications are discussed in this dissertation. They are low temperature proton exchange membrane fuel cell (PEMFC) and high temperature solid oxide fuel cell (SOFC).

Dynamic Models and Model Validation for PEMFCIntroduction

PEMFCs show great promise for use as distributed generation (DG) sources. Compared with other DG technologies such as wind and photovoltaic (PV) generation, PEMFCs have the advantage that they can be placed at any site in a distribution system, without geographic limitations, to achieve optimal performance. Electric vehicles are another major application of PEMFCs. The increased desire for vehicles with less emission has made PEMFCs attractive for vehicular applications since they emit essentially no pollutants and have high power density and quick start.

PEMFCs are good energy sources to provide reliable power at steady state, but they

cannot respond to electrical load transients as fast as desired. This is mainly due to their slow internal electrochemical and thermodynamic responses. The transient properties of PEMFCs need to be studied and analyzed under different situations, such as electrical faults on the fuel cell terminals, motor starting and electric vehicle starting and acceleration.

Some work has been reported in the literature on steady state fuel cell modeling, e.g. [4.1]–[4.7], as well as dynamic modeling [4.8]–[4.11]. These studies are mostly based on empirical equations and/or electrochemical reactions inside the fuel cell. In recent years attempts have been made to study dynamic modeling of fuel cells with emphasis on the electrical terminal characteristics, e.g. [4.12]–[4.16]. A detailed explanation of the electrochemical properties of fuel cells and a simple equivalent electrical circuit including a capacitor due to the double-layer charging effect inside fuel cells are reported in [4.17].

In this dissertation, dynamic models are presented for PEMFCs using electrical circuits. First, through mechanistic analysis, the equivalent internal voltage source and equivalent resistors for activation loss, ohmic voltage drop and concentration voltage drop are given. Then the double-layer charging effect is considered by adding an equivalent capacitor to the circuit. The thermodynamic characteristic inside the fuel cell is also integrated into the model according to the energy balance equation. A dynamic model is built in MATLAB/SIMULINK<sup>®</sup> and an electrical model is developed in Pspice<sup>®</sup> using equivalent electrical components from an electrical engineer's point of view. Simulation results are given and validated with experimental data both for steady-state and transient responses of PEMFCs. The models show great potential to be useful in

other related studies, such as real-time control of fuel cells and hybrid alternative energy systems.

### Dynamic Model Development

In this section a mathematical approach is presented for building a dynamic model for a PEMFC stack. To simplify the analysis, the following assumptions are made [4.1], [4.5], [4.8], [4.17], [4.18]:

- (1) One-dimensional treatment.
- (2) Ideal and uniformly distributed gases.
- (3) Constant pressures in the fuel cell gas flow channels.
- (4) The fuel is humidified H<sub>2</sub> and the oxidant is humidified air. Assume the effective anode water vapor pressure is 50% of the saturated vapor pressure while the effective cathode water pressure is 100%.
- (5) The fuel cell works under 100 °C and the reaction product is in liquid phase.
- (6) Thermodynamic properties are evaluated at the average stack temperature, temperature variations across the stack are neglected, and the overall specific heat capacity of the stack is assumed to be a constant.
- (7) Parameters for individual cells can be lumped together to represent a fuel cell stack.

A schematic diagram of a PEMFC and its internal voltage drops are shown in Figure 4.1.

Gas Diffusion in the Electrodes. In order to calculate the fuel cell output voltage, the effective partial pressures of H<sub>2</sub> and O<sub>2</sub> need to be determined. In a gas mixture consisting of N species, the diffusion of component i through the porous electrodes can be described by the Stefan-Maxwell formulation [4.1], [4.5].

$$\nabla x_i = \frac{RT}{P} \sum_{j=1}^N \frac{x_i N_j - x_j N_i}{D_{i,j}} \quad (4.1)$$

where  $x_i$  ( $x_j$ ) = Mole fractions of species  $i$  ( $j$ );

$D_{i,j}$  = effective binary diffusivity of  $i$ - $j$  pair (m<sup>2</sup>/s);

$N_i$  ( $N_j$ ) = Superficial gas flux of species  $i$  ( $j$ ) [mol/(m<sup>2</sup>·s)];

$R$  = gas constant, 8.3143 J/(mol·K);

$T$  = gas temperature (K);

$P$  = overall pressure of the gas mixture (Pa).

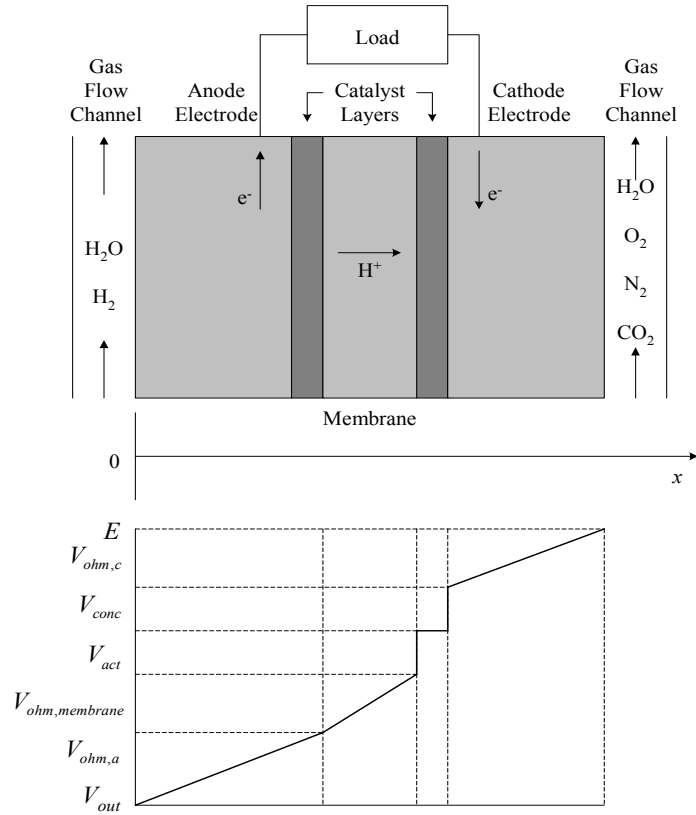


Figure 4.1. Schematic diagram of a PEMFC and voltage drops across it.

In the anode channel, the gas stream is a mixture of  $H_2$  and  $H_2O_{(g)}$ . The molar flux of water (in gas phase) normal to anode surface  $N_{H_2O}$  can be set to zero according to assumptions (1) – (3).

In the one-dimensional transport process along the  $x$  axis, shown in Figure 4.1, the diffusion of water can be simplified as

$$\frac{dx_{H_2O}}{dx} = \frac{RT}{P_a} \left( \frac{x_{H_2O}N_{H_2} - x_{H_2}N_{H_2O}}{D_{H_2O,H_2}} \right) = \frac{RT}{P_a} \left( \frac{x_{H_2O}N_{H_2}}{D_{H_2O,H_2}} \right) \quad (4.2)$$

where  $P_a$  = overall gas pressure at the anode (Pa).

The molar flux of  $H_2$  can be determined by Faraday's Law [4.1], [4.20].

$$N_{H_2} = \frac{I_{den}}{2F} \quad (4.3)$$

where  $I_{den}$  = current density (A/m<sup>2</sup>);

$F$  = Faraday constant (96487 C/mol).

By combining (4.2) and (4.3) and integrating the expression with respect to  $x$  from the anode channel to the catalyst surface, it gives:

$$x_{H_2O}^* = x_{H_2O}^{ch} \exp\left(\frac{RTI_{den}l_a}{2FP_a D_{H_2O,H_2}}\right) \quad (4.4)$$

where  $l_a$  = distance from anode surface to the reaction site (m);

Superscript \* denotes the effective value;

Superscript “*ch*” denotes the conditions at the anode or cathode channel.

Since  $x_{H_2O}^* + x_{H_2}^* = 1$ , the effective partial pressure of H<sub>2</sub> is

$$p_{H_2}^* = \frac{p_{H_2O}^*}{x_{H_2O}^*} (1 - x_{H_2O}^*) \quad (4.5)$$

According to assumption (4),  $p_{H_2O}^*$  at the anode is  $0.5p_{H_2O}^{sat}$ . Therefore,  $p_{H_2}^*$  is given as [4.1]:

$$p_{H_2}^* = 0.5p_{H_2O}^{sat} \left[ \frac{1}{x_{H_2O}^{ch} \exp\left(\frac{RTI_{den}l_a}{2FP_a D_{H_2O,H_2}}\right)} - 1 \right] \quad (4.6)$$

Superscript “*sat*” denotes the condition of saturation.

The gases flowing in the cathode channel are O<sub>2</sub>, N<sub>2</sub>, H<sub>2</sub>O<sub>(g)</sub> and CO<sub>2</sub>. Using (4.1), the diffusion of H<sub>2</sub>O<sub>(g)</sub> at the cathode side can be obtained from

$$\frac{dx_{H_2O}}{dx} = \frac{RT}{P_c} \left( \frac{x_{O_2} N_{H_2O} - x_{H_2O} N_{O_2}}{D_{H_2O,O_2}} \right) = \frac{RT}{P_c} \left( \frac{-x_{H_2O} N_{O_2}}{D_{H_2O,O_2}} \right) \quad (4.7)$$

where  $P_c$  = overall gas pressure at the cathode (Pa).

Similar to the analysis for anode, the effective molar fraction of water at the cathode catalyst interface can be found as:

$$x_{H_2O}^* = x_{H_2O}^{ch} \exp\left(\frac{RTI_{den}l_c}{4FP_c D_{H_2O,O_2}}\right) \quad (4.8)$$

where  $l_c$  = distance from cathode surface to the reaction site (m);

Through similar analytical procedures [equations (4.7)-(4.8)], the effective molar fraction of  $N_2$  and  $CO_2$  can also be determined.

$$x_{N_2}^* = x_{N_2}^{ch} \exp\left(\frac{RTI_{den}l_c}{4FP_c D_{N_2,O_2}}\right) \quad (4.9)$$

$$x_{CO_2}^* = x_{CO_2}^{ch} \exp\left(\frac{RTI_{den}l_c}{4FP_c D_{CO_2,O_2}}\right) \quad (4.10)$$

The effective molar fraction of  $O_2$  is

$$x_{O_2}^* = 1 - x_{H_2O}^* - x_{N_2}^* - x_{CO_2}^* \quad (4.11)$$

And, the corresponding effective partial pressure of  $O_2$  is

$$p_{O_2}^* = \frac{p_{H_2O}^*}{x_{H_2O}^*} x_{O_2}^* = \frac{p_{H_2O}^*}{x_{H_2O}^*} (1 - x_{H_2O}^* - x_{N_2}^* - x_{CO_2}^*) \quad (4.12)$$

According to assumption (4),  $p_{H_2O}^*$  at the cathode equals  $p_{H_2O}^{sat}$ , and the above equation can be rewritten as

$$p_{O_2}^* = p_{H_2O}^{sat} \left[ \frac{1 - x_{N_2}^* - x_{CO_2}^*}{x_{H_2O}^*} - 1 \right] \quad (4.13)$$

$p_{H_2}^*$  and  $p_{O_2}^*$ , calculated from (4.6) and (4.13), will be used in the Nernst equation to find the fuel cell output voltage. In the following subsection, material balance equations will be developed, which will also be used to determine the fuel cell output voltage.

Material Conservation Equations. The instantaneous change in the effective partial pressures of hydrogen and oxygen can be determined through the ideal gas equations as follows [4.22]:

$$\frac{V_a}{RT} \frac{dp_{H_2}^*}{dt} = M_{H_2,in} - M_{H_2,out} - \frac{i}{2F} = M_{H_2,net} - \frac{i}{2F} \quad (4.14)$$

where  $V_a$  = volume of anode channel (m<sup>3</sup>);

$M_{H_2}$  = H<sub>2</sub> mole flow rate (mol/s);

$i$  = fuel cell current (A);

Subscripts “in”, “out” and “net” denote the values related to input, output and net.

$$\frac{V_c}{RT} \frac{dp_{O_2}^*}{dt} = M_{O_2,in} - M_{O_2,out} - \frac{i}{4F} = M_{O_2,net} - \frac{i}{4F} \quad (4.15)$$

where  $V_c$  = volume of cathode channel (m<sup>3</sup>);

$M_{O_2}$  = O<sub>2</sub> mole flow rate (mol/s);

At steady-state, all partial pressures are considered to be kept constant, i.e.

$$\frac{dp_{H_2}^*}{dt} = \frac{dp_{O_2}^*}{dt} = 0 \quad (4.16)$$

Therefore, the net mole flow rates of H<sub>2</sub> and O<sub>2</sub> at steady-state are:

$$M_{H_2,net} = 2M_{O_2,net} = \frac{I}{2F} \quad (4.17)$$

Under transient state, there are delays between the change in the load current and the

flow of fuel and oxidant. The following relationships are used to represent these delay effects.

$$\begin{aligned}\tau_a \frac{dM_{H_2,net}}{dt} &= \frac{i}{2F} - M_{H_2,net} \\ \tau_c \frac{dM_{O_2,net}}{dt} &= \frac{i}{4F} - M_{O_2,net}\end{aligned}\tag{4.18}$$

where  $\tau_a$  = fuel flow delay (s);

$\tau_c$  = oxidant flow delay (s).

Fuel Cell Output Voltage. The overall reaction in a PEMFC can be simply written as:



According to assumption (5), the corresponding Nernst equation used to calculate the reversible potential is [4.20]:

$$E_{cell} = E_{0,cell} + \frac{RT}{2F} \ln[p_{H_2}^* \cdot (p_{O_2}^*)^{0.5}]\tag{4.20}$$

where  $E_{cell}$  = reversible potential of each cell (V)

$E_{0,cell}$  is the reference potential which is a function of temperature and can be expressed as follows [4.1]:

$$E_{0,cell} = E_{0,cell}^o - k_E(T - 298)\tag{4.21}$$

where  $E_{0,cell}^o$  = standard reference potential at standard state, 298 K and 1atm pressure.

To simplify the analysis, a voltage  $E_{d,cell}$  is considered to be subtracted from the right side of (4.20) for the overall effect of the fuel and oxidant delay. The steady-state value of  $E_{d,cell}$  is zero, but it will show the influence of the fuel and oxidant delays on the fuel

cell output voltage during load transients. It can be written as

$$E_{d,cell} = \lambda_e [i(t) - i(t) \otimes \exp(-t / \tau_e)] \quad (4.22)$$

where  $\lambda_e$  = constant factor in calculating  $E_d$  ( $\Omega$ );

$\tau_e$  = overall flow delay (s).

where “ $\otimes$ ” is the convolution operator. Converting (4.22) to the Laplace domain, we get

$$E_{d,cell}(s) = \lambda_e I(s) \frac{\tau_e s}{\tau_e s + 1} \quad (4.23)$$

Equation (4.23) is used for developing models both in SIMULINK and Pspice. The internal potential  $E_{cell}$  in (4.20) now becomes:

$$E_{cell} = E_{0,cell} + \frac{RT}{2F} \ln [p_{H_2}^* \cdot (p_{O_2}^*)^{0.5}] - E_{d,cell} \quad (4.24)$$

$E_{cell}$ , calculated from (4.24), is actually the open-circuit voltage of the fuel cell. However, under normal operating conditions, the fuel cell output voltage is less than  $E_{cell}$ . Activation loss, ohmic resistance voltage drop, and concentration overpotential are voltage drops across the fuel cell, as shown in Figure 4.1 [4.18]. Therefore,

$$V_{cell} = E_{cell} - V_{act,cell} - V_{ohm,cell} - V_{conc,cell} \quad (4.25)$$

where  $V_{cell}$  = output voltage of a single cell (V);

$V_{act,cell}$  = activation voltage drop of a single cell (V);

$V_{ohm,cell}$  = ohmic voltage drop of a single cell (V);

$V_{conc,cell}$  = concentration voltage drop of a single cell (V).

Applying assumption 7), the output voltage of the fuel cell stack can be obtained as

$$V_{out} = N_{cell} V_{cell} = E - V_{act} - V_{ohm} - V_{conc} \quad (4.26)$$

where  $V_{out}$  = output voltage of the fuel cell stack (V);

$N_{cell}$  = number of cells in the stack (V);

$V_{act}$  = overall activation voltage drop (V);

$V_{ohm}$  = overall ohmic voltage drop (V);

$V_{conc}$  = overall concentration voltage drop (V);

To calculate the fuel cell output voltage, the following estimations are used.

1) *Activation Voltage Drop*: Tafel equation, given below, is used to calculate the activation voltage drop in a fuel cell [4.18].

$$V_{act} = \frac{RT}{\alpha z F} \ln\left(\frac{I}{I_0}\right) = T \cdot [a + b \ln(I)] \quad (4.27)$$

On the other hand, an empirical equation for  $V_{act}$  is given in [4.1], where a constant ( $\eta_0$ ) is added to (4.27) as follows:

$$V_{act} = \eta_0 + (T - 298) \cdot a + T \cdot b \ln(I) = V_{act1} + V_{act2} \quad (4.28)$$

where  $\eta_0$ ,  $a$ ,  $b$  = empirical constants terms.

$V_{act1} = (\eta_0 + (T - 298) \cdot a)$  is the voltage drop affected only by the fuel cell internal temperature, while  $V_{act2} = (T \cdot b \cdot \ln(I))$  is both current and temperature dependent.

The equivalent resistance of activation corresponding to  $V_{act2}$  is defined as:

$$R_{act} = \frac{V_{act2}}{I} = \frac{T \cdot b \ln(I)}{I} \quad (4.29)$$

2) *Ohmic Voltage Drop*: The ohmic resistance of a PEMFC consists of the resistance of polymer membrane, the conducting resistance between the membrane and electrodes, and the resistances of electrodes. The overall ohmic voltage drop can be expressed as

$$V_{ohm} = V_{ohm,a} + V_{ohm,membrane} + V_{ohm,c} = IR_{ohm} \quad (4.30)$$

$R_{ohm}$  is also a function of current and temperature [4.1].

$$R_{ohm} = R_{ohm0} + k_{RI}I - k_{RT}T \quad (4.31)$$

where  $R_{ohm0}$  = constant part of the  $R_{ohm}$ .

$k_{RI}$  = empirical constant in calculating  $R_{ohmic}$  ( $\Omega/A$ );

$k_{RT}$  = empirical constant in calculating  $R_{ohmic}$  ( $\Omega/K$ ).

The values of  $k_{RI}$  and  $k_{RT}$  used in the simulation study are given in Table 4.3.

3) *Concentration Voltage Drop*: During the reaction process, concentration gradients can be formed due to mass diffusions from the flow channels to the reaction sites (catalyst surfaces). At high current densities, slow transportation of reactants (products) to (from) the reaction sites is the main reason for the concentration voltage drop [4.18]. Any water film covering the catalyst surfaces at the anode and cathode can be another contributor to this voltage drop [4.1]. The concentration overpotential in the fuel cell is defined as [4.18]:

$$V_{conc} = -\frac{RT}{zF} \ln \frac{C_S}{C_B} \quad (4.32)$$

where  $C_S$  is the surface concentration and  $C_B$  is the bulk concentration.

According to Fick's first law and Faraday's law [4.20], the above equation can be rewritten as:

$$V_{conc} = -\frac{RT}{zF} \ln\left(1 - \frac{I}{I_{limit}}\right) \quad (4.33)$$

where  $I_{limit}$  = limitation current (A);

$z$  = number of electrons participating.

The equivalent resistance for the concentration loss is

$$R_{conc} = \frac{V_{conc}}{I} = -\frac{RT}{zFI} \ln\left(1 - \frac{I}{I_{limit}}\right) \quad (4.34)$$

Double-Layer Charging Effect. In a PEMFC, the two electrodes are separated by a solid membrane (Figure 4.1) which only allows the  $H^+$  ions to pass, but blocks the electron flow [4.17], [4.18]. The electrons will flow from the anode through the external load and gather at the surface of the cathode, to which the protons of hydrogen will be attracted at the same time. Thus, two charged layers of opposite polarity are formed across the boundary between the porous cathode and the membrane [4.17], [4.21]. The layers, known as electrochemical double-layer, can store electrical energy and behave like a super-capacitor. The equivalent circuit of fuel cell considering this effect is given in Figure 4.2 which is similar to the circuit reported in [4.17]. But the values of  $R_{act}$  [see (4.29)] and the voltage source are different from what are defined in [4.17].  $R_{act}$  in [4.17] is defined as  $V_{act}/I$ , and the value of voltage source used in [4.17] is  $E$ .

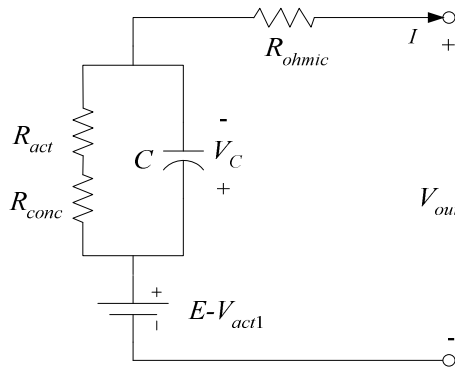


Figure 4.2. Equivalent circuit of the double-layer charging effect inside a PEMFC.

In the above circuit,  $C$  is the equivalent capacitor due to double-layer charging effect. Since the electrodes of a PEMFC are porous, the capacitance  $C$  is very large and can be in the order of several Farads [4.17], [4.26].  $R_{act}$  and  $R_{conc}$  are equivalent resistances of

activation and concentration voltage drops, which can be calculated according to (4.29) and (4.34). The voltage across  $C$  is

$$V_C = (I - C \frac{dV_C}{dt})(R_{act} + R_{conc}) \quad (4.35)$$

The double-layer charging effect is integrated into the modeling, by using  $V_C$  instead of  $V_{act2}$  and  $V_{conc}$ , to calculate  $V_{out}$ . The fuel cell output voltage now turns out to be

$$V_{out} = E - V_{act1} - V_C - V_{ohm} \quad (4.36)$$

Energy Balance of the Thermodynamics. The net heat generated by the chemical reaction inside the fuel cell, which causes its temperature to rise or fall, can be written as:

$$\dot{q}_{net} = \dot{q}_{chem} - \dot{q}_{elec} - \dot{q}_{sens+latent} - \dot{q}_{loss} \quad (4.37)$$

where  $q_{net}$  = net heat energy (J);

$q_{chem}$  = Chemical, or heat energy (J);

$q_{elec}$  = Electrical energy (J);

$q_{loss}$  = Heat loss (J).

The available power released due to chemical reaction is calculated by

$$\dot{q}_{chem} = \dot{n}_{H_2,consumed} \cdot \Delta H \quad (4.38)$$

where  $\Delta H$  = the enthalpy change of the chemical reaction inside the fuel cell.

$\dot{n}_{H_2,consumed}$  = H<sub>2</sub> consumption rate (mol/s).

The maximum available amount of electrical energy is [4.18], [4.20]

$$\Delta G = \Delta H - T\Delta S = \Delta G_0 - RT \ln [p_{H_2}^* \cdot (p_{O_2}^*)^{0.5}] \quad (4.39)$$

where  $\Delta G$  = Gibbs free energy (J/mol);

$\Delta G_0$  = Gibbs free energy at standard condition<sup>4</sup> (J/mol).

$\Delta S$  = entropy change (J/mol·K<sup>-1</sup>).

The electrical output power is computed as

$$\dot{q}_{elec} = V_{out} \cdot I \quad (4.40)$$

The sensible and latent heat absorbed during the process can be estimated by the following equation [4.8], [4.22].

$$\begin{aligned} \dot{q}_{sens+latent} = & (\dot{n}_{H2,out} \cdot T - \dot{n}_{H2,in} \cdot T_{room}) \cdot C_{H2} \\ & + (\dot{n}_{O2,out} \cdot T - \dot{n}_{O2,in} \cdot T_{room}) \cdot C_{O2} \\ & + \dot{n}_{H2O,generated} \cdot (T - T_{room}) \cdot C_{H2O,l} \\ & + \dot{n}_{H2O,generated} \cdot H_V \end{aligned} \quad (4.41)$$

where  $q_{sens+latent}$  = sensible and latent heat (J);

$\dot{n}_i$  = flow rate of species  $i$  (mol/s);

$C_i$  = specific heat capacity of species  $i$  [J/(mol·K)];

$H_V$  = Vaporization heat of water (J/mol).

$T_{room}$  = room temperature (K);

The heat loss, which is mainly transferred by air convection, can be estimated by the following formula [4.22]:

$$\dot{q}_{loss} = h_{cell}(T - T_{room})N_{cell}A_{cell} \quad (4.42)$$

where  $h_{cell}$  = convective heat transfer coefficient [W/(m<sup>2</sup>·K)]. It can be obtained through experiments [4.8].

At steady state  $\dot{q}_{net} = 0$ , and the fuel cell operates at a constant temperature. During transitions, the temperature of fuel cell will rise or drop according to the following

---

<sup>4</sup> 1atm, 298K

equation [4.22]:

$$M_{FC} C_{FC} \frac{dT}{dt} = \dot{q}_{net} \quad (4.43)$$

where  $M_{FC}$  is the total mass of the fuel cell stack and  $C_{FC}$  is the overall specific heat capacity of the stack.

#### Dynamic Model Built in Matlab/Simulink

A dynamic model for the PEMFC has been developed in MATLAB/SIMULINK, based on the electrochemical and thermodynamic characteristics of the fuel cell discussed in the previous section. The fuel cell output voltage, which is a function of temperature and load current, can be obtained from the model. Figure 4.3 shows the block diagram, based on which the MATLAB/SIMULINK model has been developed. In this figure, the input quantities are anode and cathode pressures, initial temperature of the fuel cell, and room temperature. At any given load current and time, the internal temperature  $T$  is determined and both the load current and temperature are fed back to different blocks, which take part in the calculation of the fuel cell output voltage.

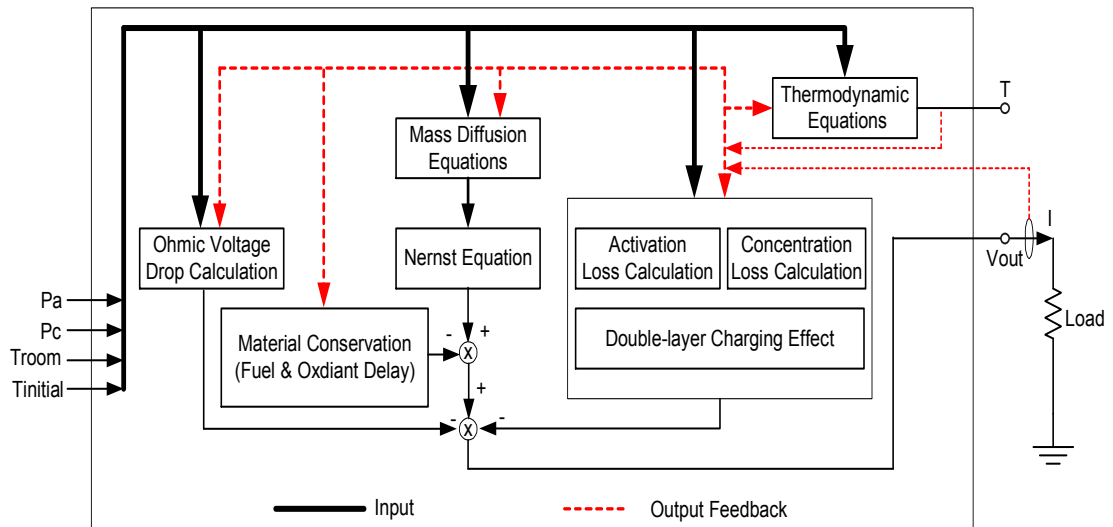


Figure 4.3. Diagram of building a dynamic model of PEMFC in SIMULINK.

In this block diagram, mass diffusion equations (4.1)-(4.13) are used to calculate the effective partial pressures of  $H_2$  and  $O_2$ . Then, the Nernst equation (4.20) and the overall fuel and oxidant delay effect, given by (4.22), are employed to determine the internal potential ( $E$ ) of the fuel cell. The ohmic voltage drop equations (4.30)-(4.31), activation voltage drop equations (4.27)-(4.29) and concentration voltage drop equations (4.33)-(4.34) together with the double-layer charging effect equation (4.35) are applied to determine the terminal (output) voltage of the fuel cell. Thermodynamic effects are also considered via energy balance equations (4.37)-(4.43).

#### Equivalent Electrical Model in Pspice

In practice, fuel cells normally work together with other electrical devices, such as power electronic converters. Pspice is a valuable simulation tool used to model and investigate the behavior of electrical devices and circuits. An electrical equivalent model of fuel cell, built in Pspice, can be used with electrical models of other components to

study the performance characteristics of the fuel cell power generation unit. A block diagram to build such model for PEMFC is given in Figure 4.4, which is also based on the characteristics discussed previously. The development of electrical circuit model for different blocks in Figure 4.4 is discussed below.

Internal Potential E. According to (4.20)-(4.26), the internal potential  $E$  is a function of load current and temperature. An electrical circuit for the internal potential block is given in Figure 4.5. The current and temperature controlled voltage source  $f_1(I, T)$  in the figure represents the current and temperature dependent part of (4.20). Note that the effective partial pressures ( $p_{H_2}^*$  and  $p_{O_2}^*$ ) given in (4.20) are current dependent. The current controlled voltage source  $f_2(I)$  stands for  $E_{d,cell}$  in (4.22).

$$f_1(I, T) = -\frac{N_{cell}RT}{2F} \ln[p_{H_2}^* \cdot (p_{O_2}^*)^{0.5}] + N_{cell}k_E(T - 298) \quad (4.44)$$

$$f_2(I) = N_{cell}E_{d,cell} \quad (4.45)$$

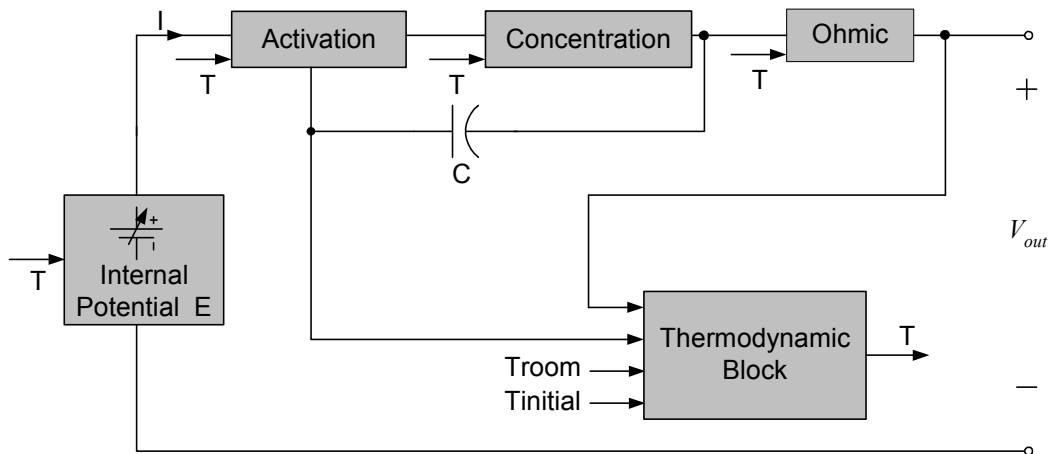


Figure 4.4. Diagram of building an electrical model of PEMFC in Pspice.

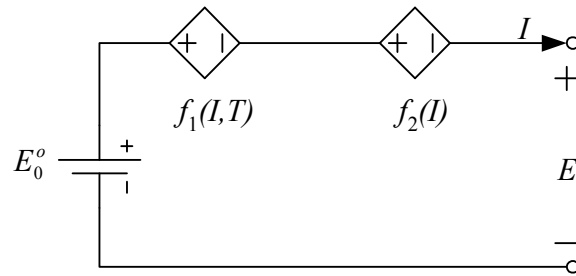


Figure 4.5. Electrical circuit for internal potential  $E$ .

Circuit for Activation Loss. From (4.28), the activation voltage drop can be divided into two parts:  $V_{act1}$  and  $V_{act2}$ .  $V_{act1}$  can be modeled by a constant voltage source in series with a temperature controlled voltage source.  $V_{act2}$  can be represented by a temperature and current dependent resistor  $R_{act}$ . This resistor is assumed to be composed of a constant-value resistor ( $R_{act0}$ ), a current-dependent resistor ( $R_{act1}$ ) and a temperature-dependent resistor ( $R_{act2}$ ). A current-dependent resistor can be easily built in Pspice by using the polynomial current controlled voltage source model, “*HPOLY*”. A temperature-dependent resistor can be built by Analog Behavioral Models (ABMs) in Pspice [4.24]. The electrical circuit for activation voltage drop is given in Figure 4.6. In this figure, with reference to (4.28), we can write

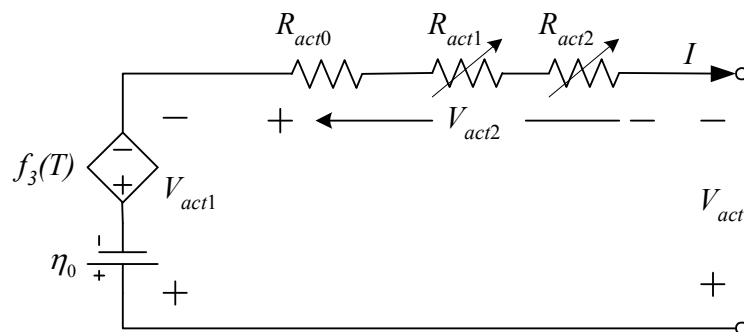


Figure 4.6. Electrical circuit for activation loss.

$$f_3(T) = (T - 298) \cdot a \quad (4.46)$$

$$R_{act} = R_{act0} + R_{act1} + R_{act2} \quad (4.47)$$

Circuits for Ohmic and Concentration Voltage Drops. According to (4.31) and (4.34), both  $R_{ohm}$  and  $R_{conc}$  are current and temperature dependent resistors. Therefore, they can be modeled in Pspice the same way  $R_{act}$  is modeled. Figure 4.7 shows the equivalent circuit for ohmic voltage drop.

$$R_{ohm} = R_{ohm0} + R_{ohm1} + R_{ohm2} \quad (4.48)$$

$R_{ohm0}$  is the constant part of  $R_{ohm}$ . With reference to (4.31),  $R_{ohm1} = k_{RI}I$  is the current-dependent part of  $R_{ohm}$  and  $R_{ohm2} = -k_{RT}T$  is its temperature-dependent part.

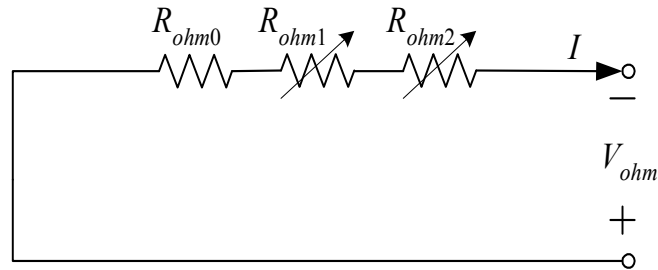


Figure 4.7. Electrical circuit for ohmic voltage drop.

The electrical circuit model for concentration voltage drop is shown in Figure 4.8.

$$R_{conc} = R_{conc0} + R_{conc1} + R_{conc2} \quad (4.49)$$

where  $R_{conc0}$  is the constant part of  $R_{conc}$  and  $R_{conc1}$ ,  $R_{conc2}$  are its current-dependent and temperature-dependent parts.

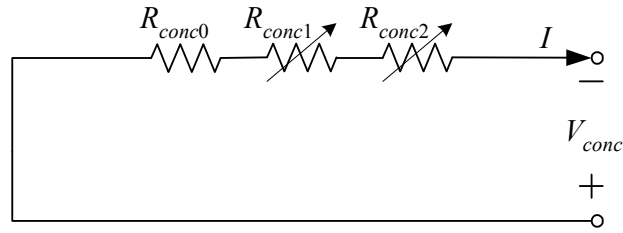


Figure 4.8. Electrical circuit for concentration voltage drop.

Equivalent Capacitor of Double-layer Charging Effect. In Figure 4.4,  $C$  is the equivalent capacitance of double-layer charging effect discussed in the previous section. This capacitance can be estimated through the measurement of the dynamic response of a real fuel cell stack [4.17]. Figure 4.2 shows how this capacitance is added into the circuit.

Thermodynamic Block. The analogies between the thermodynamic and electrical quantities, given in Table 4.1, are employed to develop the electrical circuit model for the thermodynamic block shown in Figure 4.4 [4.23]. The thermodynamic property inside the fuel cell (4.37)-(4.43) can therefore be simulated by the circuit shown in Figure 4.9. The power consumed by activation, ohmic and concentration losses is considered as the heat source which causes the fuel cell temperature to rise.

$$\dot{q}_{in} = (E - V_{out}) \cdot I \quad (4.50)$$

The thermal resistance due to air convection is:

$$R_T = 1 / (h_{cell} \cdot N_{cell} \cdot A_{cell}) \quad (4.51)$$

In Figure 4.9, the constant voltage source  $E_T$  represents the environmental temperature, and the voltage across the capacitance ( $C_h$ ) is the overall temperature of the fuel cell stack,  $T$ .

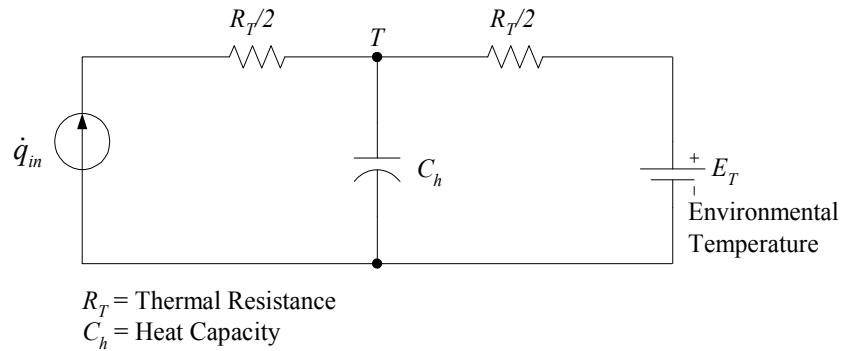


Figure 4.9. Equivalent circuit of thermodynamic property inside PEMFC.

TABLE 4.1. ANALOGIES BETWEEN THERMODYNAMIC AND ELECTRICAL QUANTITIES

Electrical Potential: $U$ (V)	Temperature: $T$ (K)
Electrical Current: $I$ (A)	Heat Flow Rate: $P_h$ (W)
Electrical Resistance: $R$ (Ohm)	Thermal Resistance: $\theta$ (K/W)
Electrical Capacitance: $C$ (F)	Heat Capacity: $C_h$ (J/K)
$RI = U$	$\theta P_h = T$
$I = C \frac{dU}{dt}$	$P_h = C_h \frac{dT}{dt}$

### Model Validation

By applying the equations and the equivalent electrical circuits discussed in the previous sections, dynamic models for an Avista Labs (Relion now) SR-12 PEMFC stack were built both in MATLAB/SIMULINK and Pspice environments. The specifications of SR-12 fuel cell stack are given in Table 4.2 [4.25]. The electrical model parameter values used in the simulation studies are listed in Table 4.3.

TABLE 4.2. SPECIFICATIONS OF SR-12

Description	Value
Capacity	500W
Number of cells	48
Operating environmental temperature	5°C to 35°C
Operating pressures*	$P_{H_2} \approx 1.5\text{atm}$ $P_{\text{cathode}} \approx 1.0\text{atm}$
Unit Dimensions (W×D×H)	56.5×61.5×34.5 cm
Weight	44kg

\*: The 99.95% pure hydrogen flows at manifold pressure of about 7psi. The environmental air is driven by the SR-12's internal fan to pass through the cathode to provide oxygen.

Experimental Setup. To validate the models built in SIMULINK and Pspice, real input and output data were measured on the 500W SR-12 Avista Labs (Relion now) PEMFC. The block diagram of the experimental setup is shown in Figure 4.10. The Chroma 63112 programmable electronic load was used as a current load. Current signals were measured by LEM LA100-P current transducers; the output voltage was measured by a LEM LV25-P voltage transducer and the temperature was measured by a k-type thermocouple together with an analog connector. The current, voltage and temperature data were all acquired by a 12-bit Advantech data acquisition card in a PC.

TABLE 4.3. ELECTRICAL MODEL PARAMETER VALUES FOR SR-12 STACK

$E_0^o$ (V)	58.9	$C_h$ (F)	22000
$k_E$ (V/K)	0.00085	$R_T$ ( $\Omega$ )	0.0347
$\tau_e$ (s)	80.0	$C$ (F)	0.1F (4.8F for each cell)
$\lambda_e$ ( $\Omega$ )	0.00333	$R_{ohm0}$ ( $\Omega$ )	0.2793
$\eta_0$ (V)	20.145	$R_{ohm1}$ ( $\Omega$ )	$0.001872 \times I$
$a$ (V/K)	-0.1373	$R_{ohm2}$ ( $\Omega$ )	$-0.0023712 \times (T-298)$
$R_{act0}$ ( $\Omega$ )	1.2581	$R_{conc0}$ ( $\Omega$ )	0.080312
$R_{act2}$ ( $\Omega$ )	$0.00112 \times (T-298)$	$R_{conc2}$ ( $\Omega$ )	$0.0002747 \times (T-298)$
$R_{act1}$ ( $\Omega$ )	$-1.6777 \times 10^{-6} I^5 + 1.2232 \times 10^{-4} I^4$ $- 3.4 \times 10^{-3} I^3 + 0.04545 I^2 - 0.3116 I$		
$R_{conc1}$ ( $\Omega$ )	$5.2211 \times 10^{-8} I^6 - 3.4578 \times 10^{-6} I^5 + 8.6437 \times 10^{-5} I^4$ $- 0.010089 I^3 + 0.005554 I^2 - 0.010542 I$		

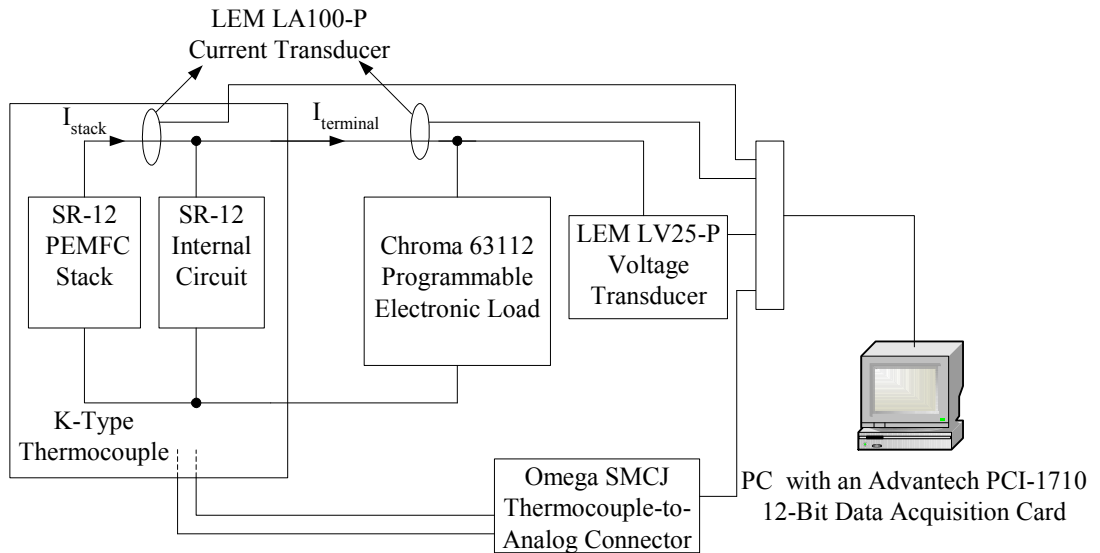


Figure 4.10. Experimental configuration on the SR-12 PEMFC stack.

Steady-State Characteristics. The steady state characteristics of SR-12 were obtained by increasing the load current from 1.1A to 20.5A in steps of 0.2A every 40 seconds. Both the stack current and terminal current (Figure 4.10) were measured, but only the stack current is used to validate the models since it is the current directly from the fuel cell stack. The experimental average value of V-I curve of the fuel cell is shown in Figure 4.11. The steady-state responses of the models in SIMULINK and Pspice are also given in Figure 4.11 in order to compare them with the experimental data. Both the SIMULINK and Pspice model responses agree very well with the real data from the fuel cell stack. The voltage drop at the beginning and end of the curves shown in Figure 4.11 are due to activation and concentration losses, respectively. The voltage drop in the middle of the curves (which is approximately linear) is due to the ohmic loss in the fuel cell stack [4.18].

Figure 4.12 shows the power vs. current (P-I) curves of the PEMFC stack, obtained from the experimental data and the models. The model responses also match well with experimental data in this case. Note that peak output power occurs near the fuel cell rated output, beyond which the fuel cell goes into the concentration zone. In this region, the fuel cell output power will decrease with increasing load current due to a sharp decrease in its terminal voltage.

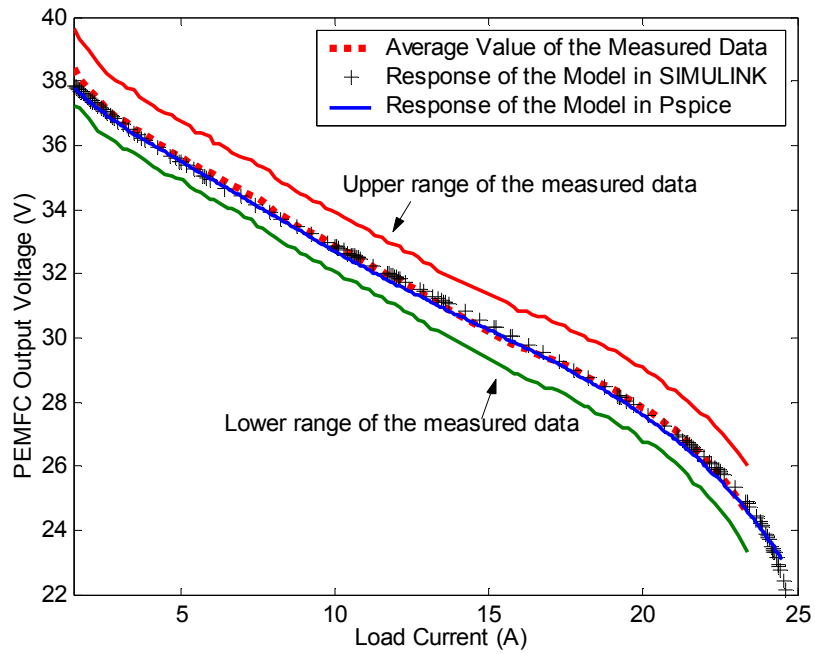


Figure 4.11. V-I characteristics of SR-12 and models.

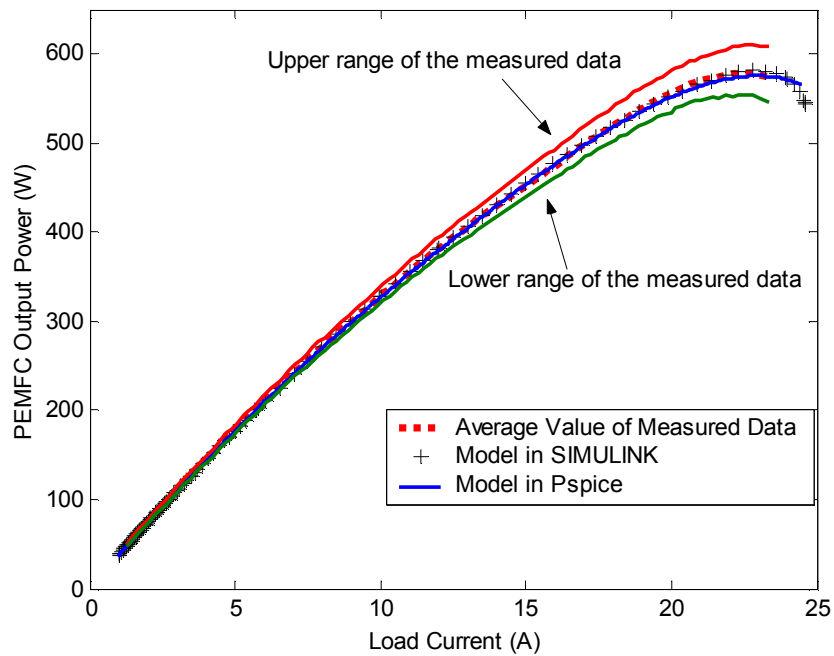


Figure 4.12. P-I characteristics of SR-12 and models.

Temperature Response. The temperature response of the PEMFC stack, shown in Figure 4.13, was measured under the same ramp load current as given in the previous sub-section. The temperature was measured as the current increased from 1.1A to 20.5A with a slew rate of 5mA/s. The temperature response of the SIMULINK and Pspice models are also given in Figure 4.13 for comparison with the measured values. Although there are some differences between the model responses and the measured data, the models can predict the temperature response of the fuel cell stack within 3.5K in the worst case.

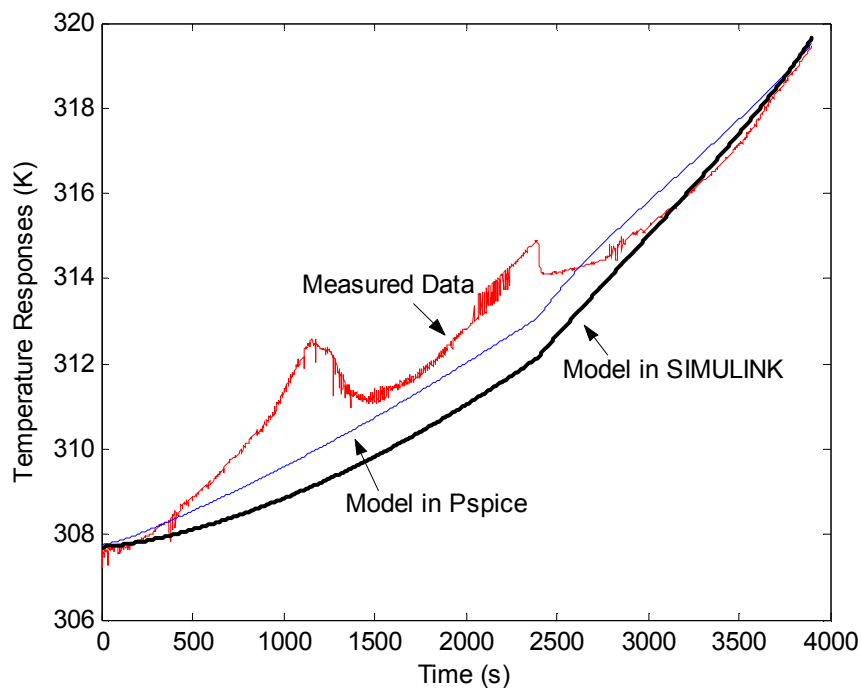


Figure 4.13. Temperature responses of the SR 12 stack and models.

Transient Performance. The dynamic property of PEMFC depends mainly on the following three aspects: double-layer charging effects, fuel and oxidant flow delays, and thermodynamic characteristics inside the fuel cells. Although the capacitance ( $C$ ) due to the double-layer charging effect is large (in the order of several Farads for each cell), the time constant  $\tau=(R_{act}+R_{conc})\cdot C$  is normally small (less than 1 second) because  $(R_{act}+R_{conc})$  is small (less than  $0.05\Omega$  for the single cell used in this study) when the fuel cell works in the linear zone. Therefore, capacitor  $C$  will affect the transient response of PEMFC in the short time range. The transient responses of the models to a fast step load change are given in Figure 4.14. It is noted that when the load current steps up, the voltage drops simultaneously to some value due to the voltage drop across  $R_{ohm}$ , and then it decays exponentially to its steady-state value due to the capacitance ( $C$ ).

On the other hand, the fuel and oxidant flows cannot follow the load current changes instantaneously. The delays can be in the range from several tens of seconds to several hundreds of seconds. Also, the temperature of fuel cell stack cannot change instantaneously. The thermodynamic time constant of a PEMFC can be in the order of minutes. Thus the fuel and oxidant flow delays and the thermodynamic characteristics will normally dominate the transient responses in the long time operation. The corresponding SIMULINK and Pspice model responses are given in Figure 4.15. From this figure it is noticed that the voltage drops below its steady-state value when the load steps up and then recovers back to its steady-state value in a relatively long time range (in the order of about hundred seconds to several minutes). As shown in Figures. 4.14 and 4.15, simulation results agree well with the measured data.

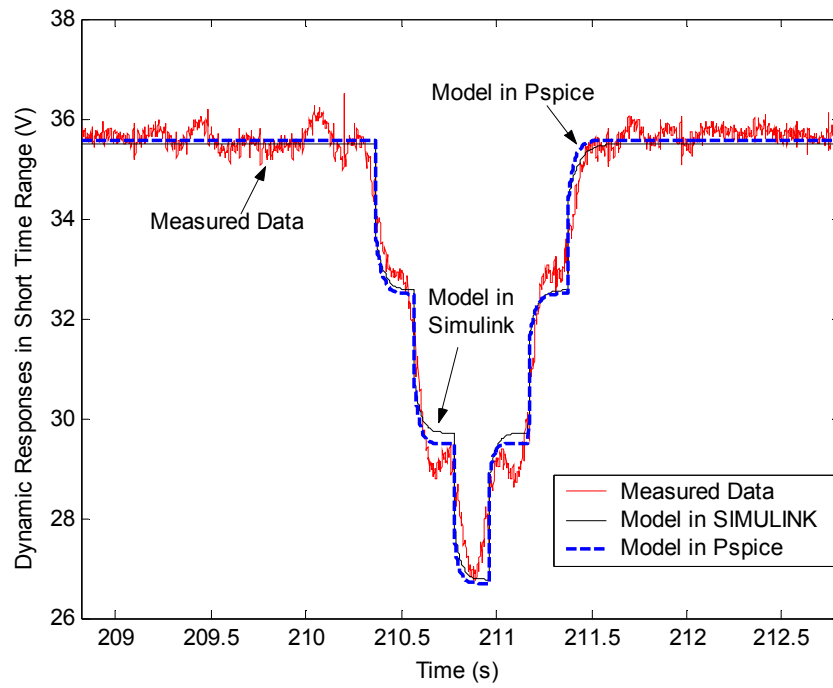


Figure 4.14 Transient responses of the models in short time range.

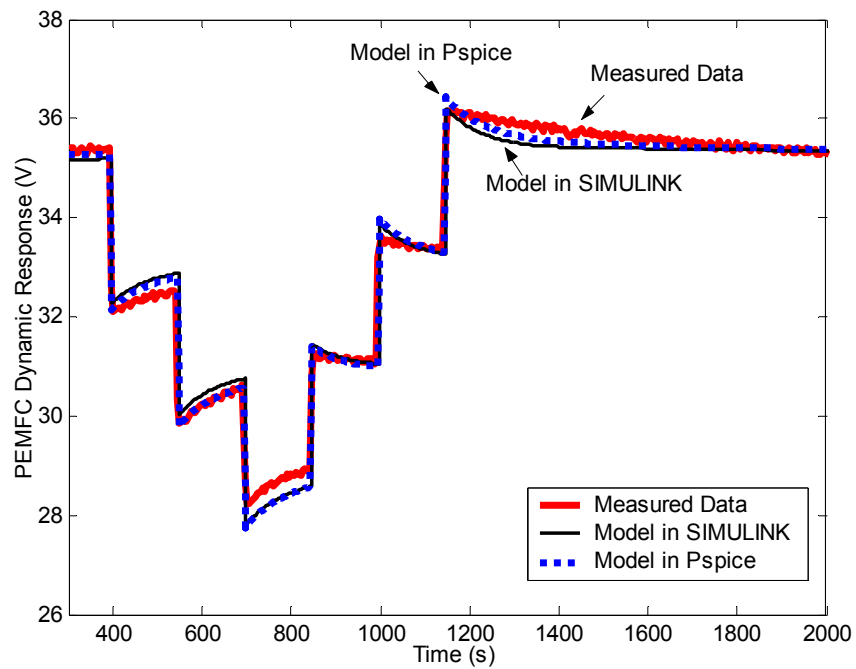


Figure 4.15. Transient responses of the models in long time range.

## Dynamic Models for SOFC

### Introduction

Solid oxide fuel cells are advanced electrochemical energy conversion devices operating at a high temperature, converting the chemical energy of fuel into electric energy at high efficiency. They have many advantages over conventional power plants and show great promise in stationary power generation applications [4.27], [4.28]. The energy conversion efficiency of a SOFC stack can reach up to 65%, and its overall efficiency, when used in combined heat and power (CHP) applications, i.e., as an integrated SOFC-combustion turbine system, can even reach 70% [4.29]. Despite slow start-up and thermal stresses due to the high operating temperature, SOFC allows for internal reforming of gaseous fuel inside the fuel cell, which gives its multi-fuel capability [4.18], [4.30].

SOFC modeling is of interest for its performance prediction and controller design. Many SOFC models have been developed; some are highly theoretical and are based on empirical equations, e.g. [4.31]-[4.33], and some are more application oriented [4.34]-[4.37]. Increased interest in SOFC power plant design and control has led to a need for appropriate application oriented SOFC models. An integrated SOFC plant dynamic model for power system simulation (PSS) software was presented in [4.34]. Three operation limits of SOFC power plants were addressed in that paper in order to achieve a safe and durable cell operation. However, the thermodynamic properties of SOFCs were not discussed in the paper. A transient model of a tubular SOFC consisting of an electrochemical model and a thermal model was given in [4.35]. However, the

dynamic response of the model due to load variations was only investigated in large (minute) time scale.

In this section, a dynamic model of a tubular SOFC stack is presented based on its thermodynamic and electrochemical properties, and on the mass and energy conservation laws with emphasis on the fuel cell electrical (terminal) characteristics. The SOFC model, implemented in MATLAB/Simulink<sup>®</sup>, mainly consists of an electrochemical sub-model and a thermodynamic sub-model. The double-layer charging effect [4.39] is also taken into account in the model. The model responses are studied under both constant fuel flow and constant fuel utilization operating modes. The effect of temperature on the steady-state V-I (output voltage vs. current) and P-I (output power vs. current) characteristics are also studied. The dynamic responses of the model are given and discussed in different time scales, i.e., from small time scale ( $10^{-3}$ - $10^{-1}$  s) to large time scale ( $10^2$ - $10^3$ s). The temperature response of the model is given as well. The SOFC model has been used to study the SOFC overloading capability and to investigate the performance of a SOFC distributed generation system, which is reported in Chapters 5 and 6. The model shows the potential to be useful in SOFC related studies such as real-time control of SOFC and its distributed generation applications.

### Dynamic Model Development

In this section a mathematical approach is presented for building a dynamic model for a tubular SOFC fuel cell stack. To simplify the analysis, the following assumptions are made:

- (1) One-dimensional treatment.

- (2)  $O^-$  conducting electrolytes and ideal gases.
- (3)  $H_2$  fuel and large stoichiometric quantity of  $O_2$  at cathode.
- (4)  $H_2$  and  $O_2$  partial pressure are uniformly decreased along the anode channel while the water vapor partial pressure is uniformly increased for normal operations.
- (5) Lumped thermal capacitance is used in the thermodynamic analysis, and the effective temperature of flowing gases in gas channels (anode and cathode channels) is represented by its arithmetical mean value,  $T_{gas}^{ch} = (T_{gas}^{in} + T_{gas}^{out})/2$ .
- (6) The combustion zone is not modeled in this SOFC thermal model. The fuel and air are assumed to be pre-heated.
- (7) Parameters for individual cells can be lumped together to represent a fuel cell stack.

A schematic diagram of a SOFC is shown in Figure 4.16. Two porous electrodes (anode and cathode) are separated by a solid ceramic electrolyte. This electrolyte material (normally dense yttria-stabilized zirconia) is an excellent conductor for negatively charged ions (such as  $O^-$ ) at high temperatures [4.18]. At the cathode, oxygen molecules accept electrons from the external circuit and change to oxygen ions. These negative ions pass across the electrolyte and combine with hydrogen, at the anode, to produce water. For the details of principle of operation of SOFC, the reader is referred to [4.18], [4.27]-[4.29].

Effective Partial Pressures. In this part, expressions for  $H_2$ ,  $O_2$  and  $H_2O$  partial pressures at anode and cathode channels and their effective values at actual reaction sites are derived in terms of the fuel cell operating parameters (e.g., fuel cell temperature, fuel

and oxidant flow rates, and anode and cathode inlet pressures) and the physical and electrochemical parameters of the fuel cell. These partial pressure values will be used to calculate the fuel cell output voltage.

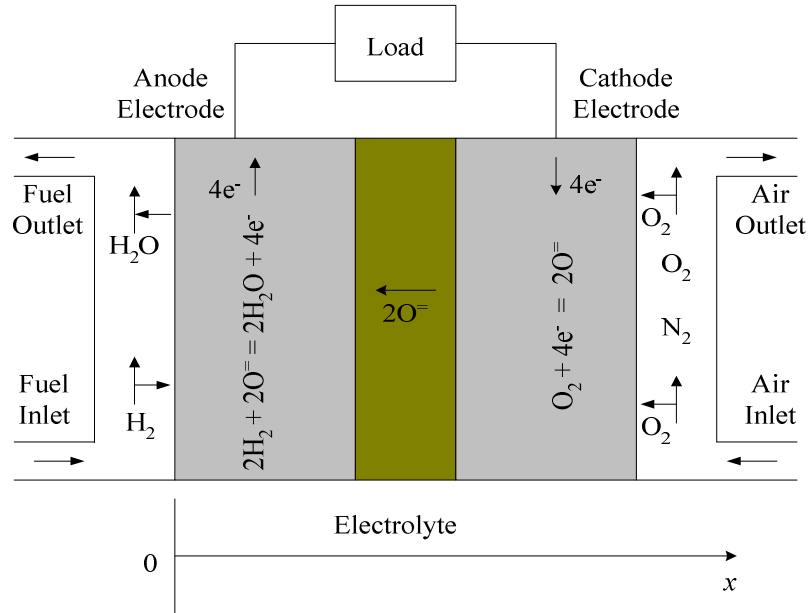


Figure 4.16. Schematic diagram of a solid oxide fuel cell.

As shown in Figure 4.16, when load current is being drawn, H<sub>2</sub> and O<sub>2</sub> will diffuse through the porous electrodes to reach the reaction sites, and the reactant H<sub>2</sub>O will diffuse from the reaction sites to the anode channel. As a result, H<sub>2</sub>, H<sub>2</sub>O and O<sub>2</sub> partial pressure gradients will be formed along the anode and cathode channels when the fuel cell is under load. Assuming uniform variation of gas partial pressures [assumption (4)], the arithmetic mean values are used to present the overall effective gas partial pressures in the channels.

$$p_{H_2}^{ch} = \frac{p_{H_2}^{in} + p_{H_2}^{out}}{2} \quad (4.52.a)$$

$$p_{H_2O}^{ch} = \frac{p_{H_2O}^{in} + p_{H_2O}^{out}}{2} \quad (4.52.b)$$

$$p_{O_2}^{ch} = \frac{p_{O_2}^{in} + p_{O_2}^{out}}{2} \quad (4.53)$$

The effective partial pressures of H<sub>2</sub> and O<sub>2</sub> at the actual reaction sites will be less than those in the gas flow channels due to mass diffusion. In contrast, the vapor partial pressure at reaction sites is higher than that in the anode flow channel. In order to calculate the fuel cell output voltage, the effective partial pressures of H<sub>2</sub>, H<sub>2</sub>O and O<sub>2</sub> at the reaction sites need to be determined. In a gas mixture consisting of  $N$  species, the diffusion of component  $i$  through the porous electrodes can be described by the Stefan-Maxwell formulation [4.1].

$$\nabla x_i = \frac{RT}{P} \sum_{j=1}^N \frac{x_i N_j - x_j N_i}{D_{i,j}} \quad (4.54)$$

where  $x_i$  ( $x_j$ ) = Mole fractions of species  $i$  ( $j$ );

$D_{i,j}$  = effective binary diffusivity of  $i$ - $j$  pair (m<sup>2</sup>/s);

$N_i$  ( $N_j$ ) = Superficial gas flux of species  $i$  ( $j$ ) [mol/(m<sup>2</sup>·s)];

$R$  = gas constant, 8.3143 J/(mol·K);

$T$  = gas temperature (K);

$P$  = overall pressure of the gas mixture (Pa).

In the anode channel, the gas stream is a mixture of H<sub>2</sub> and H<sub>2</sub>O. In the one-dimensional transport process along the  $x$  axis, shown in Figure 4.16, the diffusion of H<sub>2</sub> can be simplified as

$$\frac{dx_{H_2}}{dx} = \frac{RT}{P_a^{ch}} \left( \frac{x_{H_2} N_{H_2O} - x_{H_2O} N_{H_2}}{D_{H_2, H_2O}} \right) \quad (4.55)$$

The molar flux of H<sub>2</sub> and H<sub>2</sub>O can be determined by Faraday's Law [4.20].

$$N_{H_2} = -N_{H_2O} = \frac{i_{den}}{2F} \quad (4.56)$$

Note that  $x_{H_2} + x_{H_2O} = 1$ , then (4.55) can be written as

$$\frac{dp_{H_2}}{dx} = -\frac{RT}{D_{H_2, H_2O}} \frac{i_{den}}{2F}. \quad (4.57)$$

Similarly, we can get the one-dimensional Stefan-Maxwell diffusion equation for H<sub>2</sub>O

$$\frac{dp_{H_2O}}{dx} = \frac{RT}{D_{H_2, H_2O}} \frac{i_{den}}{2F} \quad (4.58)$$

Integrating equations (4.57) and (4.58) with respect to  $x$  from the anode channel surface to the actual reaction site will yield

$$p_{H_2}^* = p_{H_2}^{ch} - \frac{RTl_a}{2FD_{H_2, H_2O}} i_{den}, \quad (4.59)$$

$$p_{H_2O}^* = p_{H_2O}^{ch} + \frac{RTl_a}{2FD_{H_2, H_2O}} i_{den}. \quad (4.60)$$

In the cathode channel, the oxidant is air that mainly consists of O<sub>2</sub>, and N<sub>2</sub>, that is  $x_{O_2} + x_{N_2} \approx 1$ . Applying the same procedure as above, the one-dimensional Stefan-Maxwell diffusion equation for O<sub>2</sub> can be expressed as

$$\frac{dx_{O_2}}{dx} = \frac{RT}{P_c^{ch}} \left( \frac{x_{O_2} N_{N_2} - x_{N_2} N_{O_2}}{D_{O_2, N_2}} \right) \quad (4.61)$$

Since nitrogen does not take part in the chemical reaction, the net nitrogen molar flux normal to the cathode surface can be set to zero:

$$N_{N_2} = 0 \quad (4.62)$$

The molar flux of O<sub>2</sub> is determined by Faraday's Law

$$N_{O_2} = \frac{i_{den}}{4F}. \quad (4.63)$$

Equation (4.61) can now be rewritten as

$$\frac{dx_{O_2}}{dx} = \frac{RTi_{den}}{4FP_c^{ch}D_{O_2,N_2}}(x_{O_2} - 1). \quad (4.64)$$

Similar to the analysis for the anode, the effective partial pressure of oxygen at the reaction site can be found as

$$p_{O_2}^* = P_c^{ch} - (P_c^{ch} - p_{O_2}^{ch}) \exp\left(\frac{RTi_{den}l_c}{4FP_c^{ch}D_{O_2,N_2}}\right). \quad (4.65)$$

$p_{H_2}^*$ ,  $p_{H_2O}^*$  and  $p_{O_2}^*$ , calculated from (4.59), (4.60) and (4.65), will be used in the Nernst equation to find the fuel cell output voltage. In the following subsection, material balance equations, which will be also used to determine the fuel cell output voltage, will be developed.

Material Conservation Equations. The instantaneous change of the effective partial pressures of hydrogen and water vapor in the anode gas flow channel can be determined through the ideal gas equations as follows [4.22]:

$$\frac{V_a}{RT} \frac{dp_{H_2}^{ch}}{dt} = M_{H_2}^{in} - M_{H_2}^{out} - \frac{i}{2F}, \quad (4.66.a)$$

$$\frac{V_a}{RT} \frac{dp_{H_2O}^{ch}}{dt} = M_{H_2O}^{in} - M_{H_2O}^{out} + \frac{i}{2F}, \quad (4.66.b)$$

$$\frac{V_c}{RT} \frac{dp_{O_2}^{ch}}{dt} = M_{O_2}^{in} - M_{O_2}^{out} - \frac{i}{4F}. \quad (4.67)$$

Based on assumption (3), mass flow rate for  $H_2$ ,  $H_2O$  and  $O_2$  at the inlet and outlet of the flow channels can be expressed as

$$\begin{cases} M_{H_2}^{in} = M_a \cdot x_{H_2}^{in} = M_a \cdot \frac{P_{H_2}^{in}}{P_a^{ch}} \\ M_{H_2}^{out} = M_a \cdot x_{H_2}^{out} = M_a \cdot \frac{P_{H_2}^{out}}{P_a^{ch}} \end{cases} \quad (4.68.a)$$

$$\begin{cases} M_{H_2O}^{in} = M_a \cdot x_{H_2O}^{in} = M_a \cdot \frac{P_{H_2O}^{in}}{P_a^{ch}} \\ M_{H_2O}^{out} = M_a \cdot x_{H_2O}^{out} = M_a \cdot \frac{P_{H_2O}^{out}}{P_a^{ch}} \end{cases} \quad (4.68.b)$$

$$\begin{cases} M_{O_2}^{in} = M_c \cdot x_{O_2}^{in} = M_c \cdot \frac{P_{O_2}^{in}}{P_c^{ch}} \\ M_{O_2}^{out} = M_c \cdot x_{O_2}^{out} = M_c \cdot \frac{P_{O_2}^{out}}{P_c^{ch}} \end{cases} \quad (4.69)$$

Rewriting (4.66) and (4.67) will give

$$\frac{dp_{H_2}^{ch}}{dt} = \frac{2M_a RT}{V_a P_a^{ch}} p_{H_2}^{in} - \frac{2M_a RT}{V_a P_a^{ch}} p_{H_2}^{ch} - \frac{RT}{2FV_a} i, \quad (4.70.a)$$

$$\frac{dp_{H_2O}^{ch}}{dt} = \frac{2M_a RT}{V_a P_a^{ch}} p_{H_2O}^{in} - \frac{2M_a RT}{V_a P_a^{ch}} p_{H_2O}^{ch} + \frac{RT}{2FV_a} i, \quad (4.70.b)$$

$$\frac{dp_{O_2}^{ch}}{dt} = \frac{2M_c RT}{V_c P_c^{ch}} p_{O_2}^{in} - \frac{2M_c RT}{V_c P_c^{ch}} p_{O_2}^{ch} - \frac{RT}{4FV_c} i. \quad (4.71)$$

Putting the above equations into Laplace's form, we obtain

$$P_{H_2}^{ch}(s) = \frac{1}{(1 + \tau_a s)} \left[ P_{H_2}^{in}(s) + \tau_a P_{H_2}^{ch}(0) - \frac{P_a^{ch}}{4FM_a} I(s) \right], \quad (4.72.a)$$

$$P_{H_2O}^{ch}(s) = \frac{1}{(1 + \tau_a s)} \left[ P_{H_2O}^{in}(s) + \tau_a P_{H_2O}^{ch}(0) + \frac{P_a^{ch}}{4FM_a} I(s) \right], \quad (4.72.b)$$

$$P_{O_2}^{ch}(s) = \frac{1}{(1 + \tau_c s)} \left[ P_{O_2}^{in}(s) + \tau_c P_{O_2}^{ch}(0) - \frac{P_c^{ch}}{8FM} I(s) \right]. \quad (4.73)$$

where the time constant  $\tau_a = \frac{V_a P_a^{ch}}{2M_a RT}$  and  $\tau_c = \frac{V_c P_c^{ch}}{2M_c RT}$ .

The physical meaning of the time constant  $\tau_a$  is that it will take  $\tau_a$  seconds to fill a tank of volume  $V_a/2$  at pressure  $P_a^{ch}$  if the mass flow rate is  $M_a$ . Similar physical meaning holds for  $\tau_c$ .

Fuel Cell Output Voltage. The overall reaction in a solid oxide fuel cell is [4.18]



where subscript “g” indicates the product H<sub>2</sub>O is in gas form. The corresponding Nernst equation used to calculate the reversible potential is [4.18], [4.20]

$$E_{cell} = E_{0,cell} + \frac{RT}{4F} \ln \left[ \frac{(P_{H_2}^{ch})^2 \cdot P_{O_2}^{ch}}{(P_{H_2O}^{ch})^2} \right]. \quad (4.75)$$

$E_{0,cell}$  is a function of temperature and can be expressed as [4.18]:

$$E_{0,cell} = E_{0,cell}^o - k_E (T - 298), \quad (4.76)$$

where  $E_{0,cell}^o$  is the standard reference potential at standard state, 298 K and 1atm pressure.

$E_{cell}$ , calculated from (4.75), is actually the open-circuit voltage of the fuel cell.

However, when the fuel cell is under load, its output voltage is less than  $E_{cell}$  due to activation loss, ohmic resistance voltage drop and concentration overpotential [4.18], [4.31]. The output voltage of a cell can therefore be written as:

$$V_{cell} = E_{cell} - V_{act,cell} - V_{ohm,cell} - V_{conc,cell} \quad (4.77)$$

Applying assumption (7), the output voltage of the fuel cell stack can be obtained as:

$$V_{out} = N_{cell}V_{cell} = E - V_{act} - V_{ohm} - V_{conc} \quad (4.78)$$

To calculate the fuel cell output voltage, the above three voltage drops will be calculated first.

1) *Activation Voltage Drop*: Action voltage loss is caused by an activation energy barrier that must be overcome before the chemical reaction occurs. The Butler-Volmer equation is normally used to calculate the activation voltage drop [4.31]:

$$i = i_0 \left\{ \exp\left(\beta \frac{zFV_{act}}{RT}\right) - \exp\left[-(1-\beta) \frac{zFV_{act}}{RT}\right] \right\} \quad (4.79)$$

where  $i_0$  = apparent exchange current (A);

$\beta$  = electron transfer coefficient;

$i_0$  is the apparent exchange current, which is mainly a function of temperature [4.38], [4.39]

$$i_0 = k_{a1} \cdot T \cdot \exp(-k_{a2}/T) \quad (4.80)$$

where  $k_{a1}$ ,  $k_{a2}$  are empirical constants.

Under high activation condition, the first term in (4.79) is much higher than the second term and the well-known Tafel equation can be obtained from (4.79) by neglecting its second term [4.18], thus

$$V_{act,cell} = \frac{RT}{z\beta F} \ln\left(\frac{i}{i_0}\right). \quad (4.81)$$

Equation (4.81) will yield an unreasonable value for  $V_{act}$  when  $i = 0$ . According to [4.38], the value of  $\beta$  is about 0.5 for fuel cell applications, and (4.79) can be written as

$$V_{act,cell} = \frac{2RT}{zF} \sinh^{-1}\left(\frac{i}{2i_0}\right). \quad (4.82)$$

The equivalent activation resistance can then be defined as

$$R_{act,cell} = \frac{V_{act,cell}}{i} = \frac{2RT}{zFi} \sinh^{-1}\left(\frac{i}{2i_0}\right). \quad (4.83)$$

According to (4.82), the activation voltage drop will be zero when load current is zero. The ohmic and concentration voltage drops (discussed in the next two sub-sections) are also zero when the fuel cell is not loaded ( $i=0$ ). However, even the open-circuit voltage of a SOFC is known to be less than the theoretical value given by (75) [4.17]. Similar to the computation of activation voltage of a proton exchange membrane fuel cell [4.1], a constant and a temperature-dependent term can also be added to (4.82) for activation voltage drop computation of SOFC as follows

$$V_{act,cell} = \xi_0 + \xi_1 T + iR_{act,cell} = V_{act0,cell} + V_{act1,cell} \quad (4.84)$$

where  $\xi_0 =$  constant term of activation voltage drop (V);

$\xi_1 =$  temperature coefficient of second term in activation voltage drop (V/K).

$V_{act0,cell} = \xi_0 + \xi_1 T$  is the part of activation drop affected only by the fuel cell internal temperature, while  $V_{act1,cell} = iR_{act,cell}$  is both current and temperature dependent.

2) *Ohmic Voltage Drop*: The ohmic resistance of a SOFC consists mainly of the resistance of the electrolyte, electrodes and interconnection between fuel cells. In this

model, only ohmic losses of electrolyte and interconnection are included while the resistance of electrodes is neglected. The overall ohmic voltage drop can be expressed as

$$V_{ohm,cell} = V_{ohm,elect} + V_{ohm,interc} = iR_{ohm,cell} \quad (4.85)$$

$R_{ohm,cell}$  normally decrease as temperature increases; it can be expressed as [4.38]

$$R_{ohm,cell} = \frac{a_{elect} \exp(b_{elect}/T)}{A_{cell}} \delta_{elect} + \frac{a_{interc} \exp(b_{interc}/T)}{A_{cell}} \delta_{interc} \quad (4.86)$$

3) *Concentration Voltage Drop*: During the reaction process, concentration gradients can be formed due to mass diffusion from the flow channels to the reaction sites (catalyst surfaces). The effective partial pressures of hydrogen and oxygen at the reaction site are less than those in the electrode channels, while the effective partial pressure of water at the reaction site is higher than that in the anode channel. At high current densities, slow transportation of reactants (products) to (from) the reaction site is the main reason for the concentration voltage drop [4.17], [4.18]. The concentration overpotential in the fuel cell can be obtained as

$$V_{conc,cell} = \frac{RT}{4F} \left\{ \ln \left[ \frac{(p_{H_2}^{ch})^2 \cdot p_{O_2}^{ch}}{(p_{H_2O}^{ch})^2} \right] - \ln \left[ \frac{(p_{H_2}^*)^2 \cdot p_{O_2}^*}{(p_{H_2O}^*)^2} \right] \right\} \quad (4.87)$$

$$= V_{conc,a} + V_{conc,c}$$

$$V_{conc,a} = \frac{RT}{2F} \ln \left[ \frac{1 + (RTl_a i_{den}) / (2FD_{H_2O,H_2} p_{H_2O}^{ch})}{1 - (RTl_a i_{den}) / (2FD_{H_2O,H_2} p_{H_2}^{ch})} \right] \quad (4.88)$$

$$V_{conc,c} = -\frac{RT}{4F} \ln \left\{ \frac{1}{p_{O_2}^{ch}} \left[ p_c^{ch} - (p_c^{ch} - p_{O_2}^{ch}) \exp \left( \frac{RTi_{den} I_c}{4F p_c^{ch} D_{O_2,N_2}} \right) \right] \right\} \quad (4.89)$$

The equivalent resistance for the concentration voltage drop can be calculated as

$$R_{conc,cell} = \frac{V_{conc,cell}}{i}. \quad (4.90)$$

4) *Double-layer charging effect*: In a SOFC, the two electrodes are separated by the electrolyte (Figure 4.16) and two boundary layers are formed, e.g. anode-electrolyte layer and electrolyte-cathode layer. These layers can be charged by polarization effect, known as electrochemical double-layer charging effect [4.17], during normal fuel cell operation. The layers can store electrical energy and behave like a super-capacitor. The model for SOFC considering this effect can be described by the equivalent circuit shown in Figure 4.17 [4.17], [4.44].

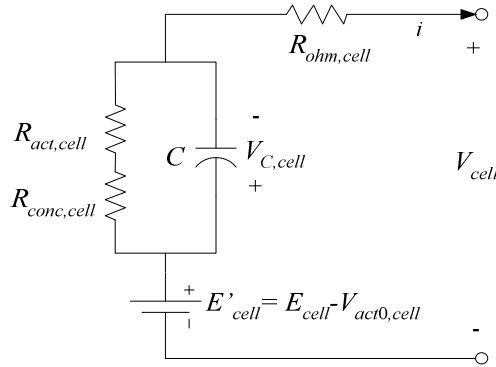


Figure 4.17. Equivalent electrical circuit of the double-layer charging effect inside a SOFC.

In the above circuit,  $R_{ohm,cell}$ ,  $R_{act,cell}$  and  $R_{conc,cell}$  are equivalent resistances of ohmic voltage drop, activation and concentration voltage drops, which can be calculated according to (4.86), (4.83) and (4.90), respectively.  $C$  is the equivalent capacitance of the double-layer charging effect. Since the electrodes of a SOFC are porous, the value of  $C$  is large and can be in the order of several Farads [4.17]. The voltage across  $C$  is

$$V_{C,cell} = (i - C \frac{dV_{C,cell}}{dt})(R_{act,cell} + R_{conc,cell}). \quad (4.91)$$

The double-layer charging effect is integrated into the modeling, by using  $V_{C,cell}$  instead of  $V_{act1,cell}$  and  $V_{conc,cell}$ , to calculate  $V_{cell}$ . The fuel cell output voltage now turns out to be

$$V_{cell} = E_{cell} - V_{C,cell} - V_{act0,cell} - V_{ohm,cell} . \quad (4.92)$$

Then (4.92) and (4.78) can be used to calculate the output voltage,  $V_{out}$ , of a SOFC stack.

Energy Balance of the Thermodynamics. The cross section profile and heat transfer inside a tubular SOFC are shown in Figure 4.18 [4.18], [4.40]. One advantage of this tubular structure is that it eliminates the seal problems between cells since the support tube of each cell is closed at one end [4.18]. The air is fed through a central air supply tube (AST) and forced to flow back past the interior of the cell (cathode surface) to the open end. The fuel gas flows past the exterior of the cell (anode surface) and in parallel direction to the air [4.18].

The thermal analysis for fuel reformer and combustor are not included in this model. Heat exchanges between cells are also not considered in this model by assuming that temperature differences between adjacent cells can be neglected. Heat transport inside the fuel cell occurs mainly by means of radiation, convection and mass flow.

The heat generated by the chemical reaction inside the fuel cell can be written as

$$\dot{q}_{gen} = \dot{q}_{chem} - \dot{q}_{elec} . \quad (4.93)$$

The available power released due to chemical reaction is calculated by

$$\dot{q}_{chem} = \dot{n}_{H_2,consumed} \cdot \Delta H . \quad (4.94)$$

where  $\Delta H$  is the enthalpy change of the chemical reaction inside the fuel cell.

The real electrical output power is

$$\dot{q}_{elec} = V_{out} \cdot i. \quad (4.95)$$

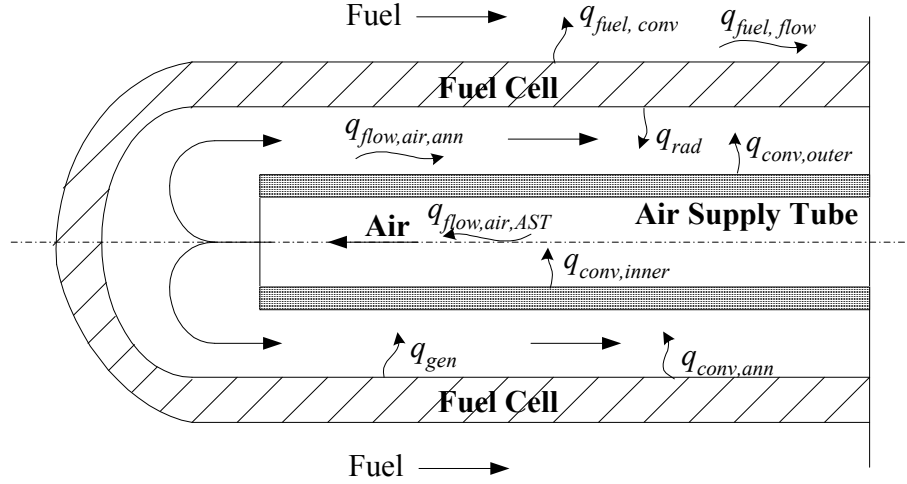


Figure 4.18. Heat transfer inside a tubular solid oxide fuel cell.

The thermodynamic and energy balance analysis for different parts inside the cell are discussed below [4.22], [4.40].

1) Cell Tube:

$$\dot{q}_{in,cell} = \dot{q}_{gen} = \dot{q}_{chem} - \dot{q}_{elec} \quad (4.96.a)$$

$$\dot{q}_{out,cell} = \dot{q}_{rad} + \dot{q}_{conv,ann} + \dot{q}_{flow,air,ann} + \dot{q}_{conv,fuel} + \dot{q}_{flow,fuel} \quad (4.96.b)$$

$$\dot{q}_{net,cell} = \dot{q}_{in,cell} - \dot{q}_{out,cell} = m_{cell} C_{cell} \frac{dT_{cell}}{dt} \quad (4.96.c)$$

$$\dot{q}_{rad} = \varepsilon_{AST}^* \sigma A_{AST,outer} (T_{cell}^4 - T_{AST}^4) \quad (4.96.d)$$

$$\dot{q}_{conv,ann} = h_{cell} A_{cell,inner} (T_{cell} - T_{air,ann}) \quad (4.96.e)$$

$$\dot{q}_{flow,air,ann} = M_{air} M_{mw,air} C_{air} (T_{in,air,ann} - T_{out,air,ann}) \quad (4.96.f)$$

$$\dot{q}_{conv,fuel} = h_{cell} A_{cell,outer} (T_{cell} - T_{fuel}) \quad (4.96.g)$$

$$\dot{q}_{flow,fuel} = \dot{q}_{flow,H_2} + \dot{q}_{flow,H_2O} \quad (4.96.h)$$

$$\dot{q}_{flow,H_2} = (M_{H_2}^{in} + M_{H_2}^{out})(T_{fuel}^{out} - T_{fuel}^{in})C_{H_2}M_{mw,H_2} \quad (4.96.i)$$

$$\dot{q}_{flow,H_2O} = (M_{H_2O}^{in} + M_{H_2O}^{out})(T_{fuel}^{out} - T_{fuel}^{in})C_{H_2O}M_{mw,H_2O} \quad (4.96.j)$$

2) *Fuel*:

$$\dot{q}_{in,fuel} = \dot{q}_{conv,fuel} + \dot{q}_{flow,fuel} \quad (4.97.a)$$

$$\dot{q}_{out,fuel} = \dot{q}_{flow,fuel} \quad (4.97.b)$$

$$\dot{q}_{net,fuel} = \dot{q}_{in,fuel} - \dot{q}_{out,fuel} = m_{fuel}C_{fuel} \frac{dT_{fuel}}{dt} \quad (4.97.c)$$

3) *Air between Cell and Air Supply Tube (AST)*:

$$\dot{q}_{in,air,ann} = \dot{q}_{conv,cell,ann} + \dot{q}_{flow,air,ann} \quad (4.98.a)$$

$$\dot{q}_{out,air,ann} = \dot{q}_{flow,air,ann} \quad (4.98.b)$$

$$\dot{q}_{net,air,ann} = \dot{q}_{in,air,ann} - \dot{q}_{out,air,ann} = m_{air,ann}C_{air} \frac{dT_{air,ann}}{dt} \quad (4.98.c)$$

4) *Air Supply Tube*:

$$\dot{q}_{in,AST} = \dot{q}_{rad} + \dot{q}_{conv,AST,outer} \quad (4.99.a)$$

$$\dot{q}_{out,AST} = \dot{q}_{conv,AST,inner} + \dot{q}_{flow,air,AST} \quad (4.99.b)$$

$$\dot{q}_{net,AST} = \dot{q}_{in,AST} - \dot{q}_{out,AST} = C_{AST}m_{AST} \frac{dT_{AST}}{dt} \quad (4.99.c)$$

$$\dot{q}_{conv,AST,outer} = h_{AST,outer}A_{AST,outer}(T_{air,cell} - T_{AST}) \quad (4.99.d)$$

$$\dot{q}_{conv,AST,inner} = h_{AST,inner} A_{AST,inner} (T_{AST} - T_{air,AST}) \quad (4.99.e)$$

$$\dot{q}_{air,flow,AST} = M_{air} C_{air} (T_{in,air,AST} - T_{out,air,AST}) \quad (4.99.f)$$

5) Air in AST:

$$\dot{q}_{in,air,AST} = \dot{q}_{out,AST} = \dot{q}_{conv,AST,inner} + \dot{q}_{flow,air,AST} \quad (4.100.a)$$

$$\dot{q}_{out,air,AST} = \dot{q}_{flow,air,AST} \quad (4.100.b)$$

$$\dot{q}_{net,air,AST} = \dot{q}_{in,air,AST} - \dot{q}_{out,air,AST} = C_{air} m_{air,AST} \frac{dT_{air,AST}}{dt} \quad (4.100.c)$$

The symbols in the above equations (4.93-4.100) are defined as:

$m$  = mass (kg);

$C_i$  = specific heat capacity of species  $i$  [J/(mol·K), or J/(kg·K)];

$h$  = heat transfer coefficient [W/(m<sup>2</sup>·K)];

$A$  = area (m<sup>2</sup>);

$M_i$  = mole flow rate of species  $i$  (mol/s);

$M_{mw, i}$  = molecular weight of species  $i$  (kg/mol)

$\varepsilon$  = emissivity;

$\sigma$  = Stefan-Boltzmann constant,  $5.6696 \times 10^{-8} \text{ W} \cdot \text{m}^{-2} \cdot \text{K}^{-4}$ ;

The superscripts and subscripts in the above equations are defined as:

air	Conditions for air
ann	Annulus of cell
AST	Air supply tube
cell	Conditions for a single cell

ch	Conditions at the anode or cathode channel
chem	Chemical
conv	Convective
conc	Concentration
consumed	Material consumed in chemical reaction
gen	Material (energy) generated in chemical reaction
flow	Flow heat exchange
Fuel	Conditions for fuel
H <sub>2</sub>	Hydrogen
H <sub>2</sub> O	Water
in	Conditions of input/inlet
inner/outer	Inner/outer conditions
mw	Molecular weight (kg/mol)
net	Net values
O <sub>2</sub>	Oxygen
out	Output
rad	Radiation
*	Effective value

The thermal model of SOFC will be developed according to (4.93)-(4.100).

Dynamic SOFC Model Implementation. A dynamic model for a 5kW SOFC has been developed in MATLAB/Simulink, based on the electrochemical and thermodynamic

characteristics of the fuel cell discussed in the previous section. The output voltage of the fuel cell depends on conditions including fuel composition, fuel flow, oxidant flow, anode and cathode pressures, cell temperature, load current and the electrical and thermal properties of the cell materials. Figure 4.19 shows the block diagram, based on which the model has been developed. In this figure, the input quantities are anode and cathode pressures ( $P_a$  and  $P_c$ ),  $H_2$  flow rate ( $M_{H_2}$ ),  $H_2O$  flow rate ( $M_{H_2O}$ ), air flow rate ( $M_{air}$ ) and initial temperature of the fuel cell and air ( $T_{fuelinlet}$  and  $T_{airinlet}$ ). At any given load current and time, the cell temperature  $T_{cell}$  is determined and both the load current and temperature are fed back to different blocks, which take part in the calculation of the fuel cell output voltage.

In this block diagram, material conservation equations (4.66)-(4.73) are used to calculate the partial pressures of  $H_2$ ,  $H_2O$  and  $O_2$  in flow channels. Then, the Nernst equation (4.75) is employed to determine the internal potential ( $E$ ) of the fuel cell. Diffusion equations (4.54)-(4.65) and the material conservation equations will give the concentration loss of the cell. The ohmic voltage drop is determined by (4.85) and activation voltage is computed from (4.84). Eventually, the terminal (output) voltage of the fuel cell is determined by (4.78) and (4.92) and the double-layer charging effect, (4.91). The thermal model is developed via energy balance equations (4.93)-(4.100).

### Model Responses under Constant Fuel Flow Operation

Both the steady-state and dynamic responses of the SOFC model under constant flow operating mode are given in this section. The thermodynamic response of the model and the impact of the operating temperature are also given. The dynamic responses of the model are investigated in different time scales.

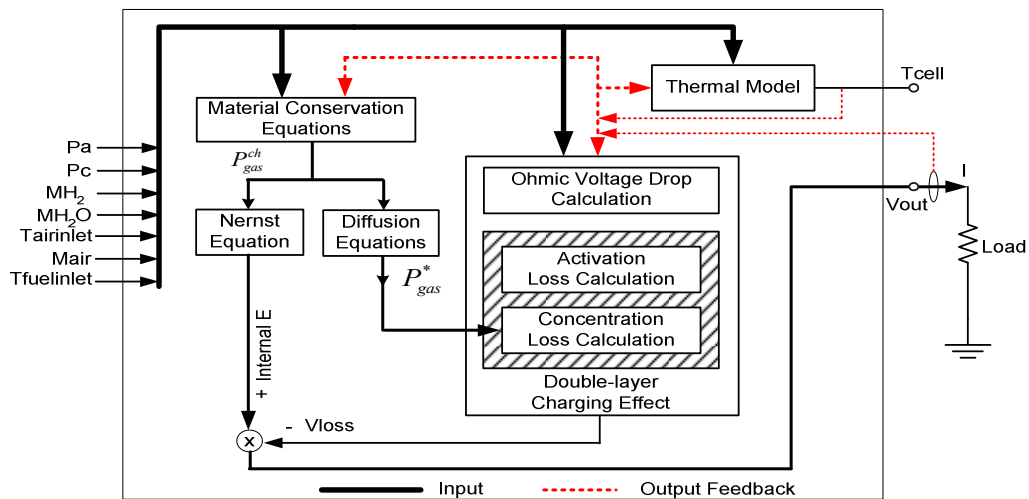


Figure 4.19. Diagram of building a dynamic model of SOFC in SIMULINK.

Steady-State Characteristics. The steady-state terminal voltage vs. current (V-I) curves of the SOFC model at different temperatures are shown in Figure 4.20. These curves are similar to the real test data reported in [4.18], [4.42]. The activation voltage drop dominates the voltage drop in the low-current region. As load current increases, the ohmic voltage drop increases fast and becomes the main contribution to the SOFC voltage drop. When the load current exceeds a certain value (140A for this SOFC model) the fuel cell output voltage will drop sharply due to large ohmic and concentration voltage drops inside SOFC. The variations of the above three voltage drops vs. load

current at three different temperatures are shown in Figure 4.21.

Figure 4.20 shows the effect of temperature on the SOFC V-I characteristic curve. The SOFC output voltage is higher at lower temperature in the low current zone while the voltage is higher at higher temperature in the high current region. These simulation results showing the effect of temperature on SOFC performance are also similar to the test data given in [4.18] and [4.42]. The negative temperature coefficient of the open-circuit internal potential  $E_{0,cell}$ , defined by (4.76), and the temperature-dependent activation voltage drop and ohmic voltage drop (shown in Figure 4.21) are the main reasons for this kind of temperature dependent performance of the SOFC model. As shown in Figure 4.21, both the activation and ohmic voltage drops decrease as the fuel cell temperature increases.

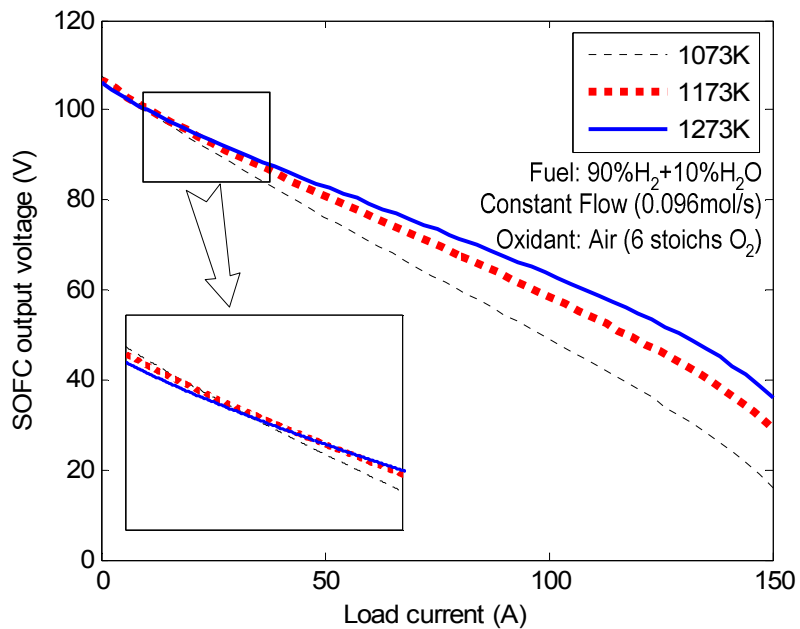


Figure 4.20. V-I characteristics of the SOFC model at different temperatures.

The corresponding output power vs. current (P-I) curves of the model at different

temperatures are shown in Figure 4.22. At higher load currents ( $I > 40$  A), higher output power can be achieved at higher operating temperatures. Under each operating temperature, there is a critical load current point ( $I_{crit}$ ) where the model output power reaches its maximum value. For example,  $I_{crit}$  is 95 A at 1073 K, 110 A at 1173 K and 120 A at 1273 K. Beyond these points, an increase in the load current will reduce the output power due to large ohmic and concentration voltage drops.

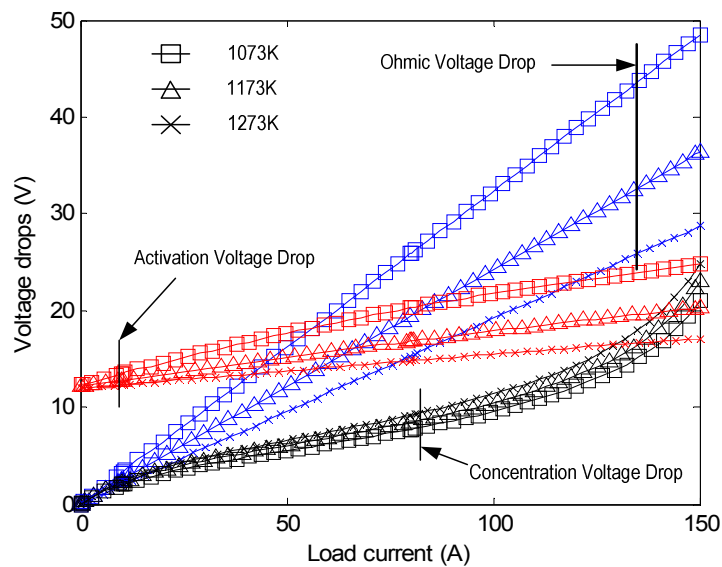


Figure 4.21. Three voltage drops at different temperatures.

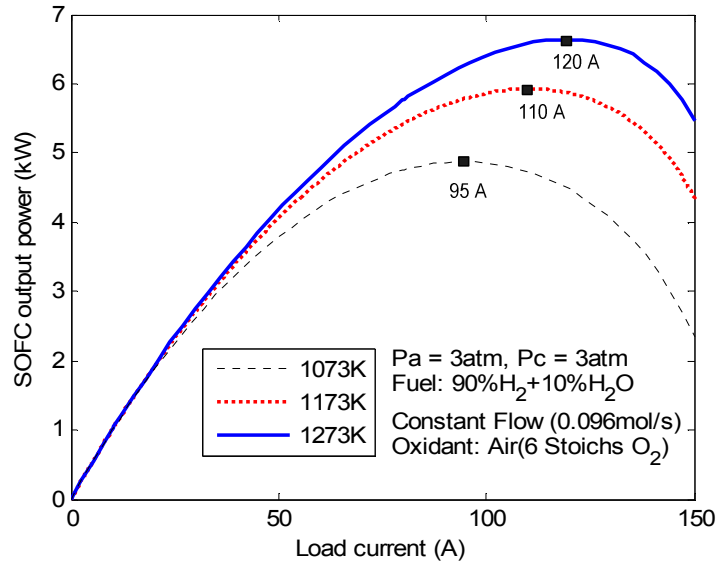


Figure 4.22. P-I characteristics of the SOFC model at different temperatures.

**Dynamic Response.** The dynamic response of the SOFC model is mainly dominated by the double-layer charging effect, the time constants  $\tau_a$  and  $\tau_c$  [defined in (4.72) and (4.73)], and the thermodynamic property of the fuel cell. Although the capacitance ( $C$ ) of the double-layer charging effect is large (in the order of several Farads), the time constant  $\tau_{dlc} = (R_{act,cell} + R_{conc,cell})C$  is normally small (in the order of around  $10^{-2}$  s) because  $(R_{act,cell} + R_{conc,cell})$  is small (less than  $2.0 \text{ m}\Omega$  for a single cell used in this study) when the fuel cell works in the linear zone. Therefore, capacitor  $C$  will only affect the model dynamic response in small time scale, i.e.,  $10^{-3}$ - $10^{-1}$  s. The operating conditions of the SOFC model for this simulation study are listed in Table 4.4. Figure 4.23 shows the model dynamic responses in this small time scale under step current changes. The load current steps up from 0 A to 80 A at 0.1s and then steps down to 30 A at 0.2 s. The lower part of the figure shows the corresponding SOFC output voltage responses with different

capacitance values for the double-layer charging effect. When the load current steps up (down), the fuel cell output voltage drops down (rises up) immediately due to the ohmic voltage drop. Then the voltage drops (rises) “smoothly” to its final value. It is noted that the larger is the capacitance  $C$ , the slower the output voltage reaches its final value because the larger is the effective time constant  $\tau_{dlc}$ .

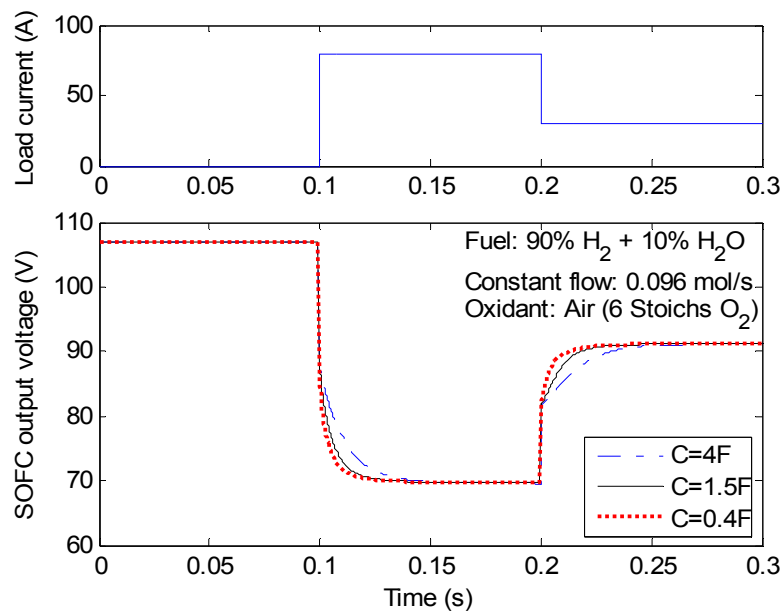


Figure 4.23. Model dynamic responses with different equivalent capacitance values for double-layer charging effect in small time scale.

TABLE 4.4. OPERATING CONDITIONS FOR THE MODEL DYNAMIC RESPONSE STUDIES

Temperature (K)	1173
Anode input pressure (atm)	3
Cathode input pressure (atm)	3
Anode H <sub>2</sub> flow rate (mol/s)	0.0864
Anode H <sub>2</sub> O flow rate (mol/s)	0.0096
Oxidant	Air (6 stoichs O <sub>2</sub> )

Time constants  $\tau_a$  and  $\tau_c$  are in the order of  $10^{-1}$ - $10^0$  s for the model parameters used in this dissertation. They mainly affect the model dynamic responses in the time scale  $10^{-1}$  to  $10^1$  s. Figure 4.24 shows the model dynamic responses in this medium time scale under the same type of step current changes as shown in Figure 4.23. The load current steps up from 0 A to 80 A at 1s and then steps down to 30 A at 11s. The operating conditions of the model are the same as given in Table 4.4 except for the operating pressures. Figure 4.24 shows the SOFC output voltage responses under different operating pressures ( $P_a = P_c = P$ ). Higher operating pressure gives higher output voltage and also increases time constants  $\tau_a$  and  $\tau_c$  [see (4.72) and (4.73)], shown in the figure.

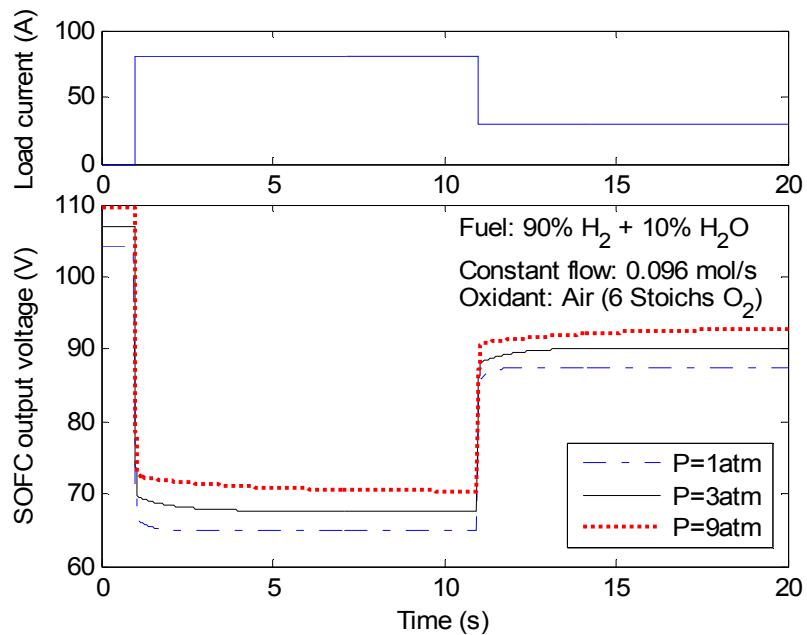


Figure 4.24. Model dynamic responses under different operating pressures in medium time scale.

The equivalent thermodynamic time constant of a SOFC can be in the order of tens of minutes [4.40], [4.43]. Thus, for large time scale ( $10^2$ - $10^3$  s), the thermodynamic characteristic will dominate the model dynamic responses. Figure 4.25 shows the

transient response of the SOFC model under load changes. The model was subjected to a step change in the load current from zero to 100 A at 10 min and then the current drops back to 30 A at 120 min. The operating conditions are also the same as given in Table 4.4 except for the varying fuel cell operating temperatures. The fuel and air inlet temperatures are given in the figure. When the load current steps up, the SOFC output voltage drops sharply, and then rises to its final value. When the load current steps down, the output voltage jumps up and then drops slowly towards its final value, as shown in Figure 4.25.

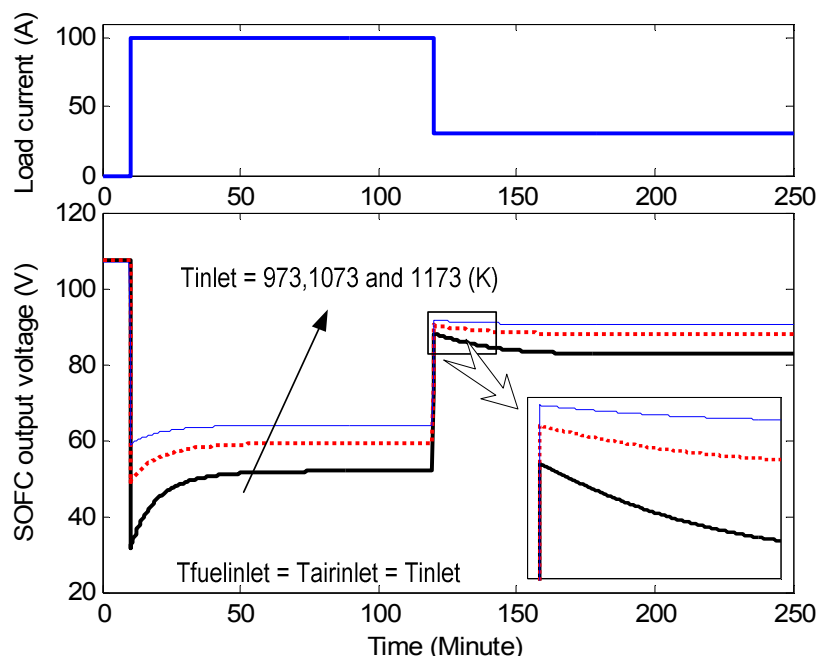


Figure 4.25. Model dynamic responses under different inlet temperatures in large time scale.

The corresponding temperature responses of the SOFC model are shown in Figure 4.26. From this figure, the equivalent overall thermodynamic time constant of the model is around 15 minutes.

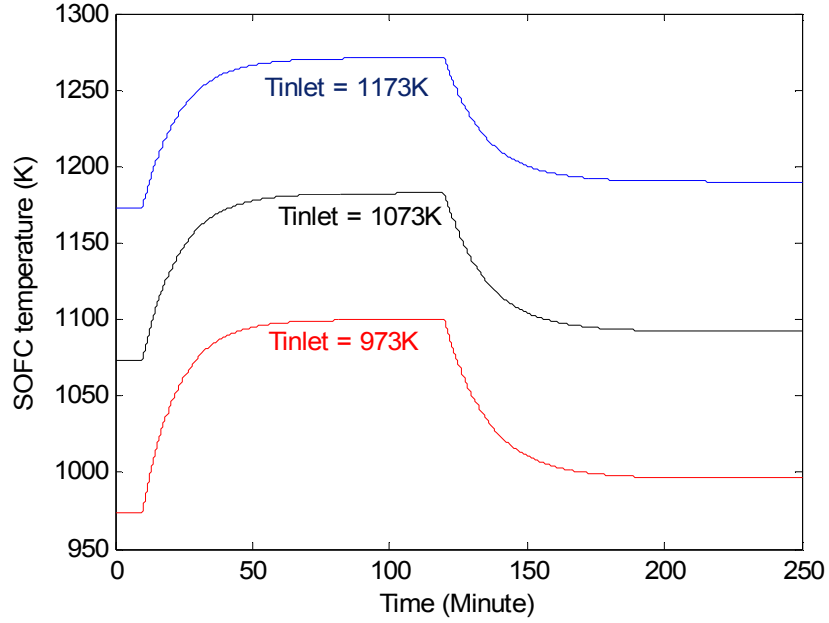


Figure 4.26. Model temperature responses.

### Constant Fuel Utilization Operation

In the previous sections, only constant flow operation for the SOFC model was discussed. The fuel cell can also be operated in constant fuel utilization mode, in which the utilization factor will be kept constant. The utilization factor is defined as [4.18]:

$$u = \frac{M_{H_2,consumed}}{M_{H_2,in}} = \frac{i / 2F}{M_{H_2,in}} \quad (4.101)$$

The direct way to achieve constant utilization operation is to feed back the load current with a proportional gain  $1/(2F \times u)$ , as shown in Figure 4.27, to control fuel flow to the fuel processor. As a result, the input  $H_2$  will change as load varies to keep the fuel utilization constant. As shown in Figure 4.27, the fuel processor is modeled by a simple delay transfer function  $1/(\tau_f s + 1)$ .  $\tau_f$  is set to 5s in this dissertation.

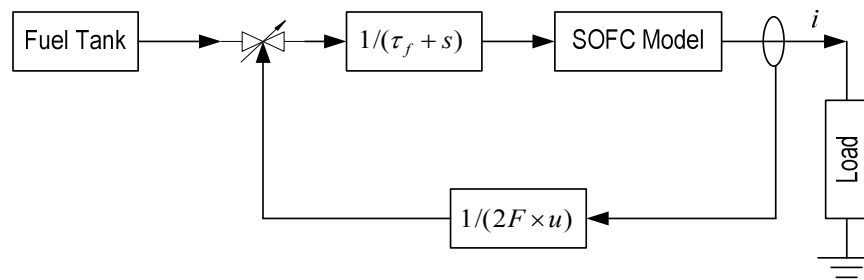


Figure 4.27. Constant utilization control.

In this section, the fuel cell's steady state characteristics and dynamic responses under constant fuel utilization mode will be discussed. The results will also be compared with those obtained under constant flow operating mode. The utilization factor is set for 0.85 (85% fuel utilization) for this study and other operating conditions are the same as listed in Table 4.4 except the fuel and water flow rates that will change as the load current changes.

Steady-state Characteristics. Figure 4.28 shows a comparison between the V-I characteristic of the SOFC model with constant fuel utilization and constant fuel flow operating modes. The operating conditions for the constant flow operating mode are listed in Table 4.4. For this specific study, the output voltage under constant flow operating mode is higher than that under constant utilization mode at the same load current. The voltage difference between the two operating modes keeps getting smaller as the load current increases. The reason for this is that the utilization factor of the constant flow operation will be getting closer to the utilization factor (0.85) of the constant utilization operation as load current increases. The corresponding P-I curves, also given in Figure 4.28, show that the SOFC can provide more power under constant flow

operation.

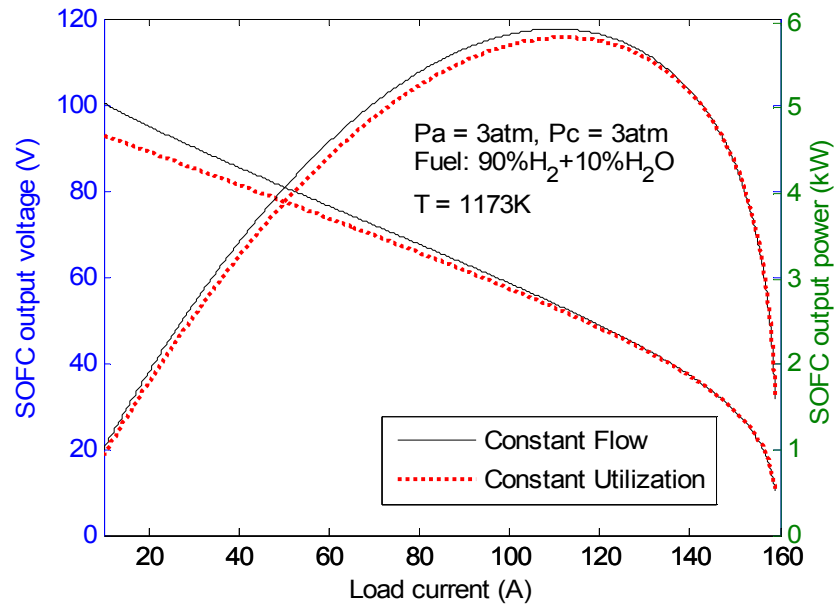


Figure 4.28. V-I and P-I characteristics of the SOFC model under constant fuel utilization and constant fuel flow operating modes.

Figure 4.29 shows the curves of input fuel versus load current for both operation modes. It shows that the constant flow operation mode requires more fuel input, especially at light loading. But the unused  $H_2$  is not just wasted; it can be used for other purposes [4.40], or recycled to use again.

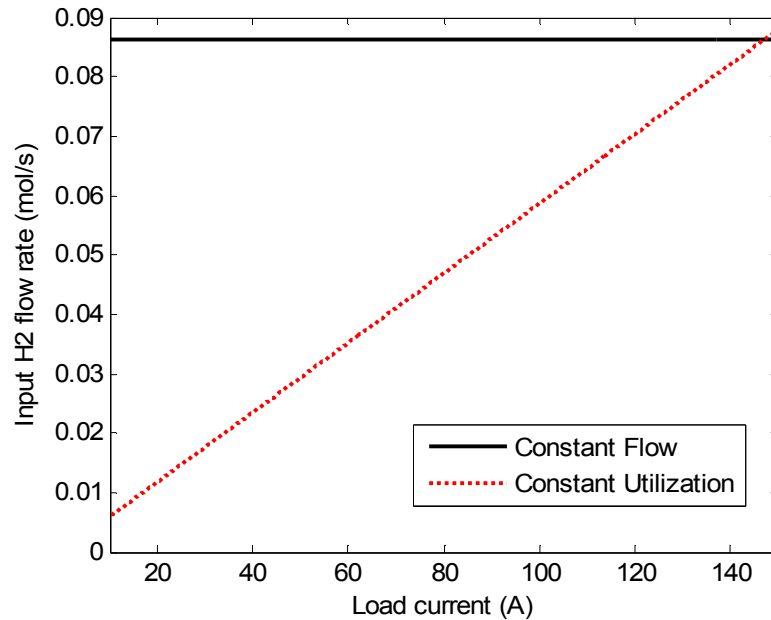


Figure 4.29. H<sub>2</sub> input for the constant utilization and constant flow operating modes.

Dynamic Responses. Dynamic response of the SOFC model in small time scale is dominated by the double-layer charging effect and in large time scale is mainly determined by the thermodynamic properties of the fuel cell. Both the double-layer charging effect and the thermodynamic characteristics of the fuel cell are determined by the fuel cell's physical and electrochemical properties. These properties are normally not affected by whether the SOFC is operating under constant fuel flow mode or constant fuel utilization mode. However, the dynamic response in medium time scale will be affected by the operating mode since the fuel flow rate will change as load varies under constant utilization operating mode. This load-dependent fuel flow rate will give a load-dependent time constant  $\tau_a$  as well. Therefore, only the dynamic response in this time scale will be discussed for the constant utilization operating mode.

Figure 4.30 shows the model dynamic responses in the medium time scale under similar step current changes used in the constant fuel flow operating mode. The load current steps up from 0 A to 80 A at 1s and then steps down to 30 A at 31 s. The lower part of Figure 4.30 shows the corresponding SOFC output voltage responses under different operating pressures. Similar to what is shown in Figure 4.24 for constant fuel flow operating mode, a higher operating pressure results in a higher output voltage and larger time constants  $\tau_a$  and  $\tau_c$  [see (4.72) and (4.73)]. In this case, the dynamic responses are not determined only by  $\tau_a$  and  $\tau_c$ , but also by the dynamics of the fuel processor. The output voltage curves (Figure 4.30) show the typical characteristic of a second order system while the dynamic responses in medium time scale for the constant flow operating mode (Figure 4.24) exhibit the characteristic of a first order system. Figure 2.30 shows that the SOFC output voltage drops as the load current steps up, undershoots, and then rises back to its final value. While the load current steps down, the voltage rises up, overshoots, and then drops back to its final value. We note that the fuel cell fails to start up at 1 atm operating pressure due to the delay in the fuel processor, which causes insufficient fuel supply.

The selection of a SOFC operating mode depends on the actual desired performance requirements and is beyond the scope of this dissertation. Only the constant fuel flow operating mode will be studied in the following chapters.

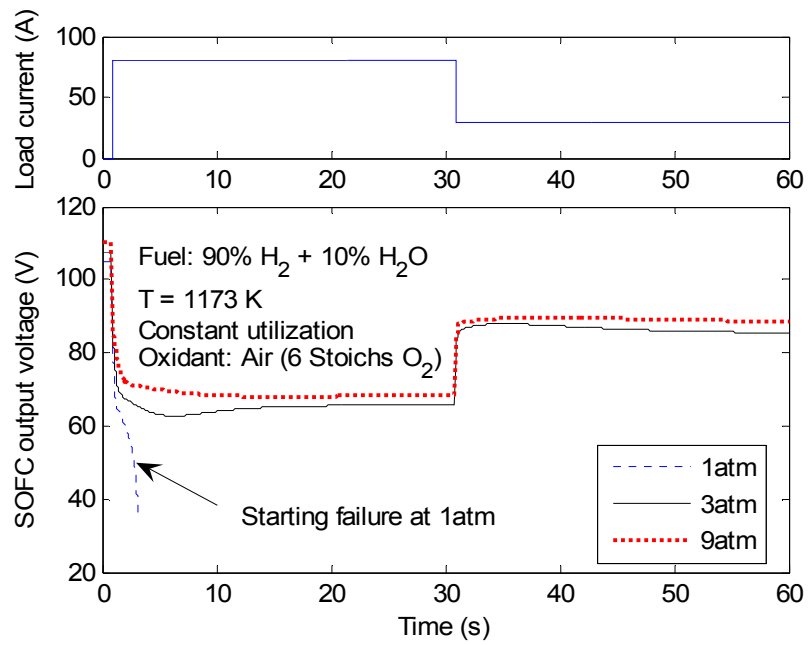


Figure 4.30. Model dynamic responses under different operating pressures in medium time scale with constant utilization operating mode.

## Wind Energy Conversion System

### Introduction

Among the renewable energy technologies for electricity production, wind energy technology is the most mature and promising one. The use of wind energy conversion systems (WECS) is increasing world-wide (see Chapter 1). Moreover, the economic aspects of wind energy technology are promising enough to justify their use in stand alone applications as well as grid connected operations.

As wind velocity in an area changes continuously the energy available from it varies continuously. This necessitates a need for dynamic models of all systems involved which are responsive to the changes in the wind, to have a better understanding of the overall system.

Induction machines (usually squirrel cage rotor type) are often used for wind power generation because of their ruggedness and low cost [4.45]. However, they are used mostly in grid-connected operation because of their excitation requirement. Induction machines can be used in stand-alone applications provided that enough reactive excitation is provided to them for self-excitation [4.46], [4.47]. Induction generators can cope with a small increase in the speed from rated value because, due to saturation, the rate of increase of generated voltage is not linear with speed. Furthermore, self excited induction generator (SEIG) has a self-protection mechanism because its output voltage collapses when overloaded [4.48]-[4.51].

In this section, modeling of variable speed wind energy conversion systems is discussed. A description of the proposed wind energy conversion system is presented; and

dynamic models for both the SEIG and wind turbine are developed. In addition, the effects of saturation characteristic on the SEIG are presented. The developed models are simulated in MATLAB/Simulink [4.57]. Different wind and load conditions are applied to the WECS model for validation purposes.

System Configuration. The configuration of the WECS system (Figure 4.31) studied in this dissertation is similar to the system shown in Figure 2.5 (c). A SEIG, driven by a pitch controlled variable speed wind turbine acting as the prime mover, is used to generate electricity. The output AC voltage (with variable frequency) of the SEIG is rectified into DC and then a DC/AC inverter is used to convert the DC into 60 Hz AC. For stand-alone operation, an excitation compensating capacitor bank is necessary to start the induction generator. For grid-connected application, the compensating capacitor bank can be eliminated from the system. However, for a weak-grid, the reactive power consumed by the induction generator will deteriorate the situation. It is better to have a generation system with self starting capability. Therefore, for the wind energy system studied in this dissertation, an excitation capacitor bank is always added regardless of the system being stand-alone or grid-connected.

In this section, only the modeling of the components inside the rectangle in Figure 4.31 is discussed. The design and modeling of power electronic circuits are discussed later in this chapter. It is noted from the figure that there are two main components inside the rectangle: the wind turbine together with the gear box and the SEIG.

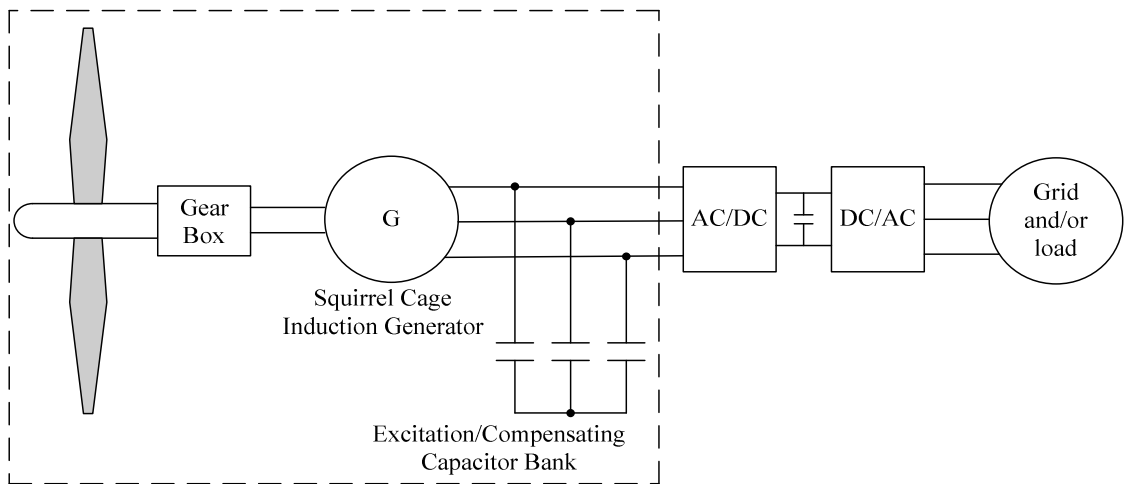


Figure 4.31. System block diagram of the WECS.

### Dynamic Model for Variable Speed Wind Turbine

The following sections explain the modeling and the control principles of the variable speed pitch controlled wind turbine.

Wind Turbine Characteristics. The power  $P_{wind}$  (in watts) extracted from the wind is given in equation 2.51. It is rewritten here as:

$$P_{wind} = \frac{1}{2} \rho A v^3 C_p(\lambda, \theta) \quad (4.102)$$

where  $\rho$  is the air density in  $\text{kg/m}^3$ ,  $A$  is the area swept by the rotor blades in  $\text{m}^2$ ,  $v$  is the wind velocity in  $\text{m/s}$ .  $C_p$  is called the power coefficient or the rotor efficiency and is function of tip speed ratio ( $TSR$  or  $\lambda$ , see equation 2.52) and pitch angle ( $\theta$ ) [4.64].

The maximum rotor efficiency  $C_p$  is achieved at a particular  $TSR$ , which is specific to the aerodynamic design of a given turbine. The rotor must turn at high speed at high wind, and at low speed at low wind, to keep  $TSR$  constant at the optimum level at all

times. For operation over a wide range of wind speeds, wind turbines with high tip speed ratios are preferred [4.53].

In the case of the variable speed pitch-regulated wind turbines considered in this dissertation, the pitch angle controller plays an important role. Groups of  $C_p-\lambda$  curves with pitch angle as the parameter obtained by measurement or by computation can be represented as a nonlinear function [4.55], [4.56], [4.66]. The following function is used.

$$C_p = C_1(C_2 - C_3\theta - C_4)\exp(-C_5) \quad (4.103)$$

where  $\theta$  is the pitch angle.

Proper adjustment of the coefficients  $C_1-C_5$  would result in a close simulation of a specific turbine under consideration. The values for  $C_1-C_5$  used in this study are listed in Table 4.5. The  $C_p-\lambda$  characteristic curves at different pitch angles are plotted in Figure 4.32. From the set of curves in Figure 4.32, we can observe that when pitch angle is equal to 2 degrees, the tip speed ratio has a wide range and a maximum  $C_p$  value of 0.35, suitable for wind turbines designed to operate over a wide range of wind speeds. With an increase in the pitch angle, the range of  $TSR$  and the maximum value of power coefficient decrease considerably.

TABLE 4.5. PARAMETER VALUES FOR C1-C5

$C_1$	0.5
$C_2$	$116/k_\theta$
$C_3$	0.4
$C_4$	5
$C_5$	$21/k_\theta$

$k_\theta$  in Table 4.5 used to calculate  $C_2$  and  $C_5$  is determined by  $\lambda$  and  $\theta$  as [4.55], [4.56],

[4.66]:

$$k_\theta = \left[ \frac{1}{\lambda + 0.08\theta} - \frac{0.035}{\theta^3 + 1} \right]^{-1} \quad (4.104)$$

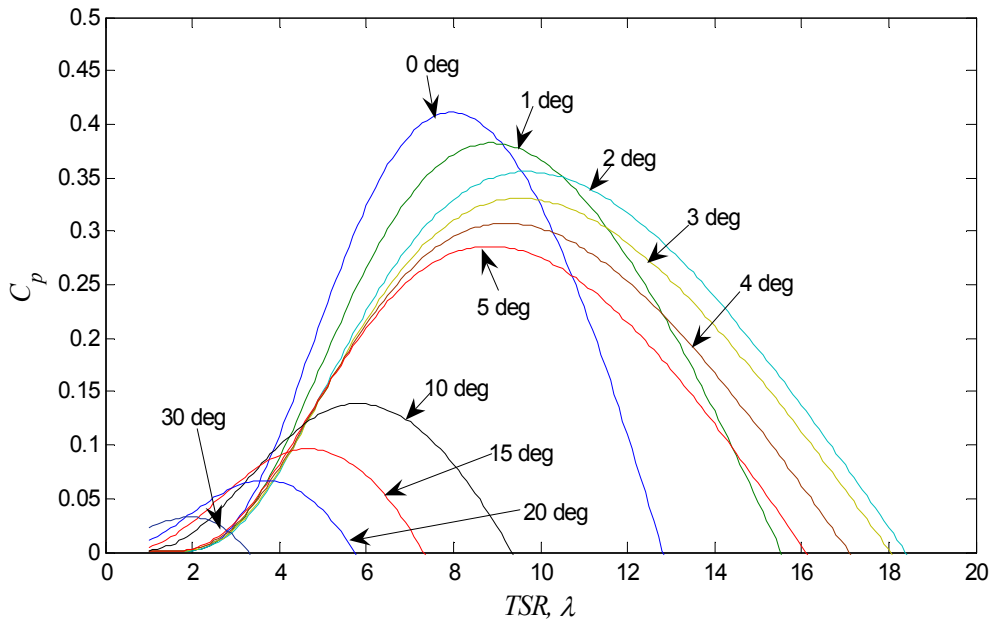


Figure 4.32.  $C_p$ - $\lambda$  characteristics at different pitch angles ( $\theta$ ).

For variable speed pitch-regulated wind turbines, two variables have direct effect on their operation, namely rotor speed and blade pitch angle [4.52]-[4.54]. *Power optimization strategy* is employed when wind speed is below the turbine rated wind speed, to optimize the energy capture by maintaining the optimum *TSR*. *Power limitation strategy* is used above the rated wind speed of the turbine to limit the output power to the rated power. This is achieved by employing a pitch angle controller which changes the blade pitch to reduce the aerodynamic efficiency, thereby reducing the wind turbine power to acceptable levels, as discussed in Chapter 2. The different regions of the

above-mentioned control strategies of a variable speed wind turbine system are as shown in the Figure 4.33.

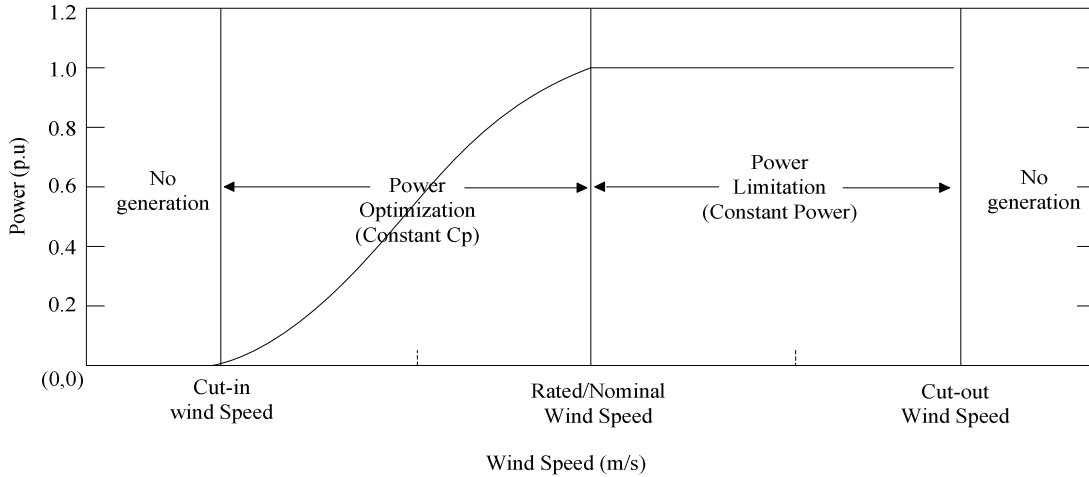


Figure 4.33. Variable speed pitch controlled wind turbine operation regions.

Pitch Angle Controller. The pitch angle controller used in this study employs PI controllers as shown in Figure 4.34 [4.52], [4.56], [4.66]. These controllers control the wind flow around the wind turbine blade, thereby controlling the torque exerted on the turbine shaft. If the wind speed is less than the rated wind speed, the pitch angle is kept constant at an optimum value. If the wind speed exceeds the rated wind speed, the controller calculates *the power error* (between the reference power and the output power of the wind turbine) and the *frequency error* (between the measured stator electrical frequency of the SEIG and the rated frequency). The output of the controllers gives the required pitch angle (Figure 4.34). In this figure, the *Pitch Angle Rate Limiter* block limits the rate of change of pitch angle as most modern wind turbines consist of huge rotor blades. The maximum rate of change of the pitch angle is usually in the order of  $3^\circ$  to  $10^\circ$ /second.

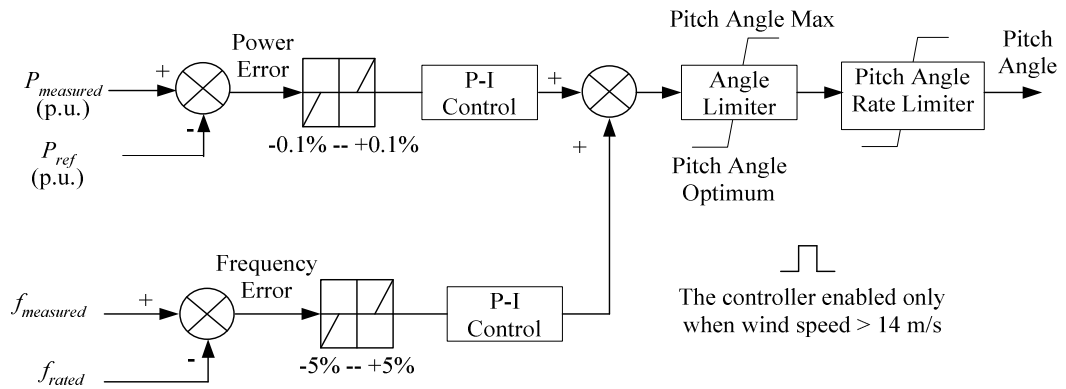


Figure 4.34. Pitch angle controller.

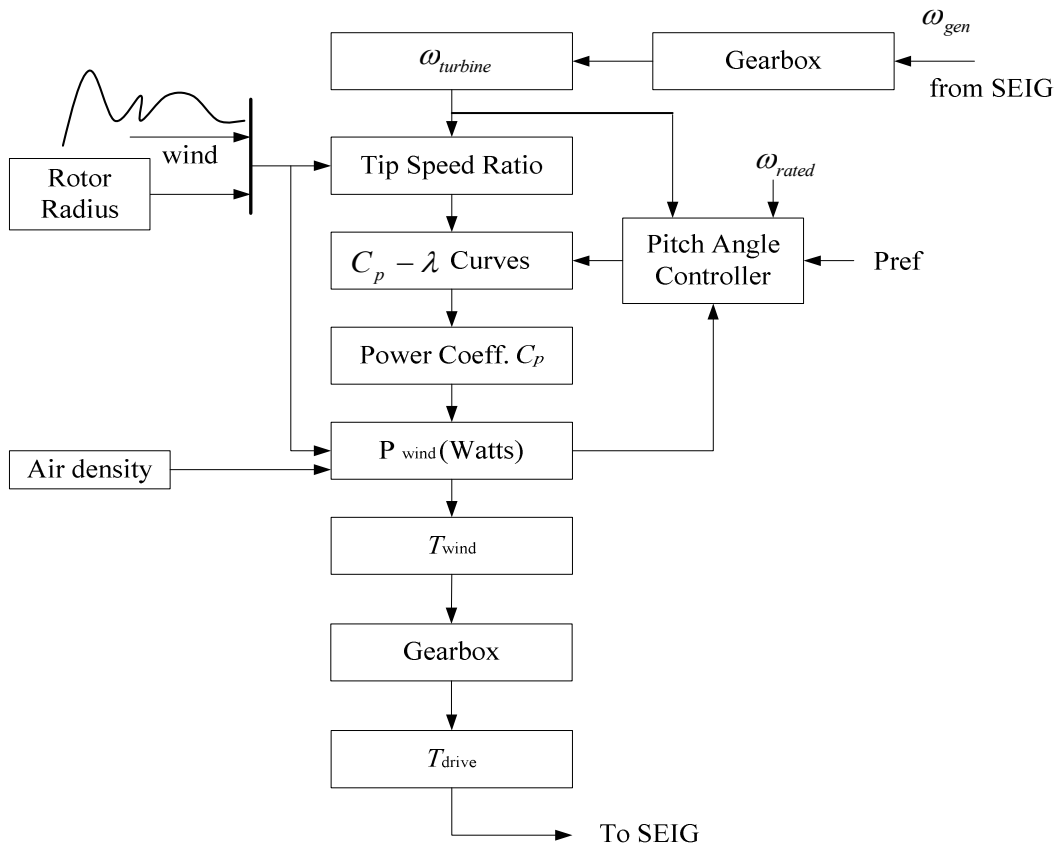


Figure 4.35. Simulation model of the variable speed pitch-regulated wind turbine.

Variable-speed Wind Turbine Model. The dynamic model of the variable speed wind turbine are developed in MATLAB/Simulink. Figure 4.35 shows the block diagram of the wind turbine model.

The inputs for the wind turbine model are, wind speed, air density, radius of the wind turbine, mechanical speed of the rotor referred to the wind turbine side and power reference for the pitch angle controller. The output is the drive torque  $T_{drive}$  which drives the electrical generator. The wind turbine calculates the tip speed ratio from the input values and estimates the value of the power coefficient from the performance curves. The pitch angle controller maintains the value of the blade pitch at optimum value until the power output of the wind turbine exceeds the reference power input.

#### Dynamic Model for SEIG

There are two fundamental circuit models employed for examining the characteristics of a SEIG. One is the per-phase equivalent circuit which includes the loop-impedance method adapted by Murthy et al [4.59] and Malik and Al-Bahrani [4.60], and the nodal admittance method proposed by Ouazene and Mcpherson [4.49] and Chan [4.61]. These methods are suitable for studying the machine's steady-state characteristics. Another method is the  $dq$ -axis model based on the generalized machine theory proposed by Elder et al [4.48] and Grantham et al [4.50], and is employed to analyze both the machine's transient as well as steady-state.

Steady-state Model. Steady-state analysis of induction generators is of interest both from the design and operational points of view. By knowing the parameters of the

machine, it is possible to determine its performance at a given speed, capacitance and load conditions.

Loop impedance and nodal admittance methods used for the analysis of SEIG are both based on per-phase steady-state equivalent circuit of the induction machine (Figure 4.36), modified for the self-excitation case. They make use of the principle of conservation of active and reactive powers, by writing proper loop equations [4.59], [4.60], [4.65] or nodal equations [4.49], [4.61], for the equivalent circuit. These methods are very effective in calculating the minimum value of capacitance needed for guaranteeing self-excitation of the induction generator. For stable operation, *excitation capacitance* must be slightly higher than the minimum value. Also, there is a speed threshold, the cutoff speed of the machine, below which no excitation is possible. In the following paragraph, a brief description of the loop impedance method is given for better understanding.

The per-unit (p.u.) per-phase steady-state circuit of a self-excited induction generator under lagging (RL) load is shown in Figure 4.36 [4.59], [4.49]. In the analysis of SEIG, the following assumptions were made [4.59]:

1. Only the magnetizing reactance  $X_m$  is assumed to be affected by magnetic saturation, and all other parameters of the equivalent circuit are assumed to be constant. Self-excitation results in the saturation of the main flux, and the value of  $X_m$  reflects the magnitude of the main flux. Leakage flux passes mainly in the air, and thus these fluxes are not affected to any large extent by saturation of the main flux.

2. Per unit values of the stator and rotor leakage reactance (referred to stator side) are assumed to be equal ( $X_{ls} = X_{lr} = X_l$ ). This assumption is normally valid in induction machine analysis.

3. Core loss in the machine is neglected.

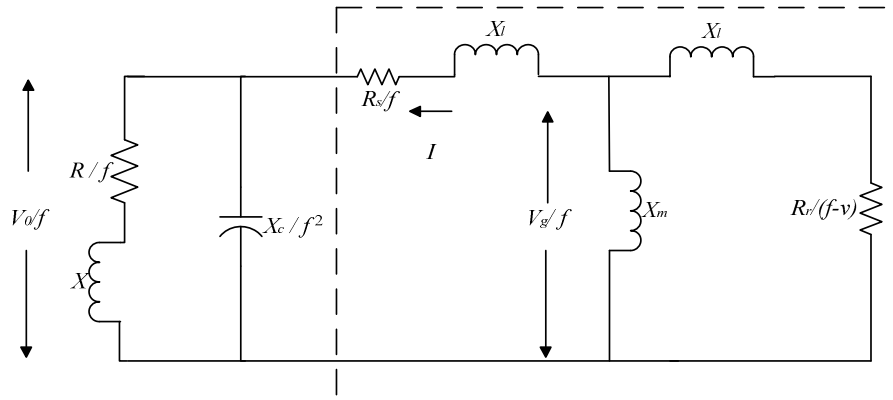


Figure 4.36. Equivalent T circuit of self-excited induction generator with R-L Load.

In the figure, the symbols are:

$R_s$ ,  $R_r$ ,  $R$  : p.u. per-phase stator, rotor (referred to stator) and load resistance, respectively.

$X_l$ ,  $X$ ,  $X_m$  : p.u. per-phase stator/rotor leakage, load and magnetizing reactances (at base frequency), respectively.

$X_c$  : p.u. per-phase capacitive reactance (at base frequency) of the terminal excitation capacitor.

$f$ ,  $v$  : p.u. frequency and speed, respectively.

$V_g$ ,  $V_0$  : p.u. per-phase air gap and output voltages, respectively.

For the circuit shown in Figure 4.36, the loop equation for the current can be written as:

$$IZ = 0 \quad (4.105)$$

where  $Z$  is the net loop impedance given by

$$Z = \left( \frac{R_r}{f - v} + jX_l \right) \parallel \left( jX_m + \frac{R_s}{f} + jX_l + \left( \frac{-jX_c}{f^2} \right) \parallel \left( \frac{R}{f} + jX \right) \right) \quad (4.106)$$

For equation (4.105) to hold true for any current  $I$ , the loop impedance ( $Z$ ) should be zero. This implies that both the real and imaginary parts of  $Z$  are zero. These two equations can be solved simultaneously for any two unknowns, such as  $f$  and  $X_c$ .

Self-excitation Process. The process of self-excitation in induction machines has been known for several decades [4.46], [4.47]. When capacitors are connected across the stator terminals of an induction machine, driven by an external prime mover, voltage will be induced at its terminals. The induced electromotive force (EMF) and current in the stator windings will continue to rise until the steady state condition influenced by the magnetic saturation of the machine is reached. At this operating point the voltage will be stabilized at a given value and frequency. In order for self-excitation to occur, for a particular capacitance value there is a corresponding minimum speed [4.47], [4.58]. Therefore, in stand-alone mode of operation, it is necessary for the induction generator to be operated in the saturation region. This guarantees one and only one intersection between the magnetization curve and the capacitor reactance line, as well as output voltage stability under load as seen in Figure 4.37 [4.45], [4.55].

Under no load, the capacitor current  $I_c = V_g / X_c$  must be equal to the magnetizing current  $I_m = V_g / X_m$  when the stator impedance ( $R_s + jX_l$ ) is neglected and the rotor circuit can be considered as open circuit, as shown in Figure 4.37. The stator phase

voltage  $V_g$  ( $V_g = V_0$  in this case) is a function of magnetizing current  $I_m$ , linearly rising until the saturation point of the magnetic core is reached. With the value of self exciting capacitance equal to  $C$ , the output frequency of the self-excited generator is  $f = 1/(2\pi CX_m)$ .

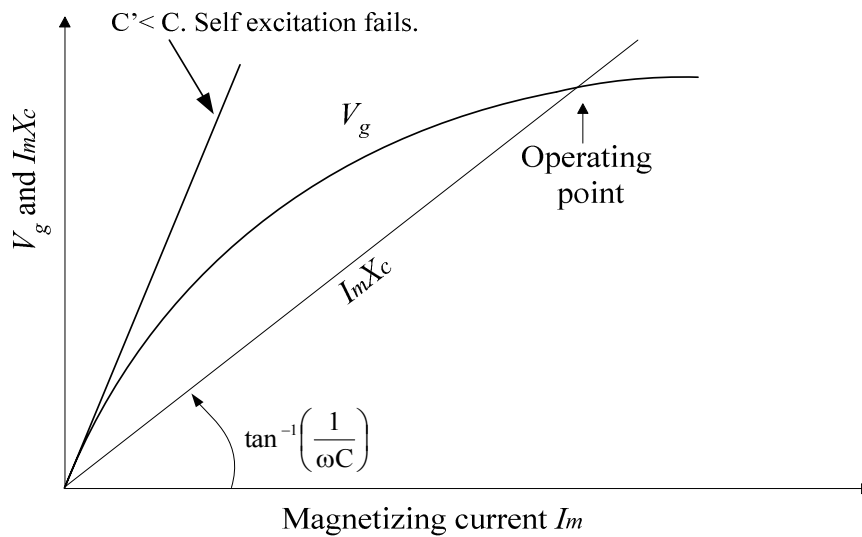


Figure 4.37. Determination of stable operation of SEIG.

Dynamic Model of SEIG in  $dq$  Representations. The process of self-excitation is a transient phenomenon and is better understood if analyzed using a transient model. To arrive at a transient model of an induction generator, an  $abc-dq0$  transformation is used.

The  $dq$  axis model, based on the generalized machine theory proposed by Elder [4.48], Salama [4.58] and Grantham [4.50], is employed to analyze the machine's transient state as well as steady state. To arrive at a transient model of an induction generator,  $abc-dq0$  transformation [4.62] has been used in this analysis.

Figure 4.38 shows the  $dq$  axis equivalent circuit of a self excited induction generator, shown in Figure 4.36, in stationary reference frame [4.51], [4.58], [4.62].

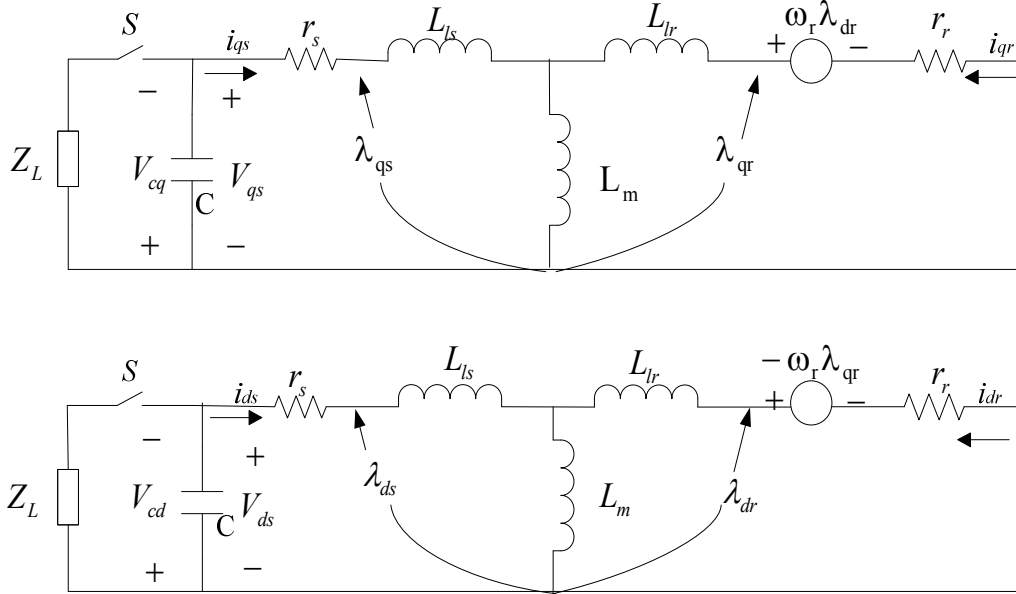


Figure 4.38.  $dq$  representation of a SEIG (All values are referred to stator).

In the figure,  $\omega_r$  is the electrical angular velocity of the rotor,  $s(r)$  subscript denotes parameters and variables associated with stator (rotor), respectively.  $V_{cq}$  ( $V_{qs}$ ) and  $V_{cd}$  ( $V_{ds}$ ) are  $q$  and  $d$  axis voltages, respectively, and  $i_{qs}$  ( $i_{ds}$ ) is the  $q$  ( $d$ ) axis component of stator current.  $I_{qr}$  ( $i_{dr}$ ) is the  $q$  ( $d$ ) axis component of rotor current.  $L_{ls}$ ,  $L_{lr}$  and  $L_m$  are stator leakage, rotor leakage and magnetizing inductances of the stator.  $\lambda_{qs}$  and  $\lambda_{ds}$  are  $q$  and  $d$  axis components of stator flux linkages.  $\lambda_{qr}$  and  $\lambda_{dr}$  are  $q$  and  $d$  axis components of rotor flux linkages.

From Figure 4.38, the equation for no-load operation of SEIG can be written as shown below:

$$\begin{bmatrix} 0 \\ 0 \\ 0 \\ 0 \end{bmatrix} = \begin{bmatrix} r_s + pL_s + 1/pC & 0 & pL_m & 0 \\ 0 & r_s + pL_s + 1/pC & 0 & pL_m \\ pL_m & -\omega_r L_m & r_r + pL_r & -\omega_r L_r \\ \omega_r L_m & pL_m & \omega_r L_r & r_r + pL_r \end{bmatrix} \begin{bmatrix} i_{qs} \\ i_{ds} \\ i_{qr} \\ i_{dr} \end{bmatrix} + \begin{bmatrix} V_{cq0} \\ V_{cd0} \\ K_q \\ K_d \end{bmatrix} \quad (4.107)$$

where  $p = d/dt$ .  $K_d$  ( $K_q$ ) is a constant representing initial induced voltage along the  $d$  ( $q$ ) axis, due to the remaining magnetic flux in the core.  $V_{cq0}$  and  $V_{cd0}$  are initial  $q$  and  $d$  component voltages across the capacitor and  $L_s = L_{ls} + L_m$ ,  $L_r = L_{lr} + L_m$ .

Equation (4.107) can be modified to obtain four first order differential equations as:

$$pI = AI + B \quad (4.108)$$

The mechanical system is described by

$$T_{drive} = J \left( \frac{2}{P} \right) p\omega_r + T_{e-gen} \quad (4.109)$$

where:

$$A = \frac{1}{L} \begin{bmatrix} -L_r r_s & -L_m^2 \omega_r & L_m r_r & -L_m \omega_r L_r \\ L_m^2 \omega_r & -L_s r_s & L_m \omega_r L_r & L_m r_r \\ L_m r_s & L_s \omega_r L_m & -L_s r_r & L_s \omega_r L_r \\ -L_s \omega_r L_m & L_m r_s & -L_s \omega_r L_r & -L_s r_r \end{bmatrix}, \quad B = \frac{1}{L} \begin{bmatrix} L_m K_q - L_r V_{cq} \\ L_m K_d - L_r V_{cd} \\ L_m V_{cq} - L_s K_q \\ L_m V_{cd} - L_s K_d \end{bmatrix}$$

$$I = \begin{bmatrix} i_{qs} \\ i_{ds} \\ i_{qr} \\ i_{dr} \end{bmatrix}, \quad L = L_s L_r - L_m^2, \quad V_{cq} = \frac{1}{C} \int_0^t i_{qs} dt + V_{cq0} \quad \text{and} \quad V_{cd} = \frac{1}{C} \int_0^t i_{ds} dt + V_{cd0}.$$

$J$  - Inertia of the rotor in (Kgm<sup>2</sup>).

$T_{drive}$  - wind turbine torque in (Nm).

$T_{e-gen}$  - electromagnetic torque by the generator in (Nm).

$P$  - number of poles.

The simulation of the SEIG can be carried out by solving (4.108). Since the magnetization inductance  $L_m$  is nonlinear in nature, an internal iteration has to be done at each integration step. Given the initial condition from the previous step, the magnetization current can be calculated as shown below [4.50]:

$$I_m = \sqrt{(i_{ds} + i_{dr})^2 + (i_{qs} + i_{qr})^2} \quad (4.110)$$

The variation of magnetizing inductance as a function of magnetizing current, used in this study is given by:

$$L_m = 0.5 \times [0.025 + 0.2974 \times \exp(-0.04878 \times I_m)] \quad (4.111)$$

Any combination of  $R$ ,  $L$  and  $C$  can be added in parallel with the self-excitation capacitance to act as load. For example, if resistance  $R$  is added in parallel with the self-excitation capacitance, then the term  $1/pC$  in the matrix (see 4.107) becomes  $R/(1+RpC)$ . The load can be connected across the capacitors, once the voltage reaches a steady-state value [4.50], [4.51]. If there is an inductive load connected across the excitation capacitor, it influences the effective value of excitation capacitance such that it results in an increase in the slope of the straight line of the capacitive reactance (Figure 4.37), reducing the terminal voltage. This phenomenon is more pronounced when the load inductance gets higher in value. A capacitor for individual compensation can be connected across the terminal of the load, in such a way that it follows the load conditions [4.63].

Ratings of the induction machine simulated are given in Table 3.2 (Chapter 3). The detailed parameters used in modeling the SEIG are given in Table 4.6. The parameters are obtained from [4.62] based on the same p.u. values of a 500 hp, 2300 V induction

machine.

TABLE 4.6. SEIG MODEL PARAMETERS

$r_s$	0.164 $\Omega$
$r_r$	0.117 $\Omega$
$X_{ls}$	0.754 $\Omega$
$X_{lr}$	0.754 $\Omega$
$L_m$	See (4.111)
$J$	1.106 kgm <sup>2</sup>
$C$	240 $\mu$ F
$P$ (Number of poles)	4

\*: All reactances are based on 60 Hz.

#### Responses of the Model for the Variable Speed WECS

The model of a 50 kW variable speed wind energy conversion system consisting of a pitch-regulated wind turbine and self excited induction generator is developed in MATLAB/Simulink environment using SimPowersystems block-set. In this sub-section, the model responses under different scenarios are discussed.

Wind Turbine Output Power Characteristic. Figure 4.39 shows the wind turbine output power of the simulated model for different wind velocities. It can be observed that the output power is kept constant at higher wind velocities even though the wind turbine has the potential to produce more power. This is done to protect the electrical system and to prevent the over speeding of the rotor.

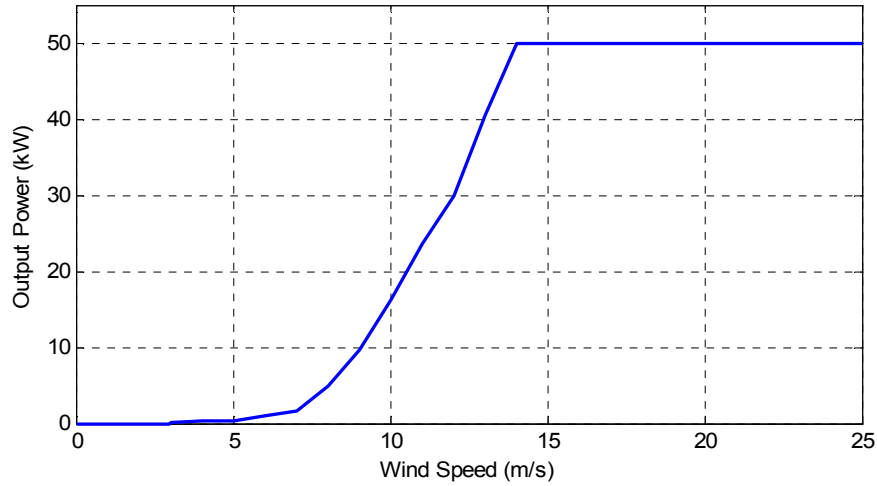


Figure 4.39. Wind turbine output power characteristic.

Process of Self-excitation in SEIG. The process of self-excitation can occur only if there is some residual magnetism. For numerical method of integration, residual magnetism cannot be zero at the beginning of the simulation. Therefore, non-zero initial values are set for  $K_q$  [and/or  $K_d$ , see equation (4.107)] and the rotor speed.

The process of voltage build up continues, starting with the help of the residual magnetism, until the iron circuit saturates and therefore the voltage stabilizes. In other terms, the effect of this saturation is to modify the magnetization inductance  $L_m$ , such that it reaches a saturated value; the transient then neither increases nor decreases and becomes a steady state quantity giving continuous self-excitation. The energy for the above process is provided by the kinetic energy of the wind turbine rotor [4.50]. Figure 4.40 shows the process of a successful self excitation in an induction machine under no load condition with wind speed at 10m/s. The value of the excitation capacitor is given in the figure. An unsuccessful self excitation process under the same condition (except a

smaller capacitor bank) is shown in Figure 4.41.

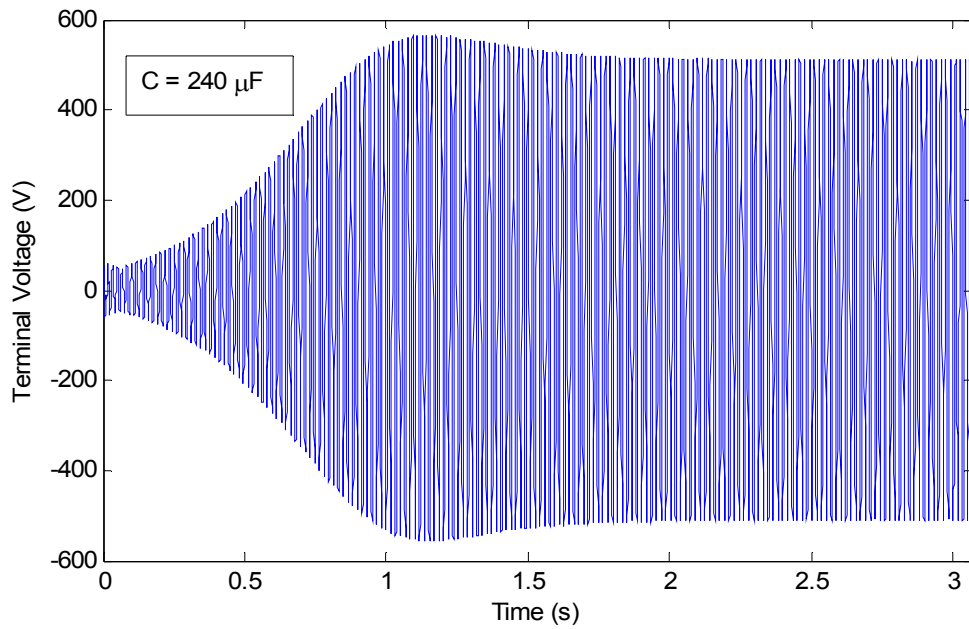


Figure 4.40. A successful self excitation process.

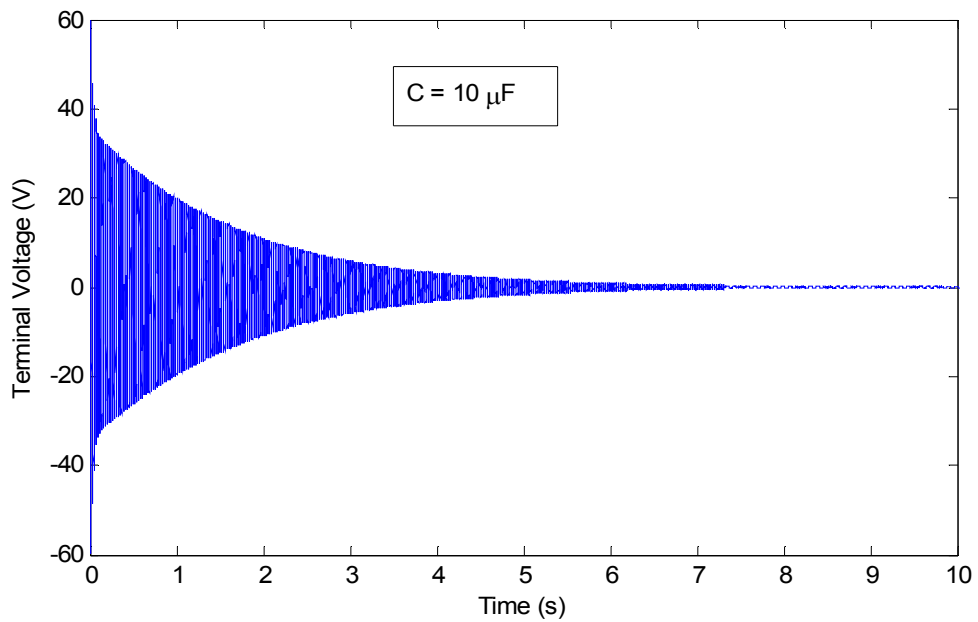


Figure 4.41. Voltage fails to build up.

Figures 4.42 and 4.43 show the variations in magnetizing current and magnetizing inductance vs. time for successful voltage build up of the SEIG. From Figures 4.40, 4.42 and 4.43, it can be observed that the phase voltage slowly starts building up and reaches a steady state value as the magnetization current starts from zero and reaches a steady state value. Also, we see that the self excitation follows the process of magnetic saturation of the core and the stable output value is reached only when the machine core is saturated.

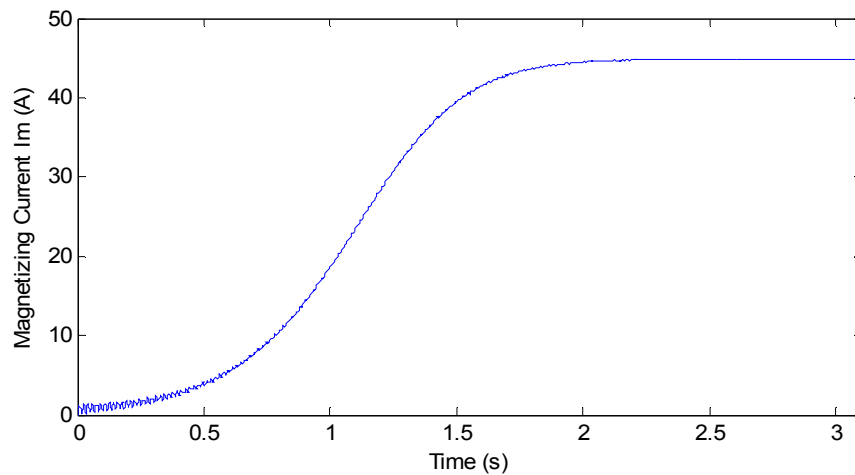


Figure 4.42. Variation of magnetizing current,  $I_m$ .

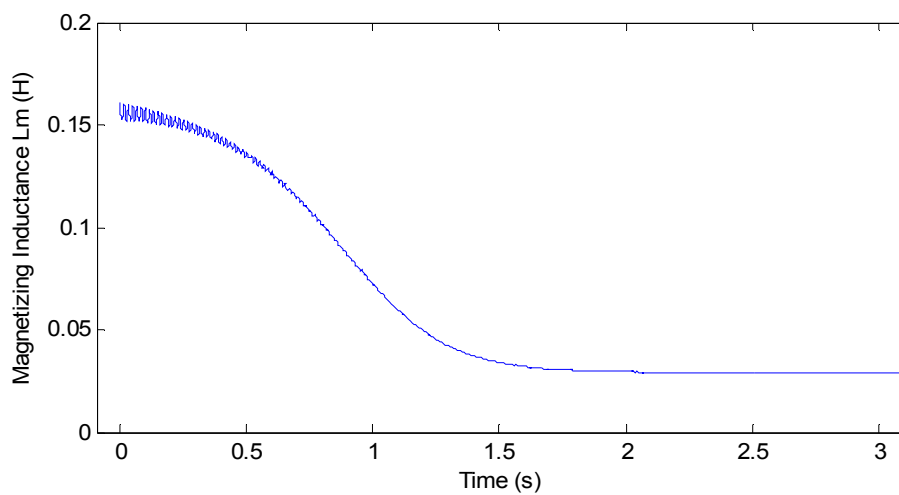


Figure 4.43. Variation of magnetizing inductance,  $L_m$ .

Model Responses under Wind Speed Changes. In this section, the responses of the model for the variable speed WECS to wind speed variations are given and discussed. The wind speed changes are shown in Figure 4.44. The wind speed used in simulation steps up from 10 m/s to 16 m/s at  $t = 30$  s and changes from 16 m/s to 8 m/s at 60 s.

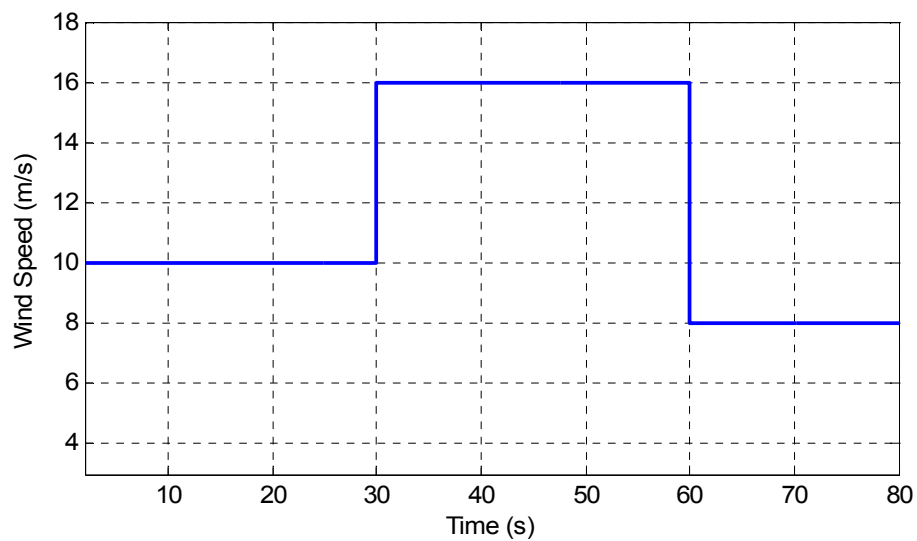


Figure 4.44. Wind speed variations used for simulation study.

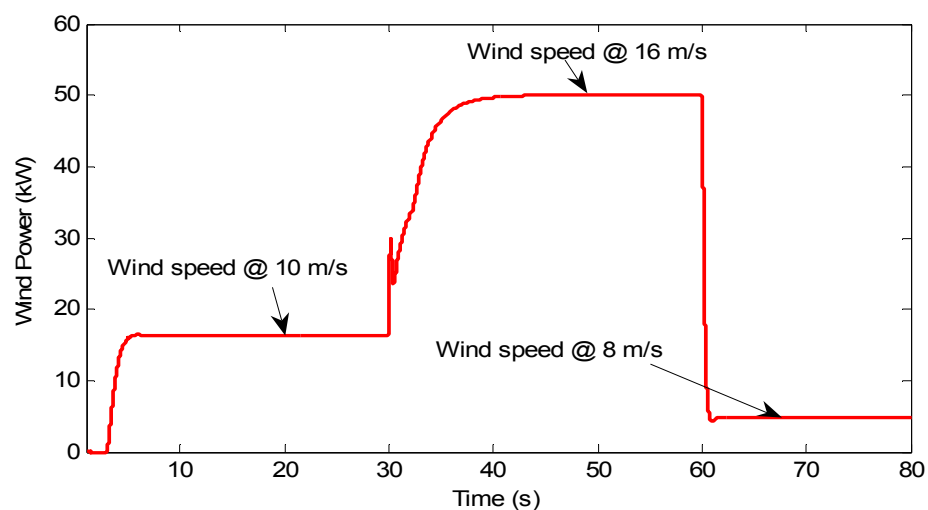


Figure 4.45. Output power of the WECS model under wind speed changes.

Figure 4.45 shows the output power of the WECS. The WECS starts to supply power at 3 s. It is noted from the figure that the output power is 16.2 kW at 10 m/s wind speed, 50 kW at 16 m/s, and 4.86 kW at 8 m/s, respectively. This matches the system output power characteristic shown in Figure 4.39.

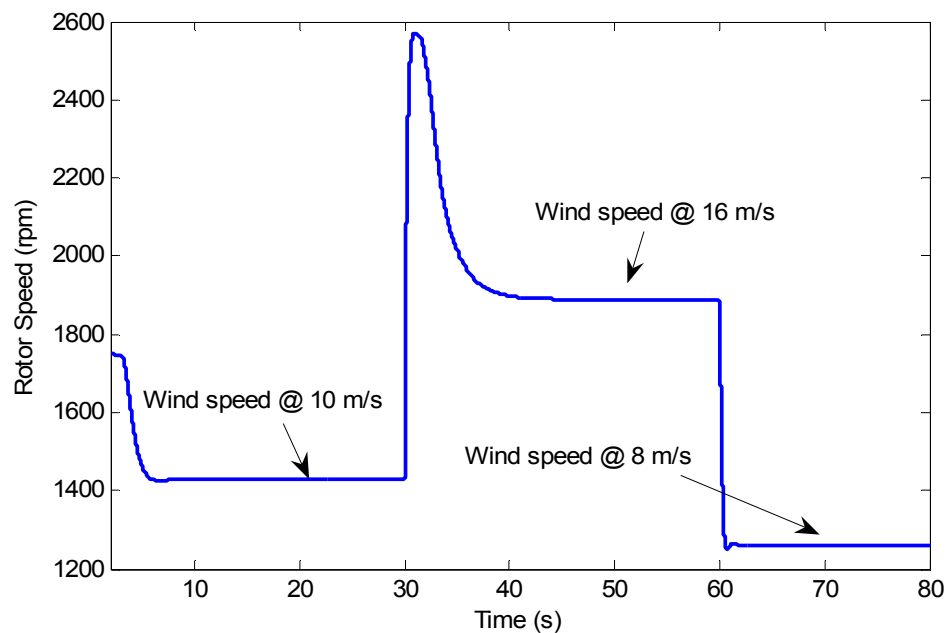


Figure 4.46. Wind turbine rotor speed.

Figure 4.46 shows the wind turbine rotor speed under the wind speed changes. The rotor speed is a slightly under 1800 rpm (rated speed) when there is no load. When the load is connected at 3 s, the speed drops to about 1430 rpm. When the wind speed is increased to 16 m/s at 30 s, there is a fast increase in rotor speed, as shown in Figure 4.46. Then the pitch controller starts operating to bring the rotor speed down to 1890 rpm, which is the upper limit (+5%) of the frequency regulation band in the pitch controller (see Figure 4.34). The rotor speed drops to 1257 rpm as the wind speed drops to 8 m/s at 60 s.

Figure 4.47 shows how the pitch angle changes during the wind speed variation. Note that the pitch angle keeps at the optimum value ( $2^\circ$  in this study) when the wind speed is below the nominal value (14 m/s). When the wind speed exceeds 14 m/s (at 30 s), the pitch controller begins to work and increases the pitch angle to about  $6.15^\circ$  to keep the output power constant (at 50 kW). The corresponding  $C_p$  is shown in Figure 4.48.

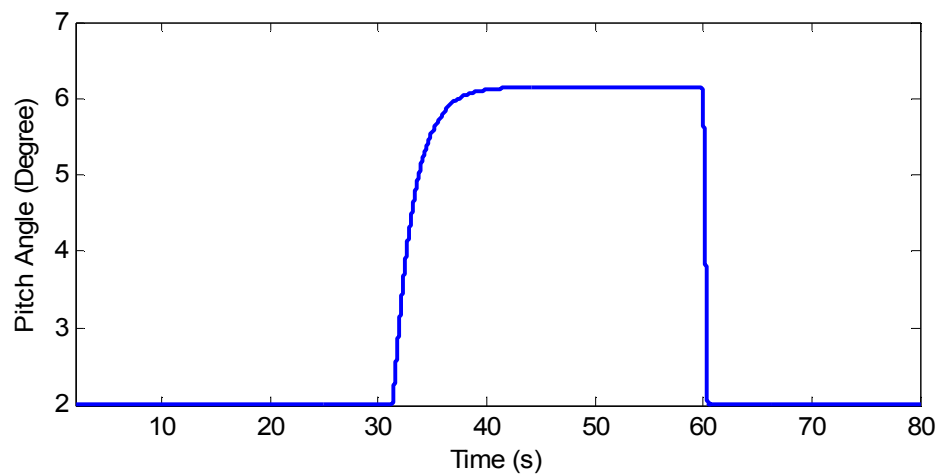


Figure 4.47. Pitch angle controller response to the wind changes.

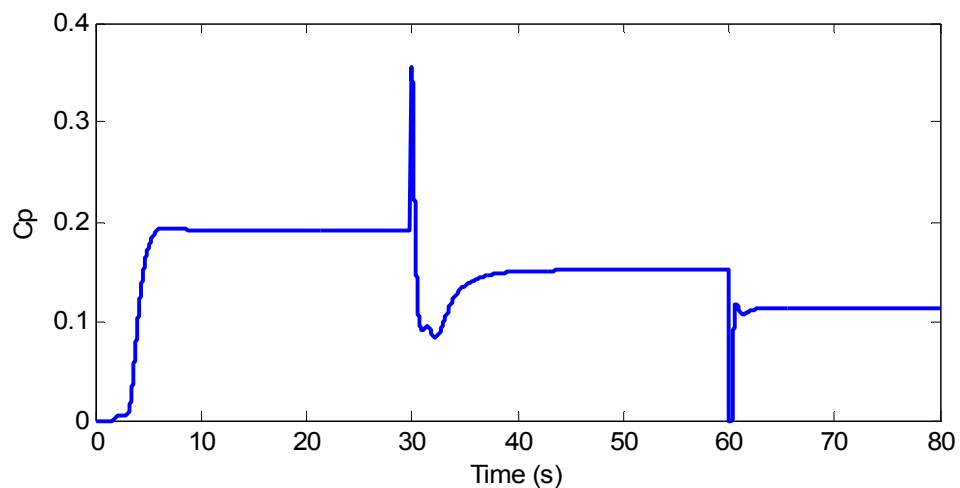


Figure 4.48. Variation of power coefficient  $C_p$

### Solar Energy Conversion System

The principle of operation of a PV cell is discussed in Chapter 2. In this section, model development of a PV module is given in details. The PV model developed for this study is based on the research work reported in [4.67]-[4.70].

#### Modeling for PV Cell/Module

The most commonly used model for a PV cell is the one-diode equivalent circuit as shown in Figure 4.49 [4.67]-[4.70]. Since the shunt resistance  $R_{sh}$  is large, it normally can be neglected. The five parameters model shown in Figure 4.49 (a) can therefore be simplified into that shown in Figure 4.49 (b). This simplified equivalent circuit model is used in this study.

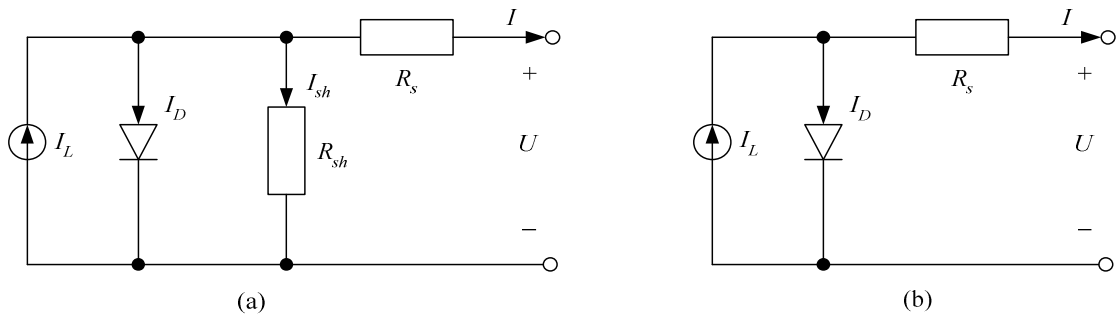


Figure 4.49. One-diode equivalent circuit model for a PV cell. (a) Five parameters model; (b) Simplified four parameters model.

The relationship between the output voltage  $V$  and the load current  $I$  can be expressed as:

$$I = I_L - I_D = I_L - I_0 \left[ \exp\left(\frac{U + IR_s}{\alpha}\right) - 1 \right] \quad (4.112)$$

where  $I_L$  = light current (A);

$I_0$  = saturation current (A);

$I$  = load current (A);

$U$  = output voltage (V);

$R_s$  = series resistance ( $\Omega$ );

$\alpha$  = thermal voltage timing completion factor (V).

There are four parameters ( $I_L$ ,  $I_0$ ,  $R_s$  and  $\alpha$ ) that need to be determined before the  $I-U$  relationship can be obtained. That is why the model is called a four-parameter model. Both the equivalent circuit shown in Figure 4.49 (b) and the equation (4.112) look simple. However, the actual model is more complicated than it looks because the above four parameters are functions of temperature, load current and/or solar irradiance. In the remainder of this section, procedures are given for determining the four parameters.

Light Current  $I_L$ . According to [4.68] and [4.69],  $I_L$  can be calculated as:

$$I_L = \frac{\Phi}{\Phi_{ref}} [I_{L,ref} + \mu_{I,SC} (T_c - T_{c,ref})] \quad (4.113)$$

where  $\Phi$  = irradiance ( $\text{W}/\text{m}^2$ );

$\Phi_{ref}$  = reference irradiance ( $1000 \text{ W}/\text{m}^2$  is used in this study);

$I_{L,ref}$  = light current at the reference condition ( $1000 \text{ W}/\text{m}^2$  and  $25 \text{ }^\circ\text{C}$ );

$T_c$  = PV cell temperature ( $^\circ\text{C}$ )

$T_{c,ref}$  = reference temperature ( $25 \text{ }^\circ\text{C}$  is used in this study);

$\mu_{I,SC}$  = temperature coefficient of the short-circuit current ( $\text{A}/^\circ\text{C}$ ).

Both  $I_{L,ref}$  and  $\mu_{I,SC}$  can be obtained from manufacturer data sheet [4.69].

Saturation Current  $I_0$ . The saturation current can be expressed in terms of its value at the reference condition as [4.68]-[4.69]:

$$I_0 = I_{0,ref} \left( \frac{T_{c,ref} + 273}{T_c + 273} \right)^3 \exp \left[ \frac{e_{gap} N_s}{q \alpha_{ref}} \left( 1 - \frac{T_{c,ref} + 273}{T_c + 273} \right) \right] \quad (4.114)$$

where  $I_{0,ref}$  = saturation current at the reference condition (A);

$e_{gap}$  = band gap of the material (1.17 eV for Si materials);

$N_s$  = number of cells in series of a PV module;

$q$  = charge of an electron ( $1.60217733 \times 10^{-19}$  C);

$\alpha_{ref}$  = the value of  $\alpha$  at the reference condition.

$I_{0,ref}$  can be calculated as:

$$I_{0,ref} = I_{L,ref} \exp \left( - \frac{U_{oc,ref}}{\alpha_{ref}} \right) \quad (4.115)$$

where  $U_{oc,ref}$  = the open circuit voltage of the PV module at reference condition (V).

The value of  $U_{oc,ref}$  is provided by manufacturers. The value calculation for  $\alpha$  is discussed in the next section.

Calculation of  $\alpha$ . According to [4.69], the value of  $\alpha_{ref}$  can be calculated as

$$\alpha_{ref} = \frac{2U_{mp,ref} - U_{oc,ref}}{\frac{I_{sc,ref}}{I_{sc,ref} - I_{mp,ref}} + \ln \left( 1 - \frac{I_{mp,ref}}{I_{sc,ref}} \right)} \quad (4.116)$$

where  $U_{mp,ref}$  = maximum power point voltage at the reference condition (V);

$I_{mp,ref}$  = maximum power point current at the reference condition (A);

$I_{sc,ref}$  = short circuit current at the reference condition (A).

$\alpha$  is a function of temperature, which as expressed as:

$$\alpha = \frac{T_c + 273}{T_{c,ref} + 273} \alpha_{ref} \quad (4.117)$$

Series Resistance  $R_s$ . Some manufacturers provide the value of  $R_s$ . If not provided, the following equation can be used to estimate its value [4.69].

$$R_s = \frac{\alpha_{ref} \ln \left( 1 - \frac{I_{mp,ref}}{I_{sc,ref}} \right) + U_{oc,ref} - U_{mp,ref}}{I_{mp,ref}} \quad (4.118)$$

$R_s$  is taken as a constant in the model of this study.

Thermal Model of PV. From equations (4.113) to (4.118), it can be noted that the temperature plays an important role in the PV performance. Therefore, it is necessary to have a thermal model for a PV cell/module. In this study, a lumped thermal model is developed for the PV module based on [4.68]. The temperature of the PV module varies with surrounding temperature, irradiance, and its output current and voltage, and can be written as

$$C_{PV} \frac{dT_c}{dt} = k_{in,PV} \Phi - \frac{U \times I}{A} - k_{loss} (T_c - T_a) \quad (4.119)$$

where  $C_{PV}$  = the overall heat capacity per unit area of the PV cell/module [ $J/(^{\circ}C \cdot m^2)$ ];

$k_{in,PV}$  = transmittance-absorption product of PV cells;

$k_{loss}$  = overall heat loss coefficient [ $W/(^{\circ}C \cdot m^2)$ ];

$T_a$  = ambient temperature ( $^{\circ}C$ )

$A$  = effective area of the PV cell/module ( $m^2$ ).

### PV Model Development in MATLAB/Simulink

Based on the mathematical equations discussed before, a dynamic model for a PV module consisting of 153 cells in series has been developed using MATLAB/Simulink. Figure 4.50 shows the block diagram of the PV model. The input quantities (solar irradiance  $\Phi$  and the ambient temperature  $T_a$ ) together with manufacturer data are used to calculate the four parameters (4.113 -4.118). Then, based on equation 4.112, the output voltage is obtained numerically. The thermal model is used to estimate the PV cell temperature. The two output quantities (PV output voltage  $U$  and the PV cell temperature  $T_c$ ), and the load current  $I$ , are fed back to participate in the calculations. The model parameters used in the simulation are given in Table 4.7, which is based on the values reported in [4.68]-[4.69].

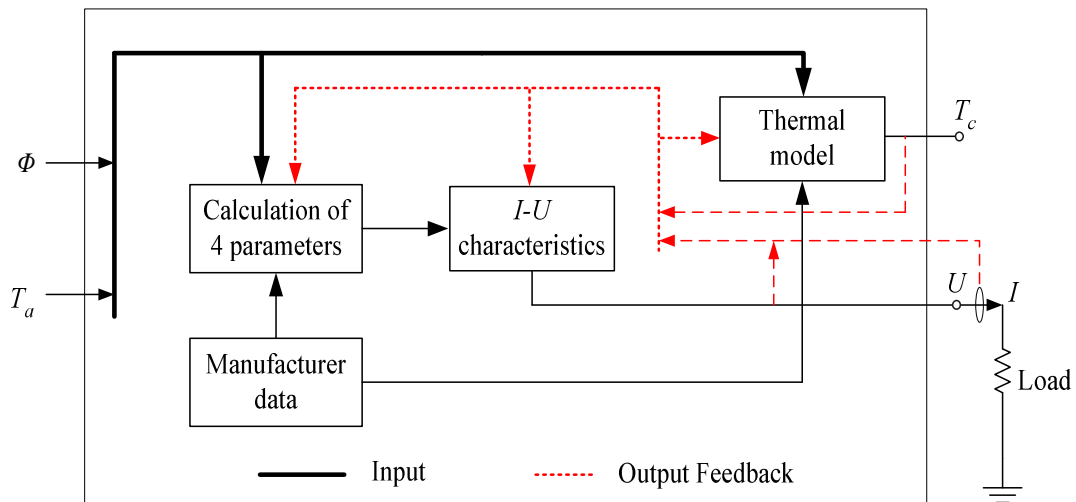


Figure 4.50. Block diagram of the PV model built in MATLAB/Simulink.

TABLE 4.7. THE PV MODEL PARAMETERS

$I_{L,ref} (I_{SC,ref})$	2.664 A
$\alpha_{ref}$	5.472 V
$R_s$	1.324 $\Omega$
$U_{oc,ref}$	87.72 V
$U_{mp,ref}$	70.731 V
$I_{mp,ref}$	2.448 A
$\Phi_{ref}$	1000 W/m <sup>2</sup>
$T_{c,ref}$	25 °C
$C_{PV}$	$5 \times 10^4$ J/(°C·m <sup>2</sup> )
$A$	1.5 m <sup>2</sup>
$k_{in,PV}$	0.9
$k_{loss}$	30 W/(°C·m <sup>2</sup> )

Model Performance. The model  $I$ - $U$  characteristic curves under different irradiances are given in Figure 4.51 at 25 °C. It is noted from the figure that the higher is the irradiance, the larger are the short-circuit current ( $I_{sc}$ ) and the open-circuit voltage ( $U_{oc}$ ). And, obviously, the larger will be the maximum power ( $P_{mp}$ ), shown in Figure 4.52. The maximum power point, short-circuit current and open-circuit voltage are also illustrated in the figures.

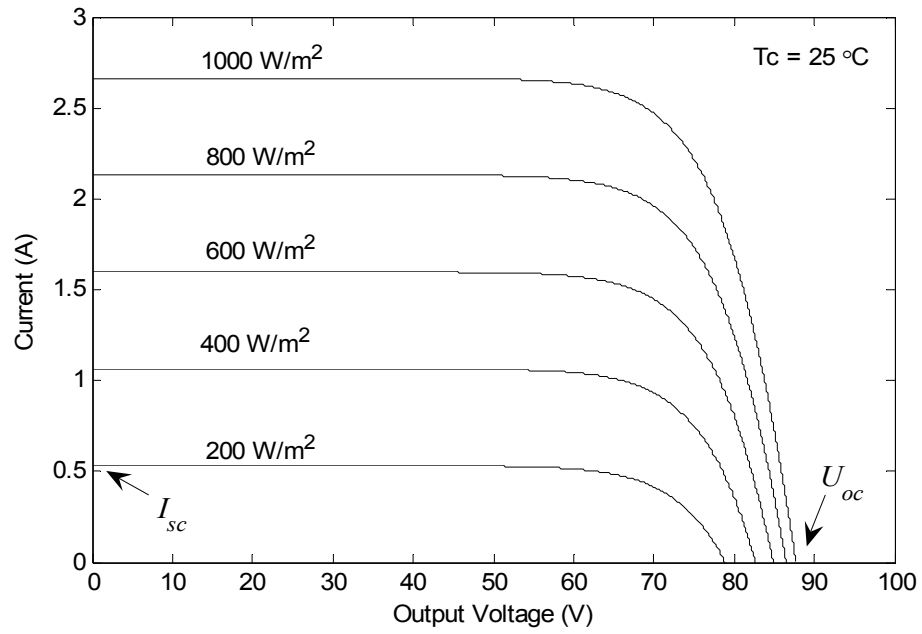


Figure 4.51.  $I-U$  characteristic curves of the PV model under different irradiances.

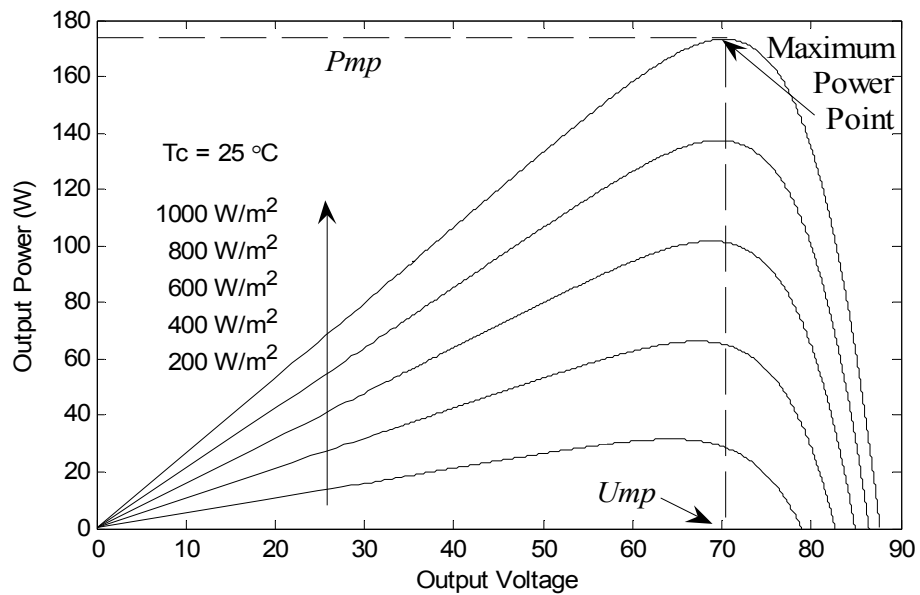


Figure 4.52.  $P-U$  characteristic curves of the PV model under different irradiances.

Temperature Effect on the Model Performance. The effect of the temperature on the PV model performance is illustrated in Figures 4.53 and 4.54. From these two figures, it is noted that the lower the temperature, the higher is the maximum power and the larger the open circuit voltage. On the other hand, a lower temperature gives a slightly lower short circuit current.

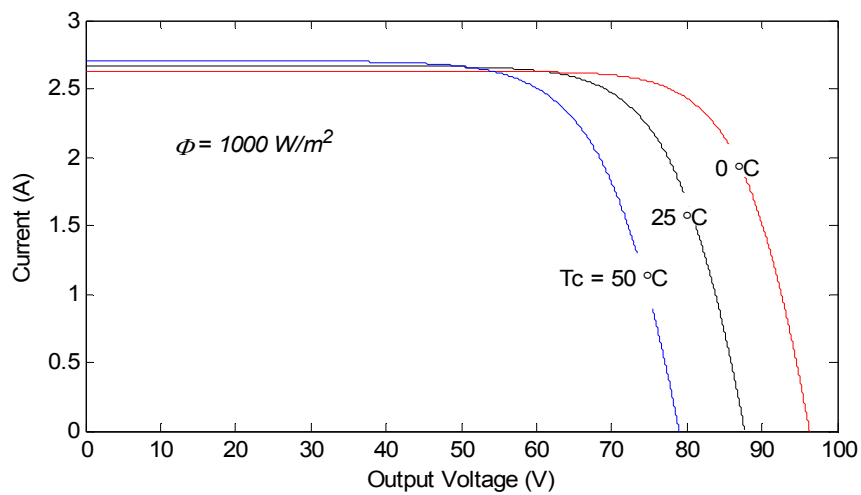


Figure 4.53.  $I$ - $U$  characteristic curves of the PV model under different temperatures.

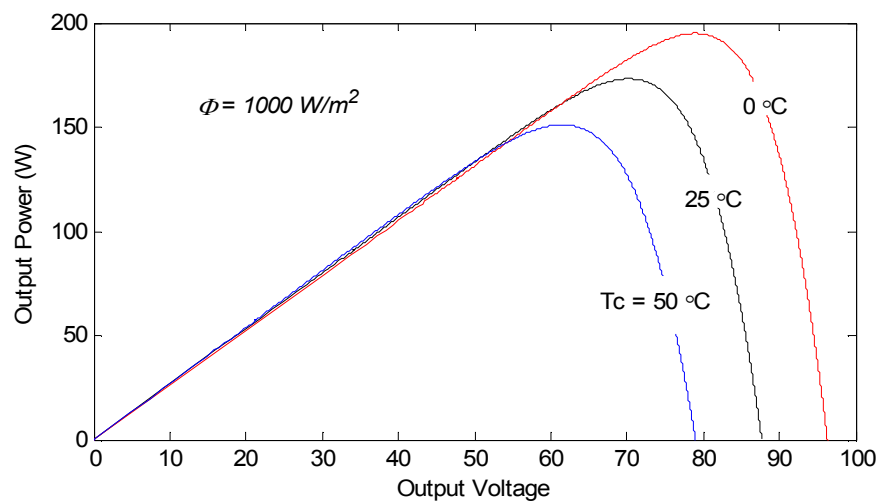


Figure 4.54.  $P$ - $U$  characteristic curves of the PV model under different temperatures.

### Maximum Power Point Tracking Control

Though the capital cost for installing a PV array is decreasing due to recent technology development (see Chapter 1), the initial investment on a PV system is still very high compared to conventional electricity generation techniques. Therefore, it is very natural to desire to draw as much power as possible from a PV array which has already been installed. Maximum power point tracking (MPPT) is one of the techniques to obtain maximum power from a PV system.

Several different MPPT techniques have been proposed in the literature. The techniques summarized in [4.72] can be classified as: (1) Look-up table methods, (2) Perturbation and observation methods, and (3) Model-based computational methods. Two major techniques in the “Model-based computational methods” category are voltage-based MPPT (VMPPT) and current-based MPPT (CMPPT) techniques. Both the CMPPT and VMPPT methods have been investigated in [4.72] for matching resistive loads and DC motor loads. A CMPPT method was reported in [4.73] for matching a DC motor load. In this study, a CMPPT method is proposed to obtain maximum power for the PV array proposed in the AC-coupled hybrid system (see Figure 3.3 in Chapter 3).

Current-Based Maximum Power Point Tracking. The main idea behind the current-based MPPT is that the current at the maximum power point  $I_{mp}$  has a strong linear relationship with the short circuit current  $I_{sc}$ .  $I_{sc}$  can either be measured on line under different operation conditions or computed from a validated model. Figure 4.55 shows the curve of  $I_{mp}$  vs  $I_{sc}$ . It can be noted that  $I_{mp}$  has a very good linear dependence on  $I_{sc}$ , which can be expressed as:

$$I_{mp} = k_{cmppt} \times I_{sc} \tag{4.120}$$

where  $k_{cmppt}$  is the current factor CMPPT control.

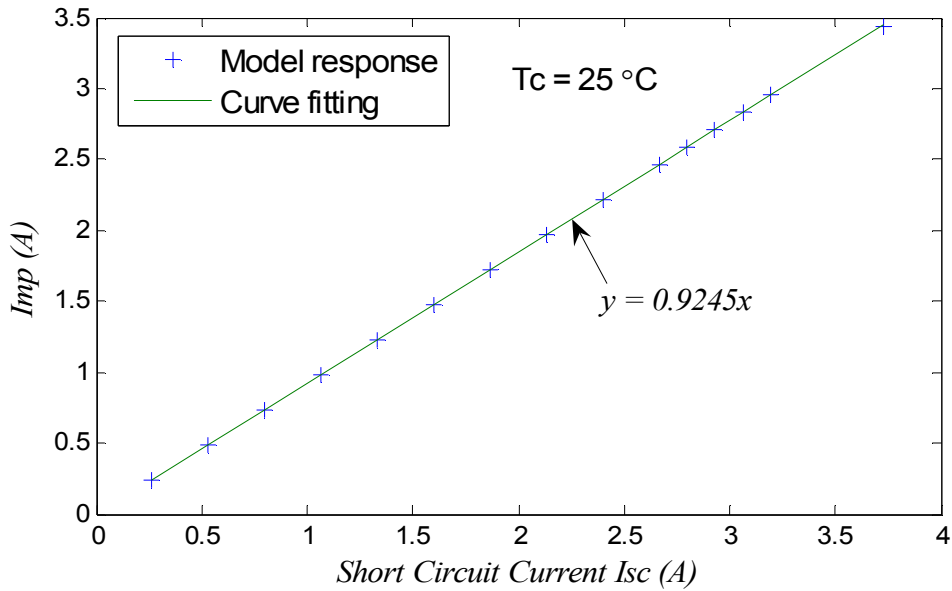


Figure 4.55. Linear relationship between  $I_{sc}$  and  $I_{mp}$  under different solar irradiances.

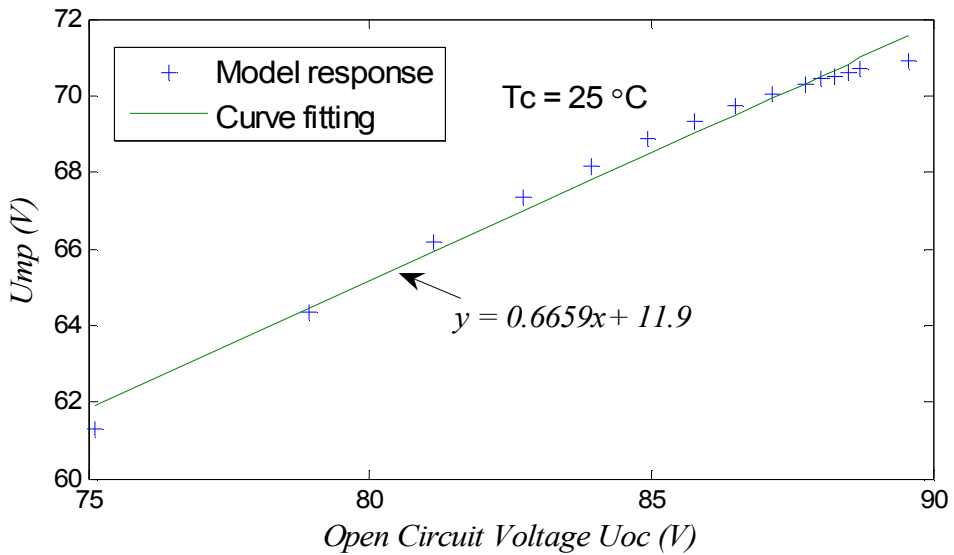


Figure 4.56.  $U_{mp}$  vs.  $U_{oc}$  curve under different solar irradiances.

The VMPPT control is based on the similar idea. Figure 4.56 shows the relationship between the voltage at the maximum power point  $U_{mp}$  and the open circuit voltage  $U_{oc}$ . By comparing Figure 4.55 and Figure 4.56, we can see that Figure 4.55 shows a stronger linear relationship. This is why the CMPPT is used in this study.

Control Scheme. The control scheme of the CMPPT for the PV system in the proposed hybrid system is shown Figure 4.57. The value of  $I_{mp}$  calculated from (4.120) is used as the reference signal to control the buck DC/DC converter so that the output current of the PV system matches  $I_{mp}$ . This reference value is also used to control the inverter so that the maximum available of power is delivered to the AC bus, shown in Figure 4.57.

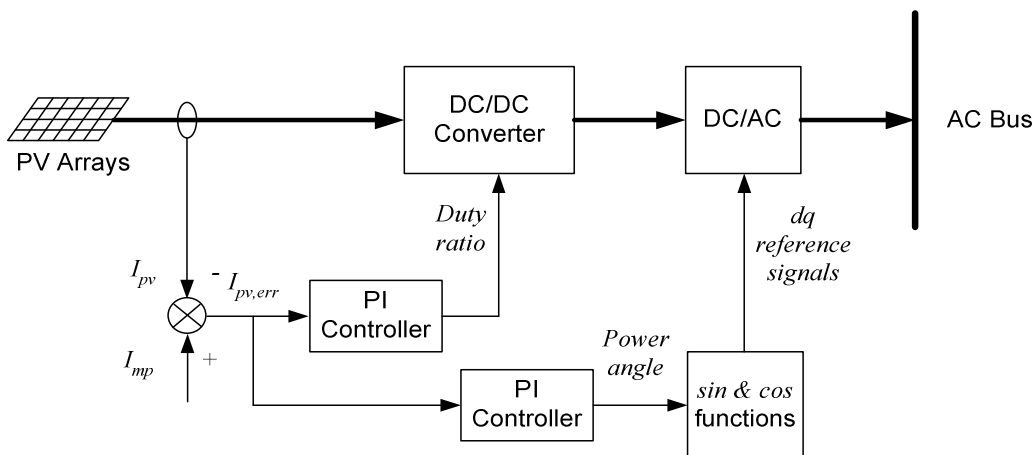


Figure 4.57. CMPPT control scheme.

The details on how to control the power electronic devices will be discussed later in this chapter.

Simulation Results. Simulation studies have been carried out to verify the proposed CMPPT method. For the purpose of simulation, the solar irradiance is kept constant at a value at  $600\text{W/m}^2$  for  $t < 40$  s. At  $t = 40$  s, the irradiance changes from  $600\text{ W/m}^2$  to  $1000\text{ W/m}^2$ , shown in Figure 4.58. This figure also shows the PV output current  $I_{pv}$  and the reference  $I_{mp}$ , which is calculated based on (4.120). The error between these two currents is also illustrated in the figure. Note that the proposed CMPPT controller works well to match the PV output current with  $I_{mp}$ . The corresponding PV output power and the calculated maximum power curves of the PV system are shown in Figure 4.59. The figure also shows that the maximum power point is tracked well with the proposed CMPPT method.

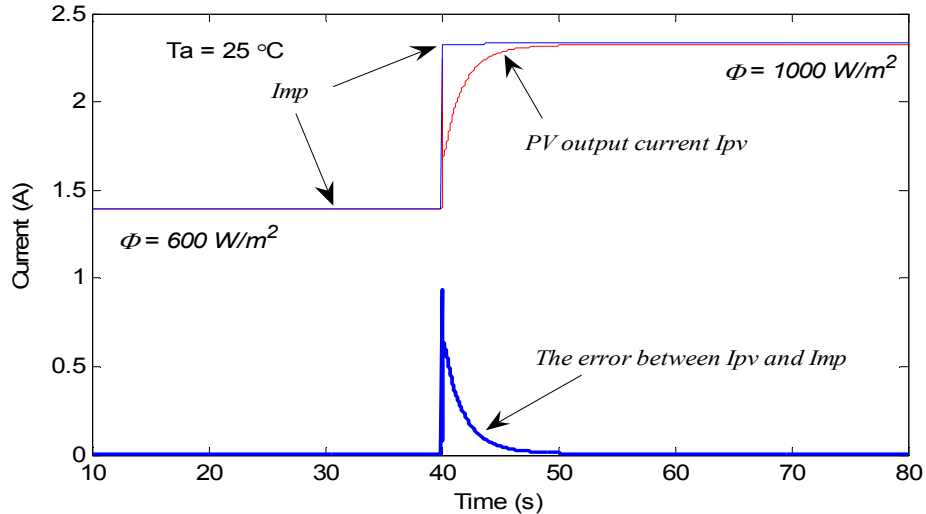


Figure 4.58.  $I_{mp}$  and  $I_{pv}$  curves under the CMPPT control

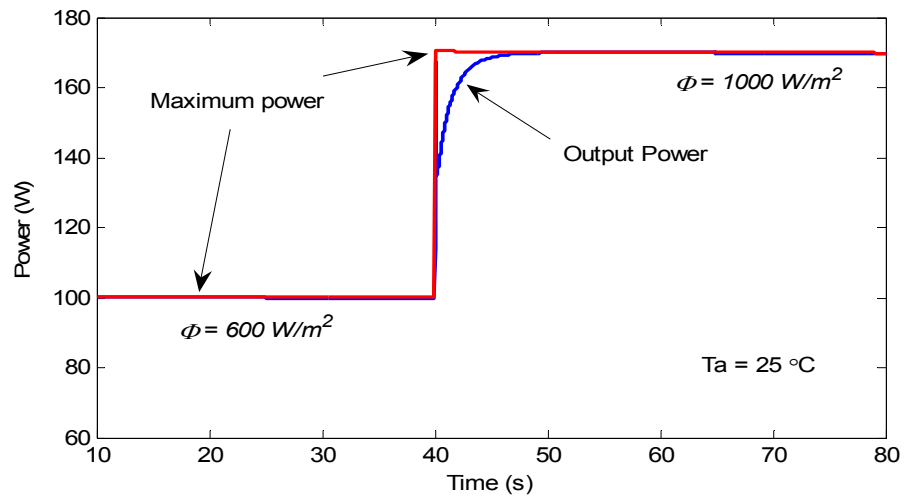


Figure 4.59. PV output power and the maximum power curves.

## Electrolyzer

The fundamentals of operation of electrolyzer have been discussed in Chapter 2. From electrical circuit aspect, an electrolyzer can be considered as a voltage-sensitive nonlinear DC load. For a given electrolyzer, within its rating range, the higher DC voltage applied, the larger is the load current. That is, by applying a higher DC voltage, we can get more H<sub>2</sub> generated. Of course, more electrical power is consumed at the same time. The model for an electrolyzer stack developed in this study is based on the empirical  $I$ - $U$  equations reported in [4.68] and [4.75], described below.

### $U$ - $I$ Characteristic

The  $U$ - $I$  characteristic of an electrolyzer cell can be expressed as [4.68], [4.75]:

$$U_{elec,cell} = U_{rev} + \frac{r_1 + r_2 T}{A} I + k_{elec} \ln \left( \frac{k_{T1} + k_{T2} / T + k_{T3} / T^2}{A} I + 1 \right) \quad (4.121)$$

where  $U_{elec,cell}$  = is the cell terminal voltage (V)

$U_{rev}$  = reversible cell voltage (V)

$r_1, r_2$  = parameters for ohmic resistance ( $\Omega \cdot m^2, \Omega \cdot m^2 / ^\circ C$ );

$k_{elec}, k_{T1}, k_{T2}, k_{T3}$  = parameters for overvoltage (V,  $m^2/A, m^2 \cdot ^\circ C/A, m^2 \cdot ^\circ C^2/A$ );

$A$  = area of cell electrode ( $m^2$ );

$I$  = electrolyzer current (A)

$T$  = cell temperature ( $^\circ C$ )

The reversible voltage  $U_{rev}$  is determined by the Gibbs free energy change of the electrochemical process as:

$$U_{rev} = -\frac{\Delta G}{2F} \quad (4.122)$$

It is a function of temperature, which can be expressed by an empirical equation as:

$$U_{rev} = U_{rev}^0 - k_{rev}(T - 25) \quad (4.123)$$

where  $U_{rev}^0$  = reversible cell voltage at standard condition (V);

$k_{rev}$  = empirical temperature coefficient of reversible voltage (V/°C)

For an electrolyzer stack consisting of  $n_c$  cells in series, the terminal voltage of the stack can be expressed as

$$U_{elec} = n_c U_{elec,cell} \quad (4.124)$$

where  $n_c$  = number of cells in series.

### Hydrogen Production Rate

According to Faraday' Law [4.17], [4.20], the ideal hydrogen production rate of an electrolyzer stack is given by:

$$\dot{n}_{H_2} = n_c \frac{I}{2F} \quad (4.125)$$

where  $\dot{n}_{H_2}$  = hydrogen production rate (mol/s)

However, the actual hydrogen rate is always lower than the above theoretical maximum value due to parasitic current losses. The actual hydrogen production rate can be obtained as

$$\dot{n}_{H_2} = \eta_F \frac{n_c I}{2F} \quad (4.126)$$

where  $\eta_F$  = current efficiency or Faraday efficiency.

The current efficiency ( $\eta_F$ ) will increase as the current density grows because the

percentage of the parasitic current over the total current decreases. A higher temperature will result in a lower resistance value, which leads to higher parasitic current and a lower current efficiency [4.75]. However, in high current density regions, the effect of temperature upon current efficiency is small and can be neglected [4.68]. Hence, in this study,  $\eta_F$  is considered as function of current density only. An empirical formula for  $\eta_F$  is given in [4.75] as:

$$\eta_F = \frac{(I/A)^2}{k_{f1} + (I/A)^2} k_{f2} \quad (4.127)$$

where  $k_{f1}, k_{f2}$  = parameters in current efficiency calculation.

### Thermal Model

The operating temperature of an electrolyzer stack affects its performance significantly [see (4.121)]. Therefore, it is necessary to have a thermal model for an electrolyzer stack. In this study, a lumped thermal model is developed based on the findings reported in [4.68] and [4.75].

$$C_{elec} \frac{dT}{dt} = \dot{Q}_{gen} - \dot{Q}_{loss} - \dot{Q}_{cool} \quad (4.128)$$

where  $T$  = overall electrolyzer temperature ( $^{\circ}\text{C}$ );

$C_{elec}$  = overall heat capacity of the electrolyzer stack ( $\text{J}/^{\circ}\text{C}$ ).

$\dot{Q}_{gen}$  is the heat power generated inside the electrolyzer stack. It can be written as:

$$\dot{Q}_{gen} = n_c (U_{elec,cell} - U_{th}) I \quad (4.129)$$

where  $U_{th}$  is the thermal voltage which is expressed as

$$U_{th} = -\frac{\Delta H}{2F} = -\left(\frac{\Delta G + T\Delta S}{2F}\right) = U_{rev} - \frac{T\Delta S}{2F} \quad (4.130)$$

$\dot{Q}_{loss}$  is the heat power loss. It can be determined by

$$\dot{Q}_{loss} = \frac{T - T_a}{R_{T,elec}} \quad (4.131)$$

where  $T_a$  = ambient temperature ( $^{\circ}\text{C}$ );

$R_{T,elec}$  = equivalent thermal resistance ( $^{\circ}\text{C}/\text{W}$ ).

$\dot{Q}_{cool}$ , the heat power loss due to cooling, can be written as

$$\dot{Q}_{cool} = C_{cm} (T_{cm,o} - T_{cm,i}) \quad (4.132)$$

where  $C_{cm}$  = overall heat capacity of the flowing cooling medium per second ( $\text{W}/^{\circ}\text{C}$ );

$T_{cm,o}$ ,  $T_{cm,i}$  = outlet and inlet temperature of the cooling medium ( $^{\circ}\text{C}$ ).

Water is used as the cooling medium for the eletrolyzer stack used in this study.  $T_{cm,o}$  can be estimated as [4.68]:

$$T_{cm,o} = T_{cm,i} + (T - T_{cm,i}) \left[ 1 - \exp\left(\frac{-k_{HX}}{C_{cm}}\right) \right] \quad (4.133)$$

where  $k_{HX}$  = effective heat exchange coefficient for the cooling process. It can be obtained by the following empirical equation [4.68], [4.75]:

$$k_{HX} = h_{cond} + h_{conv} \cdot I \quad (4.134)$$

where  $h_{cond}$  = coefficient related to conductive heat exchange ( $\text{W}/^{\circ}\text{C}$ );

$h_{conv}$  = coefficient related to convective heat exchange [ $\text{W}/(^{\circ}\text{C}\cdot\text{A})$ ];

### Electrolyzer Model Implementation in MATLAB/Simulink

Based on the mathematical equations discussed previously, a dynamic model for an electrolyzer stack consisting of 40 cells in series (50 kW stack) has been developed in MATLAB/Simulink. Figure 4.60 shows the block diagram of the electrolyzer model. The input quantities are the applied DC voltage  $U_{elec}$ , ambient temperature  $T_a$ , inlet temperature of the cooling water  $T_{cm,i}$ , and the cooling water flow rate  $n_{cm}$ . The two output quantities are the hydrogen production rate  $\dot{n}_{H_2}$  and the stack temperature  $T$ . The  $U$ - $I$  characteristic block [(4.121) - (4.124)] calculates the electrolyzer current and the electrolyzer temperature is estimated by the thermal model block (4.128-4.134). Based on the calculated electrolyzer current  $I$ , the current efficiency block (4.126-4.127) gives the hydrogen production rate. The model parameters are given in Table 4.8, which is based on the values reported in [4.68] and [4.75].

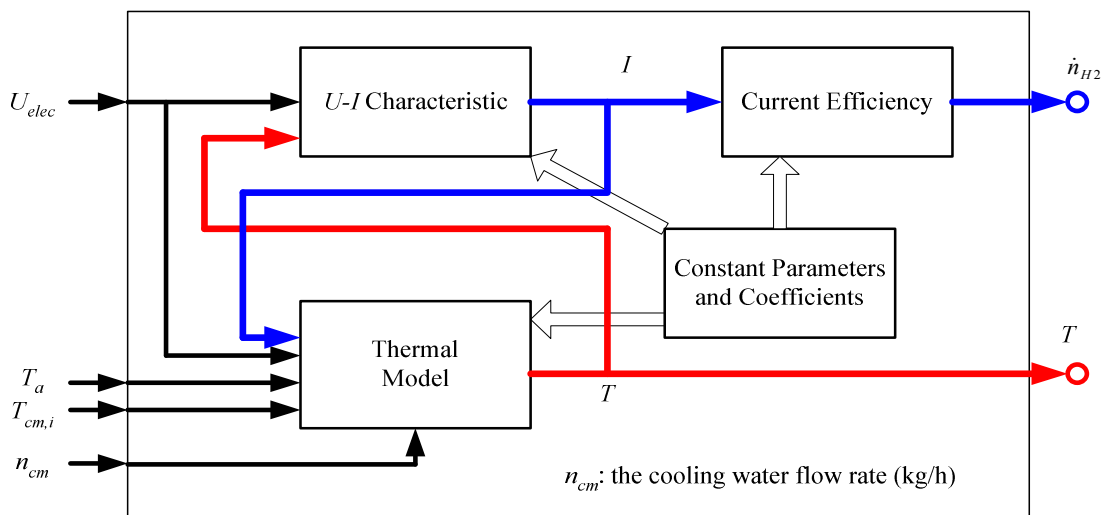


Figure 4.60. Block diagram of the electrolyzer model built in MATLAB/Simulink.

TABLE 4.8. THE ELECTROLYZER MODEL PARAMETERS

$r_1$	$8.05 \times 10^{-5} \Omega \cdot \text{m}^2$
$r_2$	$-2.5 \times 10^{-7} \Omega \cdot \text{m}^2 / ^\circ\text{C}$
$k_{elec}$	0.185 V
$t_1$	$-1.002 \text{ m}^2/\text{A}$
$t_2$	$8.424 \text{ m}^2 \cdot ^\circ\text{C}/\text{A}$
$n_c$	40
$k_{rev}$	$1.93 \times 10^{-3} \text{ V}/^\circ\text{C}$
$C_{elec}$	$6.252 \times 10^5 \text{ J}/^\circ\text{C}$
$R_{T,elec}$	$0.167 \text{ }^\circ\text{C}/\text{W}$
$A$	$0.25 \text{ m}^2$
$k_{f1}$	$2.5 \times 10^4 \text{ A}/\text{m}^2$
$k_{f2}$	0.96
$h_{cond}$	$7.0 \text{ W}/^\circ\text{C}$
$h_{conv}$	$0.02 \text{ W}/(^\circ\text{C} \cdot \text{A})$
$n_{cm}$	600 kg/h
$C_{cm}$ (Based on the value of $n_{cm}$ )	$697.67 \text{ W}/^\circ\text{C}$

### Electrolyzer Model Performance

The  $U$ - $I$  characteristics of the electrolyzer model under different cell temperatures are given in Figure 4.61. At the same current, the higher the operating temperature, the lower the terminal voltage is needed. Figure 4.62 shows the model temperature responses. The ambient temperature and the inlet temperature of the cooling water are set to 25 °C for the simulation study. The applied DC voltage starts at 70 V and steps up to 80 V at hour 5. The stack temperature increases from 25 °C to 25.37 °C and stays at that temperature as long as the applied voltage is 70 V. The temperature increases slowly (in approximately 5 hours) to about 30.2 °C when the output voltage jumps to 80 V.

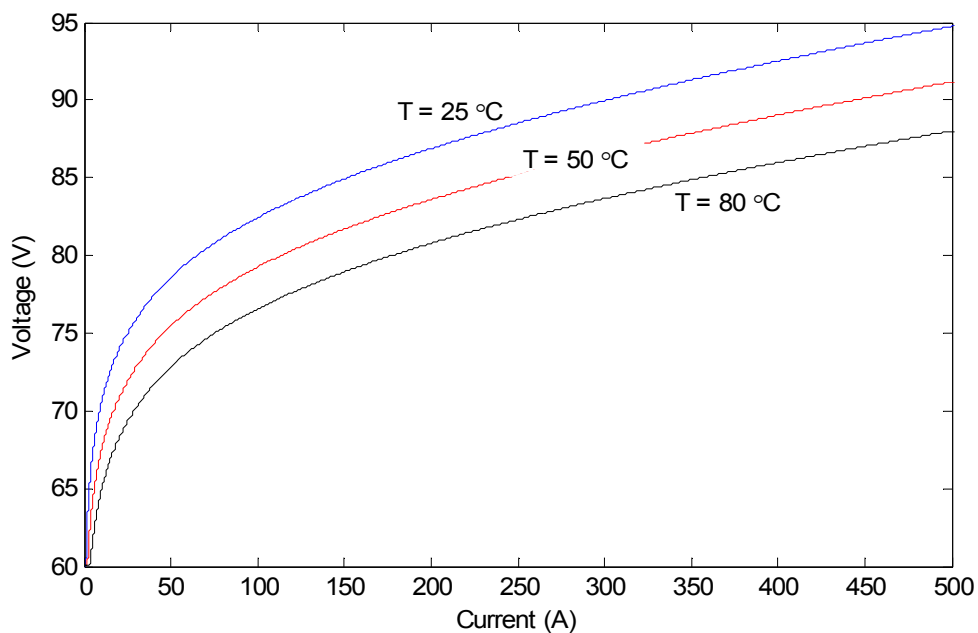


Figure 4.61.  $U$ - $I$  characteristics of the electrolyzer model under different temperatures.

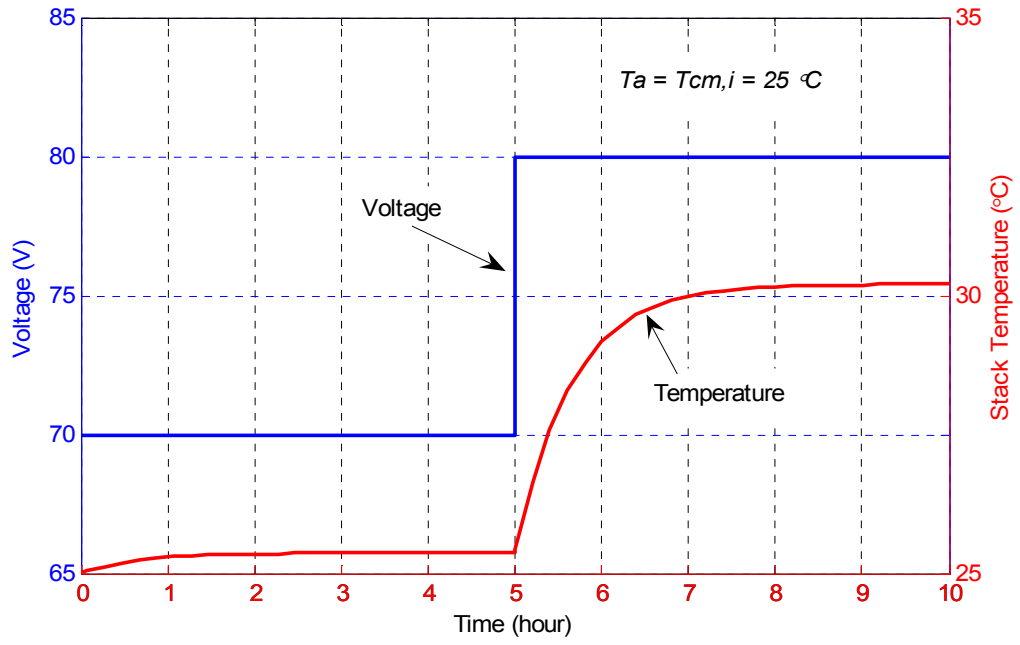


Figure 4.62. Temperature response of the model.

### Power Electronic Interfacing Circuits

Power electronic (PE) interfacing circuits, also called power conditioning circuits, are necessary for a hybrid energy system like the one proposed in Chapter 3 (see Figure 3.3). In this section, the electrical circuit diagrams, state-space models, and effective average-models (for long-time simulation studies) for the main PE interfacing circuits in the proposed hybrid energy system are discussed. They are AC/DC rectifiers, DC/DC converters, DC/AC inverters.

A detailed model for a PE device together with the control switching signals will dramatically decrease the simulation speed using MATLAB/Simulink. The detailed models for PE devices, such as those given in the SimPowerSystems block-set, are not suitable for long time simulation studies. Effective average-models for PE devices will be developed in this section, which help improve the simulation speed significantly and at the same time keep the desirable accuracy.

#### AC/DC Rectifiers

Circuit Topologies. Basically, there are two types of AC/DC rectifiers: controllable/uncontrollable rectifiers. Uncontrollable rectifiers are normally referred to diode (or diode bridge) rectifiers. Figure 4.63 shows a typical three-phase full diode bridge rectifier [4.41].

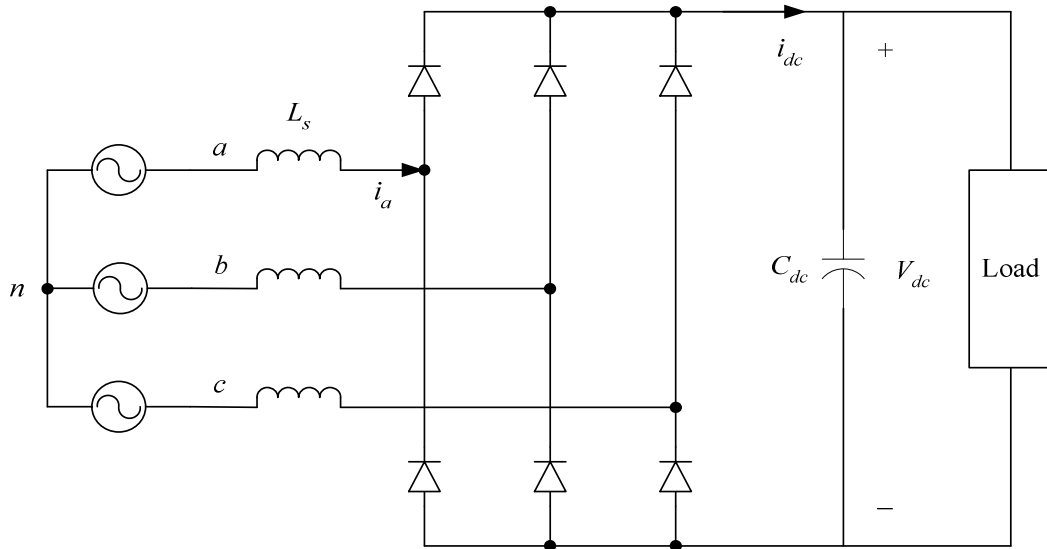


Figure 4.63. Three-phase full diode bridge rectifier.

If  $L_s = 0$  in the above figure, the average value of the output DC voltage  $V_{dc}$  is given as [4.41]:

$$V_{dc} = \frac{3}{\pi} \sqrt{2} V_{LL} \quad (4.135)$$

where  $V_{LL}$  is the AC source line-line RMS voltage.

The quality of the output DC voltage is fairly good. The voltage ripple is within  $\pm 5\%$ . However, the input AC current,  $i_a$  for example, is distorted. The AC side inductor  $L_s$  can be increased to reduce the current distortion. But this will cause extra voltage drop across the inductor. Another way is to use a Y-Y and a Y- $\Delta$  connection transformer to form a 12-diode bridge rectifier as shown in Figure 4.64. There is a  $30^\circ$  phase shift between the two transformer outputs, which reduces the transition period from  $60^\circ$  to  $30^\circ$  in one ( $360^\circ$ ) period. The average value of the DC output voltage now is:

$$V_{dc} = \frac{6}{\pi} \sqrt{2} V_{LL} \quad (4.136)$$

where  $V_{LL}$  is the line-line RMS voltage of the transformers' output.

The output DC voltage ripple now is reduced to within  $\pm 1.15\%$ , and the harmonics of the AC side current are much reduced. The total harmonic distortion (THD) of a 12-pulse rectifier is typically 12%, with the 11th and 13th harmonics dominant while the THD of a 6-pulse rectifier is about 30%, with the 5th and 7th harmonics dominant [4.41], [4.76].

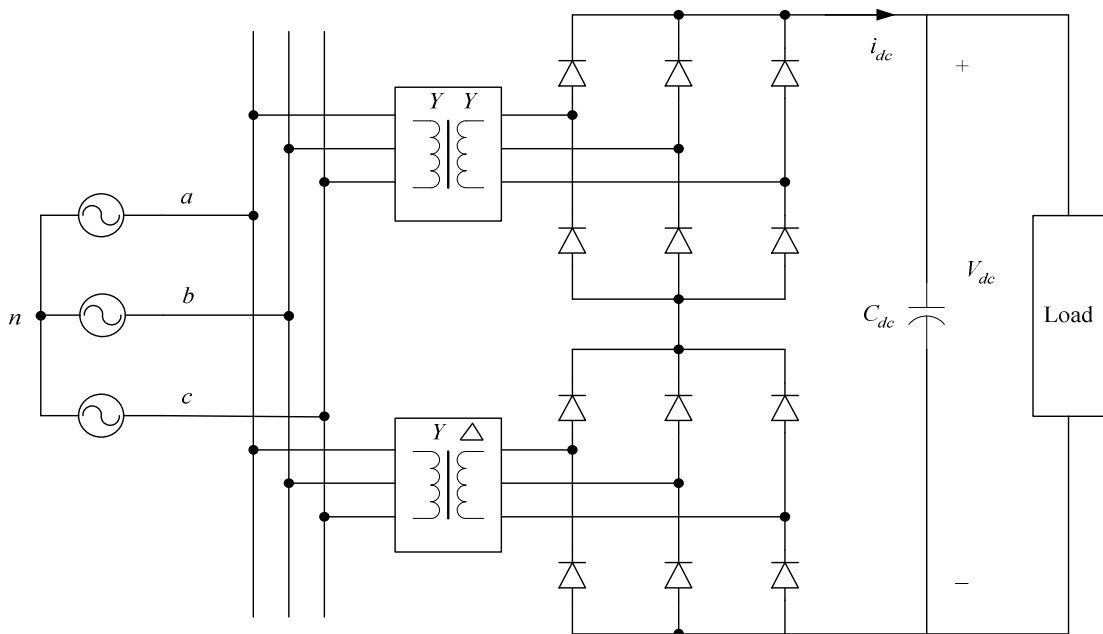


Figure 4.64. Three-phase 12-diode bridge rectifier with a Y-Y and a Y-Δ transformer.

Based on the same principle, a 24-diode rectifier can be built using zig-zag transformer group [4.76]. But it is not used commonly in low power rating applications.

Controllable rectifiers are normally firing angle controlled thyristor rectifiers and pulse width modulated (PWM) rectifiers. A PWM rectifier has the same circuit topology as a PWM inverter, which will be discussed later in this section. It is just the same circuit

working at a different operation modes: inverter mode vs. rectifier mode. Therefore, only the thyristor rectifier is discussed here.

A thyristor can work just like a diode with the exception that: it starts to conduct when it is not only forward biased but also its gate receives a positive current pulse; and it continues to be conducting as long as it is still forward biased. Thyristors can be used in Figure 4.63 and 4.74 to replace the diodes. Figure 4.65 shows a 6-pulse thyristor rectifier. The output DC voltage can be regulated by controlling the firing angles of thyristors. The firing angle  $\alpha$ , shown in Figure 4.65, is the angular delay between the time when a thyristor is forward biased and the time when a positive current pulse is applied to its gate. For a 6-pulse thyristor rectifier, the output DC voltage is [4.41]:

$$V_{dc} = \frac{3}{\pi} \sqrt{2} V_{LL} \cos(\alpha) \quad (4.137)$$

where  $\alpha$  = firing angle.

If  $\cos(\alpha)$  is taken as the control variable, it is noted from the above equation that the output voltage of a thyristor rectifier is proportional to the control input.

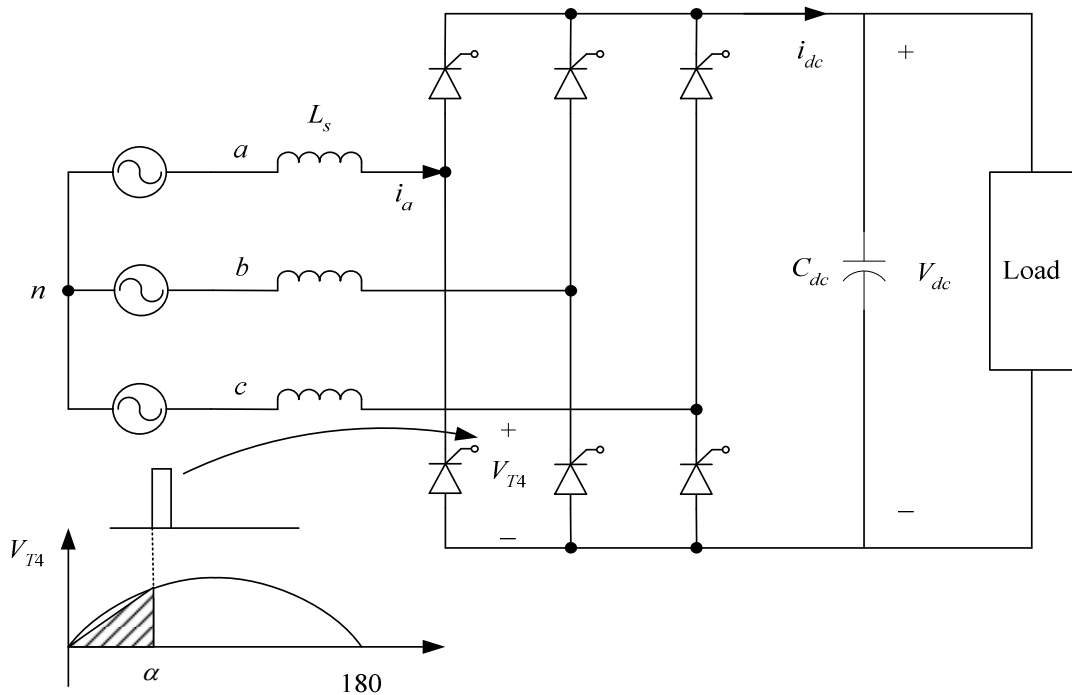


Figure 4.65. A 6-pulse thyristor rectifier.

Simplified Model for Controllable Rectifiers. Figure 4.66 shows the block diagram of the simplified ideal model for controllable three phase rectifiers. This model is developed for long time simulation studies. The “line-line voltage peak value” block calculates the peak value of the AC line-line voltage,  $\sqrt{2}V_{LL}$ . The input quantity  $g$ , which can be considered as  $\cos(\alpha)$ , is the control variable to regulate the output DC voltage. The output DC voltage is calculated based on (4.137). For 6-pulse rectifiers, gain  $k_{dc}$  is  $3/\pi$ . Then the signal  $E_{dc}$  is fed to control a controlled voltage source, which actually is the DC output of the model. The series resistor  $R_s$  is used to model the power and voltage losses within a real rectifier. The “P, Q Calculation” block calculates the amount of the real and reactive power consumed at the AC side based on the DC side real power and the input

quantity power angle  $\theta$ , shown in Figure 4.66. The “dynamic load” block is a built-in model in Simulink, which consumes the real and reactive power assigned by its P & Q inputs.

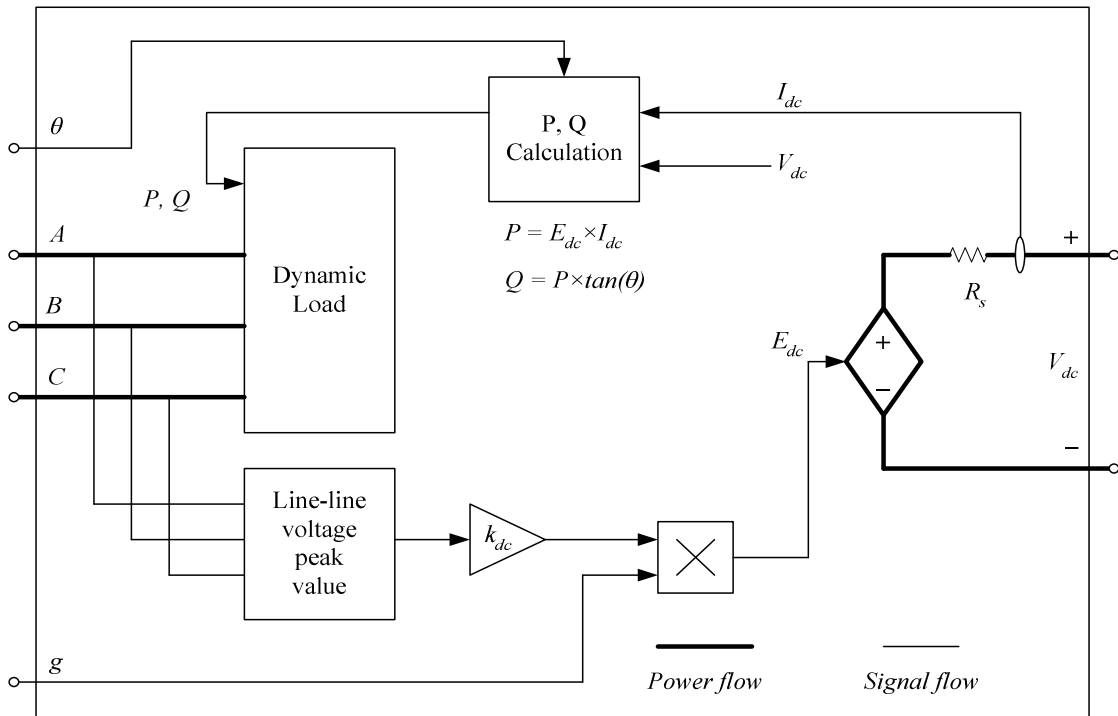


Figure 4.66. Block diagram of the simplified model for 3-phase controllable rectifiers.

Figures 4.67 and 4.68 compare the voltage and current responses of the simplified ideal rectifier model with the detailed rectifier models, a 6-pulse model and a 12-pulse model, with the same AC source and the same DC load. Figure 4.67 shows that the average output DC voltage of the ideal model is slightly higher than those of the detailed rectifier models. Figure 4.68 shows the AC side phase current of the different models. It is noted that the AC current is distorted for the 6-pulse rectifier model. However, the harmonic is much reduced for the 12-pulse rectifier model, and the response of this rectifier model is very close to that of the ideal rectifier model. The simplified ideal

controllable rectifier model shown in Figure 4.66 is used in the proposed hybrid energy system. It can improve the simulation speed and at the same time keep the desired accuracy.

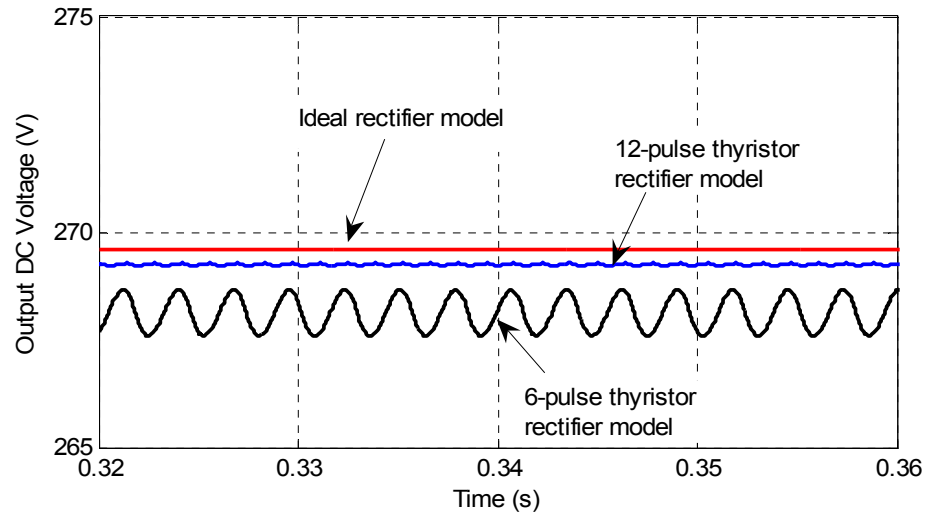


Figure 4.67. DC output voltages of the different rectifier models.

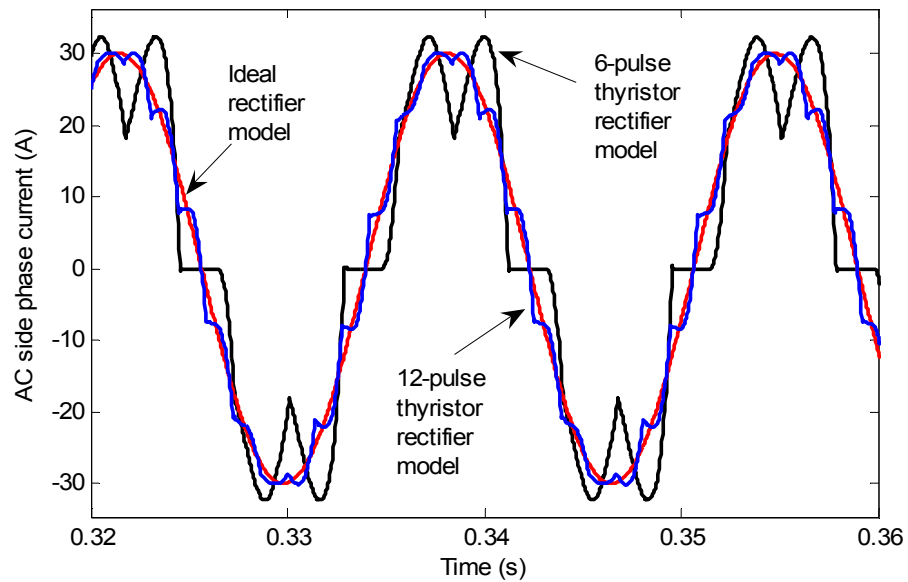


Figure 4.68. AC side phase current of the different rectifier models.

### DC/DC Converters

There are many types of DC/DC converters. In this section, only typical boost converters and buck converters are discussed.

Circuit Topologies. Figure 4.69 shows the circuit diagram of a boost DC/DC converter (inside the rectangle). The output voltage regulation feedback is also given in the figure. At steady-state, the average value of the output voltage is given as:

$$V_{dd\_out} = \frac{V_{dd\_in}}{(1-d)} \quad (4.138)$$

where  $d$  is the duty ratio of the switching pulse.

Since  $0 \leq d < 1$ , the output voltage is always higher than the input voltage<sup>5</sup>. That is why the circuit (in Figure 4.69) is called a boost DC/DC converter. The controller for the converter is to regulate the DC bus voltage within a desirable range. The output voltage is measured and compared with the reference value. The error signal is processed through the PWM controller, which can be a simple PI controller. The output of the controller is used to generate a PWM pulse with the right duty ratio so that the output voltage follows the reference value.

---

<sup>5</sup> When  $d=1$ , the input is short circuited and the circuit will not work. This situation should be avoided.  $d$  normally is less than 0.85 [4.76].

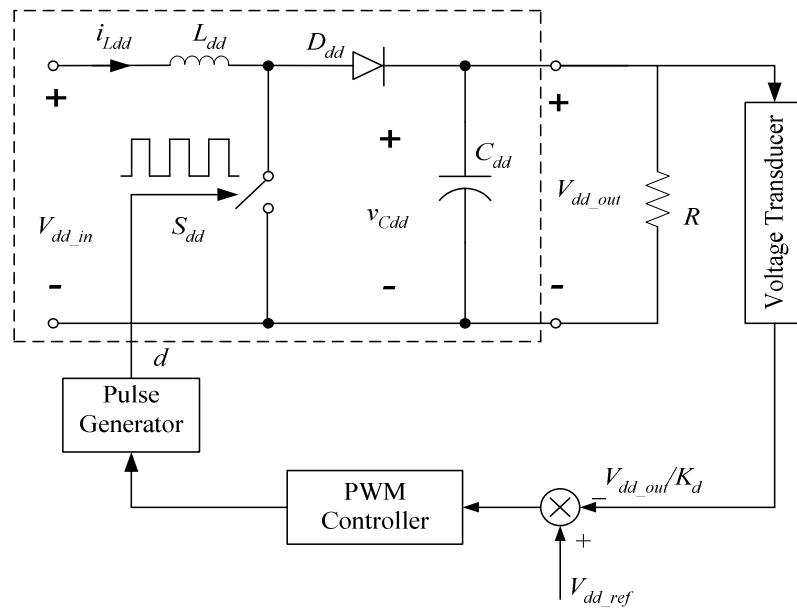


Figure 4.69. Boost DC/DC converter.

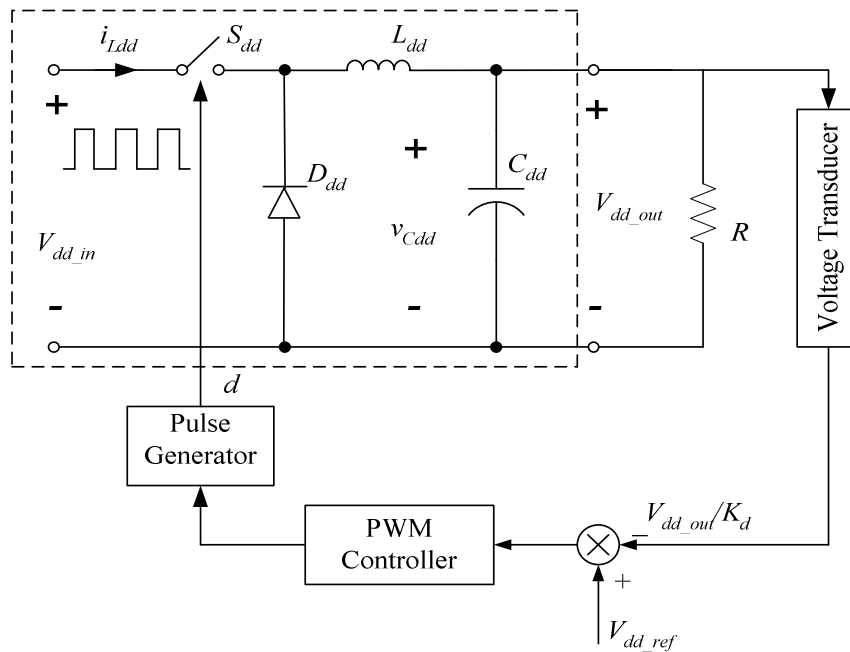


Figure 4.70. Buck DC/DC converter.

A buck DC/DC converter is shown in Figure 4.70. At steady-state, the average value of the output voltage is given as:

$$V_{dd\_out} = dV_{dd\_in} \quad (4.139)$$

Since  $0 \leq d \leq 1$ , the output voltage of a buck converter is always lower than its input voltage. In contrast to a boost converter, a buck converter is a step-down DC/DC converter. Its output voltage can also be regulated by controlling the duty ratio ( $d$ ) of the switching signals. The voltage regulation feedback loop is also shown in Figure 4.70.

State-space Models Based on the State-space Averaging Technique. In order to apply classical control analysis and design methods (such as Nyquist criterion, Bode plots and root loci analysis) in converter controls, state-space small-signal models for the above boost and buck converters are needed and are discussed in this section. These models are based on the state-space averaging technique developed by Middlebrook, Cúk and their colleagues [4.77].

*1) State-space model for boost DC/DC converters*

In Figure 4.69, take  $x_1 = i_{L_{dd}}$  and  $x_2 = v_{C_{dd}}$  as state variables. Let  $x = X + \tilde{x}$ ,  $d = D + \tilde{d}$ ,  $v_{dd\_in} = V_{dd\_in} + \tilde{v}_{dd\_in}$  and  $v_{dd\_out} = V_{dd\_out} + \tilde{v}_{dd\_out}$ . “ $\tilde{\sim}$ ” here is used to denote small perturbation signals, and state variable  $X$  denotes the system operating point.

When the switch  $S_{dd}$  is on and diode  $D_{dd}$  is off, the state-space representation of the main circuit can be written as

$$\begin{aligned} \dot{x} &= A_1 x + B_1 v_{dd\_in} \\ v_{dd\_out} &= C_1^T x \end{aligned} \quad (4.140)$$

where  $A_1 = \begin{bmatrix} 0 & 0 \\ 0 & -1/RC_{dd} \end{bmatrix}$ ,  $B_1 = \begin{bmatrix} 1/L_{dd} \\ 0 \end{bmatrix}$  and  $C_1^T = [0 \ 1]$ .

When switch  $S_{dd}$  is off and diode  $D_{dd}$  is on, the state-space equation of the circuit turns out to be:

$$\begin{aligned}\dot{x} &= A_2 x + B_2 v_{dd\_in} \\ v_{dd\_out} &= C_2^T x\end{aligned}\quad (4.141)$$

$$\text{where } A_2 = \begin{bmatrix} 0 & \frac{-1}{L_{dd}} \\ \frac{1}{C_{dd}} & \frac{-1}{RC_{dd}} \end{bmatrix}, \quad B_2 = \begin{bmatrix} 1/L_{dd} \\ 0 \end{bmatrix} \quad \text{and} \quad C_2^T = [0 \quad 1].$$

Therefore, the average state-space model of the main circuit at the operating point is

$$\begin{aligned}\dot{\tilde{x}} &= A \tilde{x} + B v_{dd\_in} \\ v_{dd\_out} &= C^T \tilde{x}\end{aligned}\quad (4.142)$$

$$\text{where } A = \begin{bmatrix} 0 & \frac{-(1-d)}{L_{dd}} \\ \frac{1-d}{C_{dd}} & \frac{-1}{RC_{dd}} \end{bmatrix}, \quad B = B_1 = B_2 = \begin{bmatrix} 1/L_{dd} \\ 0 \end{bmatrix} \quad \text{and} \quad C^T = C_1^T = C_2^T = [0 \quad 1].$$

Then the small signal model for the boost DC/DC converter can be obtained as:

$$\begin{aligned}\dot{\tilde{x}} &= A_d \tilde{x} + B_d \tilde{d} + B_v \tilde{v}_{dd\_in} \\ \tilde{v}_{dd\_out} &= C^T \tilde{x}\end{aligned}\quad (4.143)$$

$$\text{where } A_d = \begin{bmatrix} 0 & \frac{-(1-D)}{L_{dd}} \\ \frac{1-D}{C_{dd}} & \frac{-1}{RC_{dd}} \end{bmatrix}, \quad B_d = \begin{bmatrix} X_2/L_{dd} \\ -X_1/C_{dd} \end{bmatrix}, \quad B_v = \begin{bmatrix} 1/L_{dd} \\ 0 \end{bmatrix}, \quad X_1 \text{ and } X_2 \text{ are the steady}$$

state values of  $x_1$  and  $x_2$ , respectively.

Using Eq. (4.143) and only considering the perturbation of duty ratio  $\tilde{d}$  ( $\tilde{v}_{dd\_in}=0$ ),

the transfer function  $T_{vd}(s) = \frac{\tilde{v}_{dd\_out}(s)}{\tilde{d}(s)}$  is obtained as

$$T_{vd}(s) = C^T [SI - A_d]^{-1} B_d = \frac{1}{s(s + \frac{1}{RC_{dd}}) + \frac{(1-D)^2}{L_{dd}C_{dd}}} \left[ -\frac{X_1 s}{C_{dd}} + \frac{(1-D)X_2}{L_{dd}C_{dd}} \right] \quad (4.144)$$

## 2) State-Space model for buck DC/DC converters

Similar to the procedure discussed in the previous part, a small-signal state-space model of a buck converter can be obtained, which has been reported in [4.41] and [4.76] as:

$$\begin{aligned} \dot{x} &= A_b x + B_b d \\ v_{dd\_out} &= C_b^T x \end{aligned} \quad (4.145)$$

$$\text{where } x = \begin{bmatrix} i_{L_{dd}} \\ v_{C_{dd}} \end{bmatrix}, \quad A_b = \begin{bmatrix} 0 & -\frac{1}{L_{dd}} \\ \frac{1}{C_{dd}} & -\frac{1}{RC_{dd}} \end{bmatrix}, \quad B_b = \begin{bmatrix} \frac{V_{dd\_in}}{L_{dd}} \\ 0 \end{bmatrix}, \quad C_b^T = [0 \quad 1].$$

The small signal model can be obtained as:

$$\begin{aligned} \tilde{\dot{x}} &= A_b \tilde{x} + \tilde{B}_b \tilde{d} \\ \tilde{v}_{dd\_out} &= C_b^T \tilde{x} \end{aligned} \quad (4.146)$$

$$\text{where } \tilde{x} = \begin{bmatrix} \tilde{i}_{L_{dd}} \\ \tilde{v}_{C_{dd}} \end{bmatrix} \quad \text{and} \quad \tilde{B}_b = \begin{bmatrix} V_{dd\_in} / L_{dd} \\ 0 \end{bmatrix}.$$

Similarly, the transfer function for the output voltage over duty ratio can be obtained:

$$T_p(s) = \frac{\tilde{v}_{dd\_out}(s)}{\tilde{d}(s)} = \frac{V_{dd\_in}}{L_{dd}C_{dd} \left( s^2 + \frac{s}{RC_{dd}} + \frac{1}{L_{dd}C_{dd}} \right)} \quad (4.147)$$

Averaged Models for DC/DC Converters. Averaged models for boost and buck DC/DC converters suitable for long time simulation studies are given in this part. These models simulate the DC/DC converter transient behavior in large scale rather than the detailed cycle-to-cycle variations of values of voltages and currents. The models discussed here are based on the models reported in [4.76].

1) *Averaged model for boost DC/DC converters*

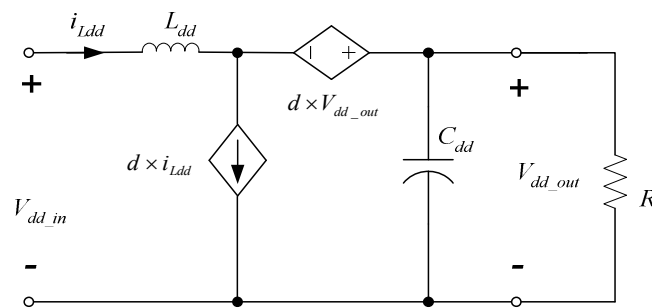


Figure 4.71. Averaged model for boost DC/DC converters.

Comparing the circuit diagram of boost converter in Figure 4.69 and its averaged model shown in Figure 4.71, we can see that the power electronic switch and diode are replaced by the combination of controlled current and voltage sources in the averaged model. This gives the same performance as the detailed circuit model at large time scale. Figures 4.72 and 4.73 show the simulation results of the averaged model and the detailed circuit model under a load change. It is noted from these two figures that the averaged model can simulate the converter behavior precisely at large time scale with reasonable accuracy.

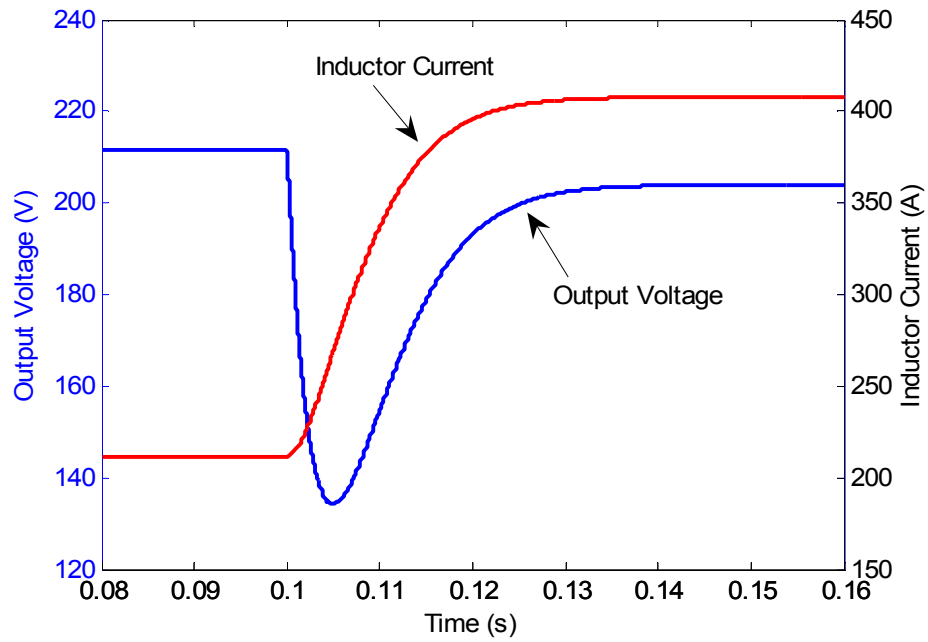


Figure 4.72. Simulation result of the averaged model for boost DC/DC converter.

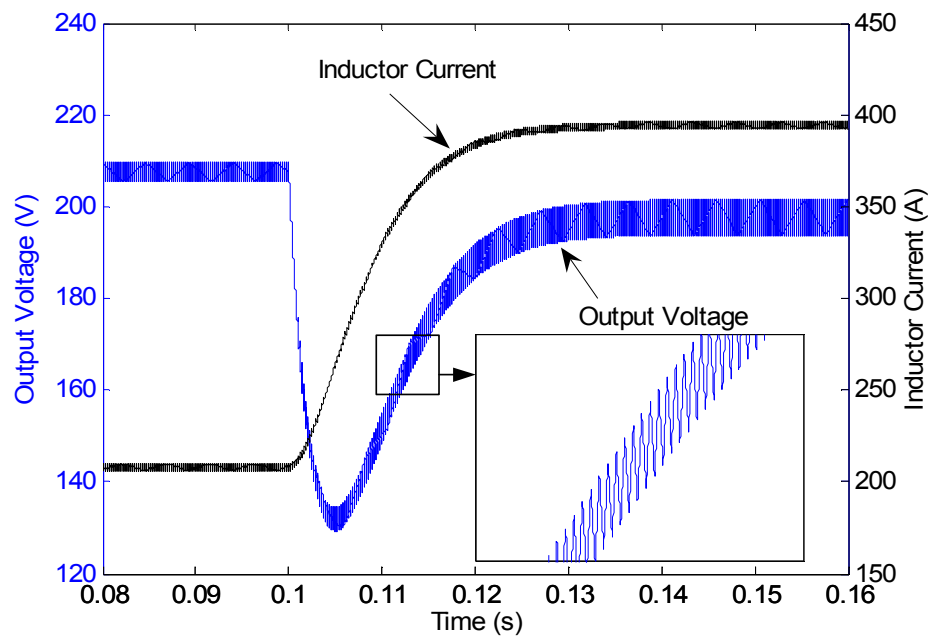


Figure 4.73. Simulation result of the detailed model for boost DC/DC converter.

## 2) Averaged model for buck DC/DC converters

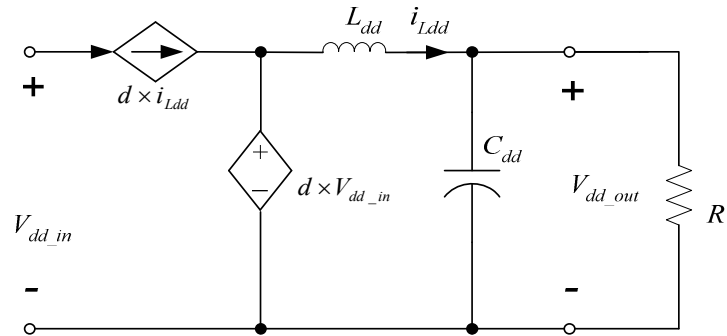


Figure 4.74 Averaged model for buck DC/DC converters.

Figure 4.74 shows the averaged model for buck converters. Simulation results shown in Figures 4.75 and 4.76 illustrate the effectiveness of the averaged model for buck DC/DC converters.

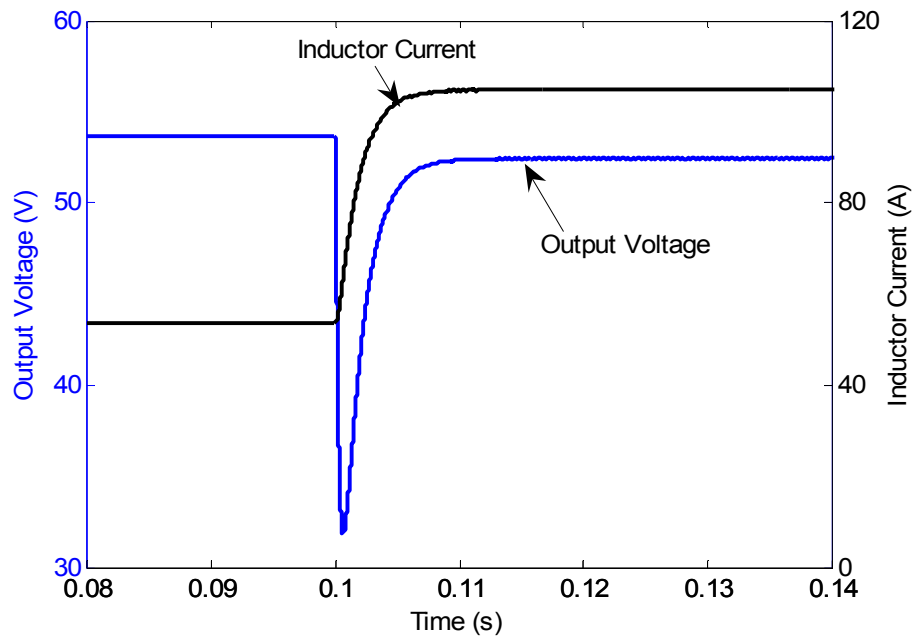


Figure 4.75. Simulation result of the averaged model for buck DC/DC converter.

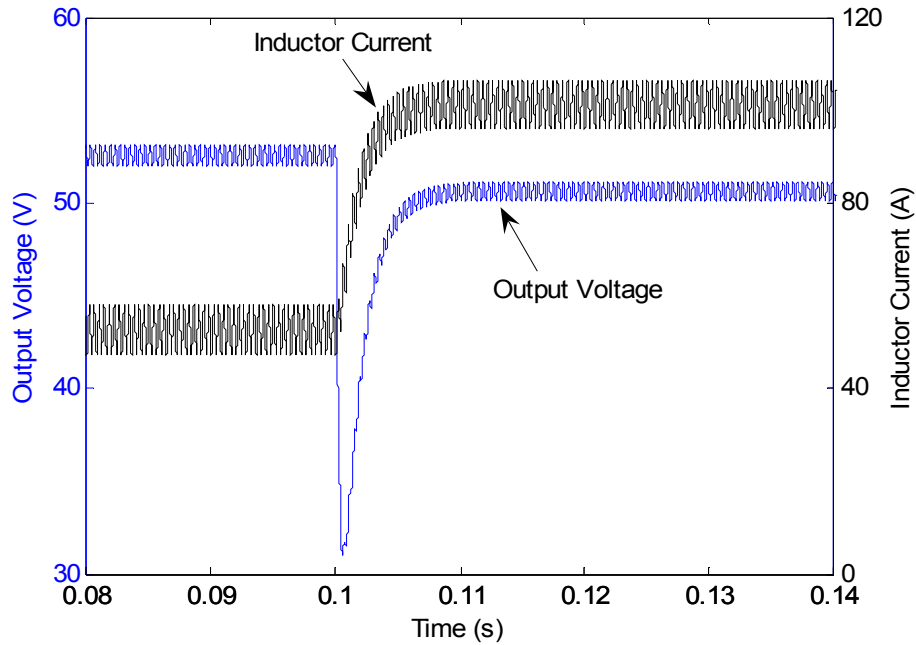


Figure 4.76. Simulation result of the detailed model for buck DC/DC converter.

### DC/AC Inverters

Circuit Topology. A 3-phase 6-switch DC/AC PWM voltage source inverter is used to convert the power from DC to AC. Figure 4.77 shows the main circuit of a 3-phase voltage source inverter (VSI), which is connected to the AC bus or utility grid through LC filters and coupling inductors.

State-Space Model. For deducing convenience, the neutral point  $N$  of the AC system is chosen as the common potential reference point. For the purpose of simplicity, only the inverter under balanced loads and without a neutral line (used in this dissertation) is discussed. Define the following switching functions:

$$d_1^* = \begin{cases} 1 & S_a^+ & ON \\ -1 & S_a^- & OFF \end{cases}$$

$$d_2^* = \begin{cases} 1 & S_b^+ & ON \\ -1 & S_b^- & OFF \end{cases} \quad (4.148)$$

$$d_3^* = \begin{cases} 1 & S_c^+ & ON \\ -1 & S_c^- & OFF \end{cases}$$

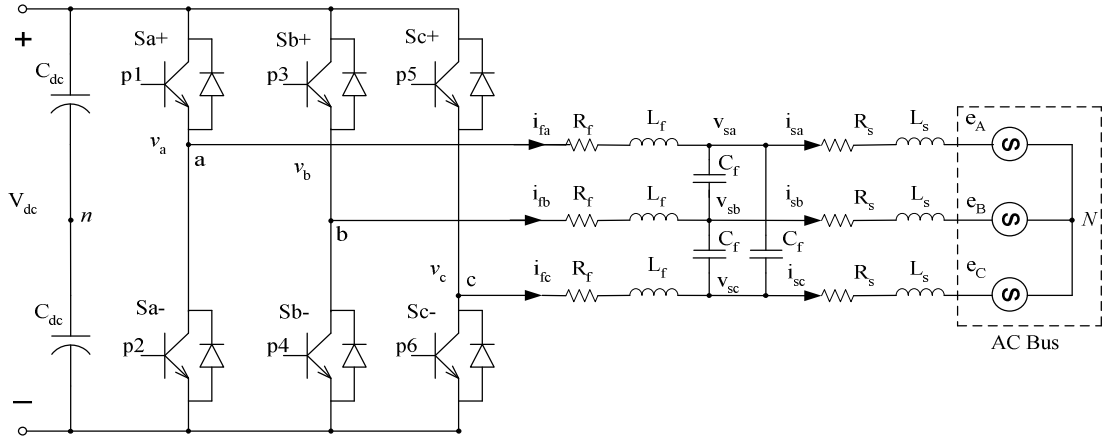


Figure 4.77. 3-phase DC/AC voltage source inverter.

$v_{an}$ ,  $v_{bn}$  and  $v_{cn}$  (the inverter output voltages between each phase and its imaginary neutral point  $n$ ) can be expressed as:

$$\begin{cases} v_{an} = \frac{d_1^*}{2} V_{dc} \\ v_{bn} = \frac{d_2^*}{2} V_{dc} \\ v_{cn} = \frac{d_3^*}{2} V_{dc} \end{cases} \quad (4.149)$$

where  $V_{dc}$  is the DC bus voltage.

The output phase potentials of the inverter,  $v_a$ ,  $v_b$  and  $v_c$ , can be obtained as:

$$\begin{cases} v_a = v_{an} + v_n \\ v_b = v_{bn} + v_n \\ v_c = v_{cn} + v_n \end{cases} \quad (4.150)$$

where  $v_n$  is the voltage between the point  $n$  and the common reference neutral point  $N$ .

Since  $i_{fa} + i_{fb} + i_{fc} = 0$  and  $e_A + e_B + e_C = 0$ ,  $v_n$  is obtained as [4.78]-[4.79]:

$$v_n = -\frac{V_{dc}}{6} \sum_{k=1}^3 d_k^* \quad (4.151)$$

For the circuit shown in Figure 4.77, the following dynamic equations can be obtained:

$$\begin{cases} v_a = L_f \frac{di_{fa}}{dt} + R_f i_{fa} + v_{sa} \\ v_b = L_f \frac{di_{fb}}{dt} + R_f i_{fb} + v_{sb} \\ v_c = L_f \frac{di_{fc}}{dt} + R_f i_{fc} + v_{sc} \end{cases} \quad (4.152)$$

$$\begin{cases} i_{fa} = i_{sa} + C_f \frac{d(v_{sa} - v_{sb})}{dt} + C_f \frac{d(v_{sa} - v_{sc})}{dt} \\ i_{fb} = i_{sb} + C_f \frac{d(v_{sb} - v_{sa})}{dt} + C_f \frac{d(v_{sb} - v_{sc})}{dt} \\ i_{fc} = i_{sc} + C_f \frac{d(v_{sc} - v_{sa})}{dt} + C_f \frac{d(v_{sc} - v_{sb})}{dt} \end{cases} \quad (4.153)$$

$$\begin{cases} R_s i_{sa} + L_s \frac{di_{sa}}{dt} = v_{sa} - e_A \\ R_s i_{sb} + L_s \frac{di_{sb}}{dt} = v_{sb} - e_B \\ R_s i_{sc} + L_s \frac{di_{sc}}{dt} = v_{sc} - e_C \end{cases} \quad (4.154)$$

Writing the above equations into the state-space form:

$$\dot{X}_{abc} = A_{abc} X_{abc} + B_{abc} U_{abc} \quad (4.155)$$

where  $X_{abc} = [i_{fa}, i_{fb}, i_{fc}, v_{sa}, v_{sb}, v_{sc}, i_{sa}, i_{sb}, i_{sc}]^T$ ,  $U_{abc} = [V_{dc}, e_A, e_B, e_C]^T$ ,

$$A_{abc} = \begin{bmatrix} -\frac{R_f}{L_f} & 0 & 0 & \frac{-1}{L_f} & 0 & 0 & 0 & 0 & 0 \\ 0 & -\frac{R_f}{L_f} & 0 & 0 & \frac{-1}{L_f} & 0 & 0 & 0 & 0 \\ 0 & 0 & -\frac{R_f}{L_f} & 0 & 0 & \frac{-1}{L_f} & 0 & 0 & 0 \\ \frac{1}{3C_f} & 0 & 0 & 0 & 0 & 0 & \frac{-1}{3C_f} & 0 & 0 \\ 0 & \frac{1}{3C_f} & 0 & 0 & 0 & 0 & 0 & \frac{-1}{3C_f} & 0 \\ 0 & 0 & \frac{1}{3C_f} & 0 & 0 & 0 & 0 & 0 & \frac{-1}{3C_f} \\ 0 & 0 & 0 & \frac{1}{L_s} & 0 & 0 & -\frac{R_s}{L_s} & 0 & 0 \\ 0 & 0 & 0 & 0 & \frac{1}{L_s} & 0 & 0 & -\frac{R_s}{L_s} & 0 \\ 0 & 0 & 0 & 0 & 0 & \frac{1}{L_s} & 0 & 0 & -\frac{R_s}{L_s} \end{bmatrix}$$

$$\text{and } B_{abc} = \begin{bmatrix} \left( \frac{d_1^*}{2} - \frac{1}{6} \sum_{k=1}^3 d_k^* \right) / L_f & 0 & 0 & 0 \\ \left( \frac{d_2^*}{2} - \frac{1}{6} \sum_{k=1}^3 d_k^* \right) / L_f & 0 & 0 & 0 \\ \left( \frac{d_3^*}{2} - \frac{1}{6} \sum_{k=1}^3 d_k^* \right) / L_f & 0 & 0 & 0 \\ 0 & 0 & 0 & 0 \\ 0 & 0 & 0 & 0 \\ 0 & -\frac{1}{L_s} & 0 & 0 \\ 0 & 0 & -\frac{1}{L_s} & 0 \\ 0 & 0 & 0 & -\frac{1}{L_s} \end{bmatrix}$$

*dq* Representation of the State-Space Model. The *dq* transformation transfers a stationary 3-coordinate (*abc*) system to a rotating 2-coordinate (*dq*) system. The *dq* signals can be used to achieve zero tracking error control [4.78]. Due to this merit, the *dq* transformation has been widely used in PWM converter and rotating machine control [4.62], [4.78], [4.80].

Using the *dq* transformation explained in [4.62] (see Appendix A), the system state-space equation given in (4.155) can be represented in the rotating *dq* frame as

$$\dot{X}_{dq} = A_{dq}X_{dq} + B_{dq}U_{dq} \quad (4.156)$$

where

$$X_{dq} = [i_{dd}, i_{dq}, v_{sd}, v_{sq}, i_{sd}, i_{sq}]^T, U_{dq} = [V_{dc}, e_d, e_q]^T$$

$$\begin{bmatrix} i_{dd} \\ i_{dq} \end{bmatrix} = T_{abc/dq} \begin{bmatrix} i_{da} \\ i_{db} \\ i_{dc} \end{bmatrix}, \begin{bmatrix} v_{sd} \\ v_{sq} \end{bmatrix} = T_{abc/dq} \begin{bmatrix} v_{sa} \\ v_{sb} \\ v_{sc} \end{bmatrix}, \text{ and } \begin{bmatrix} e_d \\ e_q \end{bmatrix} = T_{abc/dq} \begin{bmatrix} e_A \\ e_B \\ e_C \end{bmatrix}.$$

$$A_{dq} = \begin{bmatrix} -\frac{R_f}{L_f} & \omega & \frac{-1}{L_f} & 0 & 0 & 0 \\ -\omega & -\frac{R_f}{L_f} & 0 & \frac{-1}{L_f} & 0 & 0 \\ \frac{1}{3C_f} & 0 & 0 & \omega & \frac{-1}{3C_f} & 0 \\ 0 & \frac{1}{3C_f} & -\omega & 0 & 0 & \frac{-1}{3C_f} \\ 0 & 0 & \frac{1}{L_s} & 0 & -\frac{R_s}{L_s} & \omega \\ 0 & 0 & 0 & \frac{1}{L_s} & -\omega & -\frac{R_s}{L_s} \end{bmatrix}, B_{dq} = \begin{bmatrix} \frac{f_1(t, d_1^*, d_2^*, d_3^*)}{L_f} & 0 & 0 \\ \frac{f_2(t, d_1^*, d_2^*, d_3^*)}{L_f} & 0 & 0 \\ 0 & 0 & 0 \\ 0 & 0 & 0 \\ 0 & -1 & 0 \\ 0 & 0 & -1 \end{bmatrix}$$

$f_1$  and  $f_2$  are obtained as:

$$f_1(t, d_1^*, d_2^*, d_3^*) = \frac{1}{3} \left[ \begin{aligned} & \sin(\omega t) \left( d_1^* - \frac{1}{3} \sum_{k=1}^3 d_k^* \right) + \sin\left(\omega t - \frac{2\pi}{3}\right) \left( d_2^* - \frac{1}{3} \sum_{k=1}^3 d_k^* \right) \\ & + \sin\left(\omega t + \frac{2\pi}{3}\right) \left( d_3^* - \frac{1}{3} \sum_{k=1}^3 d_k^* \right) \end{aligned} \right]$$

$$f_2(t, d_1^*, d_2^*, d_3^*) = \frac{1}{3} \left[ \begin{aligned} & \cos(\omega t) \left( d_1^* - \frac{1}{3} \sum_{k=1}^3 d_k^* \right) + \cos\left(\omega t - \frac{2\pi}{3}\right) \left( d_2^* - \frac{1}{3} \sum_{k=1}^3 d_k^* \right) \\ & + \cos\left(\omega t + \frac{2\pi}{3}\right) \left( d_3^* - \frac{1}{3} \sum_{k=1}^3 d_k^* \right) \end{aligned} \right]$$

$T_{abc/dq}$  is the  $abc/dq$  transformation matrix. The methodology for developing the  $abc/dq$  transformation is explained in [4.62] (see Appendix A).

Ideal Model for Three-phase VSI. Figure 4.78 shows the ideal model for a three-phase VSI. It is not a detailed model with all the power electronic switches and switching signals; it is an idealized model used for long time simulation studies. The load current of the input DC voltage source ( $I_{dc}$ ) is determined by the power consumed at the AC side. The other three input quantities are the desired output AC frequency  $f$ , AC voltage amplitude index (similar to the modulation index in a real VSI control)  $m$ , and the initial phase of the three-phase AC output voltages  $\phi_0$ . The “*abc* signal formation” block gives the base signals for the three phases,  $v_a(t)$ ,  $v_b(t)$  and  $v_c(t)$ .

$$\begin{cases} v_a(t) = m \sin(2\pi ft + \phi_0) \\ v_b(t) = m \sin(2\pi ft + 2\pi/3 + \phi_0) \\ v_c(t) = m \sin(2\pi ft + 4\pi/3 + \phi_0) \end{cases} \quad (4.157)$$

The output voltage values,  $V_a(t)$ ,  $V_b(t)$  and  $V_c(t)$ , are calculated by multiplying the base signal values by the possible peak of the output AC, which is  $0.5V_{dc}$ . For example,  $V_a(t) = 0.5V_{dc} \times v_a(t)$ . Then  $V_a(t)$ ,  $V_b(t)$  and  $V_c(t)$  are used to control the three controlled voltage sources, which are the AC output voltages of the inverter model. The AC power is calculated through the “Power Calculation” block as

$$P_{ac} = I_a(t) \times V_a(t) + I_b(t) \times V_b(t) + I_c(t) \times V_c(t) \quad (4.158)$$

For the purpose of comparison, a 208 V three-phase VSI is simulated to supply 100 kW to a load both by the ideal model shown in Figure 4.78 and the switched model given in Figure 4.77. Figure 4.79 shows the output AC phase voltage of the two models. It is noted that though there are harmonics in voltage from the switched model, its output voltage waveform is very close to the output from the ideal model when a properly

designed filter is applied to the system. Figure 4.80 shows the output power to the load from the two models. We can see that the ideal model output is ideal, delivering a constant power of 100 kW. On the other hand, a more practical and detailed output power curve (with ripples) is obtained from the switched model. Nevertheless, the ideal model is capable of simulating a VSI with good accuracy at large time scale.

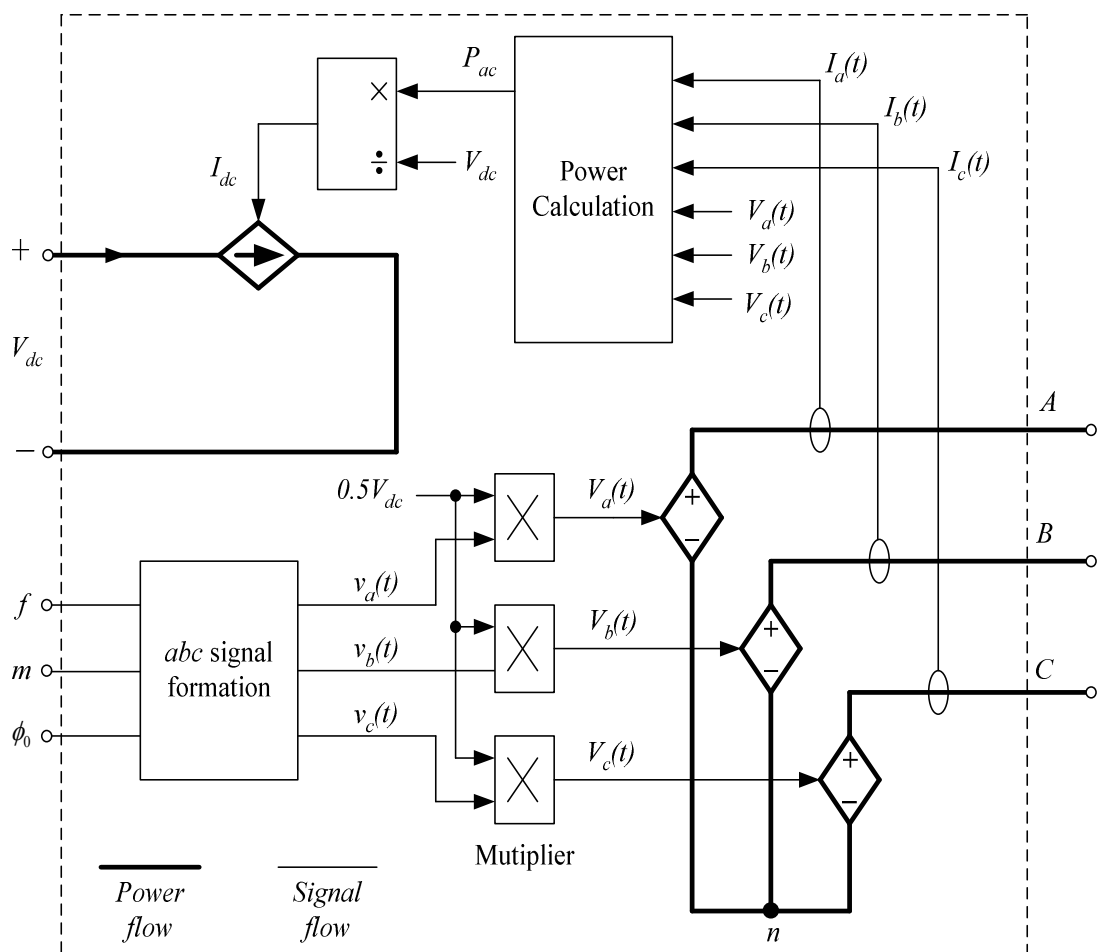


Figure 4.78. Ideal model for three-phase VSI.

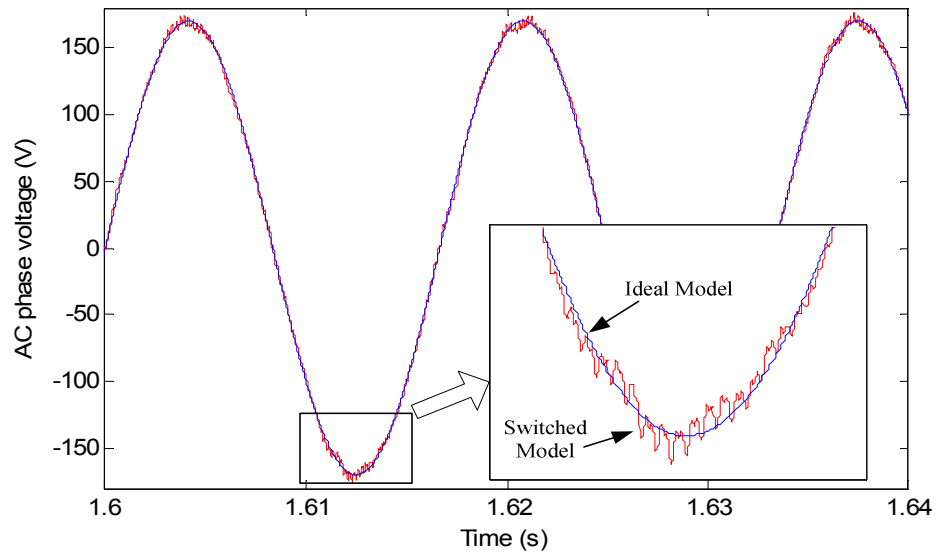


Figure 4.79. AC phase output voltages of the ideal VSI model and the switched VSI model.

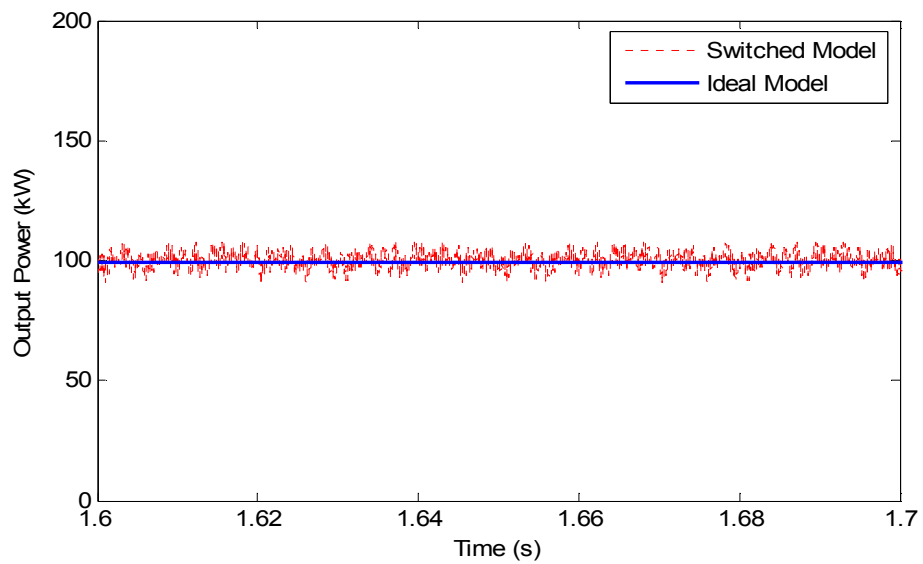
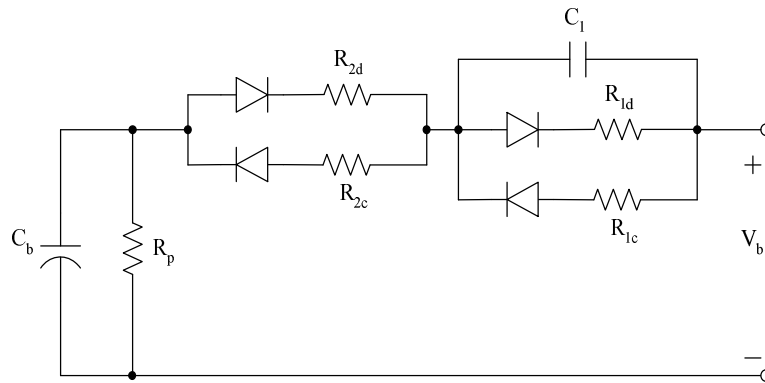


Figure 4.80. Output power of the ideal VSI model and the switched VSI model.

### Battery Model

A validated electrical circuit model for lead-acid batteries, shown in Figure 4.81, was reported in [4.81]. The diodes in the model are all ideal and just used to select different resistances for charging and discharging states. The model parameters (capacitances and resistances), defined in Figure 4.81, are functions of battery current, temperature and state of charge (SOC) [4.81], [4.82]. However, within the voltage range ( $100\pm 5\%$ ), there is not a big difference between the charge and discharge resistances [4.81]. For the purpose of analysis, these component values in the model are considered constant within the  $100\pm 5\%$  voltage range in this study. Then, the model shown in Figure 4.81 can be simplified into the circuit model given in Figure 4.82.



$C_b$  = battery capacitance;  $R_p$  = self-discharge resistance, or insulation resistance;

$R_{2c}$  = internal resistance for charge;  $R_{2d}$  = internal resistance for discharge;

$R_{1c}$  = overvoltage resistance for charge;  $R_{1d}$  = overvoltage resistance for discharge;

$C_1$  = overvoltage capacitance.

Figure 4.81. Equivalent circuit model for battery reported in [4.81].

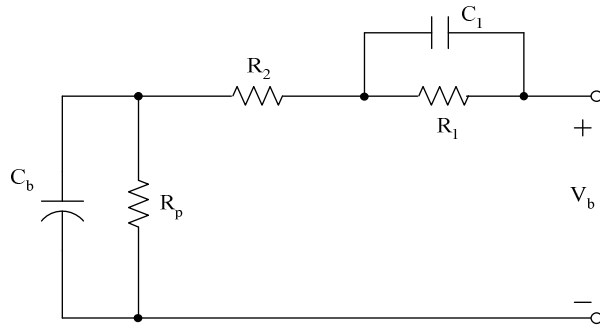


Figure 4.82. Simplified circuit model for lead-acid batteries

### Models for Accessories

#### Gas Compressor

A gas compressor can be modeled by considering the compression process as a two-stage polytropic compression which can be described as [4.22]:

$$P_i V_i^m = C \quad (4.159)$$

where  $P_i, V_i$  = the pressure and volume at stage  $i$  (1, 2);

$m$  = polytropic exponent

$C$  = constant

Based on the above equation, the power needed to compress a gas at pressure  $P_1$  to pressure  $P_2$  with the flow rate  $\dot{n}_{gas}$  can be obtained as:

$$P_{comp} = 2\dot{n}_{gas} \frac{mRT}{m-1} \left[ \left( \frac{P_2}{P_1} \right)^{\frac{m-1}{m}} - 1 \right] \frac{1}{\eta_{comp}} \quad (4.160)$$

where  $P_{comp}$  = power consumed (W);

$\dot{n}_{gas}$  = gas flow rate (mol/s);

$R$  = gas constant, 8.3144 J/(mol·K);

$T$  = gas temperature (K);

$P_2$  = exit pressure (Pa);

$P_x = \sqrt{P_1 P_2}$ , intermediate pressure (Pa);

$P_1$  = inlet pressure (Pa);

$\eta_{comp}$  = overall efficiency of the compressor.

### High Pressure H2 Storage Tank

For H<sub>2</sub> in the high pressure storage tank, shown in Figure 4.83, the ideal gas equation does not accurately describe the relation between  $P$ ,  $V$  and  $T$ ; a modified equation of state should be used. The Beattie-Bridgeman equation has been successful in fitting the measured values of pressure, volume and temperature in a high-pressure gas storage tank with good accuracy [4.22]. This modified state equation can be written as:

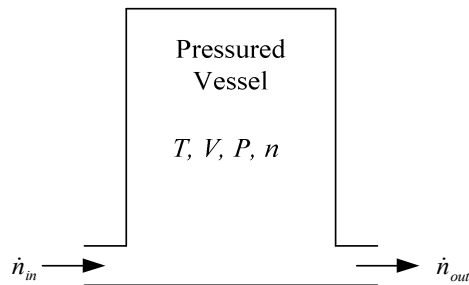


Figure 4.83. Pressured H<sub>2</sub> storage tank.

$$P = \frac{n^2 RT}{V^2} \left( 1 - \frac{cn}{VT^3} \right) \left[ \frac{V}{n} + B_0 \left( 1 - \frac{bn}{V} \right) \right] - \frac{A_0 \left( 1 - \frac{an}{V} \right) n^2}{V^2} \quad (4.161)$$

where  $P$  = pressure of hydrogen in the tank (atm);

$V$  = Volume of the tank (liter);

$T$  = temperature of H<sub>2</sub> (K)

$n$  = number of moles of H<sub>2</sub> in the tank;

$R$  = Gas constant, 0.08206 atm·liter/(mol·K);

$A_0, B_0, a, b, c$  are constants for certain type of gas. Their values for H<sub>2</sub> are given in Table 4.9.

The change of mole number of gas (H<sub>2</sub>) in the tank is governed by:

$$\frac{dn}{dt} = \dot{n}_{in} - \dot{n}_{out} \quad (4.162)$$

TABLE 4.9. CONSTANTS OF BEATTIE-BRIDGEMAN EQUATION OF STATE FOR H<sub>2</sub> [4.22]

$A_0$	0.1975 atm·liter <sup>2</sup> /mol <sup>2</sup>
$B_0$	0.02096 liter/mol
$a$	-0.00506 liter/mol
$b$	-0.04359 liter/mol
$c$	$0.0504 \times 10^4$ liter·K <sup>3</sup> /mol

### Gas Pressure Regulator

Figure 4.84 shows a schematic diagram of a commonly used gas pressure regulator [4.83]. Its function is to keep the output pressure  $P_o$  constant at a desired value ( $P_{ref}$ ) under changes of the gas flow rates  $q_o$ . The pressure regulation is achieved by the deformation of the diaphragm. Suppose there is a reduction in  $P_o$ , which will reduce the pressure against the bottom of the diaphragm. This causes the spring force to push downward to increase the valve opening in the direction axis  $x$ . Therefore, the valve flow

is increased and as a result the output pressure  $P_o$  is raised back toward the reference value. The system can be modeled by the following equations [4.83]:

$$q_i = (k_x x + k_c)(P_i - P_o) \quad (4.163)$$

where  $q_i$  = input flow rate (mol/s);

$k_x, k_c$  = constants used in calculating fluid resistance/admittance [mol/(Pa·s·m), mol/(Pa·s)].

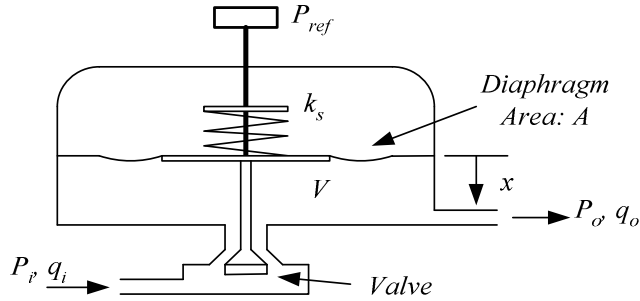


Figure 4.84. Gas pressure regulator.

The net flow entering the volume below the diaphragm is:

$$q_{net} = q_i - q_o = (k_x x + k_c)(P_i - P_o) - q_o \quad (4.164)$$

Normally, the diaphragm deformation is small, hence the volume  $V$  can be considered constant. The dynamic state equation can be written as:

$$q_{net} = C_g \dot{P}_o \quad (4.165)$$

where  $C_g = V/RT$ . The output pressure  $P_o$  can be expressed as:

$$P_o = P_{ref} - \frac{k_s x}{A} \quad (4.166)$$

where  $k_s$  = spring constant (N/m);

$A$  = diaphragm area ( $m^2$ ).

Figure 4.85 shows the model performance under output flow variations and the

variations in reference pressure. The model is adjusted to keep the output pressure at the reference value at the flow rate of 0.1 mol/s. The reference pressure steps up from 2 atm to 3 atm at 10 s. The figure shows that the output pressure follows the reference value very well. It is noted from the figure that the output pressure drops a little bit (from 2 atm to about 1.98 atm) when the output flow rate jumps up to 0.2 mol/s at 2 s. The output pressure comes back to its preset value (2 atm) when the output flow rate drops back to 0.1 mol/s at 6 s.

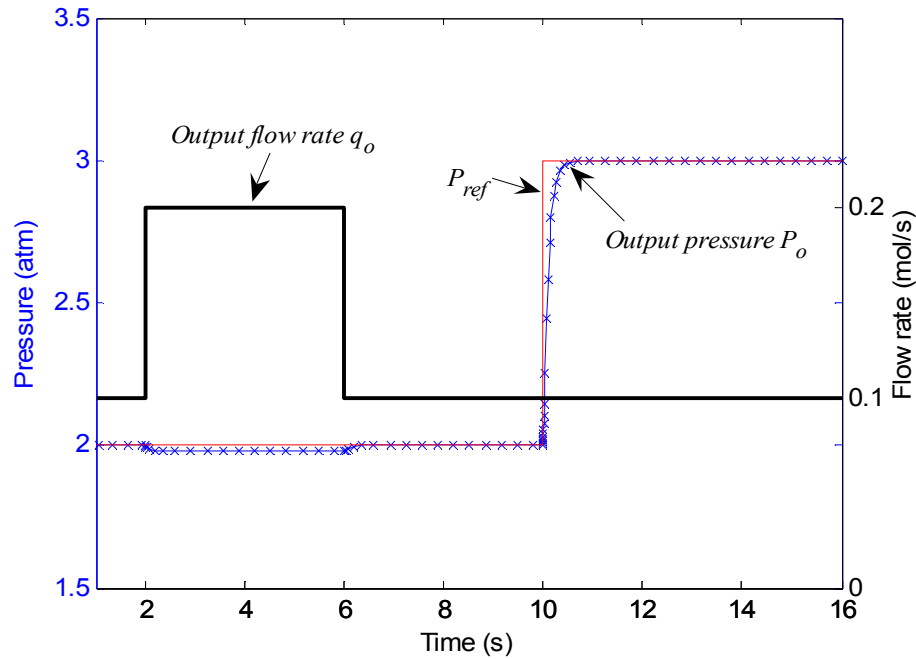


Figure 4.85. Performance of the model for gas pressure regulators.

### Summary

In this chapter, the model development for the components of the proposed hybrid alternative energy system is discussed. These components are: fuel cells (PEMFCs and SOFCs), variable speed wind energy conversion unit, solar power generation unit, electrolyzers, power electronic interfacing devices, battery bank and accessories including gas compressor, high-pressure H<sub>2</sub> storage tank and gas pressure regulator. Performance evaluation of these models is also discussed in this chapter. The models will be used in Chapters 5 and 6 to investigate grid-connected and stand-alone fuel cell power generation systems, and in Chapter 7 for the study of hybrid energy systems.

REFERENCES

- [4.1] J. C. Amphlett, R. M. Baumert, R. F. Mann, B. A. Peppley and P. R. Roberge, "Performance Modeling of the Ballard Mark IV Solid Polymer Electrolyte Fuel Cell, I. Mechanistic Model Development," *Journal of the Electrochemical Society*, Vol. 142, No. 1, pp. 1-8, Jan. 1995.
- [4.2] J. C. Amphlett, R. M. Baumert, R. F. Mann, B. A. Peppley and P. R. Roberge, "Performance Modeling of the Ballard Mark IV Solid Polymer Electrolyte Fuel Cell, II. Empirical Model Development," *Journal of the Electrochemical Society*, Vol. 142, No. 1, pp. 9-15, Jan. 1995.
- [4.3] R. Cownden, M. Nahon, M. A. Rosen, "Modeling and Analysis of a Solid Polymer Fuel Cell System for Transportation Applications," *International Journal of Hydrogen Energy*, Vol. 26, No. 6, pp. 615-623, June 2001.
- [4.4] Charles E. Chamberlin, "Modeling of Proton Exchange Membrane Fuel Cell Performance with an Empirical Equation," *Journal of the Electrochemical Society*, Vol. 142, No. 8, pp. 2670-2674, August 1995.
- [4.5] Andrew Rowe, Xianguo Li, "Mathematical Modeling of Proton Exchange Membrane Fuel Cells," *Journal of Power Sources*, Vol. 102, No. 1-2, pp.82-96, Dec. 2001.
- [4.6] D. Bevers, M. Wöhr, "Simulation of a Polymer Electrolyte Fuel Cell Electrode," *Journal of Applied Electrochemistry*, Vol.27, No. 11, pp. 1254-1264, Nov. 1997.
- [4.7] G. Maggio, V. Recupero, L. Pino, "Modeling Polymer Electrolyte Fuel Cells: An Innovative Approach," *Journal of Power Sources*, Vol. 101, No. 2, pp.275-286, Oct. 2001.
- [4.8] J. C. Amphlett, R. F. Mann, B. A. Peppley, P. R. Roberge and A. Rodrigues, "A Model Predicting Transient Responses of Proton Exchange Membrane Fuel Cells," *Journal of Power Sources*, Vol. 61, No. 1-2, pp. 183-188, July-Aug. 1996.
- [4.9] J. Hamelin, K. Agbossou, A. Laperrière, F. Laurencelle and T. K. Bose, "Dynamic Behavior of a PEM Fuel Cell Stack for Stationary Applications," *International Journal of Hydrogen Energy*, Vol. 26, No. 6, pp. 625-629, June 2001.
- [4.10] M. Wöhr, K. Bolwin, W. Schnurnberger, M. Fischer, W. Neubrand and G. Eigenberger, "Dynamic Modeling and Simulation of a Polymer Membrane Fuel Cell Including Mass Transport Limitation," *International Journal of Hydrogen Energy*, Vol. 23, No. 3, pp. 213-218, March 1998.

- [4.11] Hubertus P.L.H. van Bussel, Frans G.H. Koene and Ronald K.A.M. Mallant, "Dynamic Model of Solid Polymer Fuel Cell Water Management," *Journal of Power Sources*, Vol. 71, No. 1-2, pp. 218-222, March 1998.
- [4.12] M. Wang, M. H. Nehrir, "Fuel Cell Modeling and Fuzzy Logic-Based Voltage Control," *International Journal of Renewable Energy Engineering*, Vol. 3, No. 2, August 2001.
- [4.13] Michael D. Lukas, Kwang Y. Lee, Hossein Ghezeli-Ayagh, "Performance Implications of Rapid Load Changes in Carbonate Fuel Cell Systems," *Proceedings*, 2001 IEEE Power Engineering Society Winter Meeting, Vol. 3, pp. 979-984, 2001.
- [4.14] Robert Lasseter, "Dynamic Models for Micro-turbines and Fuel Cells," *Proceedings*, 2001 IEEE Power Engineering Society Summer Meeting, Vol. 2, pp. 761-766, 2001.
- [4.15] Padmanabhan Srinivasan, Ali Feliachi, John Ed Sneckenberger, "Proton Exchange Membrane Fuel Cell Dynamic Model for Distributed Generation Control Purposes," *Proceedings*, 34th North American Power Symposium, pp. 393-398, Oct 2002, Tempe, Arizona.
- [4.16] Pariz Famouri and Randall S. Gemmen, "Electrochemical Circuit Model of a PEM Fuel Cell," *Proceedings*, 2003 IEEE Power Engineering Society Summer Meeting, 0-7803-7990-X/03, July 2003, Toronto, Canada.
- [4.17] James Larminie and Andrew Dicks, *Fuel Cell Systems Explained*, John Wiley & Sons, Ltd., 2001.
- [4.18] *Fuel Cell Handbook (Sixth Edition)*, EG&G Services, Inc., Science Applications International Corporation, DOE, Office of Fossil Energy, National Energy Technology Lab, Nov. 2002.
- [4.19] J.A. Smith, M.H. Nehrir, V. Gerez and S.R. Shaw, "A Broad Look at the Workings, Types, and Applications of Fuel Cells," *Proceedings*, 2002 IEEE Power Engineering Society Summer Meeting, Vol. 1, pp. 70-75, July 2002, Chicago IL.
- [4.20] G. Kortum, *Treatise on Electrochemistry (2nd Edition)*, Elsevier Publishing Company, 1965.
- [4.21] A. Schneuwly, M. Bärtschi, V. Hermann, G. Sartorelli, R. Gallay and R. Koetz, "BOOSTCAP Double-Layer Capacitors for Peak Power Automotive Applications," *Proceedings*, the Second International ADVANCED AUTOMOTIVE BATTERY Conference (AABC), Las Vegas, Nevada, February 2002.

- [4.22] George N. Hatsopoulos and Joseph H. Keenan, *Principles of General Thermodynamics*, John Wiley & Sons, Inc., 1965.
- [4.23] Thomas G. Burke and David A. Schiller, "Using PSPICE for Electrical Heat Analysis," *IEEE Potentials*, Vol. 22, No. 2, pp. 35-38, April/May 2003.
- [4.24] *PSpice*<sup>®</sup>, includes *PSpice A/D*, *PSpice A/D Basics*, and *Pspice, Reference Guide*, Cadence Design Systems, Inc. Release 9.2.3.
- [4.25] *SR-12 Modular PEM Generator™ Operator's Manual*, Avista Labs, July 2000.
- [4.26] M.T. Iqbal, "Simulation of a Small Wind Fuel Cell Hybrid Energy System," *Renewable Energy*, Vol. 28, No. 4, pp. 511-522, April 2003.
- [4.27] S.C. Singhal, "Solid oxide fuel cells for stationary, mobile and military applications," *Solid State Ionics*, Vol. 152-153, pp.405-410, 2002.
- [4.28] S.C. Singhal, "Advances in tubular solid oxide fuel cell technology," *Solid State Ionics*, Vol. 135, pp.305-313, 2000.
- [4.29] O. Yamamoto, "Solid oxide fuel cells: fundamental aspects and prospects," *Electrochimica Acta*, Vol. 45, No. (15-16), pp. 2423-2435, 2000.
- [4.30] K. Eguchi, H. Kojo, T. Takeguchi, R. Kikuchi and K. Sasaki, "Fuel flexibility in power generation by solid oxide fuel cells," *Solid State Ionics*, No. 152-153: pp. 411-16, Dec. 2002.
- [4.31] S.H. Chan, K.A. Khor and Z.T. Xia, "A complete polarization model of a solid oxide fuel cell and its sensitivity to the change of cell component thickness," *Journal of Power Sources*, Vol. 93, No. (1-2), pp. 130-140, Feb 2001.
- [4.32] P. Aguiar, D. Chadwick and L. Kershenbaum, "Modeling of an indirect internal reforming solid oxide fuel cell," *Chemical Engineering Science*, Vol. 57, pp.1665-1677, 2002.
- [4.33] P. Costamagna and K. Honegger, "Modeling of solid oxide heat exchanger integrated stacks and simulation at high fuel utilization," *Journal of the Electrochemical Society*, Vol. 145, No. 11, pp. 3995-4007, Nov. 1998.
- [4.34] J. Padullés, G.W. Ault, and J. R. McDonald, "An integrated SOFC plant dynamic model for power system simulation," *J. Power Sources*, pp.495-500, 2000.
- [4.35] D.J. Hall and R.G. Colclaser, "Transient Modeling and Simulation of a Tubular Solid Oxide Fuel Cell," *IEEE Transactions on Energy Conversion*, Vol. 14, No.3, pp. 749-753, 1999.

- [4.36] R.S. Gemmen, "Analysis for the effect of inverter ripple current on fuel cell operating condition," *Transactions of the ASME - Journal of Fluids Engineering*, Vol. 125, No. 3, pp.576-585, May 2003.
- [4.37] K. Acharya, S.K. Mazumder, R.K. Burra, R. Williams, C. Haynes, *Proceeding, 38th IAS Annual Meeting (IEEE Industry Applications Society)*, Vol. 3, pp. 2026-2032, 2003.
- [4.38] S. H. Chan, C.F. Low, O.L. Ding, "Energy and exergy analysis of simple solid-oxide fuel-cell power systems," *Journal of Power Sources*, Vol. 103, No.2, pp. 188-200, Jan. 2002.
- [4.39] S. Nagata, A. Momma, T. Kato and Y. Kasuga, "Numerical analysis of output characteristics of tubular SOFC with internal reformer," *Journal of Power Sources*, Vol. 101, pp.60-71, 2001.
- [4.40] D. J. Hall, *Transient Modeling and Simulation of a Solid Oxide Fuel Cell*, Ph.D. Dissertation, School of Engineering, University of Pittsburg, Nov. 1997.
- [4.41] N. Mohan, T. M. Undeland and W. P. Robbins, *Power Electronics – Converters, Applications, and Design*, John Wiley & Sons , Inc., 2003.
- [4.42] S. C. Singhal, "Recent progress in tubular solid oxide fuel cell technology," *Proceedings, the Fifth International Symposium on SOFC (Electrochem. Soc.)*, pp. 37-50, 1997.
- [4.43] E. Achenbach, "Response of a solid oxide fuel cell to load change," *Journal of Power Sources*, Vol. 57, No. (1-2), pp. 105-109, 1995.
- [4.44] C. Wang, M.H. Nehrir, and S.R. Shaw, "Dynamic Models and Model Validation for PEM Fuel Cells Using Electrical Circuits," *IEEE Transactions on Energy Conversion*, Vol. 20, No. 2, pp.442-451, June 2005.
- [4.45] Rajib Datta and V. T. Ranganathan, "Variable-Speed Wind Power Generation Using Doubly Fed Wound Rotor Induction Machine – A Comparison with Alternative Schemes," *IEEE Transactions on Energy Conversions*, vol. 17, no. 3, pp. 414-420, Sept. 2002.
- [4.46] C. F. Wagner, "Self-excitation of induction motors," *Trans. Amer. Inst. Elect. Eng*, vol. 58, pp. 47-51, Feb. 1939.
- [4.47] E. D. Basset and F. M. Potter, "Capacitive excitation of induction generators," *Trans. Amer. Inst. Elect. Eng*, vol. 54, no. 5, pp. 540-545, May 1935.

- [4.48] J. M. Elder, J. T. Boys and J. L. Woodward, "Self-excited induction machine as a small low-cost generator," in *Proc. Inst. Elect. Eng.*, pt. C, vol. 131, no. 2, pp. 33-41, Mar. 1984.
- [4.49] L. Ouazene and G. Mcpherson Jr, "Analysis of the isolated induction generator," *IEEE Trans. Power Apparatus and Systems*, vol. PAS-102, no. 8, pp.2793-2798, Aug. 1983.
- [4.50] C. Grantham, D. Sutanto and B. Mismail, "Steady-state and transient analysis of self-excited induction generators," in *Proc. Inst. Elect. Eng.*, pt. B, vol. 136, no. 2, pp. 61-68, Mar. 1989.
- [4.51] Dawit Seyoum, Colin Grantham and M. F. Rahman, "The dynamic characteristics of an isolated self-excited induction generator driven by a wind turbine," *IEEE Trans. Industry Applications*, vol.39, no. 4, pp.936-944, July/August 2003.
- [4.52] Eduard Muljadi and C. P. Butterfield, "Pitch-Controlled Variable Wind turbine Generation," *IEEE Transactions on Industry Applications* , vol. 37, no. 1, pp. 240-246, Jan/Feb 2001.
- [4.53] Siegfried Heier, *Grid Integration of Wind energy Conversion Systems*, John Wiley& Sons, 1998, ch. 1-2.
- [4.54] J. G. Slootweg, S.W.H. de Haan, H. Polinder and W.L. Kling, "General Model for Representing Variable Speed Wind Turbines in Power System Dynamics Simulations," *IEEE Transactions on Power Systems*, vol. 18, no. 1, pp. 144-151 , Feb. 2003.
- [4.55] Bimal K. Bose, *Modern Power Electronics and Ac Drives*, Pearson Education, 2003, ch. 2.
- [4.56] P. M. Anderson and Anjan Bose., " Stability Simulation of Wind Turbine systems," *IEEE Trans. on Power and Apparatus and Systems*, vol. PAS-102, no. 12, pp. 3791-3795, Dec. 1983.
- [4.57] MatLab/Simulink SimPowerSystems Documentation. Available: <http://www.mathworks.com>
- [4.58] M. H. Salama and P. G. Holmes, "Transient and steady-state load performance of stand alone self-excited induction generator," in *Proc. IEE-Elect. Power Applicat.*, vol. 143, no. 1, pp. 50-58, Jan. 1996.
- [4.59] S. S. Murthy, O. P. Malik and A. K. Tandon, "Analysis of self excited induction generators," in *Proc. Inst. Elect. Eng.*, pt. C, vol. 129, no. 6, pp. 260-265, Nov.1982.

- [4.60] N. H. Malik and A. H. Al-Bahrani, "Influence of the terminal capacitor on the performance characteristics of a self-excited induction generator," in *Proc. Inst. Elect. Eng.*, pt. C, vol. 137, no. 2, pp. 168-173, Mar. 1990.
- [4.61] T. F. Chan, "Capacitance requirements of self-excited induction generators," *IEEE Trans. Energy Conversion*, vol. 8, no. 2, pp. 304-311, June 1993.
- [4.62] Paul. C. Krause, Oleg Wasynczuk and Scott D. Sudhoff, *Analysis of Electric Machinery*, IEEE Press, 1994, ch. 3-4.
- [4.63] M. Godoy Simoes and Felix A. Farret., *Renewable Energy Systems-Design and Analysis with Induction Generators*, CRC Press, 2004, ch. 3-6.
- [4.64] J.G. Sloopweg, "Wind power: modeling and impact on power system dynamics," PhD dissertation, Dept. Elect. Eng., Delft University of Technology, Delft, Netherlands, 2003
- [4.65] A. K. Al Jabri and A.I. Alolah, "Capacitance requirements for isolated self-excited induction generator," *Proceedings, IEE*, pt. B, vol. 137, no. 3, pp. 154-159, May 1990.
- [4.66] S.R. Guda, "Modeling and power management of a hybrid wind-microturbine power generation system," MS thesis, Montana State University, 2005.
- [4.67] Ø. Ulleberg and S. O. MØRNER, "TRNSYS simulation models for solar-hydrogen systems," *Solar Energy*, Vol. 59, No. 4-6, pp. 271-279, 1997.
- [4.68] Øystein Ulleberg, *Stand-Alone Power Systems for the Future: Optimal Design, Operation & Control of Solar-Hydrogen Energy Systems*, Ph.D. Dissertation, Norwegian University of Science and Technology, Trondheim, 1998.
- [4.69] T.U. Townsend, *A Method for Estimating the Long-Term Performance of Direct-Coupled Photovoltaic Systems*, MS thesis, University Of Wisconsin – Madison, 1989.
- [4.70] M. R. Patel, *Wind and Solar Power Systems*, CRC Press LLC, 1999.
- [4.71] H. Dehbonei, *Power conditioning for distributed renewable energy generation*, Ph.D. Dissertation, Curtin University of Technology, Australia, 2003.
- [4.72] M.A.S. Masoum, H. Dehbonei and E.F. Fuchs, "Theoretical and experimental analyses of photovoltaic systems with voltage and current-based maximum power-point tracking," *IEEE Transactions on Energy Conversion*, Vol. 17, No. 4, pp. 514 – 522, Dec. 2002.

- [4.73] J.H.R. Enslin, M.S. Wolf, D.B. Snyman, and W. Swiegers, "Integrated Photovoltaic Maximum Power Point Tracking Converter," *IEEE Transactions On Industrial Electronics*, Vol. 44, No. 6, December 1997.
- [4.74] S. M. Alghuwainem, "Matching of a dc motor to a photovoltaic generator using a step-up converter with a current-locked loop," *IEEE Transactions on Energy Conversion*, vol. 9, pp. 192–198, Mar. 1994.
- [4.75] Ø. Ulleberg, "Modeling of advanced alkaline electrolyzers: a system simulation approach," *International Journal of Hydrogen Energy*, Vol. 28, pp. 21-33, 2003.
- [4.76] D.W. Hart, *Introduction to Power Electronics*, Prentice Hall, 1997.
- [4.77] R.D. Middlebrook, "Small-signal modeling of pulse-width modulated switched-mode power converters," *Proceedings of the IEEE*, Vol. 76, No. 4, pp. 343 – 354, April 1988.
- [4.78] H. Mao, *Study on Three-Phase High-Input-Power-Factor PWM-Voltage-Type Reversible Rectifiers and Their Control Strategies*, PhD Dissertation, Zhejiang University, 2000.
- [4.79] M. Tsai; W.I. Tsai, "Analysis and Design of Three-phase AC-to-DC Converters with High Power Factor and Near-Optimum Feedforward," *IEEE Transactions on Industrial Electronics*, Vol. 46, No. 3, pp.535-543, June 1999.
- [4.80] C. T. Rim, N. S. Choi, G. C. Cho, G. H. Cho, "A Complete DC and AC Analysis of Three-Phase Controlled-Current PWM Rectifier Using Circuit D-Q Transformation," *IEEE Transactions on Power Electronics*, Vol. 9, No. 4, pp. 390-396, July 1994.
- [4.81] Z.M. Salameh, M.A. Casacca and W.A. Lynch, "A mathematical model for lead-acid batteries," *IEEE Transactions on Energy Conversion*, Vol. 7, No.1, pp. 93-98, 1992.
- [4.82] *Handbook of Batteries*, 2<sup>nd</sup> edition, D. Linden, Ed., McGraw Hill, Inc., New York, NY, 1995.
- [4.83] John Van de Vegte, *Feedback Control Systems (3<sup>rd</sup> Edition)*, Prentice Hall, 1994.

## CHAPTER 5

## CONTROL OF GRID-CONNECTED

## FUEL CELL POWER GENERATION SYSTEMS

Introduction

Fuel cells show great promise to be an important distributed generation (DG) source of the future due to many advantages they have, such as high efficiency, zero or low emission (of pollutant gases) and flexible modular structure. Fuel cell DGs can be strategically placed at any site in a power system (normally at the distribution level) for grid reinforcement, deferring or eliminating the need for system upgrades, and improving system integrity, reliability and efficiency. When connected to a utility grid, important operation and performance requirements are imposed on fuel cell DGs. For example, they should be able to deliver a pre-set amount of real and reactive power to the grid, or be able to follow a time varying load profile [5.2], [5.6], [5.27]. Therefore, proper controllers need to be designed for a fuel cell DG to make its performance characteristics as desired.

Among different types of fuel cells, proton exchange membrane fuel cells (PEMFC), solid oxide fuel cells (SOFC) and molten carbonate fuel cells (MCFC) are likely to be used in DG applications. In order to study the performance characteristics of fuel cell DGs, accurate models of fuel cells are needed [5.1]-[5.8]. Moreover, models for the interfacing power electronic circuits in a fuel cell DG are also needed to design controllers for the overall system to improve its performance and to meet certain

operation requirements [5.7]-[5.9].

In this chapter, the control of grid-connected FC systems is discussed. Both a PEMFC and a SOFC grid connected system are investigated. The PEMFC model, the SOFC model, and the models for boost DC/DC converters and a three-phase inverter together with a LC filter and transmission lines, reported in Chapter 4, are used in this study. The controller design methodologies for the DC/DC converters and the 3-phase inverter are also presented for the proposed fuel cell DG systems. Based on the individual component models developed and the controllers designed, simulation models for both a PEMFC DG system and a SOFC DG system have been built in MATLAB/Simulink using the SimPowerSystems block-set. Simulation studies are carried out to investigate the real and reactive power controllability of the fuel cell DG systems. The system performances under load-following and severe electrical faults are also discussed in this chapter.

### System Description

In order to meet the system operational requirements, a fuel cell DG needs to be interfaced through a set of power electronic devices. The interface is very important as it affects the operation of the fuel cell system as well as the power grid.

Various power electronic circuits have been proposed in recent work to interface different energy sources with the utility grid [5.9]-[5.16]. Pulse-width modulated (PWM) voltage source inverters (VSI) are widely used to interconnect a fuel cell energy system to a utility grid for real and reactive power control purposes [5.9], [5.11], [5.15], [5.16].

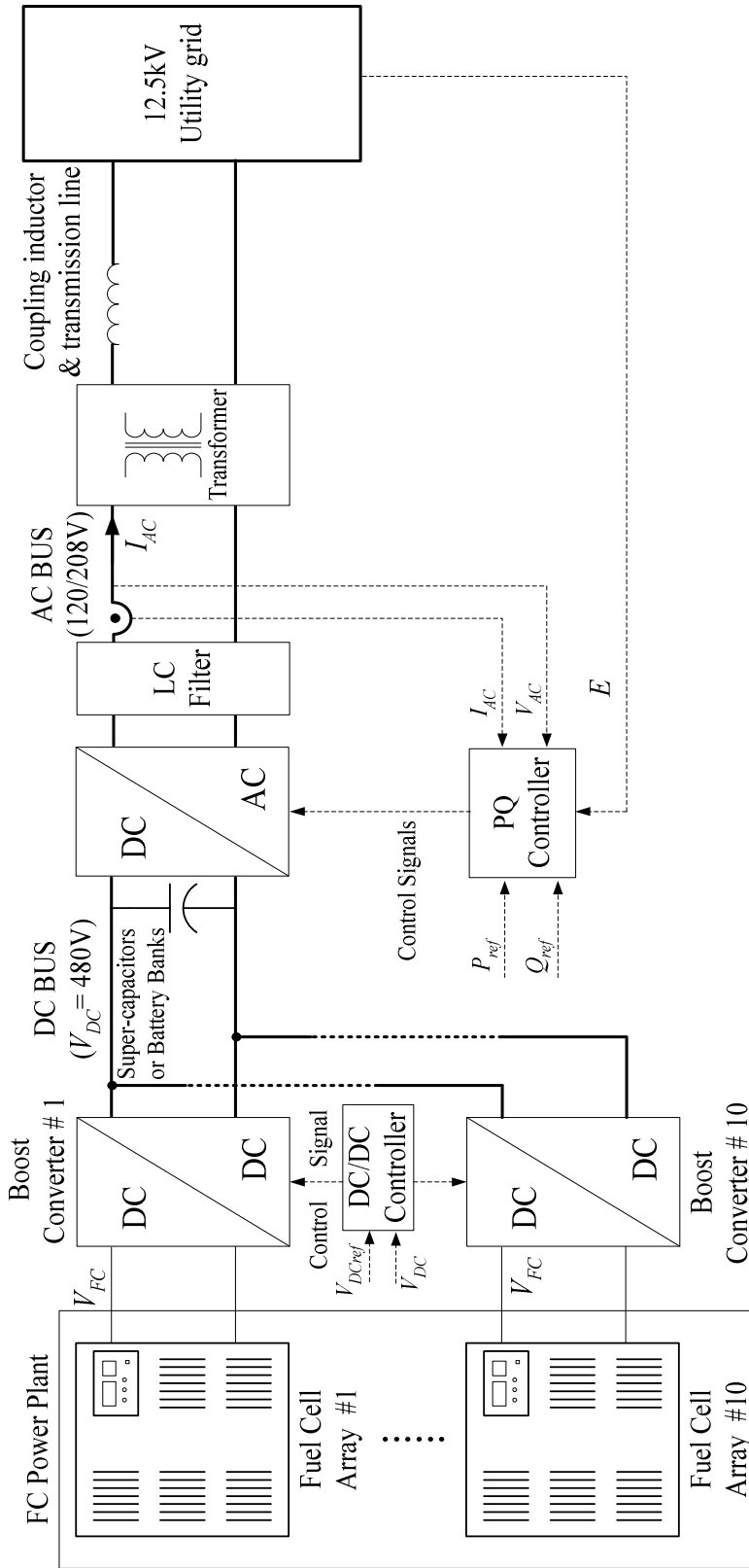


Figure 5.1. Block diagram of a fuel cell distributed generation system.

In addition, fuel cell systems normally need boost DC/DC converters to adapt the fuel cell output voltage to the desired inverter input voltage and smooth the fuel cell output current [5.17], [5.18].

Figure 5.1 shows the schematic diagram of the fuel cell DG system proposed in this study. In this dissertation, the fuel cell power plant in the figure is either PEMFC or SOFC type. The system configuration ratings and parameters are given in Table 5.1. The FC power plant consists of 10 fuel cell arrays connected in parallel. Each array is rated at 48kW, for a total of 480kW. A boost converter is used to adapt the output voltage of each fuel cell array to the DC bus voltage. In this dissertation, the DC bus voltage (DC/DC converter output) is chosen as  $V_{DC} = 480\text{V}$ , which is mainly determined by the inverter AC output voltage and the voltage drop across the LC filter. The following equation should be satisfied between the DC side and AC side voltages of the inverter [5.15]:

$$\frac{\sqrt{3}}{2\sqrt{2}} m_a V_{DC} \geq \sqrt{(V_{AC,LL})^2 + 3(\omega L_f I_{max})^2} \quad (5.1)$$

where  $V_{DC}$  is the DC bus voltage,  $V_{AC,LL}$  is the AC side line-line RMS voltage,  $L_f$  is the filter inductance,  $I_{max}$  is the RMS value of maximum AC load current ( $I_{AC}$ ), and  $m_a$  is the modulation index of the inverter. Linear pulse-width modulation (PWM) is used for the inverter, i.e.  $m_a \leq 1.0$ , in this study.

For a boost converter, the higher the duty ratio (or the larger the voltage difference between the input and output), the lower is the efficiency [5.16]. In this study a duty ratio around 55% is used for the DC/DC converter at the fuel cell's rated operating point. The approximate desired input voltage for the DC/DC converter can be obtained to be  $[(1 - 0.55) \times V_{DC} = 216\text{V}]$ . According to the  $V$ - $I$  characteristics of the PEMFC, given in

Figure 4.11, when the PEMFC load current is over 23A the fuel cell is in the concentration zone, which should be avoided [5.19], [5.20]. In order to leave some safe margin, the fuel cell is operated around the point where its current is 20A (rated operating point), and its output voltage ( $V_{PEMFC}$ ) is about 27V. Therefore, the number of PEMFC stacks we need to connect in series to get a voltage of 216V is

$$N_s = \frac{V_{FC}}{V_{PEMFC}} = \frac{216}{27} = 8 \quad (5.2)$$

The number of PEMFC series stacks needed to compose a 48kW fuel cell array is

$$N_p = \frac{P_{array}}{N_s \times P_{stack}} = \frac{48kW}{8 \times 0.5kW} = 12 \quad (5.3)$$

Therefore, each PEMFC array is composed of 8×12 stacks with the power rating of 48kW.

For a SOFC array, its configuration can be determined in a similar way. According to the SOFC  $V-I$  and  $P-I$  characteristics shown in Figures 4.20 and 4.22, when its load current is over 110 A, the SOFC stack is in the concentration zone, where its output voltage will decrease sharply as load current increases; this situation should also be avoided [5.19]. In order to leave some safe margin, the fuel cell is operated around the point where its current is 100 A (rated operating point), and its output voltage ( $V_{SOFC}$ ) is about 55 V. Therefore, the number ( $N_s$ ) of fuel cell stacks we need to connect in series to get a voltage of 220 V is

$$N_s = \frac{V_{FC}}{V_{SOFC}} = \frac{220}{55} = 4 \quad (5.4)$$

TABLE 5.1. CONFIGURATION PARAMETERS OF THE PROPOSED SYSTEM

PEMFC Power Plant	216V/480kW Ten 48kW FC arrays are connected in parallel
PEMFC Array	216V/48kW, consisting of 8 (series)×12 (parallel) 500W fuel cell stacks
SOFC Power Plant	216V/480kW Ten 48kW FC arrays are connected in parallel
SOFC Array	216V/48kW, consisting of 200V/480V, 50kW each.
Boost DC/DC Converter	10 units connected in parallel.
3-phase DC/AC Inverter	480V DC/208V AC, 500kW
LC Filter	$L_f = 0.15\text{mH}$ , $C_f = 306.5\mu\text{F}$
Step Up Transformer	$V_n = 208\text{V}/12.5\text{kV}$ , $S_n = 500\text{kW}$ $R_1=R_2=0.005$ p.u., $X_1=X_2=0.025$ p.u.
Coupling Inductor	$X_c = 50\Omega$
Transmission Line	0.5km ACSR 6/0 $R = 2.149 \Omega/\text{km}$ , $X = 0.5085 \Omega/\text{km}$
DC Bus Voltage	480V
AC Bus Voltage	120V/208V

The total power rating of the series connection of 4 SOFC stacks (5 kW each) is 20 kW. The number ( $N_p$ ) of these 20 kW SOFC units that need to be connected in parallel to compose a 40 kW fuel cell array is

$$N_p = \frac{P_{array}}{N_s \times P_{stack}} = \frac{40kW}{4 \times 5kW} = 2 \quad (5.5)$$

Therefore, each 40 kW SOFC array is composed of  $4 \times 2 = 8$  SOFC stacks (5 kW each).

Super-capacitors or battery banks are connected to the DC bus to provide storage capability and fast dynamic response to load transients. A 3-phase 6-switch inverter interfaces the DC bus with a 120/208V AC power system. An LC filter is connected to the output of the inverter to reduce the harmonics introduced by the inverter. A 208V/12.5kV step up transformer connects the fuel cell power system to the utility grid through a coupling inductor and a short transmission line. The coupling inductor is needed to control the real and reactive power flow between the fuel cell DG system and the utility grid and to limit disturbance and fault currents.

The controllers for the boost DC/DC converters are designed to keep the DC bus voltage within an acceptable band ( $\pm 5\%$  in this study). Therefore, the input to the 3-phase inverter can be considered as a fairly good constant voltage source. The inverter controller controls the real and reactive power flows to the utility grid. P, Q power flows follow their respective reference values, which can either be set as fixed values or to follow a certain load demand.

### Controller Designs for Power Electronic Devices

It was shown in Figures 4.11 and 4.20 that the output voltage of a fuel cell is a function of load. The boost DC/DC converter adapts the fuel cell output voltage to the DC bus voltage, and the voltage controller helps regulate the output voltage within a  $\pm 5\%$  tolerance band under normal operation. In this section, conventional PI controller is used for the boost DC/DC converters. In practice, a load sharing controller (not discussed in this study) can be applied on the converters, connected in parallel, to achieve a uniform load distribution among them [5.28]. Also, a  $dq$  transformed two-loop current control scheme is presented for the inverter to control the real and reactive power delivered from the fuel cell power system to the grid. Based on the models for power electronic devices discussed in Chapter 4, the designs for the controllers of power electronic devices are given in this section.

#### Controller Design for the Boost DC/DC Converter

The main components of the DC/DC converter can be determined by the prescribed technical specifications, such as the rated and peak voltage and current, input current ripple and output voltage ripple, etc., using the classic boost DC/DC converter design procedure [5.15], [5.16]. The component values for the 48kW DC/DC converter used in this study are listed in Table 5.2. For a boost DC/DC converter shown in Figure 4.69, the transfer function of the output voltage over duty ratio  $T_{vd}(s)$  is obtained as:

$$T_{vd}(s) = \frac{\tilde{v}_{dd\_out}(s)}{\tilde{d}(s)} = \frac{1}{s(s + \frac{1}{RC_{dd}}) + \frac{(1-D)^2}{L_{dd}C_{dd}}} \left[ -\frac{X_1 s}{C_{dd}} + \frac{(1-D)X_2}{L_{dd}C_{dd}} \right] \quad (5.6)$$

where  $D$  is the rated duty ratio of the switch.  $X_1$  is the average current of inductor  $L_{dd}$  and  $X_2$  is the output voltage at the rated operation point.

The transfer function of PWM generator can be expressed as [5.15], [5.16]:

$$T_{PWM}(s) = \frac{1}{V_{tri}} \quad (5.7)$$

where  $V_{tri}$  is the saw-tooth waveform amplitude of PWM generator.

The voltage ratio of the voltage transducer in Figure 4.69 is set as  $K_d = 1/480$  to normalize the output voltage. The PWM controller in the figure is chosen as a PI controller with the transfer function:

$$G_{dc}(s) = \frac{k_{dp}s + k_{di}}{s} \quad (5.8)$$

Based on the transfer function in (5.6), the PI current controller can be designed using the classic Bode-plot and root-locus method [5.21]. The overall block diagram of its control loop is shown in Figure 5.2. The parameters of the PI voltage controller are also listed in Table 5.2. Figure 5.3 shows the open loop Bode plot of the system. It is noted from the figure that the system is quite stable and has  $82.8^\circ$  phase margin.

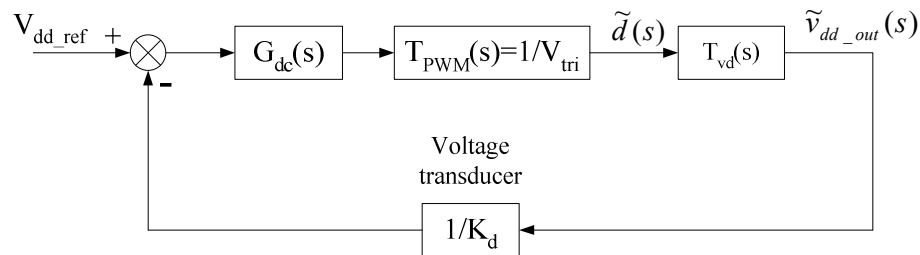


Figure 5.2. Block diagram of the control loop for the boost DC/DC converter.

TABLE 5.2. SYSTEM PARAMETERS OF THE BOOST DC/DC CONVERTER

$L_{dd}$	1.2 mH
$C_{dd}$	1000 $\mu$ F
$D_N$	0.5833
$R$	4.608 $\Omega$
$X_1$	250 A
$X_2$	480 V
$k_{di}$	50
$k_{dp}$	0.05

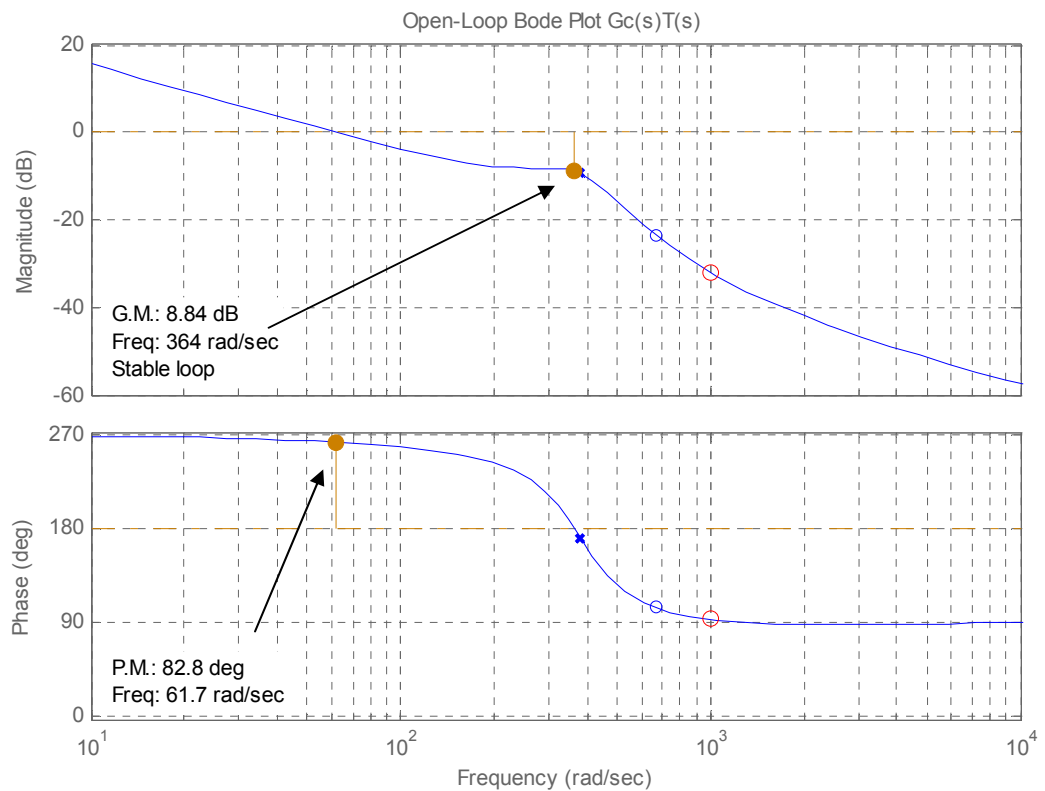


Figure 5.3. Bode plot of the control loop of the boost DC/DC converter.

### Controller Design for the 3-Phase VSI

In order to meet the requirements for interconnecting a fuel cell system to a utility grid and control the real and reactive power flow between them, it is necessary to shape and control the inverter output voltage in amplitude, angle and frequency [5.22]. In this section, a PWM controller is designed for the inverter shown in Figure 4.75 to satisfy voltage regulation as well as to achieve real and reactive power control.

Though the state-space equation (4.156) in Chapter 4 is sufficient for theoretical analysis and design, it is too complicated to be applied in the actual controller design from the engineering point of view. In order to simplify the analysis and design, a control scheme consisting of an outer voltage regulator with an inner current control loop given in [5.23] is adapted for inverter control. The inner current control loop is designed to respond faster than the outer voltage control loop so that these two loops can be considered separately [5.23], [5.24].

Current Control Loop. The ramp comparison method is used to generate the six PWM signals in this study. Base on the state-space averaging technique [5.15], [5.23], the average value of the switching functions in a switching period is:

$$\left(d_k^*\right)_{avg} = \frac{i_{ck}}{V_{m\_tri}}, \quad k = 1,2,3 \quad (5.9)$$

where  $i_{ck}$  is the modulating (control) signal and  $V_{m\_tri}$  is the amplitude of the carrier signal.

Converting the control signals from  $abc$  coordinate into the  $dq$  frame yields:

$$\begin{bmatrix} i_{cd} \\ i_{cq} \\ i_{c0} \end{bmatrix} = T_{abc/dq} \begin{bmatrix} i_{c1} \\ i_{c2} \\ i_{c3} \end{bmatrix} \quad (5.10)$$

where  $i_{cd}$  and  $i_{cq}$  are the control signals in  $dq$  frame and  $i_{c0} = 0$  for the balanced system.  $T_{abc/dq}$  is the  $abc/dq$  transformation matrix, as given in Appendix A.

For the purpose of analysis, only unity power factor operation (zero value on  $q$  axis) is discussed in the section. The effect of the capacitor  $C_f$  in the low pass  $LC$  filter (see Figure 4.77) on the power frequency current is very small. Therefore,  $C_f$  can be neglected when designing the current loop controller [5.23]. Based on the state-space formula [see (4.156)] in Chapter 4, the current control loop can be represented in the diagram shown in Figure 5.4.

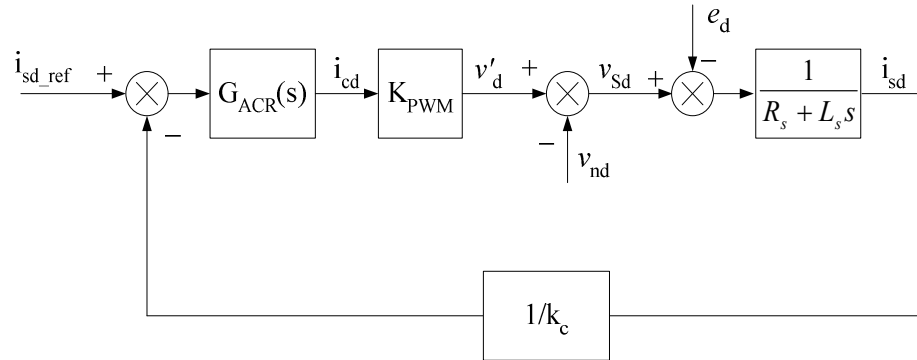


Figure 5.4. Block diagram of the current control loop of the inverter.

$G_{ACR}(s)$  in the figure is the current controller, which is chosen as a generic PI controller:

$$G_{ACR}(s) = \frac{k_{cp}s + k_{ci}}{s} \quad (5.11)$$

KPWM is the gain of the pulse generator:

$$K_{PWM} = \frac{V_{dc}}{2V_{tri\_m}} \quad (5.12)$$

In the figure,  $\frac{1}{R_s + L_s s}$  is the model of the overall equivalent admittance of the *LC* filter inductor, power transformer, coupling inductor and transmission line, and  $k_c$  is simply the current transducer ratio. The parameters of the current control loop are summarized in Table 5.3.

The transfer function of the current control loop can be obtained as:

$$T_c(s) = \frac{i_{sd}(s)}{i_{sd\_ref}(s)} = \frac{P_{1c}\Delta_{1c}}{\Delta_c} \quad (5.13)$$

where  $P_{1c} = G_{ACR} K_{PWM} \frac{1}{(R_s + L_s s)}$ ,  $\Delta_{1c} = 1$ , and  $\Delta_c = 1 + G_{ACR} \frac{K_{PWM}}{k_c} \frac{1}{(R_s + L_s s)}$ .

TABLE 5.3. PARAMETERS OF THE CURRENT CONTROL LOOP THE INVERTER

$V_{dc}$	480 V
$V_{tri\_m}$	1 V
$R_s$	0.006316 $\Omega$
$L_s$	0.1982 mH
$k_c$	1388
$k_{ci}$	250
$k_{cp}$	2.5

According to the parameters listed in Table 5.3, the Bode plot of the current control loop is given in Figure 5.5. It is noted that the system is quite stable with phase margin of 88.2°

The unit step response of the current control loop is shown in Figure 5.6. It is noted that the overshoot is about 2.5% and the equivalent dominant time constant is about 0.45ms. Therefore, the overall current control loop can be approximated by a simple lag as:

$$\hat{T}_c(s) = \frac{k_c}{1 + \tau_i s} \quad (5.14)$$

where  $\tau_i$  (0.45ms) is the equivalent time constant of the current control loop.

The unit step response of  $\hat{T}_c(s)$  is also shown in Figure 5.6. This approximated overall transfer function will be used in the following section to design the voltage control loop.

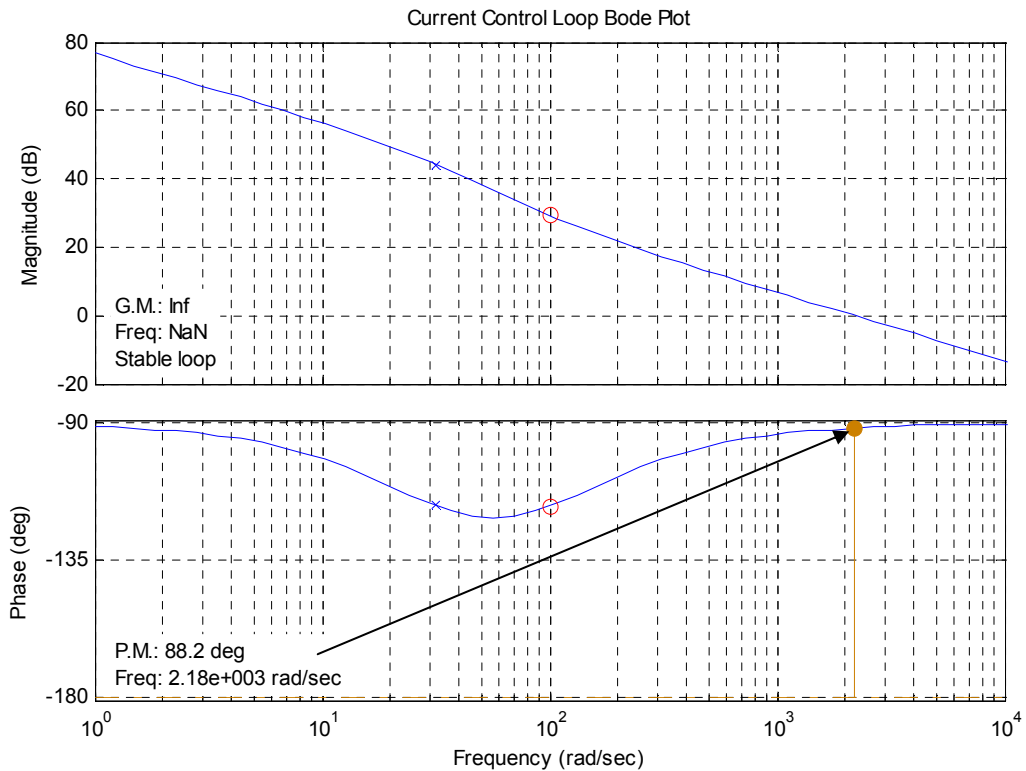


Figure 5.5. Bode plot of the current control loop.

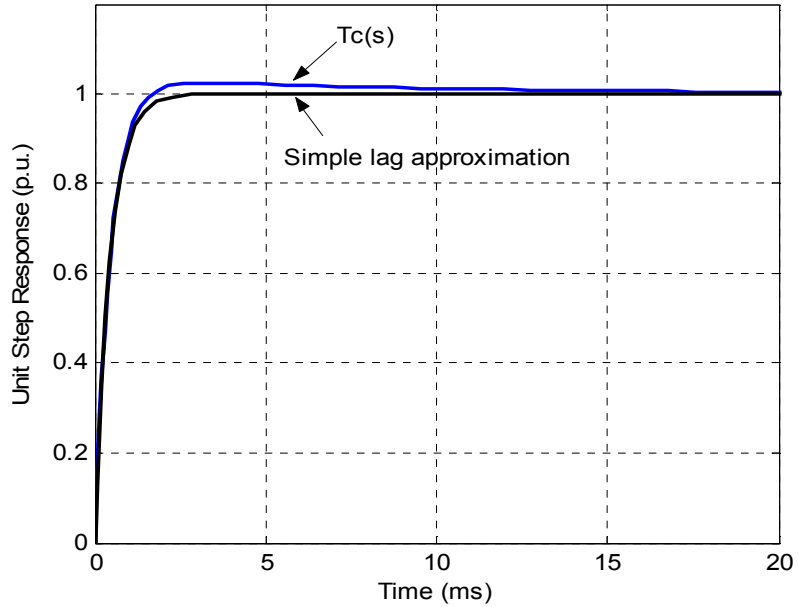


Figure 5.6. Unit step response of the current control loop and its approximation.

Voltage Control Loop. Base on the state-space model given in (4.156) in Chapter 4, the voltage control loop can be represented by the block diagram shown in Figure 5.7. For the purpose of analysis, only the condition where the q-axis voltage component is zero is discussed.

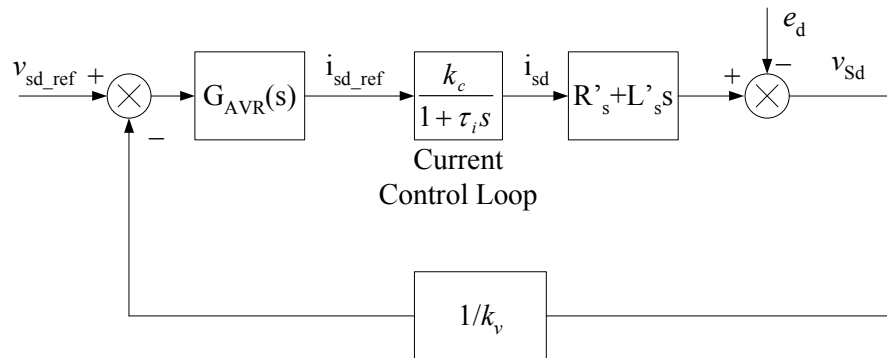


Figure 5.7. Block diagram of the voltage control loop of the inverter.

In the figure, the  $G_{AVR}(s)$  is the voltage regulator, which is also chosen as a PI

controller.

$$G_{AVR}(s) = \frac{k_{vp}s + k_{vi}}{s} \quad (5.15)$$

Since the voltage control loop is designed to respond much slower than the inner current control loop, the current control loop can be approximated as a simple lag block given in (5.14) to simplify analysis while without losing accuracy [5.24].

$R'_s + L'_s s$  in Figure 5.7 is the overall impedance of the power transformer, coupling inductor and transmission line, and  $k_v$  is the voltage transducer ratio. The parameters of the voltage control loop are listed in Table 5.4.

The transfer function of the voltage control loop can be obtained as:

$$T_v(s) = \frac{v_{sd}(s)}{v_{sd\_ref}(s)} = \frac{P_{1v} \Delta_{1v}}{\Delta_v} \quad (5.16)$$

$$\text{where } P_{1v} = G_{AVR}(s) \frac{k_c(R'_s + L'_s s)}{1 + \tau_i s}, \quad \Delta_{1v} = 1 \quad \text{and} \quad \Delta_v = 1 + G_{AVR}(s) \frac{k_c(R'_s + L'_s s)}{k_v(1 + \tau_i s)}.$$

TABLE 5.4. PARAMETERS OF THE VOLTAGE CONTROL LOOP THE INVERTER

$R'_s$	0.005316 $\Omega$
$L'_s$	0.0482 mH
$\tau_i$	0.45 ms
$k_c$	1388
$k_v$	169.8
$k_{vi}$	25
$k_{vp}$	0.2

The Bode plot of the voltage control loop is shown in Figure 5.8. It is noted that the

system is stable with phase margin  $91^\circ$ .

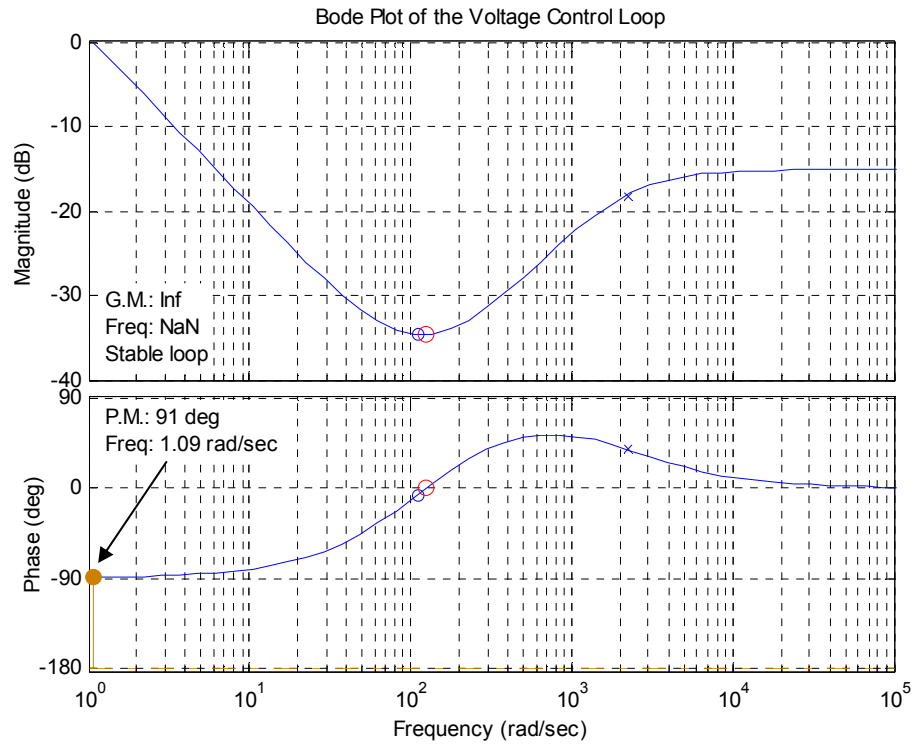


Figure 5.8. Bode plot of the voltage control loop.

Control of Power Flow. Consider a voltage source  $V_s \angle \delta$  connected to a utility grid  $E \angle 0^\circ$  through a coupling impedance  $R + jX$ , as shown in Figure 5.9. The real and reactive powers delivered to the utility grid are [5.25]:

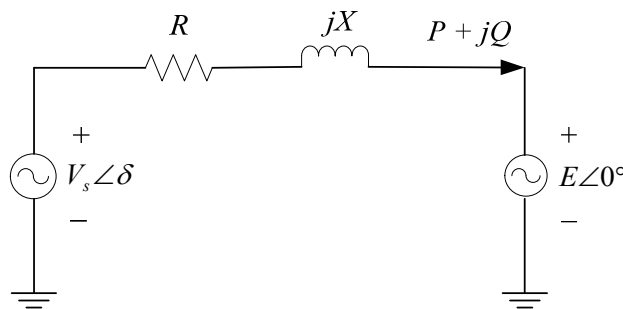


Figure 5.9. Power flow between a voltage source and utility grid.

$$P = \frac{EV_s}{Z} \cos(\theta_z - \delta) - \frac{E^2}{Z} \cos(\theta_z) \quad (5.17)$$

$$Q = \frac{EV_s}{Z} \sin(\theta_z - \delta) - \frac{E^2}{Z} \sin(\theta_z) \quad (5.18)$$

where  $Z = \sqrt{R^2 + X^2}$  and  $\theta_z = \tan^{-1}(X/R)$ .

From (5.17) and (5.18), it is clear that the real and reactive powers delivered to the utility grid are completely determined by the amplitude and angle of the sending voltage source, i.e. the output voltage of the inverter. On the other hand, if the desired values of real and reactive power are given, the values of  $V_s$  and  $\delta$  can be determined from (5.17) and (5.18):

$$V_s = \left[ \frac{Z^2}{E^2} (P^2 + Q^2) + E^2 + 2PZ \cos(\theta_z) + 2QZ \sin(\theta_z) \right]^{\frac{1}{2}} \quad (5.19)$$

$$\delta = \theta_z - \cos^{-1} \left( \frac{ZP}{EV_s} + \frac{E}{V_s} \cos(\theta_z) \right) \quad (5.20)$$

The corresponding  $dq0$  component values of the voltage can be obtained through  $abc/dq$  transformation as follows:

$$\begin{bmatrix} V_d \\ V_q \\ V_0 \end{bmatrix} = T_{abc/dq} \begin{bmatrix} V_a \\ V_b \\ V_c \end{bmatrix} = T_{abc/dq} \begin{bmatrix} V_s \angle \delta \\ V_s \angle (\delta - 120^\circ) \\ V_s \angle (\delta + 120^\circ) \end{bmatrix} \quad (5.21)$$

Overall Power Control System for the Inverter. The overall control system block diagram for the inverter is given in Figure 5.10.

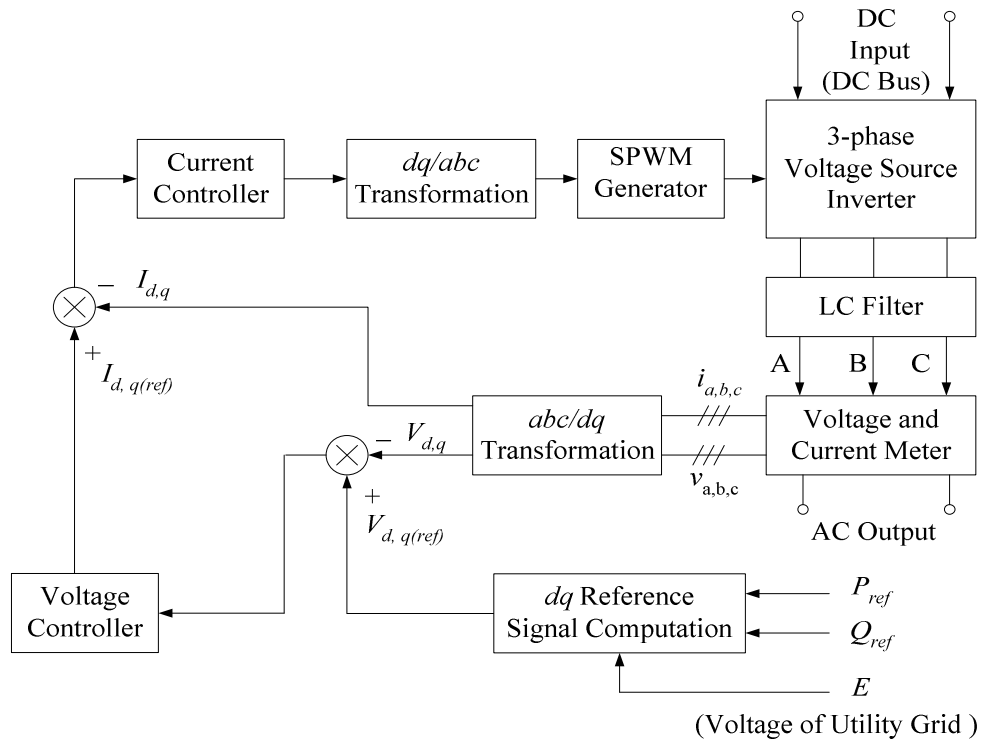


Figure 5.10. Block diagram of the overall power control system of the inverter.

In Figure 5.10, the “ $dq$  Reference Signal Computation” block, which is based on equations (5.19) and (5.20), calculates the magnitude and angle of the filtered output voltages of the inverter and then converts them into  $dq$  voltage reference signals according to (5.21). The “ $abc/dq$  Transformation” block takes the current and voltage values (in  $abc$  coordinate) from the voltage and current meters and converts them into  $dq$  values. The outer voltage controller takes the error signals between the actual output voltage in  $dq$  frame ( $V_{d,q}$ ) and the reference voltage ( $V_{d,q(ref)}$ ) and generates the current

reference signals ( $I_{d,q(ref)}$ ) for the current control loop. The inner current controller produces the  $dq$  control signals, which are converted back into the control signals in  $abc$  coordinates through the “ $dq/abc$  Transformation” block. These control signals are used to modulate the sinusoidal pulse width modulation (SPWM) pulse generator to produce the proper pulses for the inverter switches (Figure 4.77), which control the inverter output voltage.

The controllers given in this section for power electronic converters are designed on the basis of small-signal linearized models. Conceptually, there is no guarantee that the designed controllers will work well over a large operating range because of the nonlinearity of power electronic devices. Nevertheless, the majority of controllers for power electronic devices are linear time-invariant (LTI) that are designed on the basis of linearized models. The effectiveness of LTI controllers can be checked through simulations on switched (nonlinear) models, rather than the linearized ones used for the initial controller design [5.30]. We have verified the validity of the proposed control schemes over a large operating range through simulations on nonlinear converter/inverter models. The simulation results will be discussed in the following section.

### Simulation Results

Based on the individual component models developed in Chapter 4 and the controllers designed in this chapter, simulation models for both a PEMFC DG system and a SOFC DG system have been built in MATLAB/Simulink using SimPowerSystems block-set. The system was tested under several different operating conditions to investigate its power management and load-following capabilities as well as its stability

during electrical faults. Sample simulation results from the scenarios studied are given below.

#### Desired P and Q Delivered to the Grid: Heavy Loading

Normally, when a utility is under heavy load, it needs the connected DGs to deliver more real power to the grid. The DGs may also be required to deliver reactive power to the grid to help boost the grid voltage. Simulation results for such a scenario are given in this sub-section for both PEMFC and SOFC DGs.

PEMFC DG. The reference values of P and Q are set as 360kW and 32.3kVar with a ramp startup with 2s for this case study. The voltage of the utility grid was set to  $E = 0.98 \angle 0^\circ$  p.u. Using (5.19) and (5.20), the desired magnitude and angle of the filtered output voltage of the inverter turn out to be  $V_s = 1.05$  p.u.,  $\delta = 8.2678^\circ$ . Converting the values from the *abc* reference frame into *dq* coordinates yields  $V_{d(\text{ref})} = 1.0391$  p.u. and  $V_{q(\text{ref})} = 0.151$  p.u. A 3-phase AC circuit breaker connects the inverter to the utility grid at  $t=0.08$ s. Figure 5.11 shows the real and reactive power delivered from the PEMFC DG to the grid when the DG reaches its steady-state operation from the initial startup. Note that the output steady-state values of *P* and *Q* agree with their reference values very well. The corresponding *dq* components of the inverter output voltage are given in Figure 5.12. It is noted that the *dq* components of the output voltage also reach their prescribed reference values.

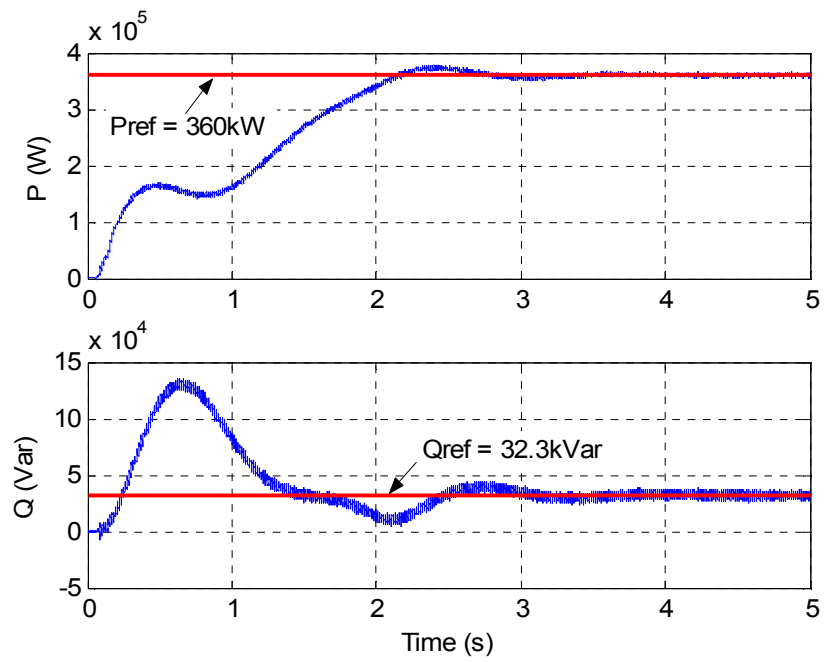


Figure 5.11. PEMFC DG: P and Q delivered to the grid under heavy loading.

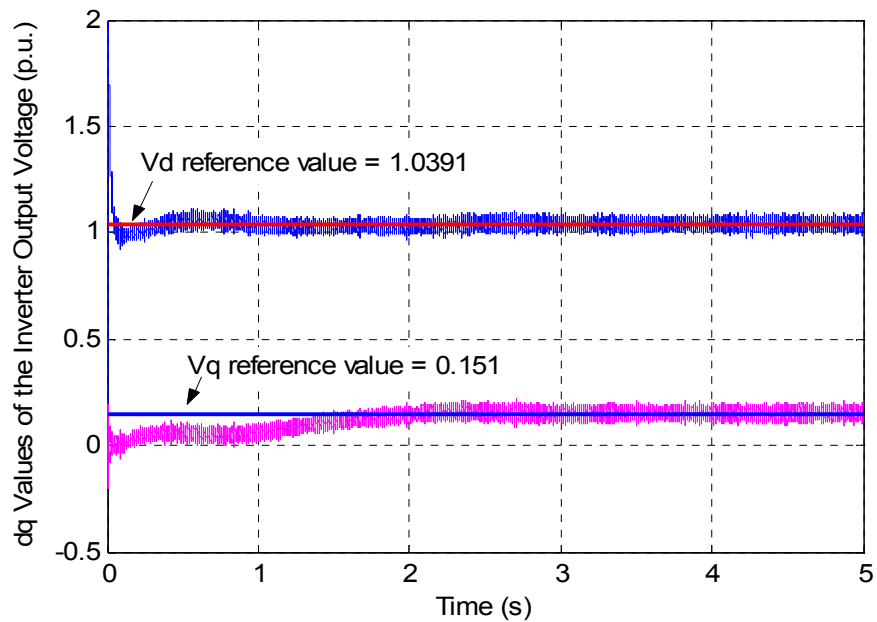


Figure 5.12. PEMFC DG: dq values of the inverter output voltage under heavy load.

The output voltage and current responses of each fuel cell array for this case are shown in Figure 5.13. Note that when the system reaches steady-state, the fuel cell output current ripple is about 10% and the fuel cell output voltage ripple is less than 3.3%. These relatively small variations of the current and voltage are indicative of the healthy operation of fuel cells [5.26]. The DC bus voltage (output voltage of the boost DC/DC converter) for this case is shown in Figure 5.14. Note that the DC bus voltage comes up to its reference value (480V) though the fuel cell terminal voltage is much lower than its no-load value under this heavy loading condition (see Figure 5.13). The voltage ripple at the DC bus is about 1.25%, which is within the acceptable range of  $\pm 5\%$ .

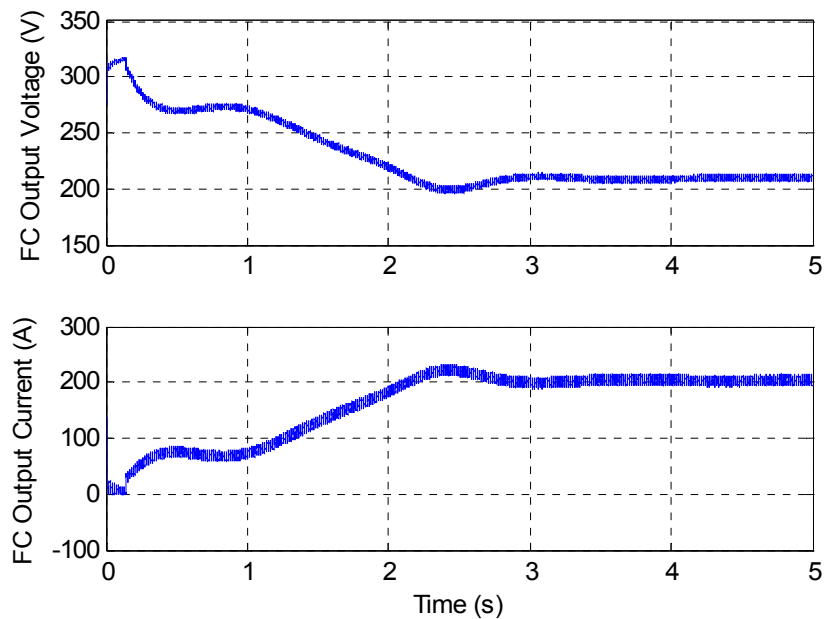


Figure 5.13. PEMFC DG: Output voltage and current of each fuel cell array under heavy load.

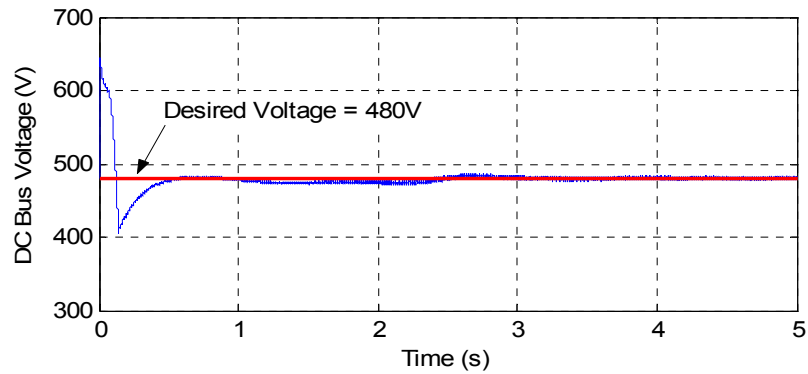


Figure 5.14. PEMFC DG: DC bus voltage waveform under heavy load.

SOFC DG. The reference values of  $P$  and  $Q$  ( $P_{ref}$  and  $Q_{ref}$  in Figure 5.10) are set as 450 kW and 84.5 kVar (heavy loading) with a ramp startup in 2s for this case study. The voltage of the utility grid was set to  $E = 0.98 \angle 0^\circ$  p.u. Figure 5.15 shows the reference and actual values of the real and reactive power delivered from the SOFC DG to the grid. Note that the final values of  $P$  and  $Q$  (delivered to the grid by the SOFC DG) agree with their reference values very well.

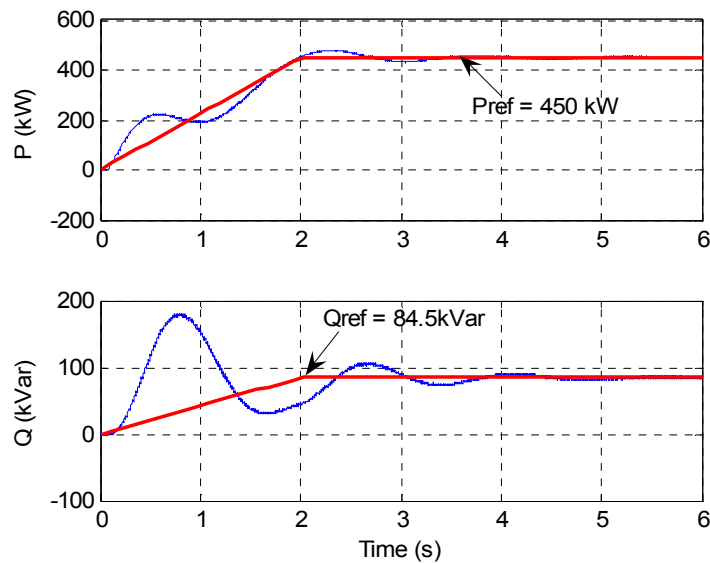


Figure 5.15. SOFC DG: P and Q delivered to the grid under heavy loading.

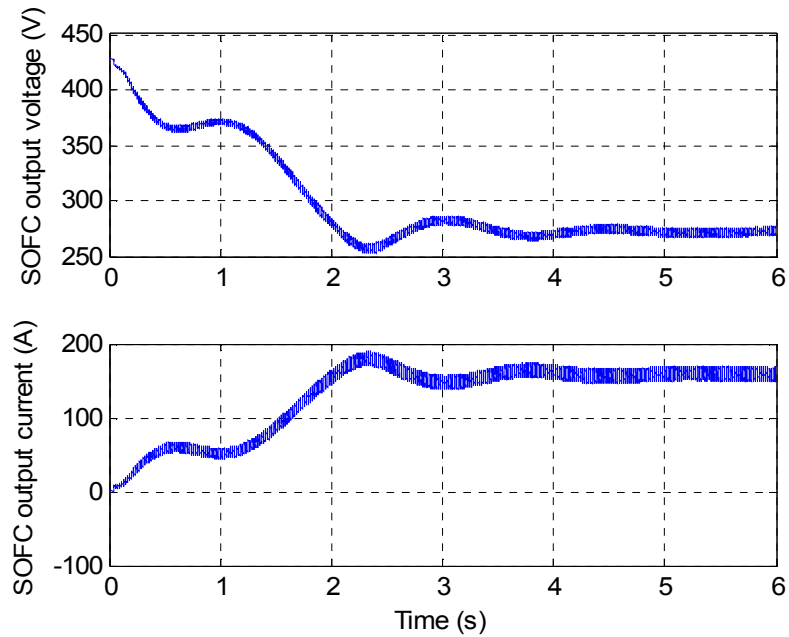


Figure 5.16. SOFC DG: Output voltage and current of each FC array under heavy load.

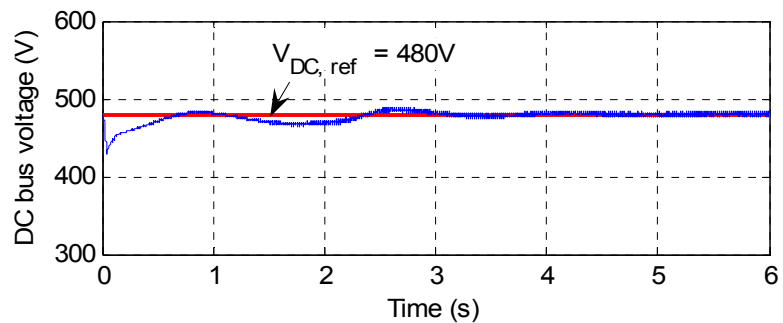


Figure 5.17. SOFC DG: DC bus voltage under heavy loading.

The output voltage and current curves of each 40 kW SOFC array (input to each DC/DC converter) for the above heavy loading case are shown in Figure 5.16. Note that when the system output power reaches its pre-set value, the fuel cell output current ripple is about 10% and the fuel cell output voltage ripple is around 3%. These relatively small variations of the current and voltage are indicative of the healthy operation of fuel cells [5.31]. The DC bus voltage (output voltage of the boost DC/DC converter) for this case is

shown in Figure 5.17. Note that the DC bus voltage comes up to its reference value (480V) though the fuel cell terminal voltage is much lower than its no-load value under this heavy loading condition (see Figure 5.16). The voltage ripple at the DC bus is about 1.5%, which is within the acceptable range.

#### Desired P Delivered to the Grid, Q Consumed from the Grid: Light Loading

PEMFC DG. Under light utility loading, the power required from the fuel cell DG is normally low, and the DG may be set to consume the excessive reactive power from the grid, i.e.  $Q < 0$ . This scenario is examined in this sub-section. The reference values of  $P$  and  $Q$  were set at  $P_{ref} = 100$  kW and  $Q_{ref} = -31.8$  kVar with an initial step-change startup. The voltage of the utility grid is set to  $E = 1.0 \angle 0^\circ$  p.u. for this case study. Using equations (5.19) and (5.20), the desired amplitude and angle of the filtered output voltage of the inverter turn out to be  $V_s = 1.0$  p.u.,  $\delta = 2.648^\circ$ . Converting the values into  $dq$  coordinates, we get  $V_{d(ref)} = 0.99893$  p.u. and  $V_{q(ref)} = 0.0463$  p.u.

Figure 5.18 shows the real and reactive power responses of the fuel cell DG. Note that at steady-state, the fuel cell power system delivers 100kW of real power to the grid and consumes 31.8 kVar of reactive power from the grid ( $Q = -31.8$  kVar), which match the reference values set for  $P$  and  $Q$ .

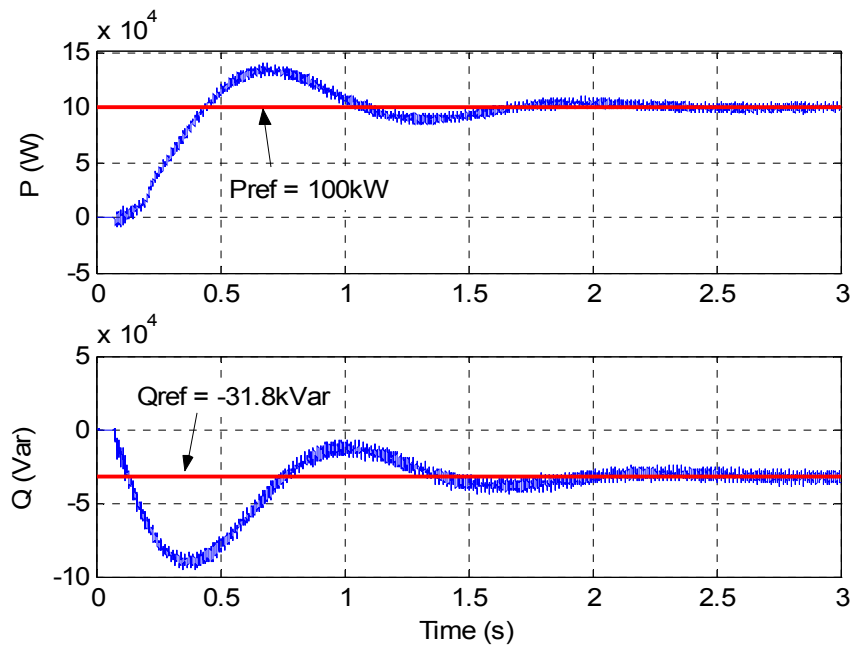


Figure 5.18. PEMFC DG: P and Q delivered to the grid: light loading.

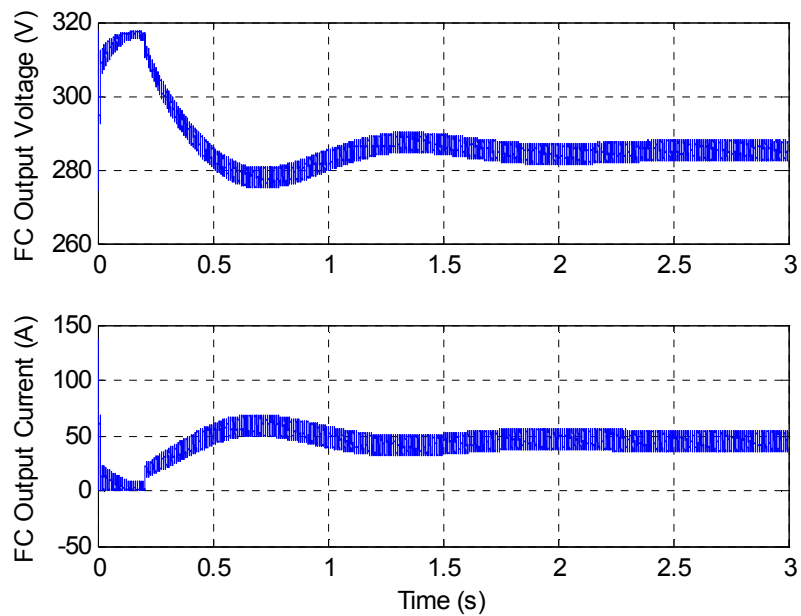


Figure 5.19. PEMFC DG: Output voltage and current of each fuel cell array under light loading.

Figure 5.20 shows the DC output voltage and current of each fuel cell array under light loading. In this case the fuel cell output current percentage ripple is bigger than that of case A, due to lighter loading. However, the fuel cell output voltage ripple is only about 2%, which is even less than that of case A due to a higher steady-state fuel cell output voltage under light loading.

SOFC DG. Similar to the case of PEMFC DG, under light loading the SOFC DG delivers less real power to the grid (compared to heavy loading condition), and may be set to consume the excessive reactive power from the grid, i.e.  $Q < 0$ . The simulation results of this scenario study are given in Figures 5.20 and 5.21. The reference values of  $P$  and  $Q$  are set as 250kW and -53.1kVar with a ramp startup in 2 s for this case study. The voltage of the utility grid was set to  $E = 1.0 \angle 0^\circ$  p.u. Figure 5.21 shows the reference and actual values of the real and reactive power delivered from the SOFC DG to the grid. Note that the output final values of  $P$  and  $Q$  agree with their reference values very well. The corresponding fuel cell array output voltage and current are given in Figure 5.21. The current ripple percentage, which is about 25%, of the SOFC output current under light loading is larger than heavy loading due to the lower average value of the load current. However, the fuel cell output voltage ripple (about 2%) under light loading is even smaller than heavy loading since the average value of the voltage is higher in this case.

From the above simulation results, it is noted that both the PEMFC and SOFC DG systems can be controlled to deliver the pre-set amount of real and reactive power. For the purpose of text length, only the simulation results of the PEMFC DG system are

given in the following simulation studies.

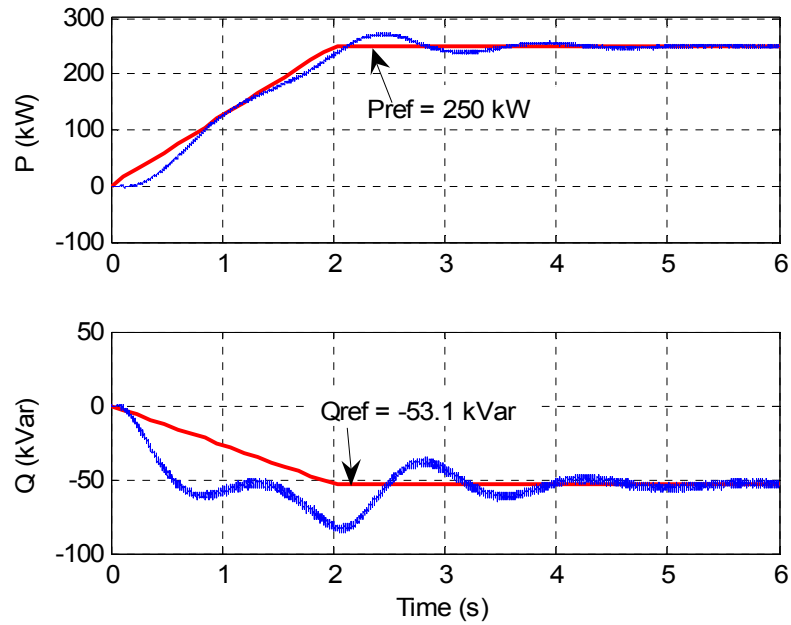


Figure 5.20. SOFC DG: P and Q delivered to the grid under light loading.

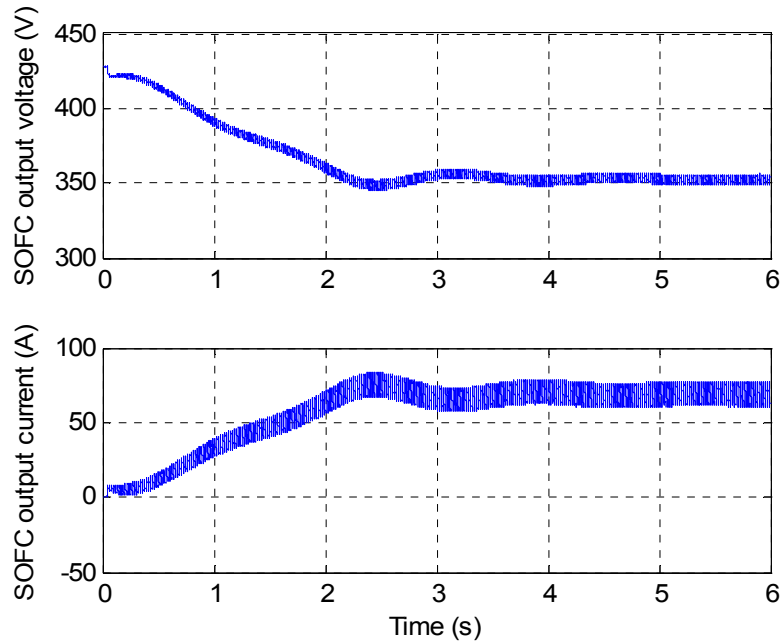


Figure 5.21. SOFC DG: Output voltage and current of each fuel cell array under light load.

### Load-Following Analysis

Fixed Grid Power. In a fuel cell DG system, a certain amount of power may be scheduled to be delivered to a load center (micro-grid) from the utility grid with the rest to be supplied by the fuel cell system. Therefore, a proper load-following controller must be designed to ensure that only scheduled power is delivered from the grid, and that the fuel cell system follows the remainder of load demand. In the deregulated power market, the ancillary service costs due to load-following operations can be as high as 20% of the total ancillary service costs [5.27]. Figure 5.22 shows the system configuration for which the load-following study was carried out for PEMFC DG. Bus 1 in the figure can be considered as a micro-grid bus, to which the PEMFC DG and the power grid are connected to supply power to the load. The power delivered from the grid ( $P_{Grid}$ ) is kept constant ( $P_{Grid,sched}$ ), and the PEMFC DG is required to follow load as it changes.

The load-following control diagram is also shown in Figure 5.22.  $P_{Grid}$  is measured and compared with the grid scheduled power. The error ( $\Delta P_{Grid}$ ) is then fed through the load-following controller to generate the adjustment power reference value ( $\Delta P_{FC,ref}$ ), which is added to the initial power reference value ( $P_{FC,ref}^0$ ) to give the new power reference value ( $P_{FC,ref}$ ) for the PEMFC DG system. The load-following controller can be a simple PI controller. Therefore, as load varies,  $P_{FC,ref}$  is adjusted to ensure that the fuel cell DG will compensate the changes of  $P_{Load}$ . It should be noted that fuel cell power adjustment is assumed to be within the safe operating range of the fuel cell DG.

In this case study  $P_{Grid}$  is set to 100kW (1 p.u.). As shown in Figure 5.23, at the beginning the load is 2 p.u., and therefore the fuel cell system delivers the remaining 1

p.u. power to the load. At  $t=0.3$ s, the load demand steps up to 3 p.u. and drops back to its original value (2 p.u.) at  $t=4.1$ s. It is noted from Figure 5.23 that the power grid responds to the initial load changes, and then the PEMFC DG picks up the load changes to keep the grid power at its scheduled value. The simulation results show that the PEMFC DG can follow the load power changes in less than 2s.

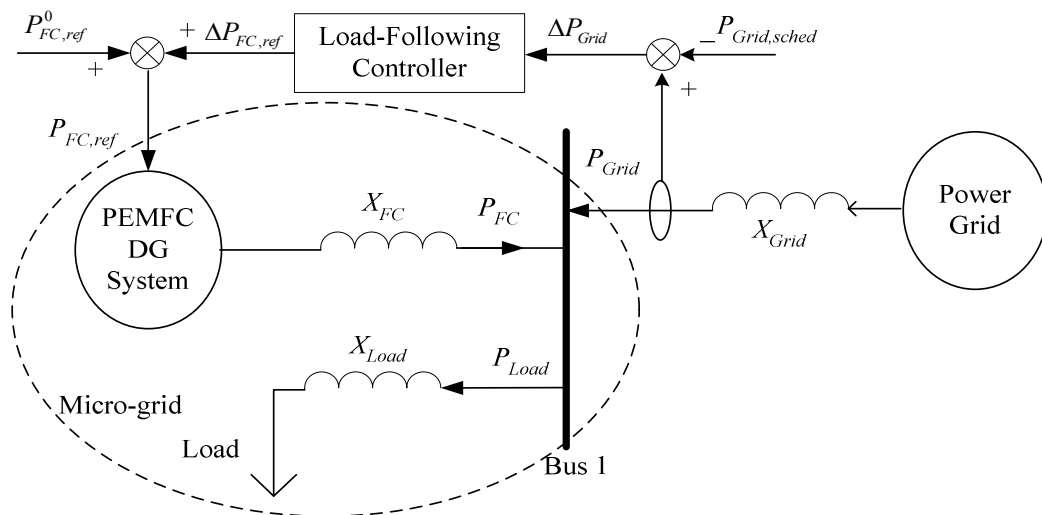


Figure 5.22. System for the PEMFC DG load-following study.

**Fixed FC Power.** Referring to the system shown in Figure 5.24, the simulation study for the scenario that the FC power plant is scheduled to supply a fixed amount of power to the micro-grid while the grid will pick up the load variations. The power delivered from the FC DG is set to 200 kW. The load changes used for this case study are the same as the previous case. The simulation results are shown in Figure 5.25. It is noted that the FC power is kept well at 200 kW. When the load changes at 0.3 s and 4.1 s, the grid balances the changes almost simultaneously, as shown in Figure 5.25.

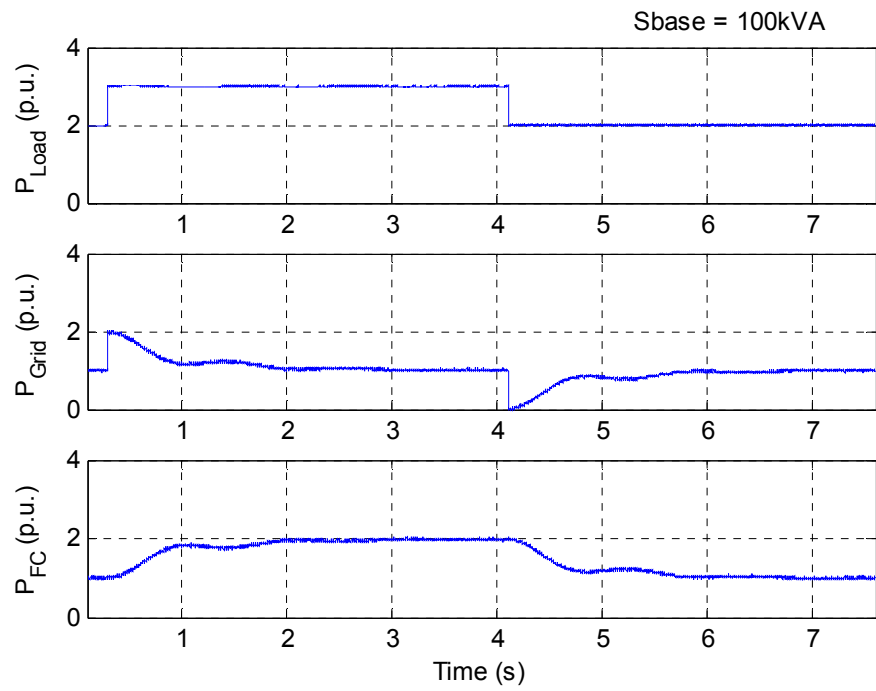


Figure 5.23. Power curves of the load-following study with fixed grid power.

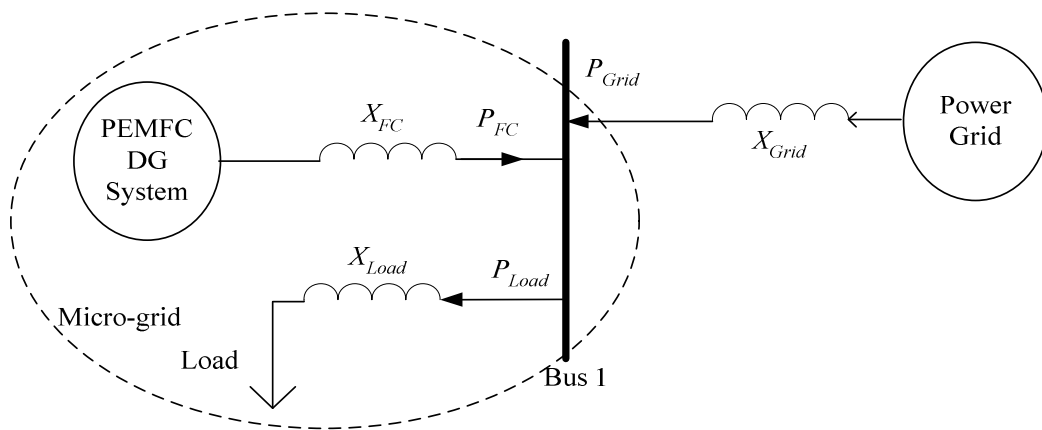


Figure 5.24. System for the PEMFC DG load-following study.

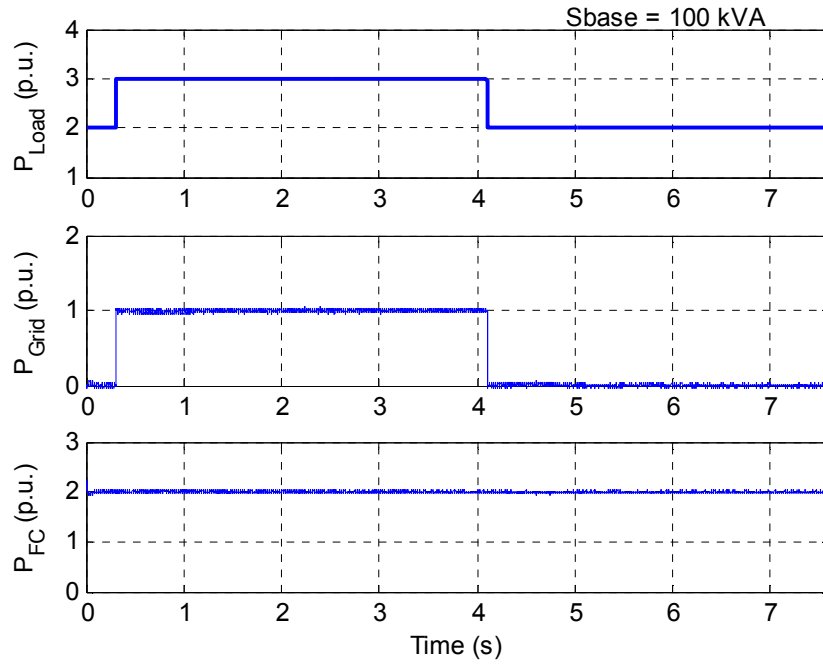


Figure 5.25. Power curves of the load-following study with fixed FC power.

### Fault Analysis

It is important to know whether the fuel cell DG system will remain stable under an electrical fault. In this section, the stability of the PEMFC DG under electrical faults is investigated. The FC DG system, shown in Figure 5.26, delivers 2 p.u. to the utility grid before the fault. A severe 3-phase fault is simulated to occur at  $t=0.7s$  at the low voltage side of the step-up transformer connecting the FC DG to the grid, as shown in Figure 5.26. The fault lasts for 5 cycles (0.0833s) and is cleared at  $t=0.7833s$ .

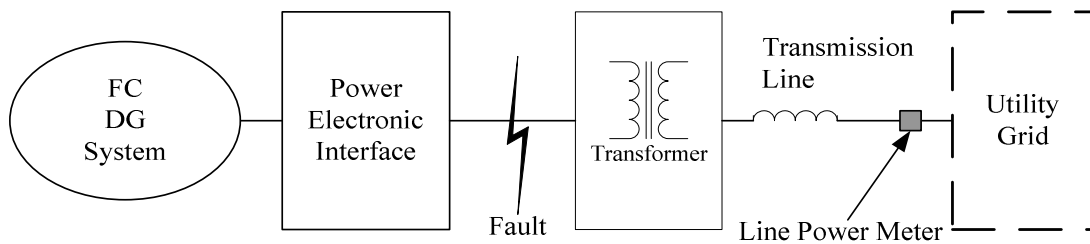


Figure 5.26. Faulted fuel cell DG system.

The power flow through the transmission line is shown in Figure 5.27. During the fault, the transmission line power changes direction (flowing from the grid toward the fault) since the utility grid also supplies power to the faulted point. As shown in the figure, the fuel cell system remains stable after the disturbance. Though the system is stable, there is a rush of power delivered from the fuel cell power plant to the utility grid when the fault is cleared. This is due to the large phase difference between the utility grid and the inverter output voltage when the fault is cleared. A soft-starting and a re-connection controller can be added to limit the peak power when the system recovers from a fault.

One advantage of the two-loop (voltage and current) inverter control is its capability to limit fault currents. To show this advantage, the simulation with the same fault on the system with only voltage control on the inverter was also conducted for comparison. The output power of the PEMFC DG under these two different inverter control strategies is shown in Figure 5.28. It is noticed that the system does not remain stable when only voltage control is applied for inverter control. Since there is no current limit control for this case, the fuel cell output current increases sharply due to the fault and exceeds the current corresponding to the fuel cell maximum power point. As a result, the fuel cell

output power drops sharply. It can be observed from Figure 5.28 that the system with two-loop inverter control comes back to the pre-fault state while the system with only voltage control on the inverter can not recover to its original state.

Similar 3-phase electrical faults were also simulated on several other points along the transmission line in Figure 5.26. In these cases, the FC DG remained stable under the two-loop control scheme.

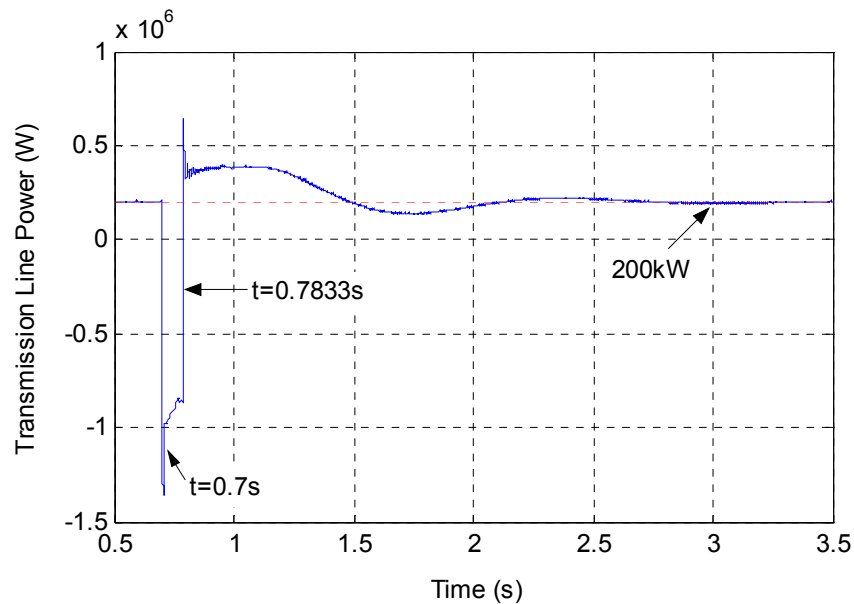


Figure 5.27. Faulted PEMFC DG: Power flow of the transmission line.

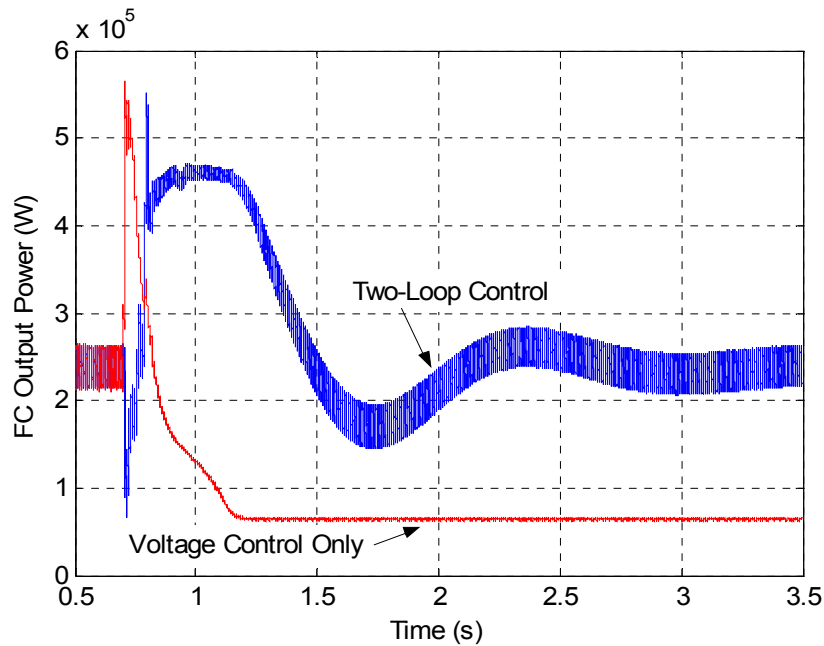


Figure 5.28. Faulted PEMFC DG: Fuel cell output powers for the fault studies.

### Summary

Control of grid-connected FC DG systems are investigated in this chapter. The PEMFC and SOFC models, the model for boost DC/DC converters, and the model for 3-phase voltage source inverters are used to develop a simulation model for a grid-connected FC system. Controller designs for the DC/DC converter and the 3-phase inverter are given using linearized small-signal converter/inverter models. Conventional PI voltage feedback controllers are used for the DC/DC converters to regulate the DC bus voltage, and a  $dq$  transformed two-loop current control scheme is used on the inverter to control the real and reactive power delivered from the fuel cell system to the utility grid.

A MATLAB/Simulink model of the proposed FC DG system was implemented using the SimPowerSystems block-set. The validity of the proposed control schemes over a

large operating range was verified through simulations on switched nonlinear converter/inverter models. Simulation results of the case studies show that the real and reactive power delivered from the fuel cell system to the utility grid can be controlled as desired while the DC bus voltage is maintained well within the prescribed range. The results also show that the fuel cell system is capable of load-following and can remain stable under the occurrence of severe electrical faults. It is noticed that a two-loop inverter control scheme has advantage over a voltage only control scheme for the inverter on fault protection and system stability.

REFERENCES

- [5.1] C. Wang, M.H. Nehrir, and S.R. Shaw, "Dynamic Models and Model Validation for PEM Fuel Cells Using Electrical Circuits," *IEEE Transactions on Energy Conversion*, vol. 20, no. 2, pp.442-451, June 2005.
- [5.2] C. J. Hatziadoniu, A.A. Lobo, F. Pourboghrat and M.Daneshdoost, "A simplified dynamic model of grid-connected fuel-cell generators," *IEEE Transactions on Power Delivery*, Vol. 17, No. 2, pp. 467-473, April 2002.
- [5.3] M. D.Lukas, K. Y. Lee, H. Ghezal-Ayagh, "Development of a Stack Simulation Model for Control Study on Direct Reforming Molten Carbonate Fuel Cell Power Plant," *IEEE Transactions on Energy Conversion*, Vol.14, No. 4, pp.1651-1657, Dec. 1999.
- [5.4] J. Padullés, G.W. Ault, and J. R. McDonald, "An integrated SOFC plant dynamic model for power system simulation," *J. Power Sources*, pp.495–500, 2000.
- [5.5] K. Sedghisigarchi and A. Feliachi, "Dynamic and Transient Analysis of Power Distribution Systems with Fuel Cells—Part I: Fuel-Cell Dynamic Model," *IEEE Transactions on Energy Conversion*, Vol. 19, No. 2, pp.423-428, June 2004.
- [5.6] K. Sedghisigarchi and A. Feliachi, "Dynamic and Transient Analysis of Power Distribution Systems with Fuel Cells—Part II: Control and Stability Enhancement," *IEEE Transactions on Energy Conversion*, Vol. 19, No. 2, pp.429-434, June 2004.
- [5.7] Z. Miao, M. A. Choudhry, R. L. Klein and L. Fan, "Study of A Fuel Cell Power Plant in Power Distribution System – Part I: Dynamic Model," *Proc. IEEE PES General Meeting*, June 2004, Denver, CO.
- [5.8] Z. Miao, M. A. Choudhry, R. L. Klein and L. Fan, "Study of A Fuel Cell Power Plant in Power Distribution System – Part II: Stability Control," *Proceedings, IEEE PES General Meeting*, June 2004, Denver, CO.
- [5.9] D. Candusso, L. Valero and A. Walter, "Modelling, control and simulation of a fuel cell based power supply system with energy management," *Proceedings, 28<sup>th</sup> Annual Conference of the IEEE Industrial Electronics Society (IECON 2002)*, Vol. 2, pp.1294-1299, 2002.
- [5.10] R. Naik, N. Mohan, M. Rogers and A. Bulawka, "A Novel Grid Interface, Optimized for Utility-scale Applications of Photovoltaic, Wind-electric, and

- Fuel-cell systems,” *IEEE Transactions on Power Delivery*, Vol. 10, No. 4, pp. 1920-1926, Oct. 1995.
- [5.11] W. Shireen and M.S. Arefeen, “An utility interactive power electronics interface for alternate/renewable energy systems,” *IEEE Transactions on Energy Conversion*, Vol. 11, No. 3, pp. 643-649, Sept. 1996.
- [5.12] G. Spiazzi, S. Buso, G.M. Martins, J.A. Pomilio, “Single phase line frequency commutated voltage source inverter suitable for fuel cell interfacing,” *2002 IEEE 33rd Annual IEEE Power Electronics Specialists Conference*, Vol. 2, pp.734-739, 2002.
- [5.13] K. Ro and S. Rahman, “Control of Grid-connected Fuel Cell Plants for Enhancement of Power System Stability,” *Renewable Energy*, Vol. 28, No. 3, pp. 397-407, March 2003.
- [5.14] H. Komurcugil and O. Kukrer, “A novel current-control method for three-phase PWM AC/DC voltage-source converters,” *IEEE Transactions on Industrial Electronics*, Vol. 46, No. 3, pp. 544-553, June 1999.
- [5.15] N. Mohan, T. M. Undeland and W. P. Robbins, *Power Electronics – Converters, Applications, and Design*, John Wiley & Sons , Inc., 2003.
- [5.16] D.W. Hart, *Introduction to Power Electronics*, Prentice Hall, 1997.
- [5.17] M. H. Todorovic, L. Palma, P. Enjeti, “Design of a Wide Input Range DC-DC Converter with a Robust Power Control Scheme Suitable for Fuel Cell Power Conversion,” *19th Annual IEEE Applied Power Electronics Conference*, CA, 2004.
- [5.18] SM N. Hasan, S. Kim, I. Husain, “Power Electronic Interface and Motor Control for a Fuel Cell Electric Vehicle,” *19th Annual IEEE Applied Power Electronics Conference*, CA, 2004.
- [5.19] *Fuel Cell Handbook (Fifth Edition)*, EG&G Services, Parsons Inc., DEO of Fossil Energy, National Energy Technology Lab, Oct. 2000.
- [5.20] James Larminie and Andrew Dicks, *Fuel Cell Systems Explained*, John Wiley & Sons, Ltd., 2001.
- [5.21] John Van de Vegte, *Feedback Control Systems (3<sup>rd</sup> Edition)*, Prentice Hall, 1994.
- [5.22] IEEE Std 1547, *IEEE Standard for Interconnecting Distributed Resources with Electric Power Systems*, 2003.

- [5.23] M. Tsai; W.I. Tsai, "Analysis and Design of Three-phase AC-to-DC Converters with High Power Factor and Near-Optimum Feedforward," *IEEE Transactions on Industrial Electronics*, Vol. 46, No. 3, pp.535-543, June 1999.
- [5.24] H. Mao, *Study on Three-Phase High-Input-Power-Factor PWM-Voltage-Type Reversible Rectifiers and Their Control Strategies*, PhD Dissertation (in Chinese), Zhejiang University, 2000.
- [5.25] J. D. Glover, M.S. Sarma, *Power System Analysis and Design*, 3<sup>rd</sup> Edition, Wadsworth Group. Brooks/Cole, 2002.
- [5.26] R.S. Gemmen, "Analysis for the effect of inverter ripple current on fuel cell operating condition," *Transactions of the ASME - Journal of Fluids Engineering*, Vol. 125, No. 3, pp.576-585, May 2003.
- [5.27] Y. Zhu and K. Tomsovic, "Development of models for analyzing the load-following performance of microturbines and fuel cells," *Journal of Electric Power Systems Research*, pp. 1-11, Vol. 62, 2002.
- [5.28] R. Wu, T. Kohama, Y. Koderu, T. Ninomiya and F. Ihara, "Load-Current-Sharing Control for Parallel Operation of DC-to-DC Converters". *IEEE PESC'93*, pp. 101-107, June 1993, Seattle, WA.
- [5.29] P.C. Krause, O. Wasynczuk, and S.D. Sudhoff, *Analysis of Electric Machinery*, IEEE Press, 1995.
- [5.30] John G. Kassakian, Martin F. Schlecht and George C. Verghese, *Principles of Power Electronics*, pp. 280-293, Addison-Wesley Publishing Company, 1991.S.K.
- [5.31] Mazumder, K. Acharya, C.L. Haynes, R. Williams, Jr., M.R. von Spakovsky, D.J. Nelson, D.F. Rancruel, J. Hartvigsen, and R.S. Gemmen, "SOFC Performance and Durability: Resolution of the Effects of Power-Conditioning Systems and Application Loads," *IEEE Transactions On Power Electronics*, Vol. 19, No. 5, pp. 1263-1278, September 2004.

## CHAPTER 6

## CONTROL OF STAND-ALONE FUEL CELL POWER GENERATION SYSTEMS

Introduction

As discussed in the previous chapters, both PEMFC and SOFC show great potential in DG and vehicular applications. They are good energy sources to provide reliable power at steady state, but they cannot respond to electrical load transients as fast as desired. This is mainly due to their slow internal electrochemical and thermodynamic responses [6.1]. Load transients will cause a low-reactant condition inside the fuel cells, which is considered to be harmful, and will shorten their life [6.2]. In order to overcome this weakness, fuel cells can be combined with other energy sources with fast dynamics, such as battery or super-capacitor, to form a hybrid power system [6.3]-[6.6]. Dynamic behavior of a PEMFC and lead-acid battery system was investigated in [6.3], while no control was discussed in the paper. Fuel cells and super-capacitor banks together with boost DC/DC converters are proposed in [6.4] to achieve a constant output dc voltage. A fuel cell-battery hybrid system is given in [6.6]; however, the paper concentrates on the design of a new DC/DC converter for fuel cell and battery applications only.

In this chapter, a load transient mitigation technique is proposed for stand-alone fuel cell-battery power generation systems. This technique is used to control the system in a way that during a load transient the fuel cell provides the steady-state load, and the battery will supply the transient load. The battery voltage is controlled to remain within a

desired range. Meanwhile, the fuel cell output current ripple is also limited in a certain low range, which is also important to fuel cell's healthy operation and life time [6.2], [6.7], [6.8].

The dynamic models for PEMFC, SOFC and lead-acid batteries, discussed in Chapter 4, are used in this chapter for FC load mitigation study. Based on these component models and the proposed control technique, simulation studies have been carried out for both PEMFC and SOFC systems to verify the effectiveness of the proposed technique.

### System Description and Control Strategy

Figure 6.1 shows the schematic diagram for the proposed FC-battery power generation system, where a boost DC/DC converter is used to adapt the fuel cell output voltage to the battery voltage (220 V in this study). Load mitigation will be investigated both for a PEMFC and a SOFC based system. The models for a 500W PEMFC and a 5 kW SOFC, discussed in Chapter 4, are used to model the FC unit shown in Figure 6.1. For the example PEMFC based system studied, the fuel cell unit consists of four 500 W PEMFC stacks connected in series to provide a 2 kW PEMFC unit. For the SOFC based system, the fuel cell unit is a single 5kW SOFC stack. The system load can either be DC or AC (interfaced through an inverter).

### Load Mitigation Control

Load mitigation control is achieved through a current controller for the DC/DC converter. Given that fuel cells are good energy sources (for providing steady-state power), but not good power sources for transient conditions [6.1], [6.3], the purpose of

the proposed control strategy is to control the fuel cell to only supply steady state power, while the battery will supply the transient power to the load. The load current ( $I_{load}$ ) is fed back through a low-pass filter to get rid of high-frequency transients. This filtered load current signal ( $I_{ref1}$ ) plus the output signal ( $I_{ref2}$ ) from the battery charging/discharging controller is taken as the reference signal ( $I_{ref}$ ) to control the DC/DC converter. Then, the output current of the DC/DC converter ( $i_{dd\_out}$ ) is compared with the reference signal  $I_{ref}$ , and the error signal is processed by the current controller to control the duty ratio of the switch in the converter.

The peak-to-peak ripple of the converter input current (fuel cell output current,  $i_{dd\_in}$  in Figure 6.1) should also be controlled within a certain range (10% in this study) for healthy operation of the fuel cell [6.2], [6.7], [6.8]. The main components of the DC/DC converter can be selected on the basis of technical specifications, such as rated and peak voltage and current, input current ripple, and output voltage ripple, etc., using the classic design procedure given in [6.12], [6.14]. The component values for the 5kW DC/DC converter model used in this study are listed in Table 6.1. The value of the coupling inductor ( $L_{dd\_out}$ ) is selected so that the combination of this inductor with the capacitor ( $C_{dd}$ ) yields a low resonant frequency ( $< 10\text{Hz}$  in this study) to smooth out the converter output current ( $i_{dd\_out}$ ).



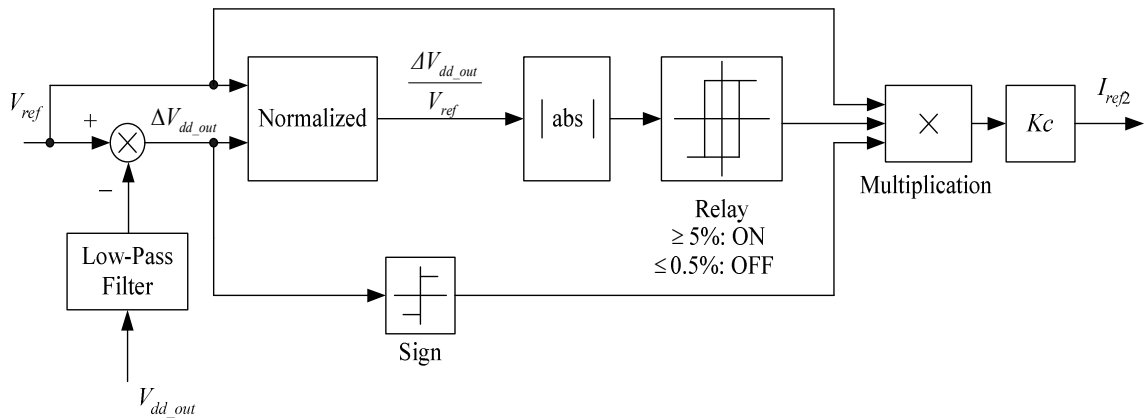


Figure 6.2. Schematic diagram of the battery charging/discharging controller.

An approximate state-space model of the converter at the rated operating point can be derived using the averaging technique proposed by Middlebrook and Cúk, explained in [6.12], [6.15]. Based on the converter model, a PI current controller ( $k_p + k_i/s$ ) can be designed using the classic Bode-plot and root-locus method [6.13]. The parameters of the PI current controller are also listed in Table 6.1. The battery charging/discharging controller design and the optimal choice of the filter will be discussed in the following sub-sections.

TABLE 6.1. PARAMETERS OF THE DC/DC CONVERTER

$L_{dd\_in}$	12 mH
$C_{dd}$	2500 $\mu$ F
$L_{dd\_out}$	120 mH
$f_s$ (Switch Frequency)	5 kHz
$k_i$	20
$k_p$	0.02

### Battery Charging/Discharging Controller

The battery in the system of Figure 6.1 is designed to buffer transient power. A 220V, 0.5kWh battery model, discussed in Chapter 4, is used in the study. The model parameters are listed in Table 6.2. For healthy operation of the battery bank, its voltage is kept within  $\pm 5\%$  of its nominal value. A battery charging/discharging controller is designed, as shown in Figure 6.2. In this figure,  $V_{ref}$  is the battery nominal voltage (220V). The regulation constant  $K_c$  in the figure is determined by assuming that the charging/discharging adjustment of 5% voltage deviation can be achieved in half hour (1800s). That is,

$$K_c = \frac{0.05C_b}{1800} \quad (6.1)$$

where  $C_b$  is the battery capacitance.

TABLE 6.2. PARAMETERS OF THE BATTERY MODEL

$C_b$	300 F
$R_p$	25 M $\Omega$
$R_2$	0.075 $\Omega$
$C_1$	500 F
$R_1$	0.1 $\Omega$

The “normalized” block normalizes the filtered battery voltage deviation ( $\Delta V_{dd\_out}$ ) with respect to the reference voltage ( $V_{ref}$ ). The “|abs|” block will give a nonnegative output  $\left( \left| \frac{\Delta V_{dd\_out}}{V_{ref}} \right| \right)$  regardless of whether  $\Delta V_{dd\_out}$  is positive or negative, i.e. whether the battery voltage is higher or lower than the reference voltage. The “relay” block in the

figure is a hysteresis block set as follows: it will turn on (output = 1) when the input is larger than 5% and will continue to be on until the input to the block is less than 0.5%. Otherwise, the output of the relay block is zero. The battery will be charged (discharged) at a constant current when its voltage is lower than 95% (higher than 105%) of its rated value. The charging (discharging) process will stop when the battery voltage is within 0.5% of its rated value. Therefore, as long as the battery voltage is lower than  $0.95V_{ref}$ , a positive extra reference signal

$$I_{ref2} = \frac{0.05C_b V_{ref}}{1800} \quad (6.2)$$

will be generated for the current controller. This reference value is kept until the voltage is higher than  $0.995V_{ref}$ . On the other hand, if the battery voltage is higher than  $1.05V_{ref}$ , a negative extra current reference value ( $-\frac{0.05C_b V_{ref}}{1800}$ ) is generated and this value will be held until the battery voltage is lower than  $1.005V_{ref}$ . Otherwise, the output of the battery charging/discharging controller is zero.

### Filter Design

The choice of the low-pass filter needed for the load transient mitigation controller is a trade-off design between the storage capacity of the battery and the smooth response of fuel cell to load transients. Figure 6.3 shows an example of the responses of different low-pass filters to a load transient. The damping factors of filters are all set to 1 to avoid any oscillation. It is noted from the figure that the higher is the cut-off frequency of the filter, the shorter is the settling time of the response. A filter with shorter settling time requires smaller storage battery capacity, but may cause undesired overshoot. On the

other hand, the lower is the filter cut-off frequency, the longer is the rise time of the filter response, and the smoother is the fuel cell response. However, a larger battery capacity is needed if a lower cut-off frequency is chosen for the filter. Therefore, a trade off has to be made to choose an optimal filter. In practical applications, one can estimate the fastest possible load transient based on the load information at the location where the fuel cell will be installed. Transients with frequencies higher than 1250Hz can be neglected since they do not affect the fuel cell performance significantly [6.2]. Then, one decides what overshoot value (current ripple) is tolerable by the fuel cell. An overshoot less than 10%, which normally will not cause any significant impact on the fuel cell's healthy operation [6.2], [6.7], can be considered a good value. The filter can therefore be chosen for the fastest load transient with the highest possible cut-off frequency, while its output overshoot will not exceed a prescribed value (10% suggested in this study).

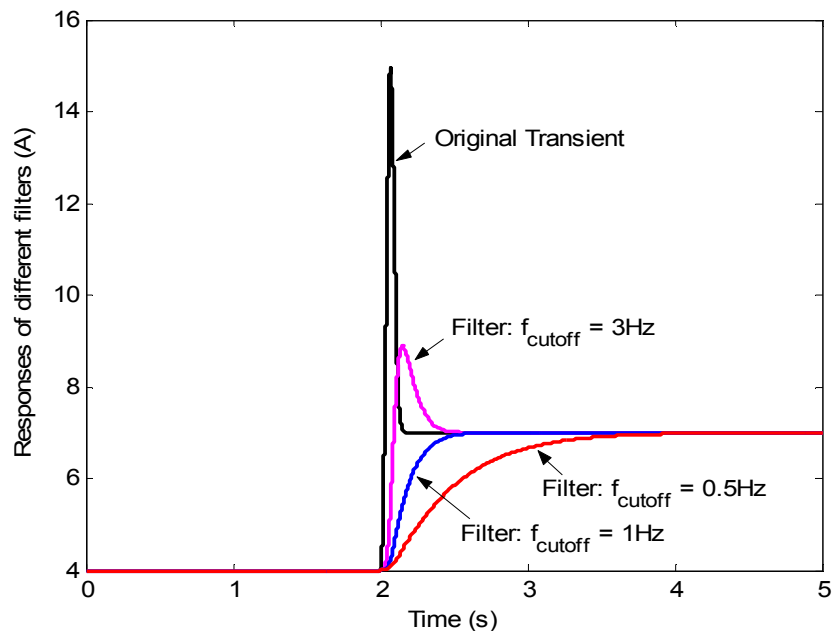


Figure 6.3. Example of the responses of different filters to a load transient.

### Simulation Results

The PEMFC and SOFC models and the battery model discussed Chapter 4 were used to develop simulation models for a stand-alone PEMFC-battery and a SOFC-battery power generation system in MATLAB/Simulink using SimPowerSystems block-set. Both systems are controlled by the load transient mitigation technique proposed in the previous section. The system performance under load transients is investigated to verify that power flow is controlled in such a way that the fuel cells only provide steady-state power while the battery will supply transient power to the load. Simulation results on charging/discharging performance of the battery are also given.

#### Load Transients

For the purpose of verifying the system performance under different load transients, both DC load transients and AC load transients were tested for the PEMFC and SOFC based power systems. Since the power rating of the PEMFC system studied is different from that of the SOFC system, different (but same type of) load transients will be used for the two systems.

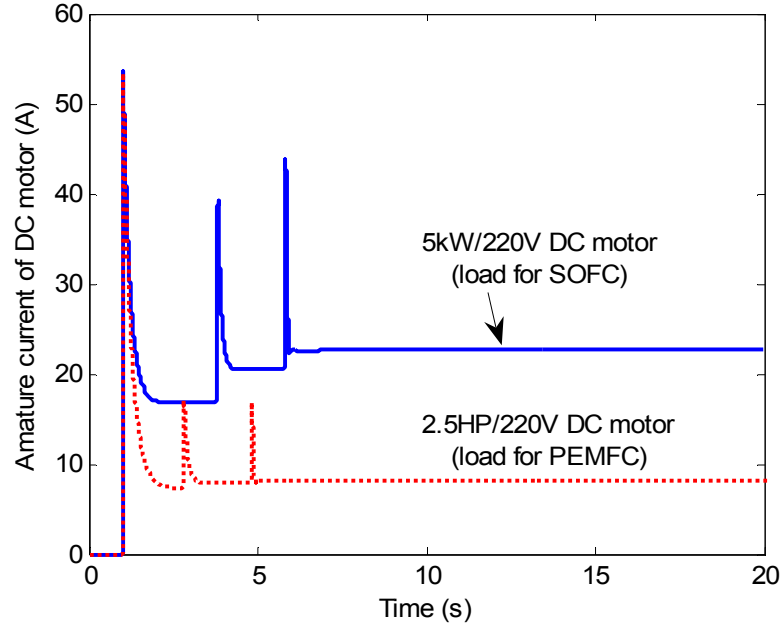


Figure 6.4. Load transient of starting a 2.5HP and a 5kW 220V DC motor.

DC Load Transients. The DC load transient due to a DC motor starting is used in the simulation study. Figure 6.4 shows the load current transient applied to the PEMFC and SOFC systems when a DC motor is started with full voltage in three steps of resistance starting. A 2.5 HP/220 V DC motor load is used for the 2 kW PEMFC-battery system and a 5 kW/220 V DC motor is used for the SOFC system.

AC Load Transients. A general dynamic load model is used to model AC load current transients. This transient current model is defined as follows:

$$i(t) = I_0 + I_1 e^{-\alpha_1 t} - I_2 e^{-\alpha_2 t} \quad (6.3)$$

where  $I_0$ ,  $I_1$  and  $I_2$  are non-negative constants and  $\alpha_2 > \alpha_1 > 0$ . It is assumed that the load transient starts at  $t=0$  in the above equation, and  $i(t)$  is the amplitude of load current at 60Hz.

The above five constant parameters can be determined by the following equations:

$$\left\{ \begin{array}{l} I_0 = i_\infty \\ I_0 + I_1 - I_2 = i_0 \\ \frac{\ln \frac{I_2 \alpha_2}{I_1 \alpha_1}}{\alpha_2 - \alpha_1} = T_p \\ I_0 + I_1 e^{-\alpha_1 T_p} - I_2 e^{-\alpha_2 T_p} = i_{peak} \\ \frac{\ln I_1 - \ln(0.02 I_0)}{\alpha_1} \approx T_S \end{array} \right. \quad (6.4)$$

where  $i_0$  and  $i_\infty$  are the initial and final values of the transient load current,  $T_p$  is the time that it takes the transient current to reach its peak value ( $i_{peak}$ ), and  $T_S$  is the settling time, which takes the transient to settle to within  $\pm 2\%$  of its final value. Therefore, by specifying the initial value ( $i_0$ ), final value ( $i_\infty$ ), peak value of the transient ( $i_{peak}$ ), how fast the transient reaches its peak ( $T_p$ ), and how long it takes the transient to reach steady state ( $T_S$ ), we can calculate the five parameters in (6.4) numerically. Figure 6.5 shows the load transient curve used for the PEMFC system, which starts at 1s. The parameters of this load transient are  $I_0 = 15.84\text{A}$ ,  $I_1 = 79.2\text{A}$ ,  $I_2 = 95.04\text{A}$ ,  $\alpha_1 = 5$  and  $\alpha_2 = 30$ . The parameters of the AC load current transient for the SOFC system studied are  $I_0 = 39.6\text{A}$ ,  $I_1 = 198\text{A}$ ,  $I_2 = 237.6\text{A}$ ,  $\alpha_1 = 5$  and  $\alpha_2 = 30$ . The load transient obtained when these are used in (6.3) is similar to the waveform shown in Figure 6.5, but with a higher magnitude.

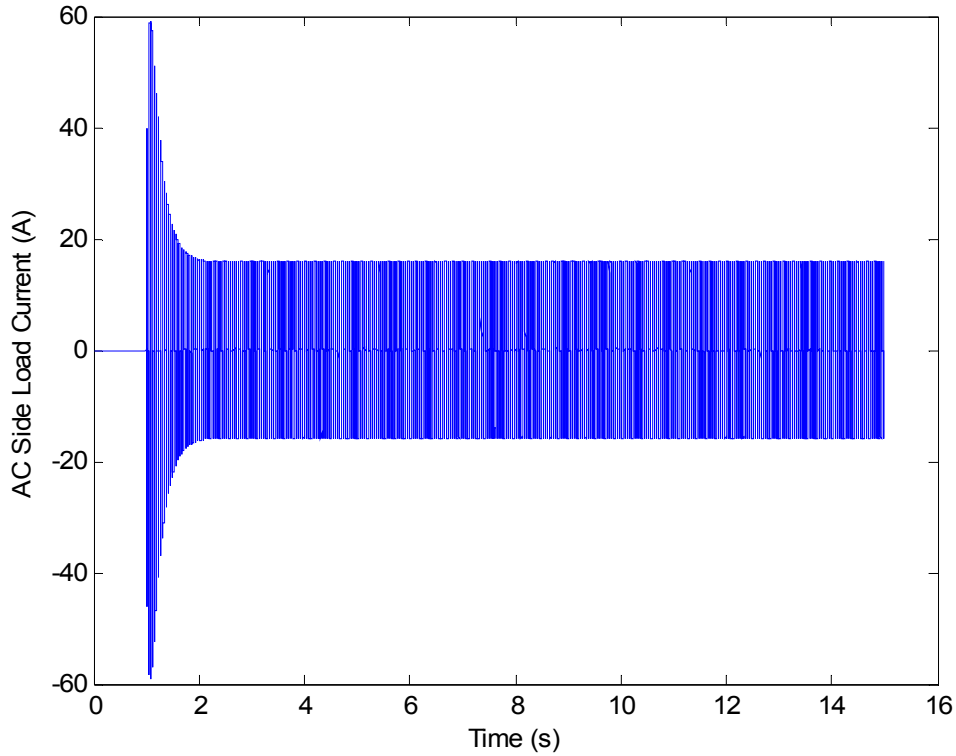


Figure 6.5. AC load transient used on PEMFC-battery system.

### Load mitigation

In this sub-section, simulation results are presented for load transient mitigation studies of PEMFC and SOFC systems. Throughout the studies in this part, it is assumed that the battery in the system studied is fully charged to its rated voltage, 220 V, before the application of load transients.

PEMFC System. First, the system is tested under the DC motor load transient shown in Figure 6.4. The cut-off frequency of the low-pass filter in this simulation is chosen to be 0.1 Hz and the damping factor is set to 1. The corresponding current reference signal ( $I_{ref}$  in Figure 6.1), shown in Figure 6.6, shows that the rise time of the filter response to

the load transient is less than 10 s, and there is no overshoot. The battery current ( $i_b$ ) and the converter output current ( $i_{dd\_out}$ ) responding to the load transient current are also shown in Figure 6.6. The figure shows that  $i_{dd\_out}$  follows the reference signal ( $I_{ref}$ ) very well; they almost overlap each other. It is noted from the figure that the battery picks up the transient current while the converter output current rises smoothly (as designed) from its previous steady-state to its next steady-state value. The corresponding PEMFC current and voltage responses are shown in Figure 6.7. It is noted that the PEMFC outputs vary smoothly during the load transient; the PEMFC is controlled to supply only the steady-state current to the load. It is also noted that the fuel cell current ripple is around 5.5%, which is within the acceptable range (10%).

For the purpose of comparison, a simulation study was carried out on the PEMFC system, shown in Figure 6.1, with a typical voltage controller for the DC/DC converter only (i.e.,  $i_{load}$  and  $i_{dd\_out}$  are not fed back and  $L_{dd\_out}$  is taken out in Figure 6.1). The controller is used to keep the converter output voltage constant under load variations. Figure 6.7 also shows the PEMFC output voltage for this case study when the DC load transient (Figure 6.4) is applied to the PEMFC system. It is noted that the system fails to start the DC motor under this case, hence, justifying the need for the current controller.

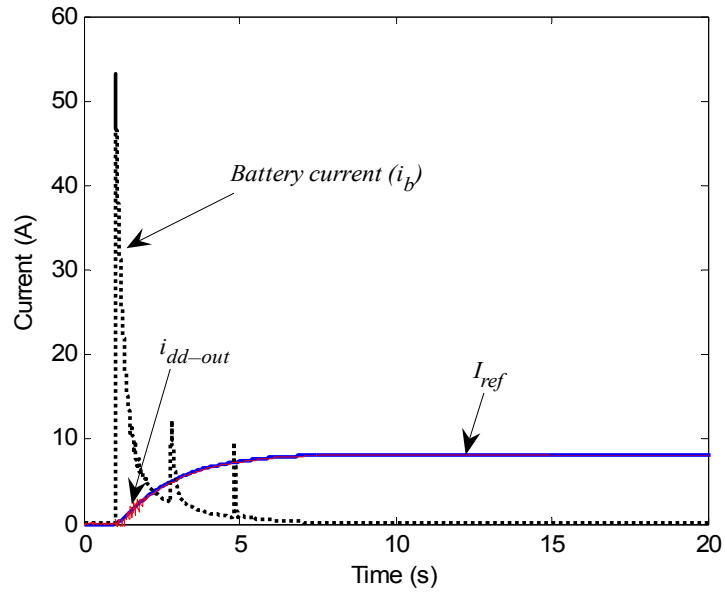


Figure 6.6. Reference signal ( $I_{ref}$ ) for the current controller, battery current ( $i_b$ ), and converter output current ( $i_{dd\_out}$ ) under the load transient for PEMFC shown in Figure 6.4.

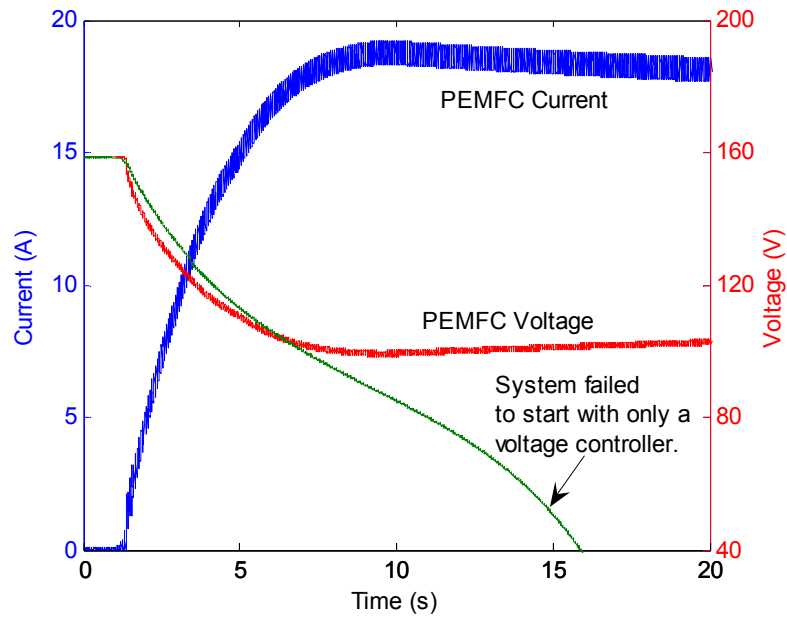


Figure 6.7. The PEMFC output current and voltage responses to the DC load transient shown in Figure 6.4.

Figures 6.8 and 6.9 show the simulation results when an AC load transient (Figure 6.5) is applied to the PEMFC-battery system. Figure 6.8 shows the reference signal ( $I_{ref}$ ) and the battery output current. The corresponding PEMFC output current and voltage are shown in Figure 6.9. The fuel cell output current ripple is around 5.5%, and the voltage ripple is around 2%. It is noted from these figures that the proposed control technique also works well under AC load transients, and the PEMFC voltage and current vary smoothly from one steady-state value to another.

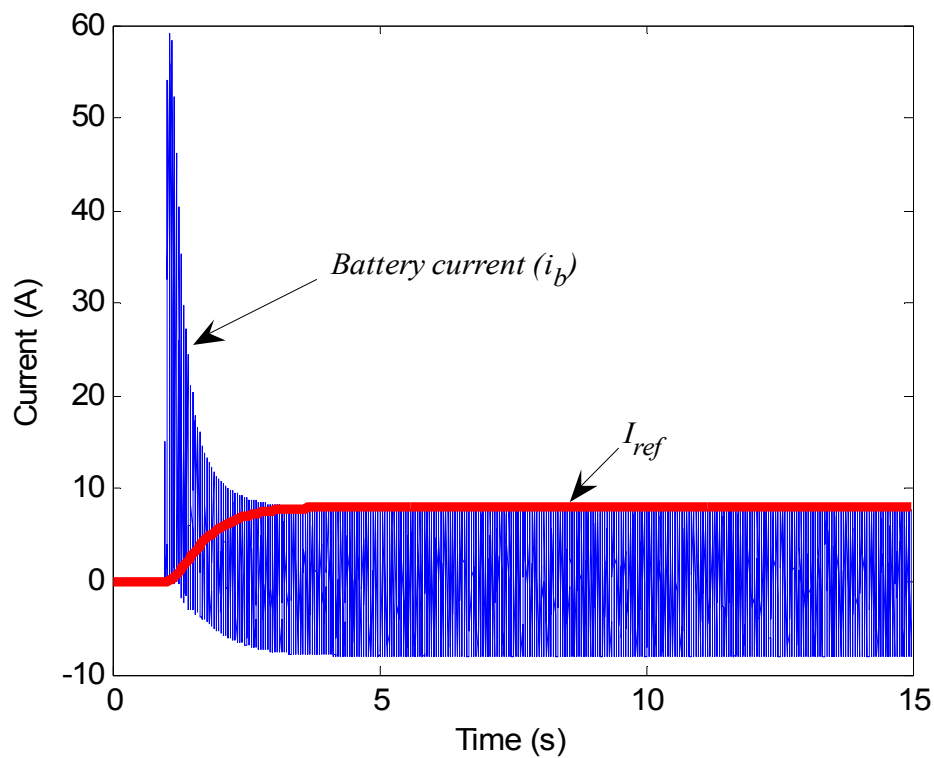


Figure 6.8. PEMFC: The control reference signal ( $I_{ref}$ ) and battery current ( $i_b$ ) under the AC load transient shown in Figure 6.5.

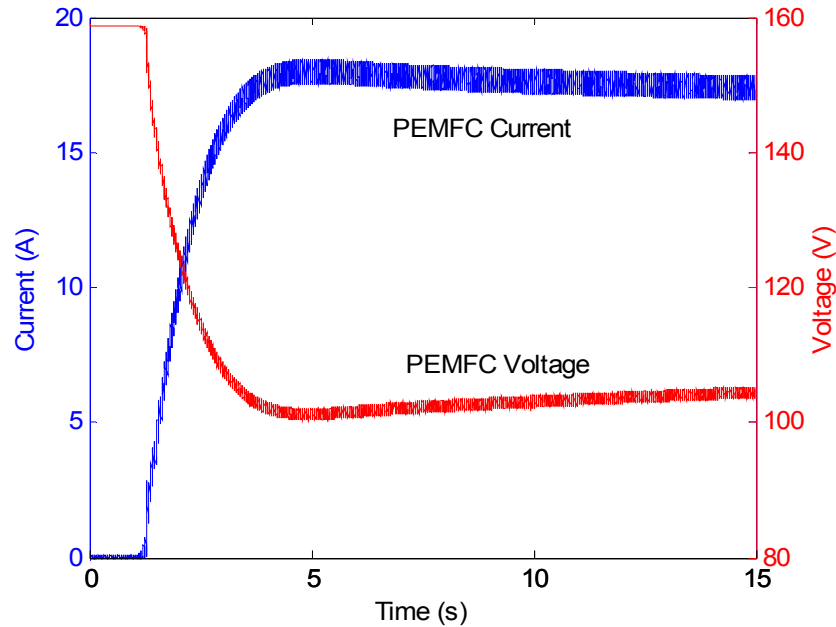


Figure 6.9. The PEMFC output current and voltage responses to the AC load transient shown in Figure 6.5.

SOFC System. Similar to the PEMFC system, the simulation study on the SOFC system under a DC load transient (Figure 6.4) is investigated first. The cut-off frequency of the low-pass filter is also chosen to be 0.1 Hz, and the damping factor is set to 1 as well. Figure 6.10 shows the current reference signal ( $I_{ref}$ ), the battery current ( $i_b$ ) and the converter output current ( $i_{dd\_out}$ ) responding to the load transient current. The figure shows that  $i_{dd\_out}$  follows the reference signal ( $I_{ref}$ ) very well for the SOFC system. The corresponding SOFC output current and voltage are given in Figure 6.11. It shows that the SOFC output voltage and current vary smoothly during the load transient. The SOFC is controlled to supply only the steady-state current to the load, and its output current ripple is less than 1.5%, which is much lower than the pre-set value (10%).

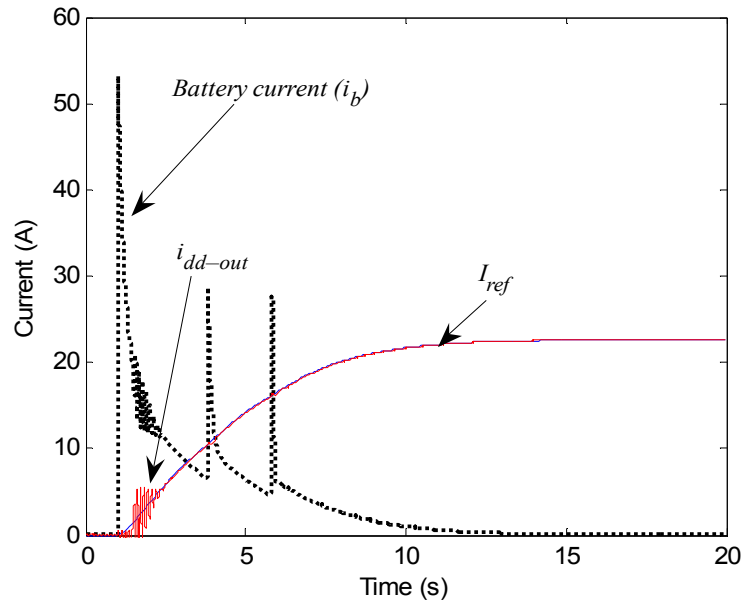


Figure 6.10. Reference signal ( $I_{ref}$ ) for the current controller, the battery current ( $i_b$ ) and the converter output current ( $i_{dd\_out}$ ) under the load transient for SOFC shown in Figure 6.4.

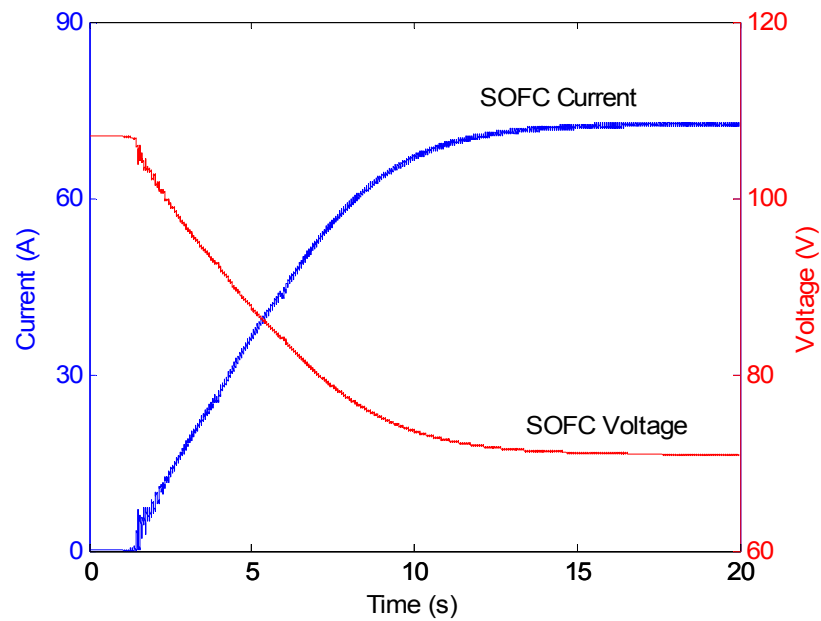


Figure 6.11. SOFC output current and voltage responses to the DC load transient shown in Figure 6.4.

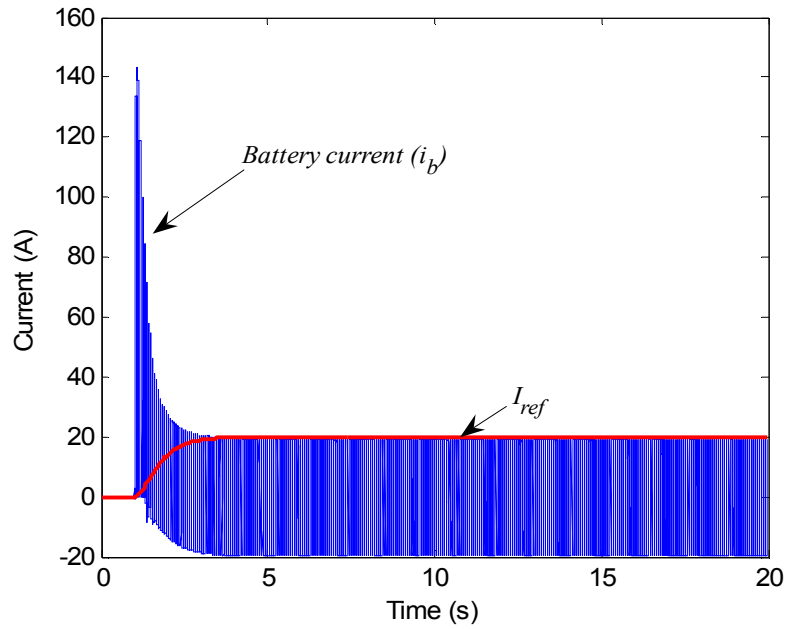


Figure 6.12. Control reference signal ( $I_{ref}$ ) and battery current ( $i_b$ ) under the AC load transient.

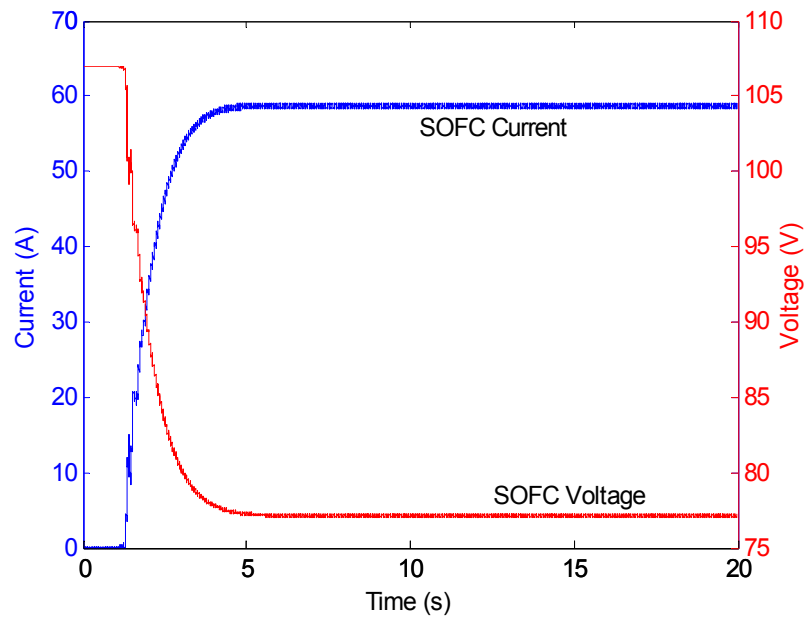


Figure 6.13. The SOFC output current and voltage responses to the AC load transient.

Figures 6.12 and 6.13 show the simulation results when an AC load transient (shown in Figure 6.5 but with different amplitude) is applied to the SOFC system. The reference signal ( $I_{ref}$ ) and the battery output current ( $i_b$ ) are given in Figure 6.12. It is clear from this figure that the battery responds to the transient part of the load, and the reference signal (for the DC/DC converter) rises smoothly to its new steady-state value. The corresponding SOFC output current and voltage under the AC load transient are shown in Figure 6.13. The SOFC output ripple is also very small in this case. Figures 6.12 and 6.13 show that the proposed control technique also works well for the SOFC system under AC load transients.

#### Battery Charging/Discharging

When the battery voltage is out of a certain range ( $\pm 5\%$  in this study), the battery charging/discharging controller (Figures 6.1 and 6.2) will start operating to bring the battery voltage back within the acceptable range. In practice, the battery normally needs to be charged after a load transient applied to the FC-battery system. This is because the transient power delivered from the battery to the load, together with the battery self-discharging characteristic, normally causes the battery voltage to drop. If the battery voltage drops below the pre-set value (95% of battery nominal voltage), the battery charging/discharging controller will start operating to charge the battery. Similarly, the battery charging/discharging controller will go into discharging mode, if the battery voltage goes above its pre-set limit (105% of battery nominal voltage). In this section simulation results are given for battery charging after the DC motor load transient (illustrated in Figure 6.4) is applied to the SOFC-battery system.

Figure 6.14 shows the battery voltage and the extra current reference ( $I_{ref2}$ , Figure 6.1) after the load transient is applied to the FC-battery system. Before the load transient starts, the battery voltage is already close to its lower limit (209V). During the transient, the battery voltage drops below the limit, which triggers the battery charging/discharging controller to start operating and generating a new  $I_{ref2}$ . This extra current reference is added to the current reference ( $I_{ref1}$ ) from the current filter to produce the new current reference signal ( $I_{ref}$ ) for the current controller (see Figure 6.1).

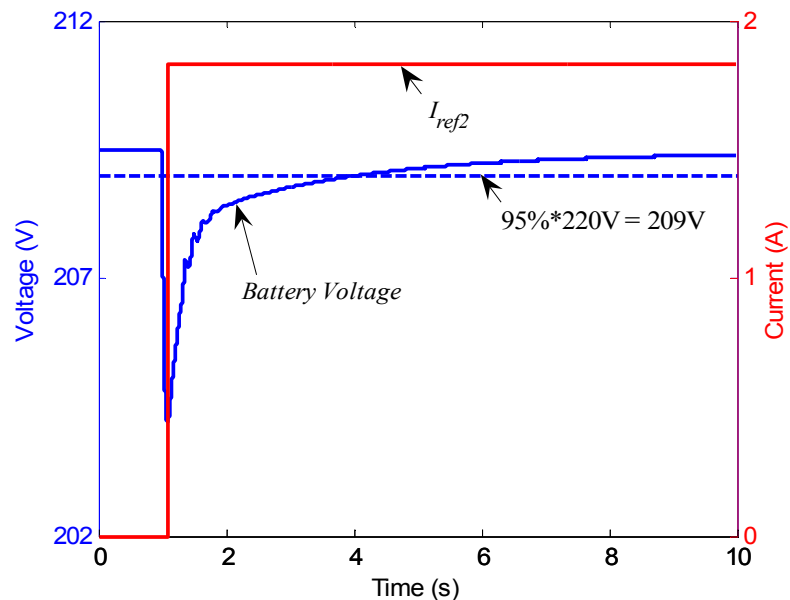


Figure 6.14. Battery voltage and extra current reference ( $I_{ref2}$ ) curves when the battery is being charged.

Figure 6.15 shows the load transient current, the overall current reference signal ( $I_{ref}$ ), the filter output reference signal ( $I_{ref1}$ ), the battery current ( $i_b$ ), and the corresponding converter output current ( $i_{dd\_out}$ ). It is clear from Figures 6.14 and 6.15 that during and after the transient load demand, the battery picks up the transient load (battery

discharging), and the reference currents ( $I_{ref1}$  and  $I_{ref}$ ) slowly increase to bring the fuel cell current to its new steady-state value and also charge the battery (battery charging). This smooth transition of FC current is essential for their improved reliability and durability.

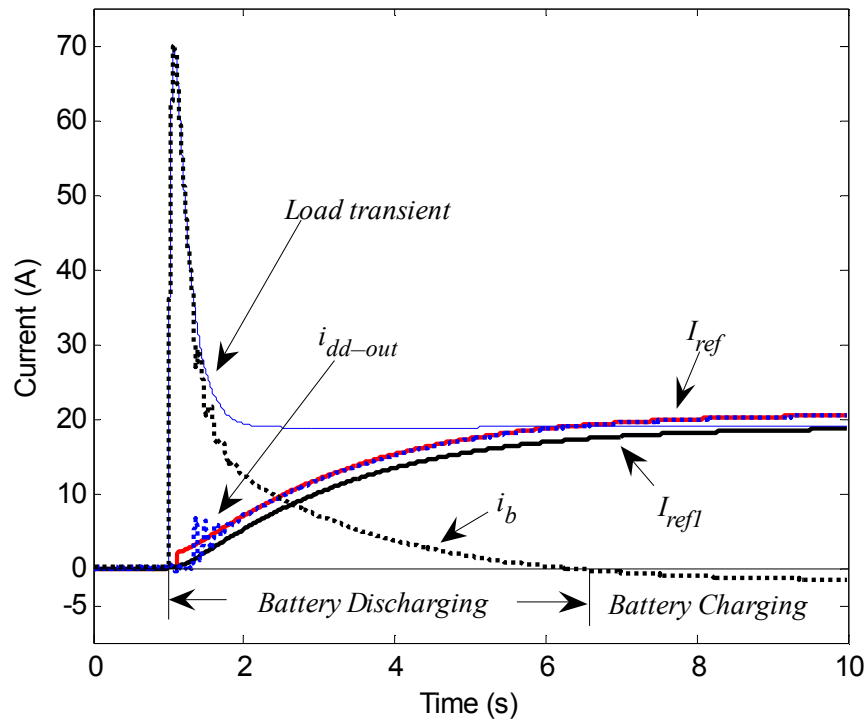


Figure 6.15. The load transient, the overall current control reference signal ( $I_{ref}$ ), the low-pass filter output signal ( $I_{ref1}$ ) and the corresponding converter output current ( $i_{dd\_out}$ ) when the battery is being charged.

### Summary

In this chapter, a load transient mitigation control strategy is proposed for fuel cell-battery power generation systems. The control strategy consists of a current controller for the DC/DC converter and a battery charging/discharging controller to keep the battery voltage within a desired range. During load transients, fuel cells are controlled (by the proposed transient mitigation technique) to supply the steady-state power to the load while the battery will supply the transient power to the load. Simulation studies under different load transients have been carried for both the PEMFC system and the SOFC system. Simulation results show that the fuel cell current can be controlled as desired and the battery voltage can be held in the prescribed range. The results show that the proposed load transient mitigation technique works well for both types of fuel cell systems (PEMFC and SOFC) studied.

REFERENCES

- [6.1] C. Wang, M.H. Nehrir, and S.R. Shaw, "Dynamic Models and Model Validation for PEM Fuel Cells Using Electrical Circuits," *IEEE Transactions on Energy Conversion*, vol. 20, no. 2, pp.442-451, June 2005.
- [6.2] R. S. Gemmen, "Analysis for the effect of inverter ripple current on fuel cell operating condition," *Transactions of the ASME - Journal of Fluids Engineering*, Vol. 125, No. 3, pp.576-585, May 2003.
- [6.3] J. C. Amphlett, E.H. de Oliveira, R.F. Mann, P.R. Roberge, Aida Rodrigues, "Dynamic Interaction of a Proton Exchange Membrane Fuel Cell and a Lead-acid Battery," *Journal of Power Sources*, Vol. 65, pp. 173-178, 1997.
- [6.4] D. Candusso, L. Valero and A. Walter, "Modelling, control and simulation of a fuel cell based power supply system with energy management," *Proceedings, 28<sup>th</sup> Annual Conference of the IEEE Industrial Electronics Society (IECON 2002)*, Vol. 2, pp.1294-1299, 2002.
- [6.5] James Larminie and Andrew Dicks, *Fuel Cell Systems Explained*, John Wiley & Sons, Ltd., pp. 362-367, 2001.
- [6.6] F. Z. Peng, H. Li; G. Su and J.S. Lawler, "A new ZVS bidirectional DC-DC converter for fuel cell and battery application," *IEEE Transactions on Power Electronics*, Vol.19, No. 1, pp.54-65, Jan. 2004.
- [6.7] K. Acharya, S.K. Mazumder, R.K. Burra, R. Williams, C. Haynes, "System-interaction analyses of solid-oxide fuel cell (SOFC) power-conditioning system," *Conference Record of the 2003 IEEE Industry Applications Conference*, Vol. 3, pp. 2026-2032, 2003.
- [6.8] S. K. Mazumder, K. Acharya, C. L. Haynes, R. Williams, Jr., M. R. von-Spakovsky, D.J. Nelson, D.F. Rancruel, J. Hartvigsen and R.S. Gemmen, "Solid-oxide-fuel-cell performance and durability: resolution of the effects of power-conditioning systems and application loads," *IEEE Transactions on Power Electronics*, Vol. 19, No. 5, pp.1263-1278, Sept. 2004.
- [6.9] C. Wang and M.H. Nehrir, "A Dynamic SOFC Model for Distributed Power Generation Applications," *Proceedings, 2005 Fuel Cell Seminar*, Nov. 14-18, 2005, Palm Springs, CA.

- [6.10] Z.M. Salameh, M.A. Casacca and W.A. Lynch, "A mathematical model for lead-acid batteries," *IEEE Transactions on Energy Conversion*, Vol. 7, No.1, pp. 93-98, 1992.
- [6.11] *Handbook of Batteries*, 2<sup>nd</sup> edition, D. Linden, Ed., McGraw Hill, Inc., New York, NY, 1995.
- [6.12] N. Mohan, T. M. Undeland and W. P. Robbins, *Power Electronics – Converters, Applications, and Design*, John Wiley & Sons , Inc., 2003.
- [6.13] John Van de Vegte, *Feedback Control Systems (3<sup>rd</sup> Edition)*, Prentice Hall, 1994.
- [6.14] D.W. Hart, *Introduction to Power Electronics*, Prentice Hall, 1997.
- [6.15] R. D. Middlebrook, "Small-signal modeling of pulse-width modulated switched-mode power converters," *Proceedings of the IEEE*, Vol. 76, No. 4, pp. 343 – 354, April 1988.

## CHAPTER 7

## CONTROL SCHEMES AND SIMULATION

## RESULTS FOR THE PROPOSED HYBRID WIND/PV/FC SYSTEM

Introduction

Based on the component models given in Chapter 4, a simulation system test-bed for the proposed hybrid alternative energy system (see Chapter 3) has been developed in MATLAB/Simulink. Figure 7.1 shows the overall diagram of the simulation model in MATLAB/Simulink. More details about the simulation model are given in Appendix B. The system is capable of being used as a test benchmark for other hybrid energy systems that are AC coupled. The overall control strategy for power management among different energy sources in the system is discussed in this chapter. The system performance under different operating conditions is evaluated and discussed as well.

System Control Strategy

Figure 7.2 shows the block diagram of the overall control strategy for the hybrid alternative energy system. The WTG, controlled by the pitch angle controller (see Chapter 4), and PV electricity generation unit, controlled by the MPPT controller (discussed in Chapter 4), are the main energy sources of the system. The power difference between the generation sources and the load demand is calculated as:

$$P_{net} = P_{wind} + P_{pv} - P_{load} - P_{sc} \quad (7.1)$$

where  $P_{wind}$  = power generated by the wind energy conversion system;

$P_{pv}$  = power generated by the PV energy conversion system;

$P_{load}$  = load demand;

$P_{sc}$  = self consumed power for operating the system.

The system self consumed power is the power consumed by the auxiliary system components to keep it running, for example, the power needed for running cooling systems, the control units, and the gas compressor. For the purpose of simplification, only the power consumed by the compressor ( $P_{comp}$ , defined in Chapter 4) is considered in this study.

#### Overall Power Management Strategy

The governing control strategy is that: At any given time any excess wind and PV generated power ( $P_{net} > 0$ ) is supplied to the electrolyzer to generate hydrogen that is delivered to the hydrogen storage tanks through a gas compressor. Therefore, power balance equation (7.1) can be written as

$$P_{wind} + P_{pv} = P_{load} + P_{elec} + P_{comp}, \quad P_{net} > 0 \quad (7.2)$$

where  $P_{elec}$  = the power consumed by the electrolyzer to generate H<sub>2</sub>;

$P_{comp}$  = the power consumed by the gas compressor.

When there is a deficit in power generation ( $P_{net} < 0$ ), the FC stack begins to produce energy for the load using hydrogen from the storage tanks. Therefore, the power balance equation can be written as

$$P_{wind} + P_{pv} + P_{FC} = P_{load}, \quad P_{net} < 0 \quad (7.3)$$

where  $P_{FC}$  = the power generated by the FC stack.

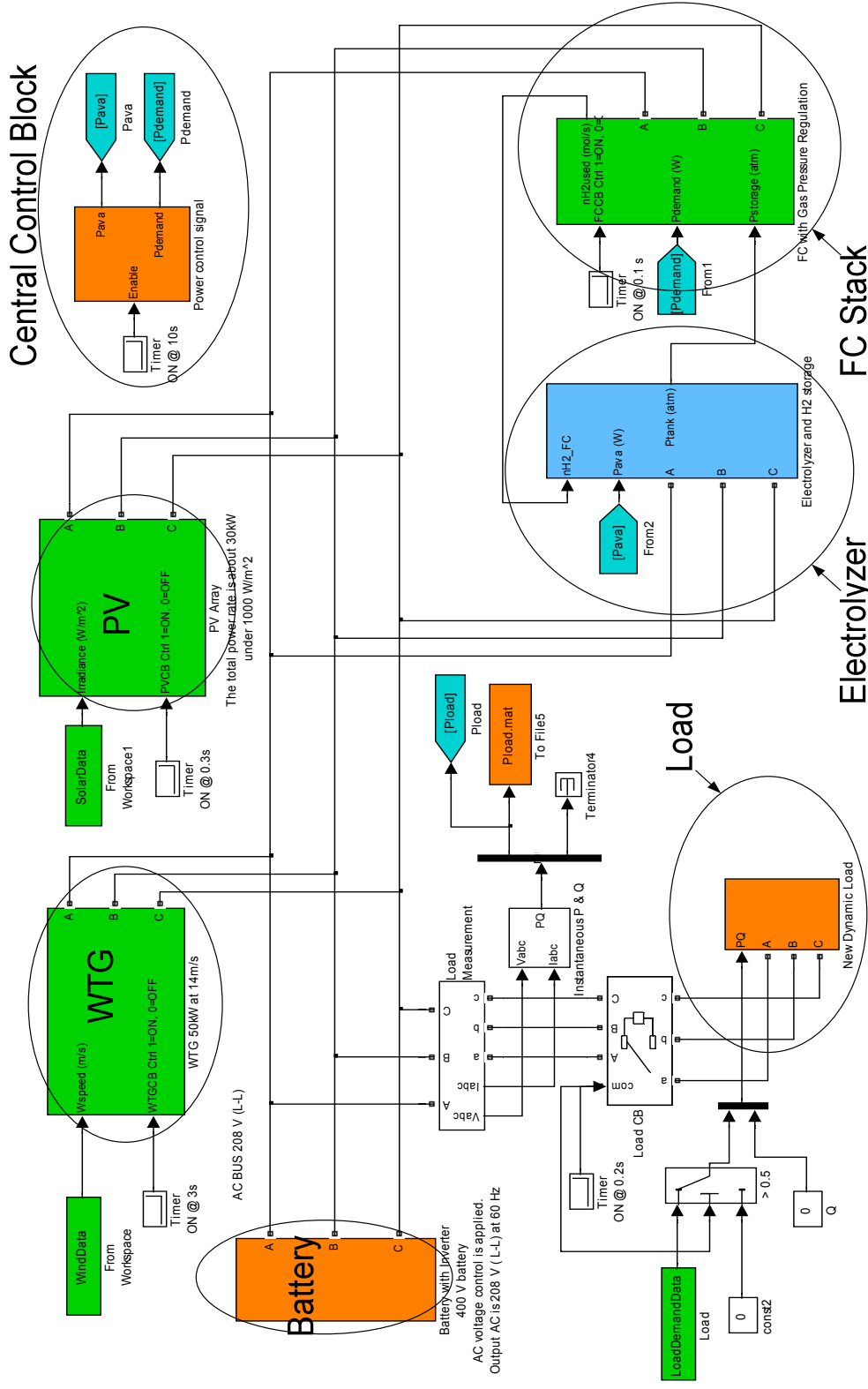


Figure 7.1. Simulation model for the proposed hybrid alternative energy system in MATLAB/Simulink.

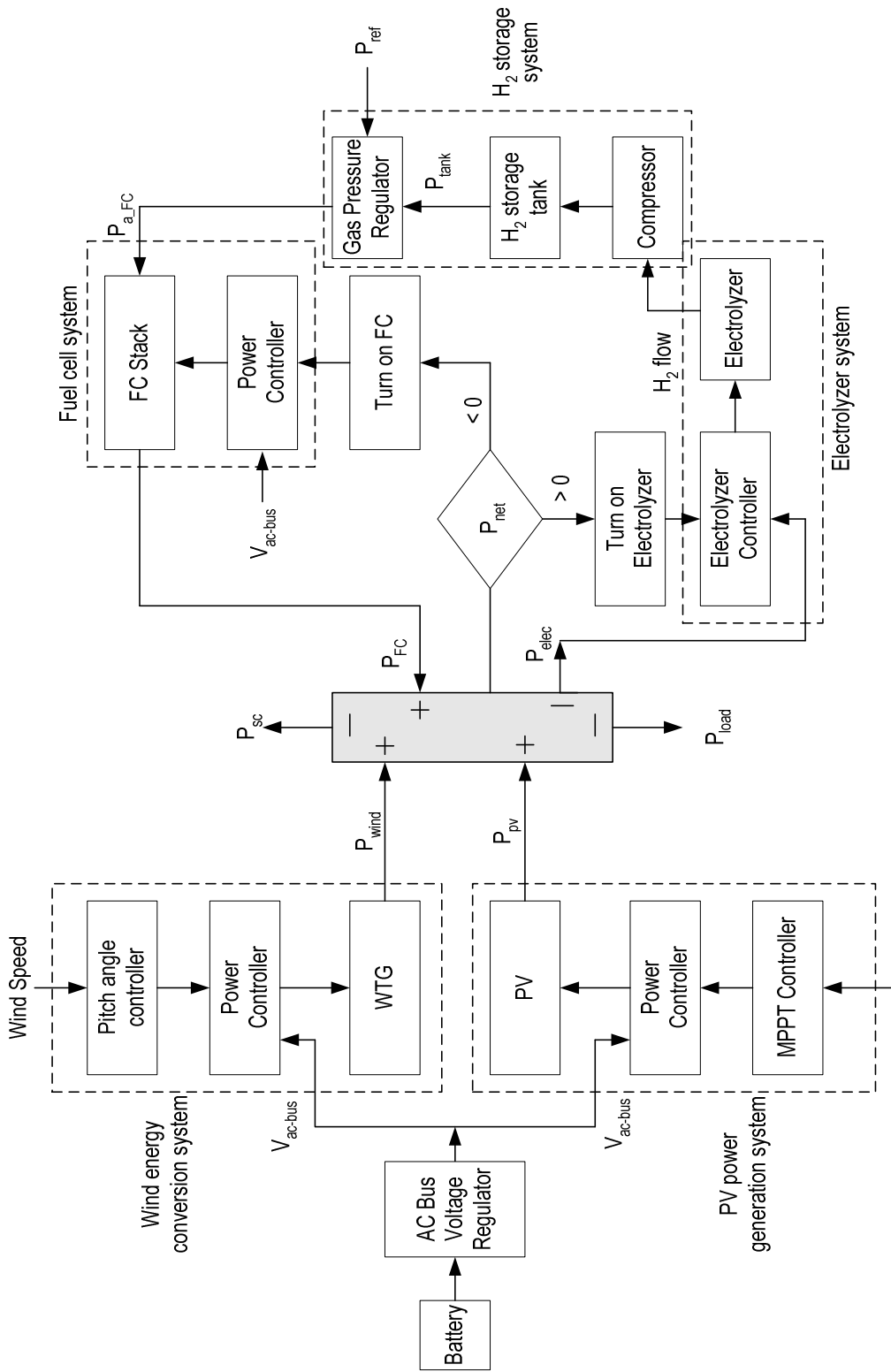


Figure 7.2. Block diagram of the overall control scheme for the proposed hybrid alternative energy system.

The power controller has been discussed in Chapter 5 (see Figure 5.11). The model for the gas pressure regulator has been discussed in Chapter 4. In the following sections, the AC bus voltage regulator and the electrolyzer controller are discussed in details.

### AC Bus Voltage Regulator

Figure 7.3 shows the block diagram of the AC bus voltage regulator. In the figure, the AC bus voltage is measured and transformed into  $dq$  values ( $V_{d,q}$ ) through the “ $abc/dq$  Transformation” block.  $V_{d,q}$  is then compared with the reference voltage  $dq$  values ( $V_{d,q(ref)}$ ) and the voltage error signals are fed into a PI controller. The controller output is transferred back into the control signals in  $abc$  coordinates through the “ $dq/abc$  Transformation” block. These control signals are used to generate proper SPWM pulses for the inverter switches, which shape the inverter output voltage (the AC bus voltage).

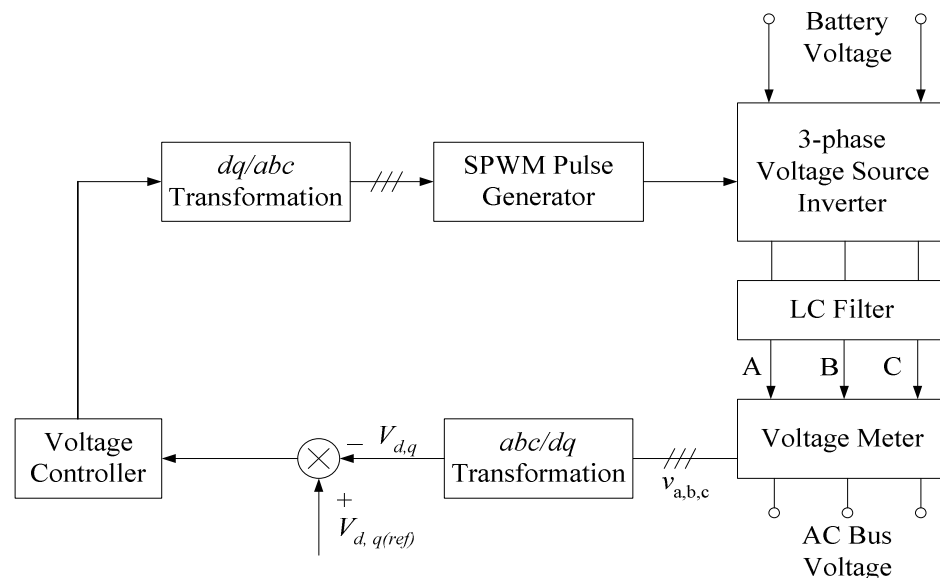


Figure 7.3. Block diagram of the AC voltage regulator.

### Electrolyzer Controller

The block diagram of the electrolyzer controller is shown in Figure 7.4. As discussed in Chapter 4 (section 4.4), an electrolyzer can be considered as a voltage-sensitive nonlinear DC load. For the given electrolyzer within its rating range, the higher the DC voltage applied to it, the larger is the load current and the more  $H_2$  is generated. The function of the electrolyzer controller is to control the controllable AC/DC rectifier to obtain a proper output DC voltage ( $V_{dc,elec}$ ) so that the excess available power can be fully used by the electrolyzer to generate  $H_2$ . For example, if more power is available, then the controller controls the rectifier to give a higher DC voltage ( $V_{dc,elec}$ ) to the electrolyzer. As a result, the power consumed by the electrolyzer ( $P_{elec}$ ) becomes greater so that it matches the excess available power.

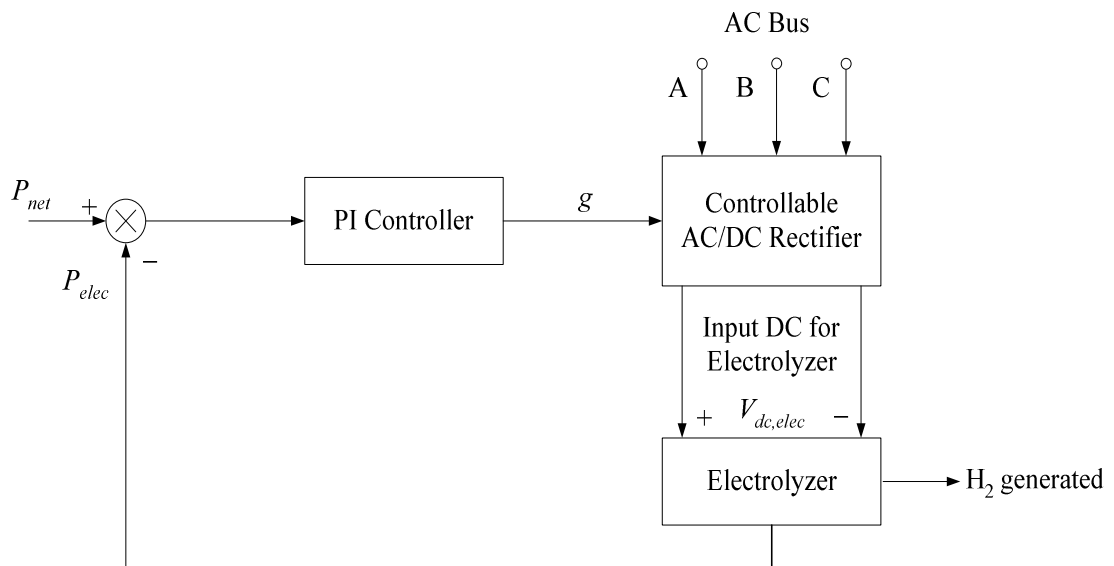


Figure 7.4. Block diagram of the electrolyzer controller.

### Simulation Results under Different Scenarios

In order to run the simulation for the hybrid alternative energy system, the load demand data and the weather data (wind speed, solar irradiance and air temperature) are needed. As discussed in Chapter 3, the system is designed to supply electric power for five houses in southeastern part of Montana. A typical load demand for a house in the Pacific Northwest regions, reported in [7.1], is used in this simulation study. The total load demand profile of five houses has already been given in Chapter 3. For the purpose of convenience, the load demand profile over 24 hours is also given in this chapter, shown in Figure 7.5. The weather data are obtained from the online records of the weather station at Deer Lodge, Montana, affiliated to the Pacific Northwest Cooperative Agricultural Weather Network (AgriMet) [7.2]. The general information about the station and the types of relevant equipment and sensors used at the station are summarized in Table 7.1 [7.2]. Simulation studies are carried out for power management during a typical winter and summer day. The load demand is kept the same for the two cases. Simulation results for the winter and summer scenarios are given and discussed in the following sections.

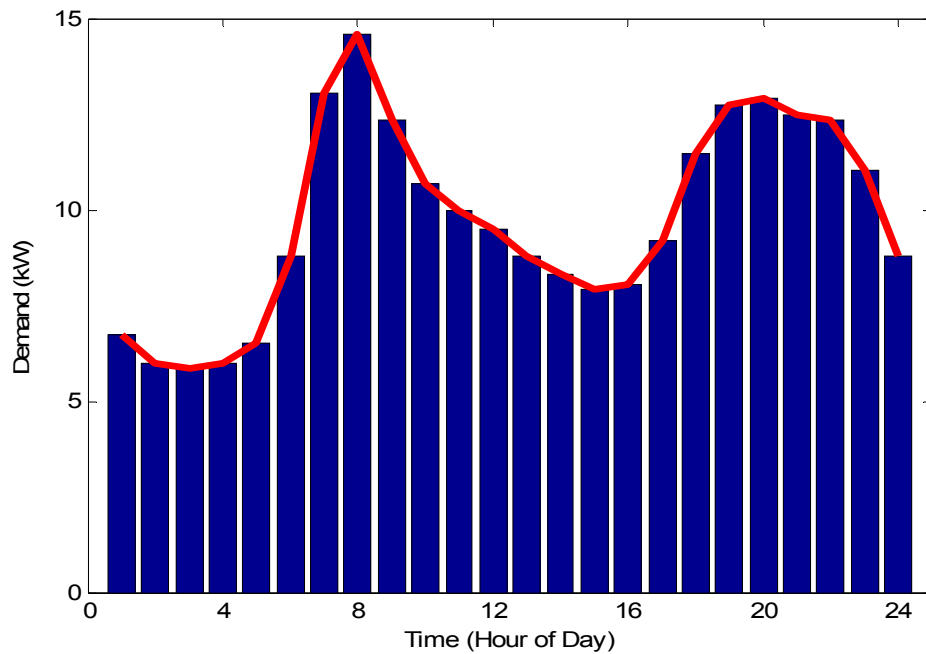


Figure 7.5. Load demand profile over 24 hours for the system simulation study.

TABLE 7.1. WEATHER STATION INFORMATION  
AT DEER LODGE, MONTANA AGRIMET STATION (DRLM)

General Information	
Latitude	46° 20' 08"
Longitude	112° 46' 00"
Elevation	4680'
Equipment and Sensors	
Sensors	Sensor Height
Pyranometer Model LI-200SB	3 meters
Wind Monitor Model 05103	2 meters
Air Temperature Thermistor Model 44030	2 meters

### Winter Scenario

Weather Data. The weather data for the winter scenario simulation were collected on February 1, 2006. The wind speed data were collected at the height of 2 m. The wind turbine hub height is. The wind speed data were corrected to the turbine hub height (assumed to be 40 meters) using the following expression [7.3], [7.4]:

$$W_{s1} = W_{s0} \left( \frac{H_1}{H_0} \right)^\alpha \quad (7.4)$$

where  $W_{s1}$  = wind speed at the height of  $H_1$ (m/s);

$W_{s0}$  = wind speed at the height of  $H_0$  (m/s);

$\alpha$  = wind speed correction exponent.

The exponent  $\alpha$  is taken as 0.13 in this study, as suggested and used in [7.3] and [7.4].

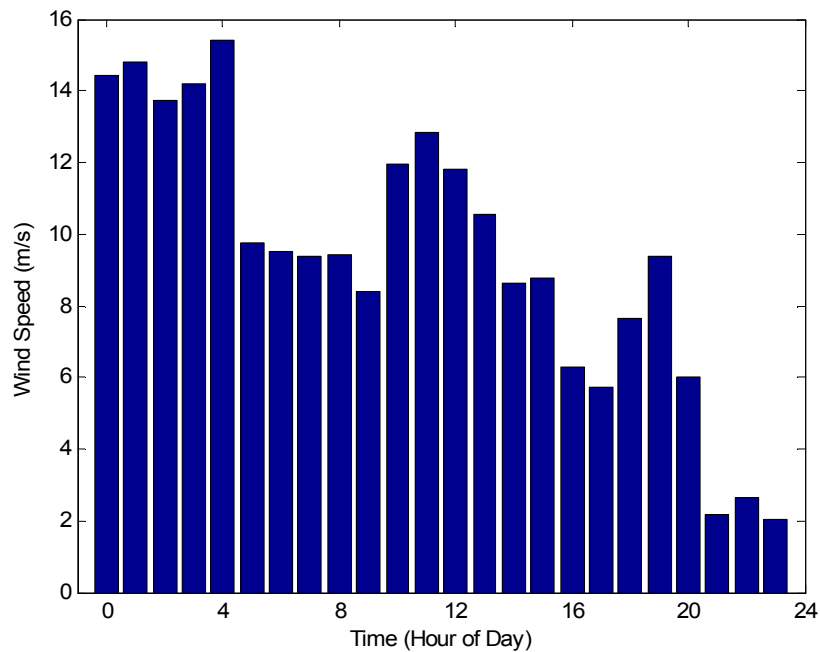


Figure 7.6. Wind speed data for the winter scenario simulation study.

Figure 7.6 shows the corrected hourly wind speed profile over 24 hours on the day the data were collected. The hourly solar irradiance data and air temperature collected on the same winter day are shown in Figures 7.7 and 7.8, respectively.

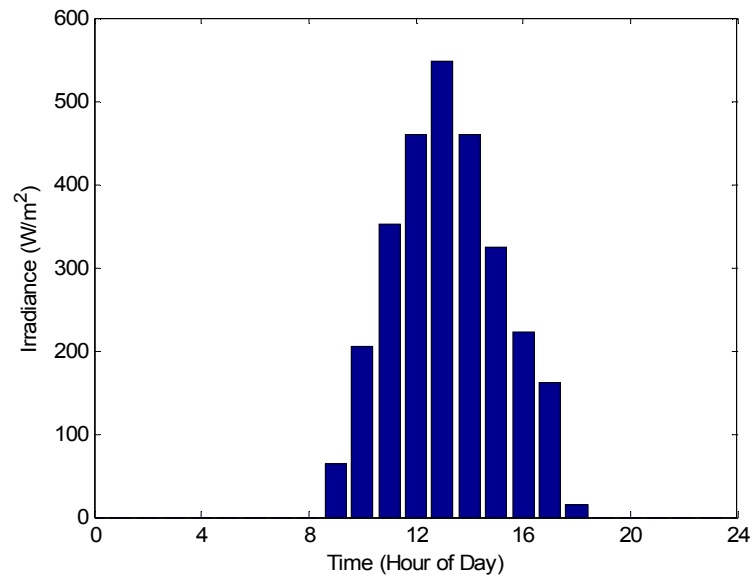


Figure 7.7. Solar irradiance data for the winter scenario simulation study.

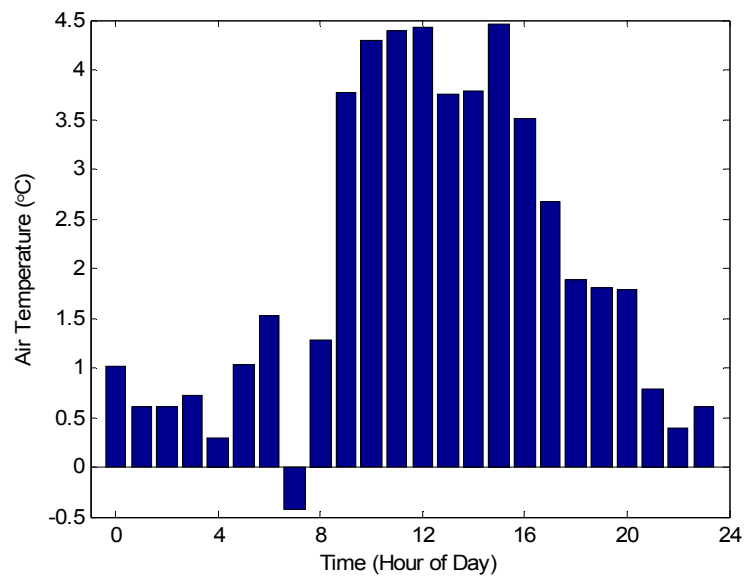


Figure 7.8. Air temperature data for the winter scenario simulation study.

Simulation Results. The system performance under the load profile given in Figure 7.5 and the weather data shown in Figures 7.6 to 7.8 is evaluated and discussed below.

The output power from the wind energy conversion unit in the hybrid energy system over the 24 hour simulation period is shown in Figure 7.9. When the wind speed is over 14 m/s, the output power is limited at 50 kW by pitch angle controller (see Figure 4.34 in Chapter 4). The pitch angle curve over the 24 hour is given in Figure 7.10. It is noted from the figure that the pitch angle is increased to limit the wind turbine output power when wind speed is greater than 14 m/s. Otherwise, the pitch angle is kept at 2° (see Figure 4.32 in Chapter 4). The corresponding rotor speed of the induction generator is given in Figure 7.11. It is noted that the rotor speed variation follows as the wind speed variation.

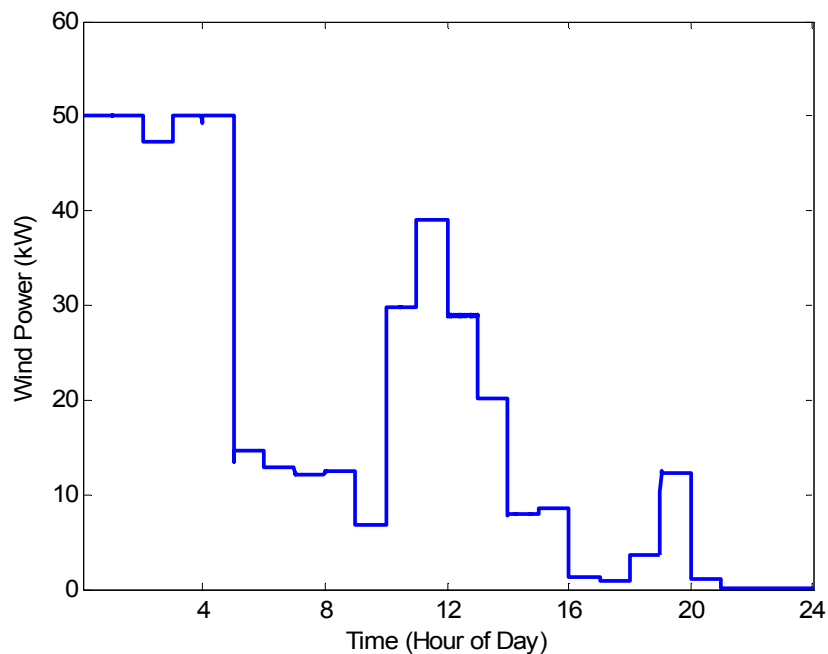


Figure 7.9. Wind power of the winter scenario study.

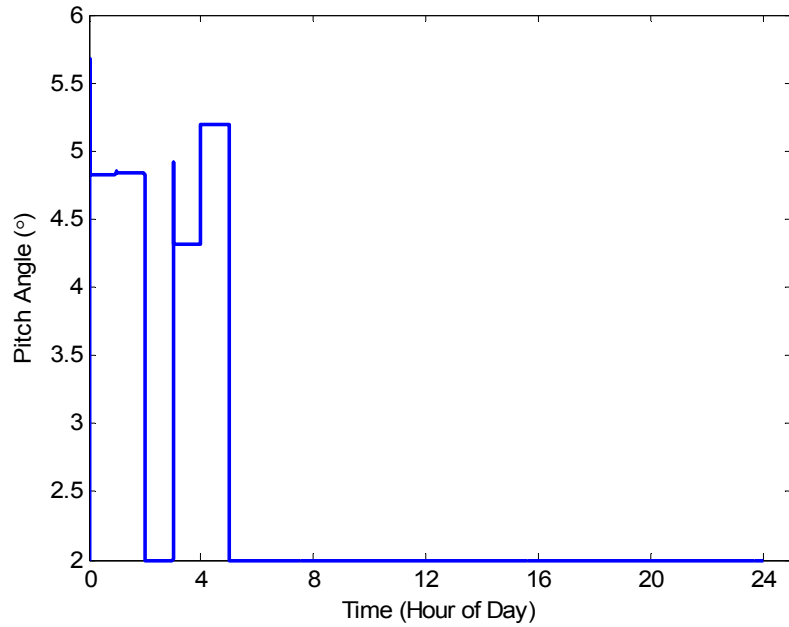


Figure 7.10. Pitch angle of the wind turbine of the winter scenario study.

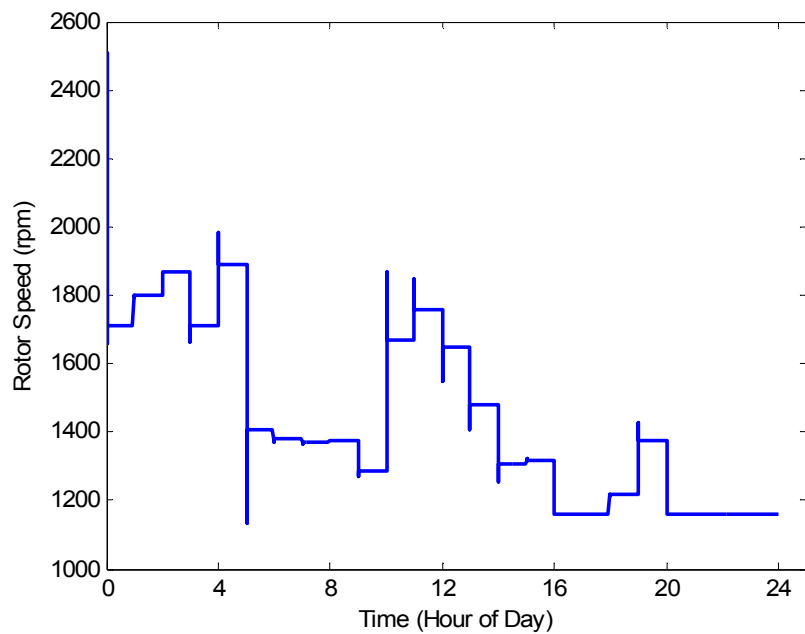


Figure 7.11. Rotor speed of the induction generator of the winter scenario study.

The output power from the PV array in the system over the 24 hour simulation period is shown in Figure 7.12. As discussed in Chapter 4, the PV array output power is controlled by the current maximum power point tracking (CMPPT, see Figure 4.57 in Chapter 4) technique to give the maximum power output under different solar irradiances. Figure 7.13 shows the current difference ( $I_{pv,err}$ ) between the actual the output current ( $I_{pv}$ ) of a PV module and the reference current ( $I_{mp}$ ) at the maximum power point. It is noted that the PV output current follows the reference current very well using the CMPPT method. The current error is almost zero at steady state.

As shown in Figures 4.53 and 4.54 in Chapter 4, temperature plays an important role in the PV cell's performance. The PV cell temperature is estimated by the PV thermal model, discussed in Chapter 4. Figure 7.14 shows the PV temperature response over the simulation period. Two main factors for determining the temperature are the solar irradiance and the air temperature (surrounding temperature) as shown in Figures 7.7 and 7.8. It is noted from Figures 4.53 and 4.54 that the higher the temperature, the lower is the maximum power value. This effect of temperature upon the PV performance is also illustrated by investigating Figure 7.12 and 7.14. For the purpose of comparison, the air temperature profile is also given in Figure 7.14.

When  $P_{net} > 0$ , there is excess power available for H<sub>2</sub> generation. Figure 7.15 shows the available power profile over the 24 hour simulation period. The available power is used by the electrolyzer to generate H<sub>2</sub> through the electrolyzer controller shown in Figure 7.4. Figure 7.16 shows the H<sub>2</sub> generation rate over the simulation period. The corresponding DC voltage applied to the electrolyzer and the electrolyzer current are shown in Figure 7.17. It is noted from Figures 7.15 to 7.17 that the more power available

for storage, the higher is the DC input voltage to the electrolyzer, and the more is the  $H_2$  generated as a result.

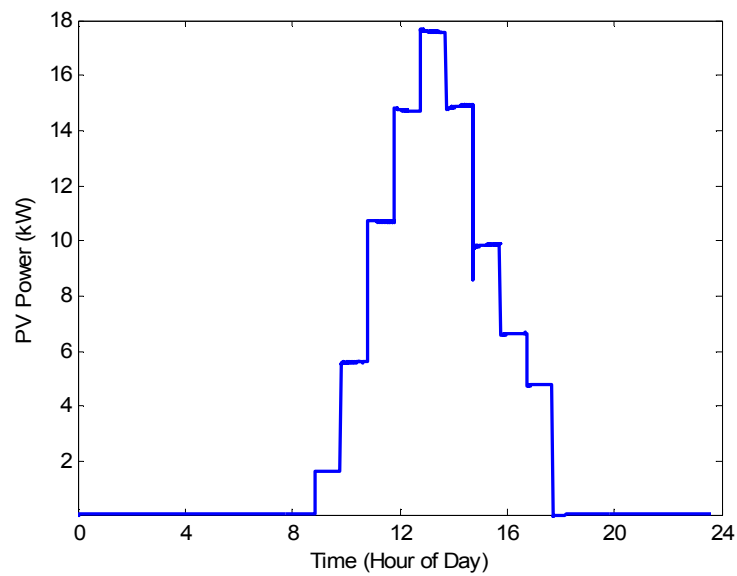


Figure 7.12. PV power for the winter scenario.

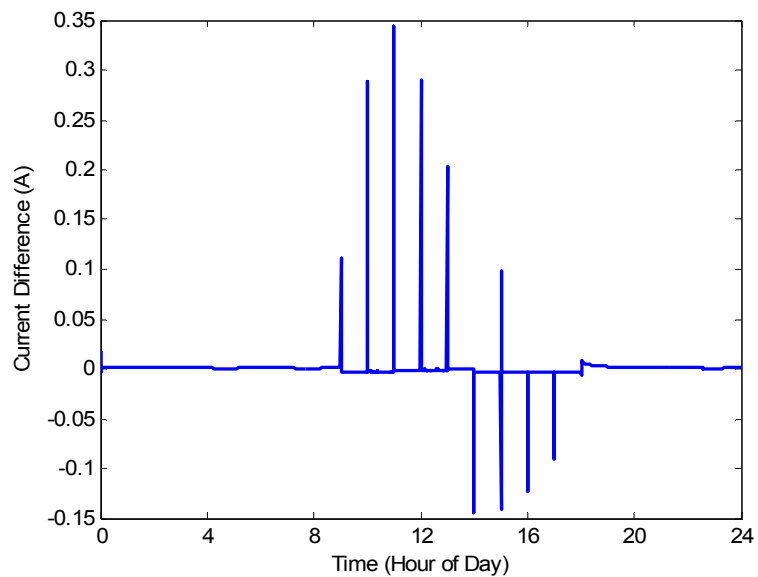


Figure 7.13. Current difference between the actual output current and the reference current for the maximum power point of the winter scenario.

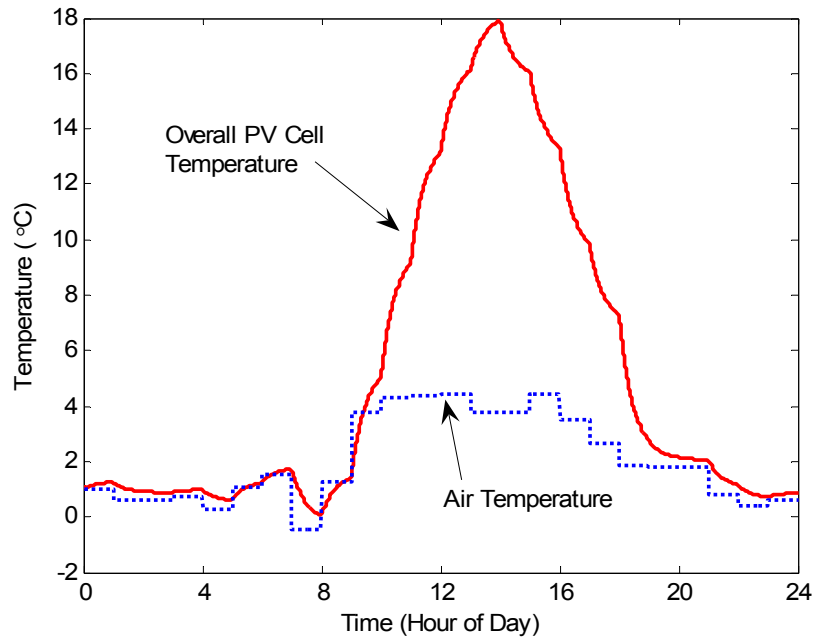


Figure 7.14. The PV temperature response over the simulation period for the winter scenario.

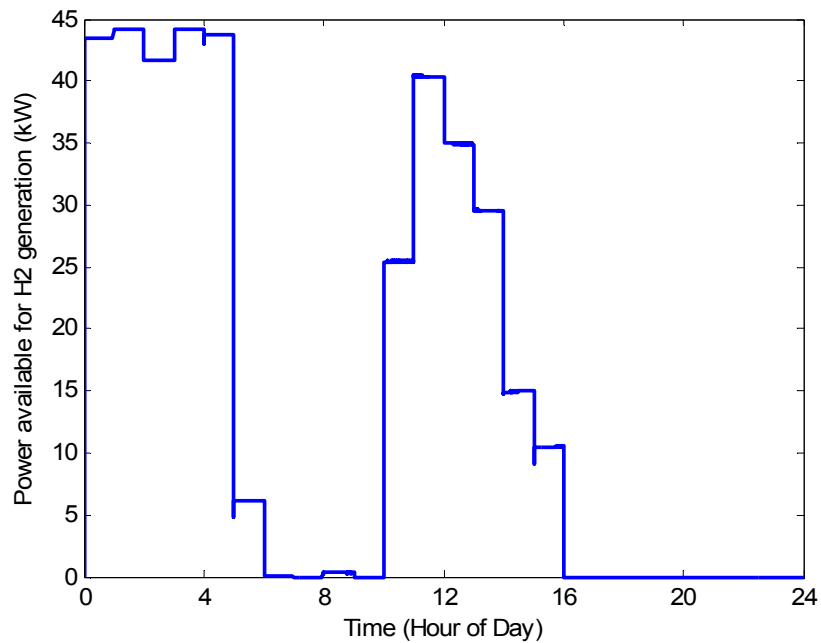


Figure 7.15. Power available for H2 generation of the winter scenario.

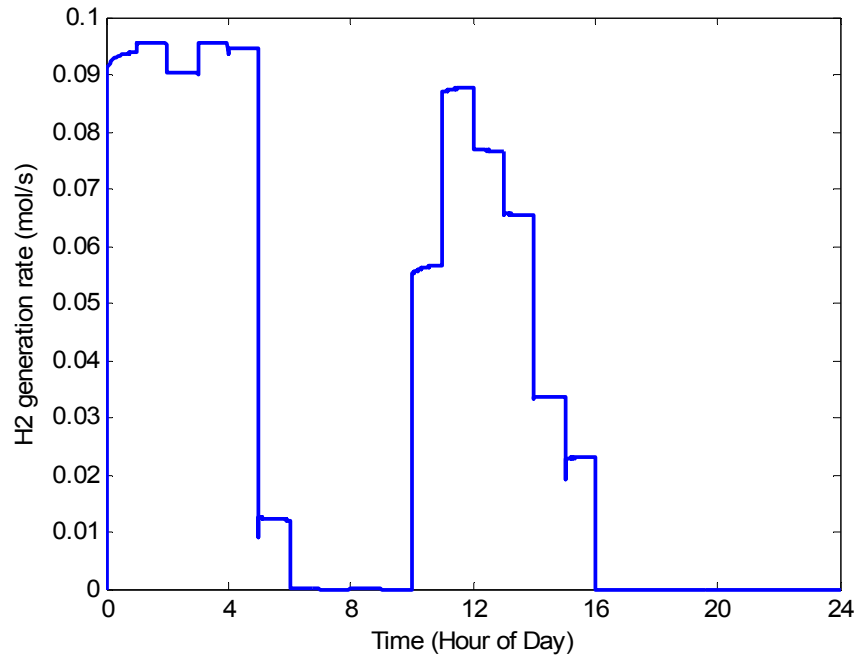


Figure 7.16. H<sub>2</sub> generation rate of the winter scenario study.

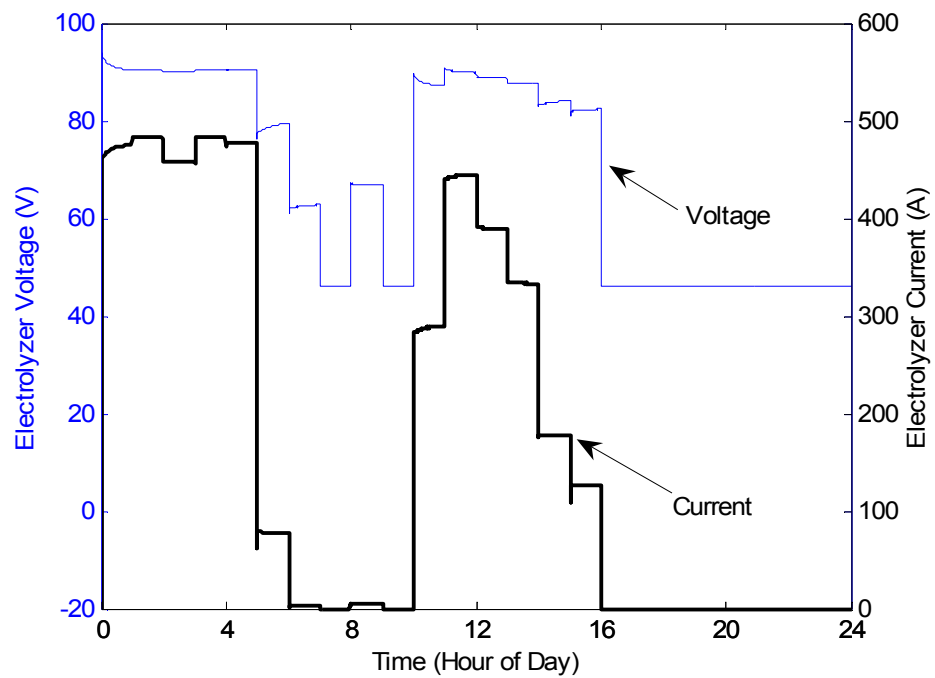


Figure 7.17. Electrolyzer voltage and current for the winter scenario study.

When  $P_{net} < 0$ , the wind and PV generated power from is not sufficient to supply the load demand. Under this condition, the fuel cell turns on to supply the power shortage. Figure 7.18 shows the power shortage which should be supplied by the FC. The actual power delivered by the FC is given in Figure 7.19 and the corresponding  $H_2$  consumption rate is given in Figure 7.20. Note that Figures 7.18, 7.19 and 7.20 have similar pattern as expected.

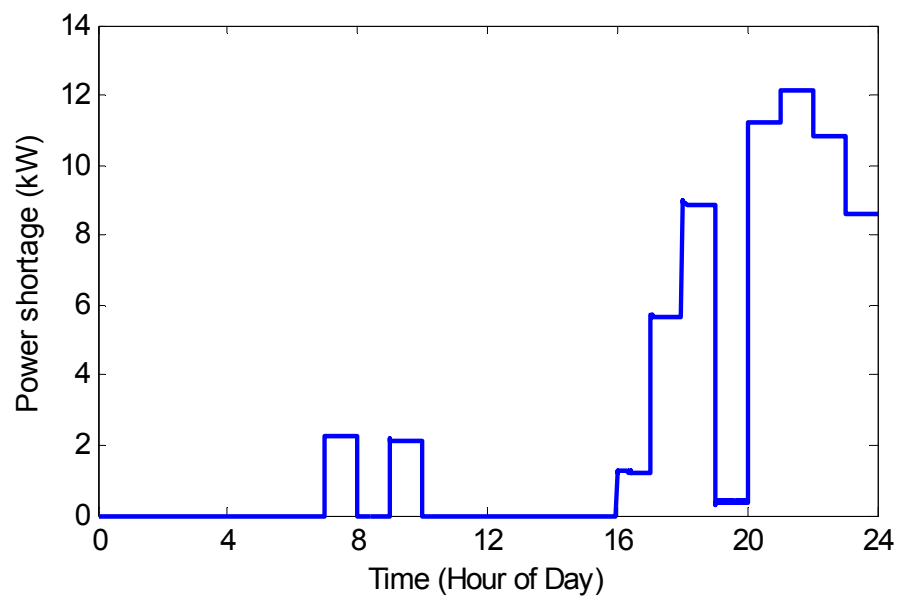


Figure 7.18. Power shortage over the simulation period of the winter scenario study.

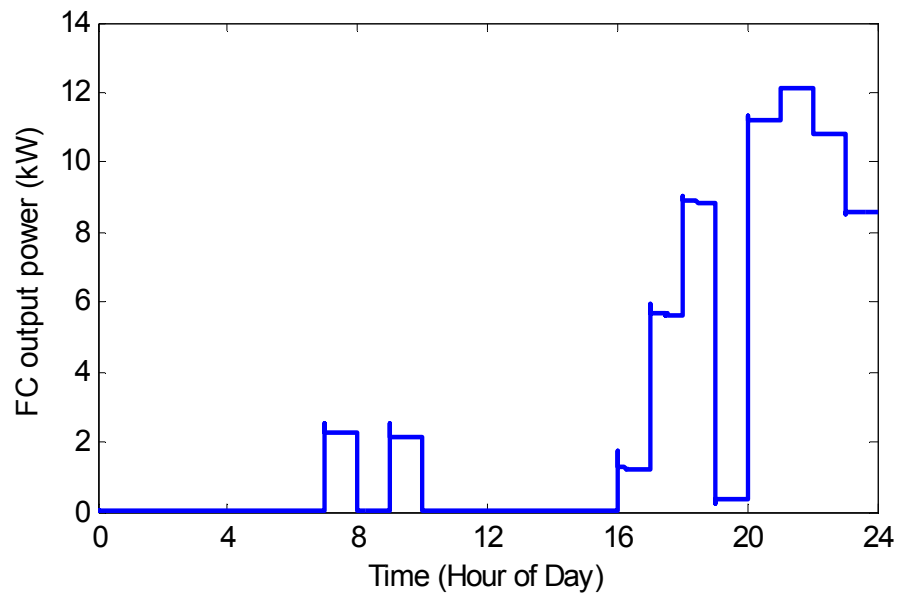


Figure 7.19. Power supplied by the FC of the winter scenario study.

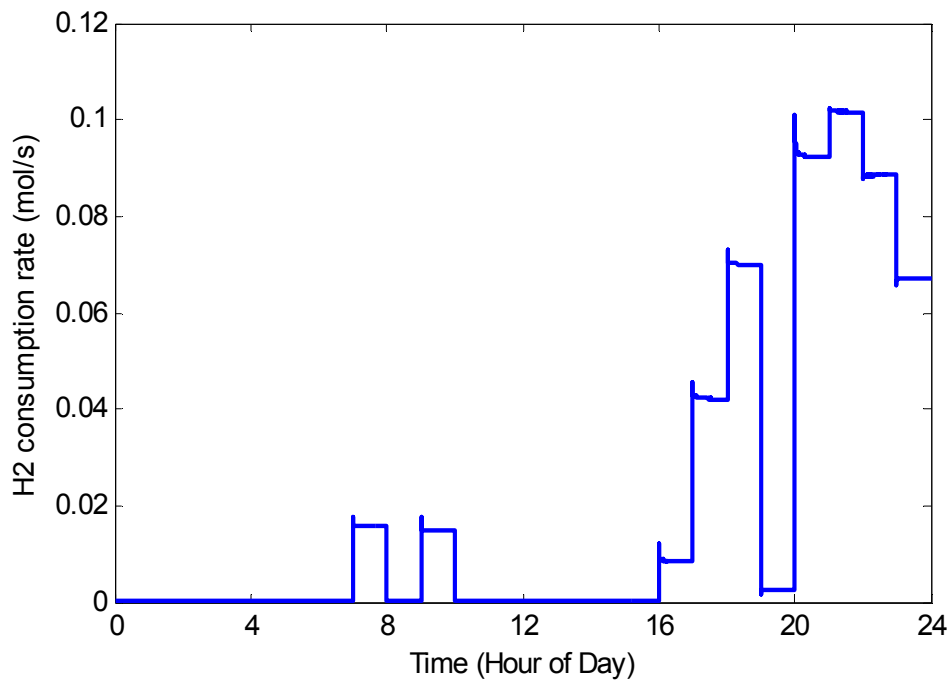


Figure 7.20. H2 consumption rate of the winter scenario study.

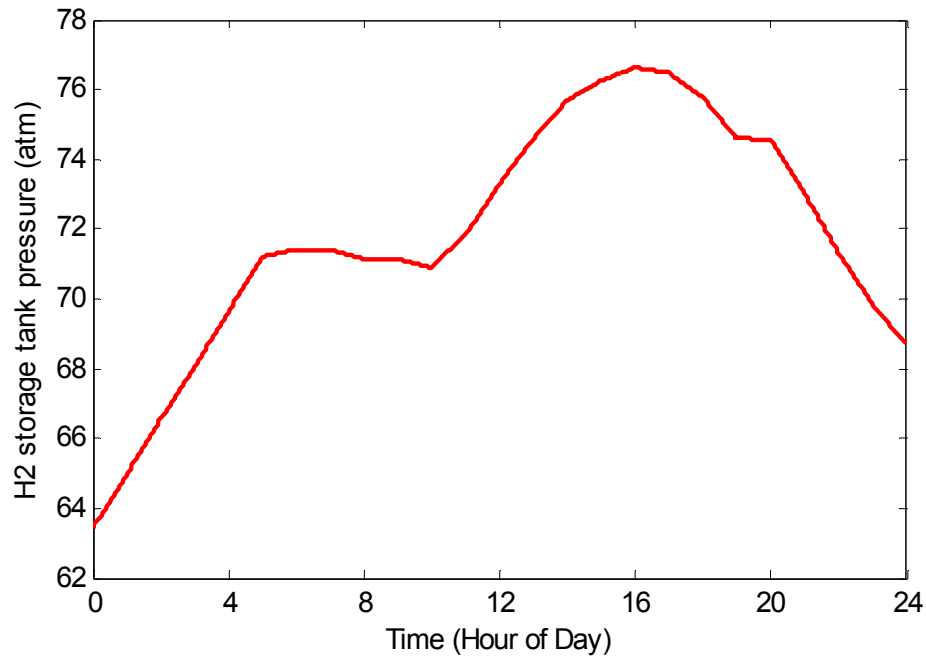


Figure 7.21. The pressure tank over the 24 hour of the winter scenario study.

The H<sub>2</sub> storage tank pressure varies as H<sub>2</sub> flows in and out. It is apparent that the storage tank pressure will go up when there is excess power available for H<sub>2</sub> generation and will decrease when the FC supplies power to load and consumes H<sub>2</sub>. Figure 7.21 shows the tank pressure variations over the 24 hour simulation period.

As discussed in Chapter 3, the capacity of the battery in the proposed hybrid system is much smaller than the one used in a conventional system where the battery is taken as the main storage device. Figure 7.22 shows the battery power profile over the 24 hour simulation period. The positive spikes indicate the battery is discharging and the negative ones indicate the battery is being charged. It is noted from the figure that the battery power is zero almost at all time. As discussed in Chapter 3, the battery only supplies the fast transient power, such as fast load transients, ripples, and spikes.

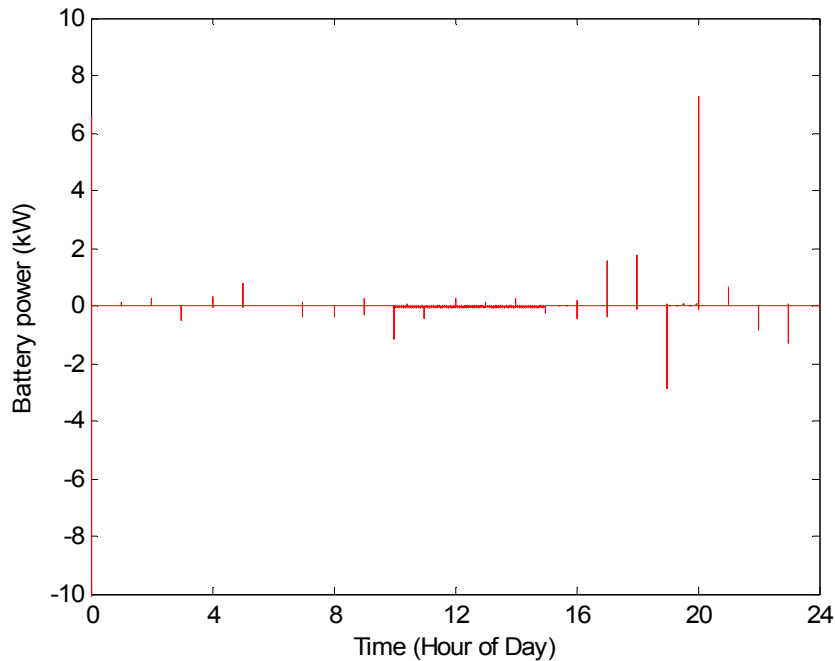


Figure 7.22. The battery power over the simulation period for the winter scenario.

### Summer Scenario

Weather Data. The weather data collected in Dear Lodge, MT on June 21, 2005 are used for the summer scenario study [7.2]. The wind speed data are corrected to the height of 40 m, shown in Figure 7.23. The solar irradiance and air temperature data at the same site on the same day are shown in Figures 7.24 and 7.25, respectively.

By comparing the winter solar irradiance data shown in Figure 7.7 and the summer solar irradiance data given in Figure 7.24, it is obvious that the time frame when solar energy is available is wider in the summer than in the winter. Another apparent difference is that the air temperature in the summer (shown in Figure 7.25) is, of course, higher than the air temperature in the winter (shown in Figure 7.8).

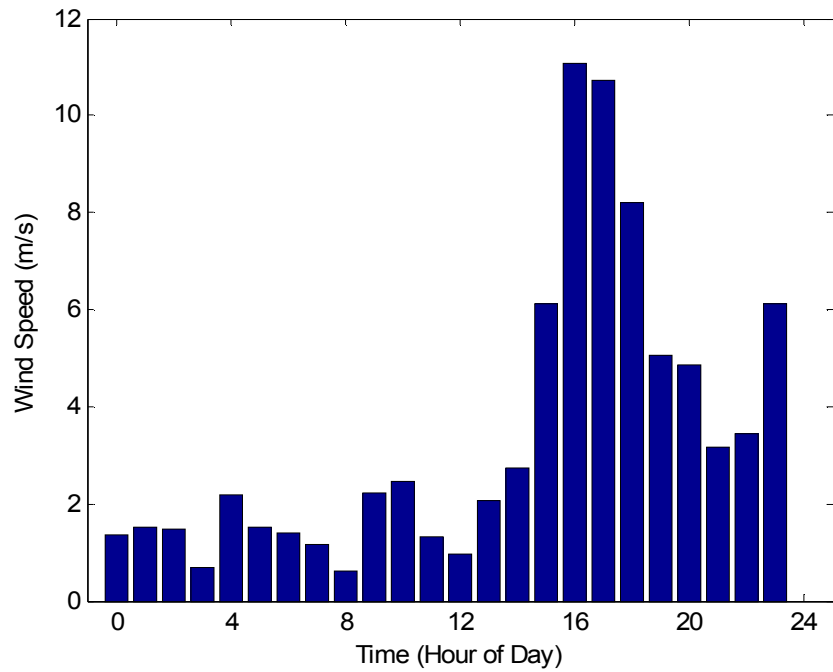


Figure 7.23. Corrected wind speed data for the summer scenario simulation study.

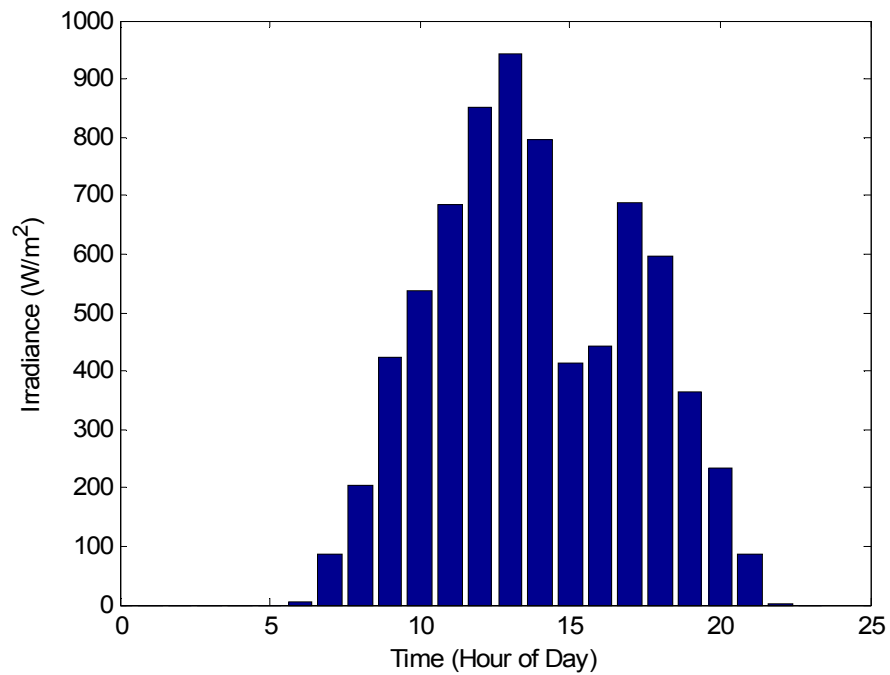


Figure 7.24. Irradiance data for the summer scenario simulation study.

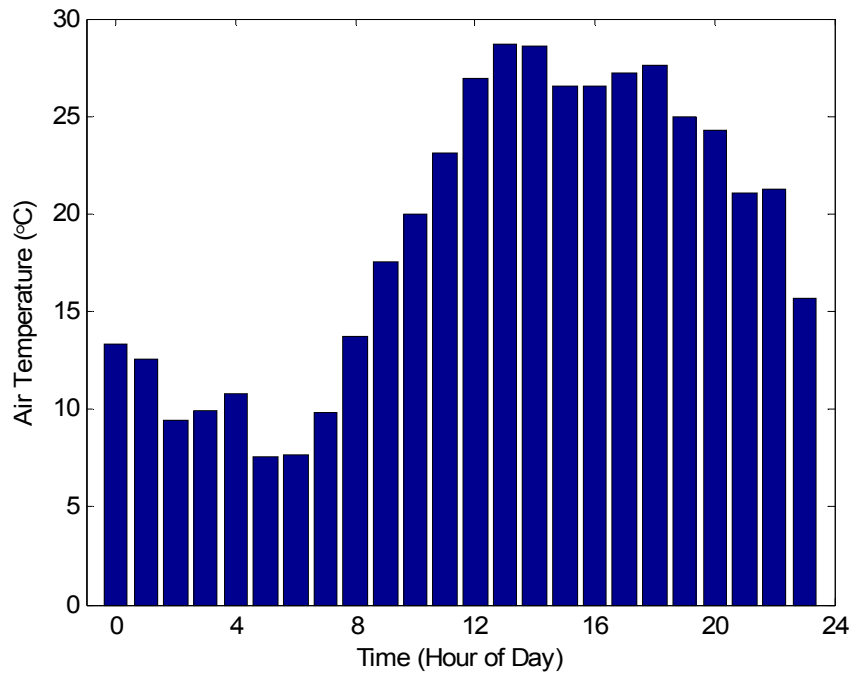


Figure 7.25. Air temperature data for the summer scenario simulation study.

Simulation Results. In this section, the system performance under the load demand profile given in Figure 7.5 and the weather data shown in Figures 7.23 to 7.25 is evaluated. The output power from the wind energy conversion unit in the hybrid energy system over the 24 hour simulation period is shown in Figure 7.26. The corresponding rotor speed of the induction generator is given in Figure 7.27.

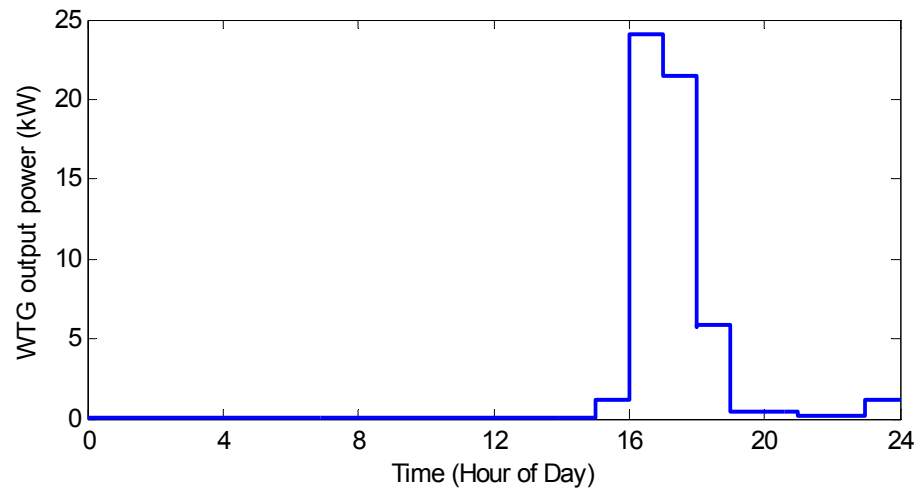


Figure 7.26. Wind power generated for the summer scenario study.

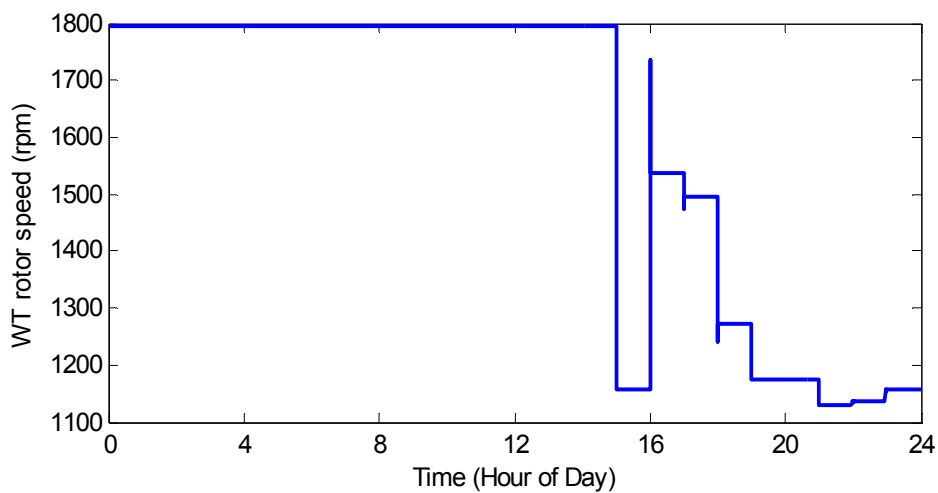


Figure 7.27. Rotor speed of the induction generator for the summer scenario study.

The output power from the PV array in the system over the 24 hour simulation period is shown in Figure 7.28. Figure 7.29 shows the PV temperature response over the simulation period. For the purpose of comparison, the air temperature profile is also illustrated in the figure. It is noted from Figure 7.29 that the PV cells cool down to about the same temperature as air when there is no sun. The cell temperature climbs up when

the sun comes out. The temperature difference between the PV cell and air can be as high as 25 °C, shown in Figure 7.29. This effect of the temperature upon the PV performance is also illustrated by investigating Figures 7.28 and 7.29. The higher cell temperature causes a lower maximum power value. The spikes in Figure 7.28 are due to the MPPT, which tries to keep the PV array operate at its maximum power points under different temperatures and solar irradiances. The time range of the spike is small (about 1 s).

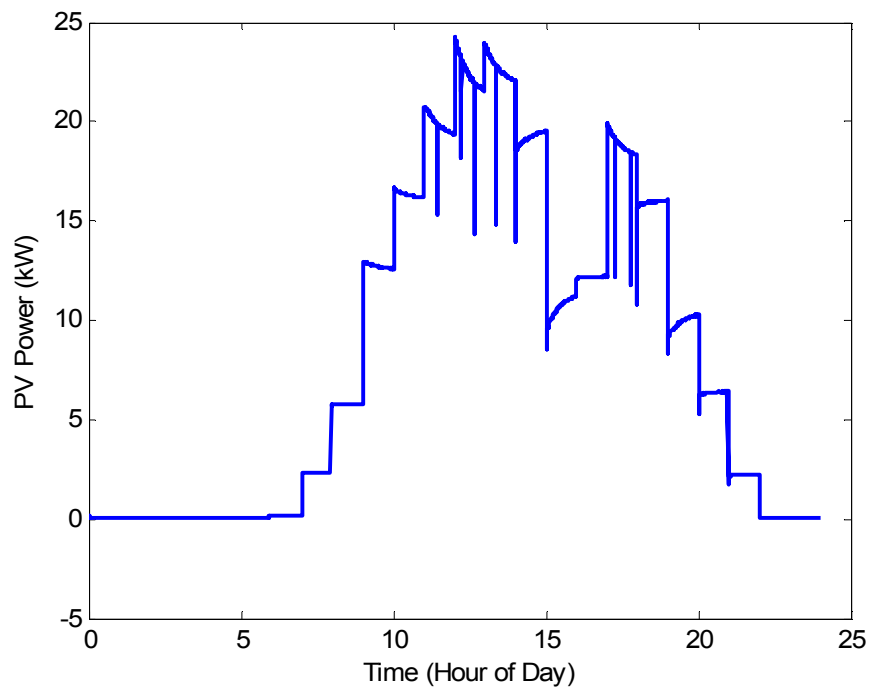


Figure 7.28. PV power generated for the winter scenario study.

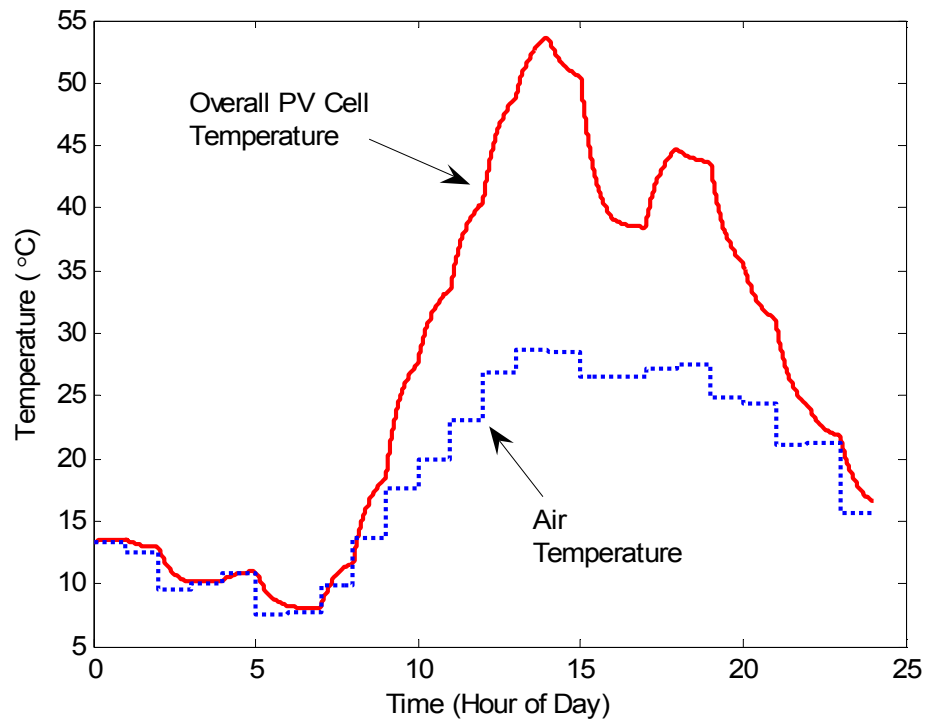


Figure 7.29. The PV and air temperature over the simulation period for the winter scenario study.

When  $P_{net} > 0$ , there is excess power available for  $H_2$  generation. Figure 7.30 shows the available power profile over the 24 hour simulation period. Figure 7.31 shows the  $H_2$  generation rate over the simulation period. The corresponding DC voltage applied to the electrolyzer and the electrolyzer current are shown in Figure 7.32. It is clear from Figures 7.30 - 7.32 that the more power is available for storage, the higher is the DC input voltage applied to the electrolyzer to balance the excess power, and the more  $H_2$  is generated as a result.

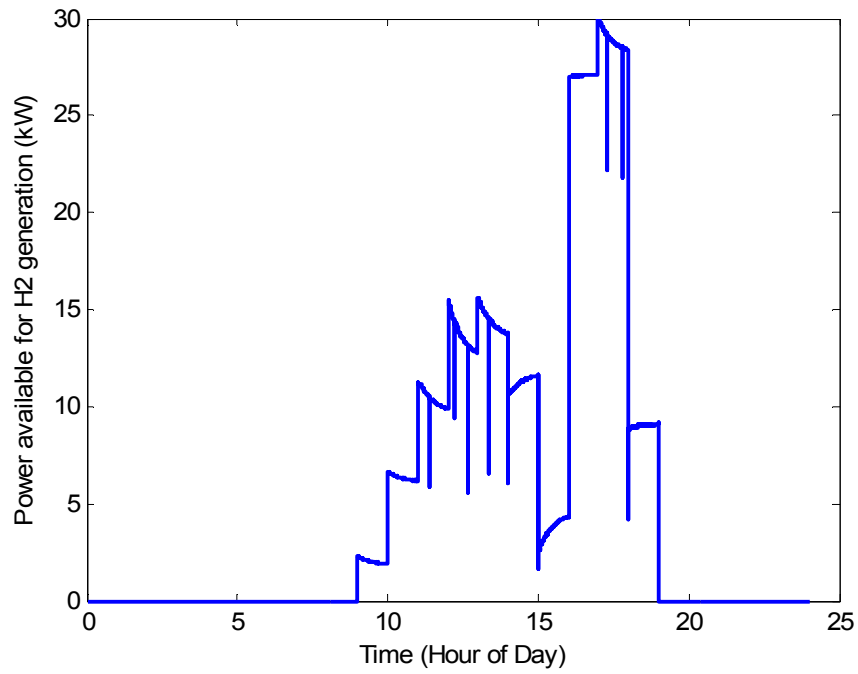


Figure 7.30. Power available for H2 generation for the summer scenario study.

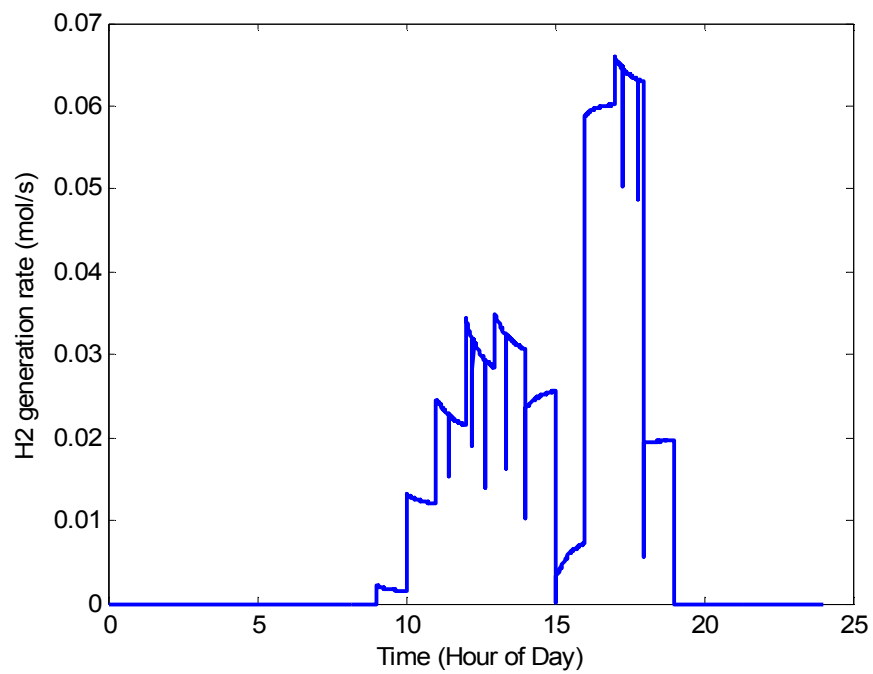


Figure 7.31. H2 generation rate for the summer scenario study.

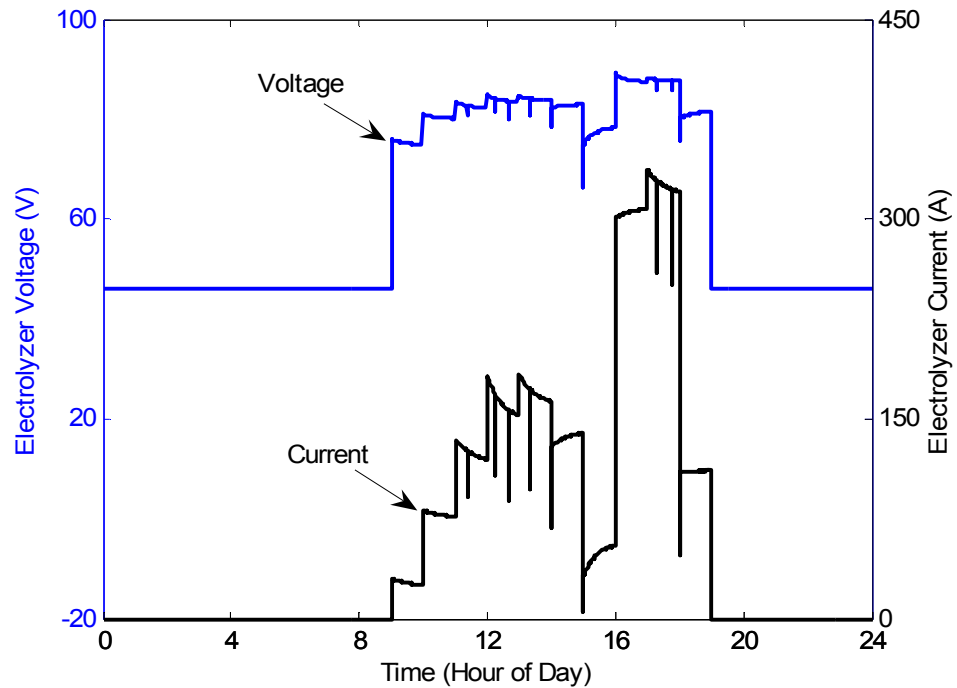


Figure 7.32. Electrolyzer voltage and current for the summer scenario study.

When  $P_{net} < 0$ , the wind and PV generated power is not sufficient to supply the load demand. Under this scenario, the fuel cell turns on to supply the power shortage. Figure 7.33 shows the power shortage which should be supplied by the FC. The actual power delivered by FC is given in Figure 7.34 and the corresponding  $H_2$  consumption rate is given in Figure 7.35. Comparing Figures 7.33 and 7.34, we can see that the power shortage is covered by the fuel cell very well.

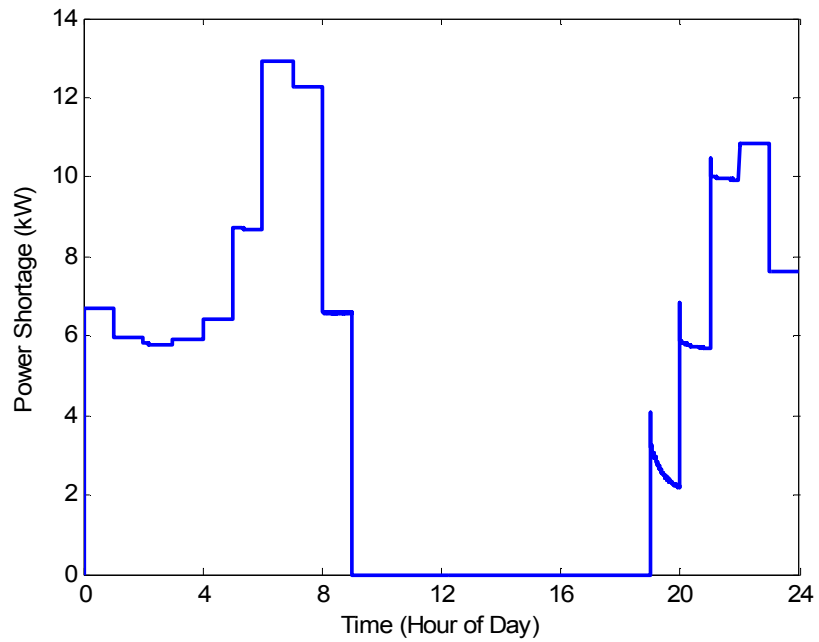


Figure 7.33. Power shortage over the simulation period for the summer scenario study.

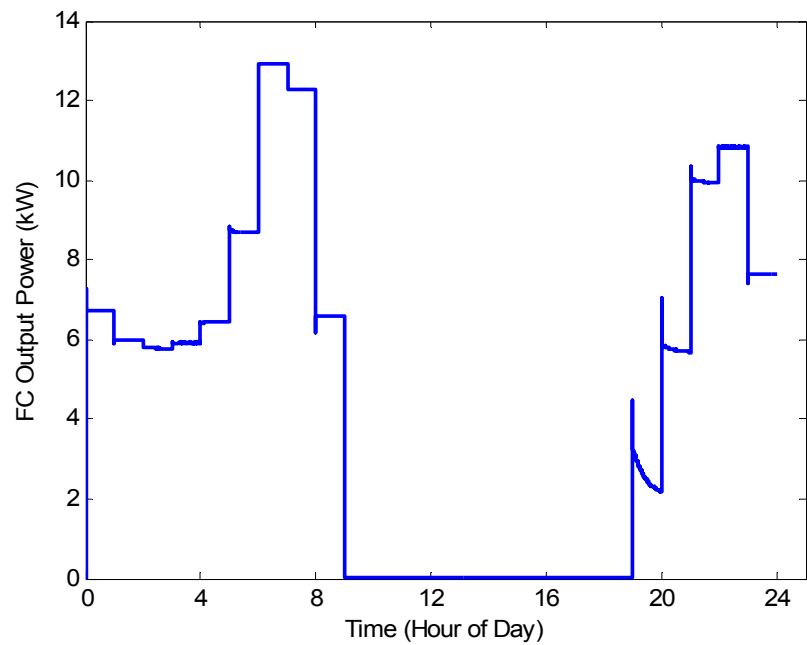


Figure 7.34. Power supplied by the FC over the simulation period for the summer scenario study.

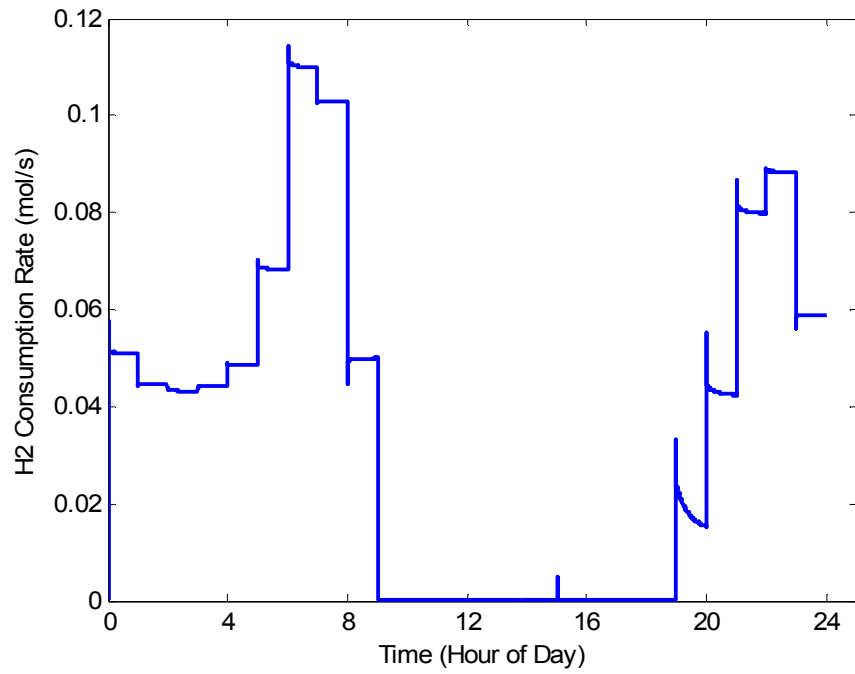


Figure 7.35. H<sub>2</sub> consumption rate for the summer scenario study.

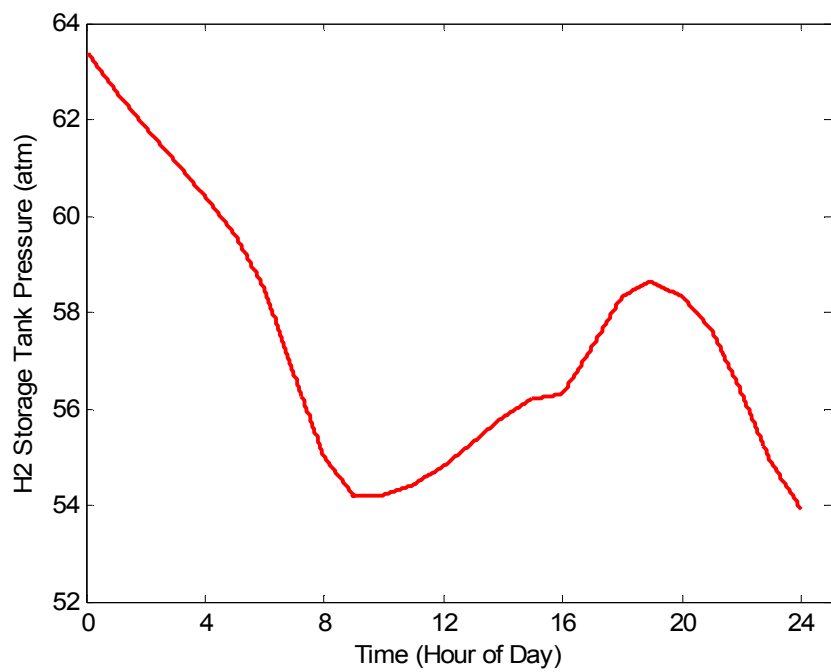


Figure 7.36. The H<sub>2</sub> tank pressure over the 24 hour for the summer scenario study.

Figure 7.36 shows the tank pressure variations over the 24 hour simulation period and Figure 7.37 shows the battery power profile over the simulation period. The large spikes shown in Figure 7.37 are due to the sudden hourly changes in the weather data and the load demand used for the simulation study.

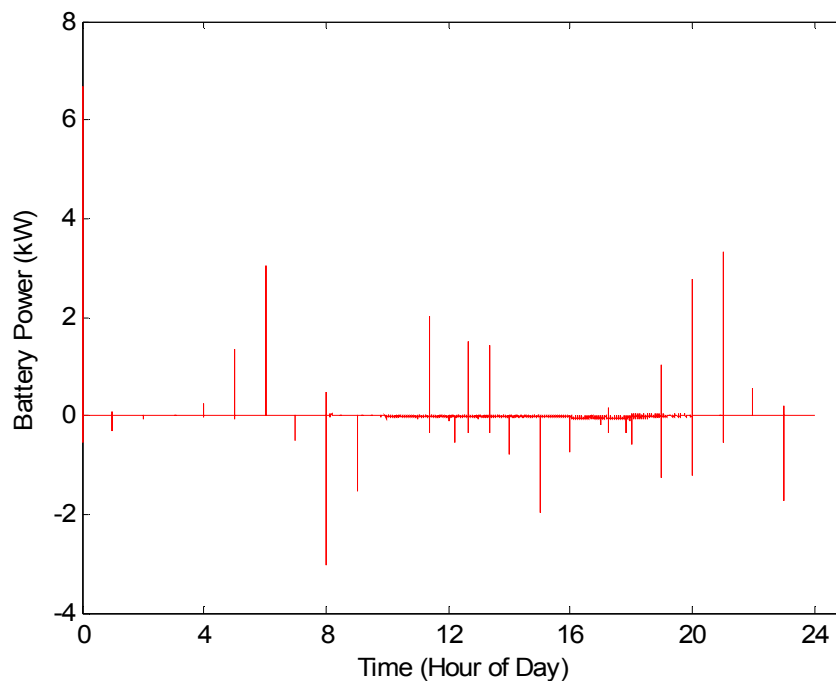


Figure 7.37. The battery power over the simulation period for the summer scenario.

Simulation studies have also been carried out using continuous weather and load demand data. The same weather and load demand data points used for the winter scenario study are used for this scenario study. However, for this case study, each input (load demand, wind speed, solar irradiance and air temperature) is a continuous piecewise linear function over the simulation time, where two adjacent data points are connected by a straight line. The continuous load demand curve shown in Figure 7.5 is used for this simulation study, and Figures 7.38 – 7.40 show the weather data used in this case.

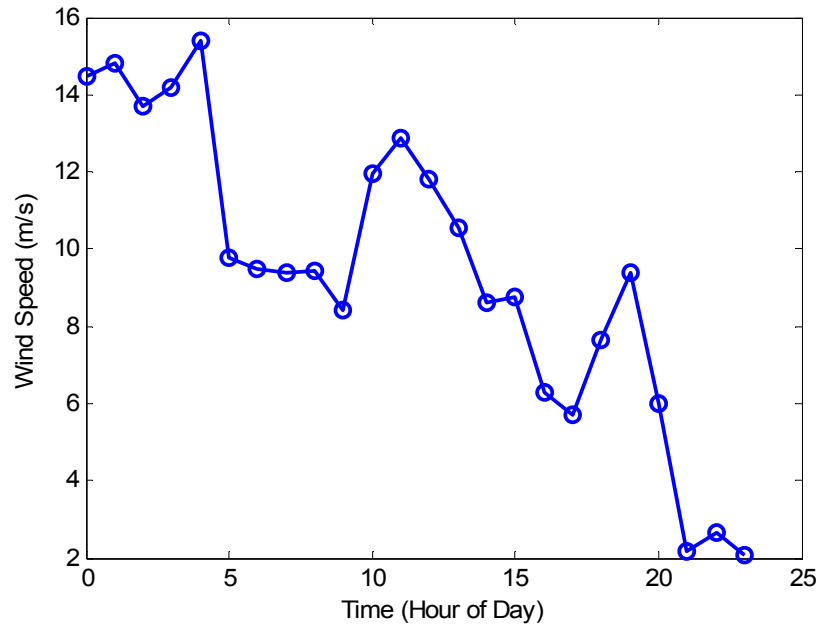


Figure 7.38. Wind speed data for the simulation study with continuous weather data and load demand.

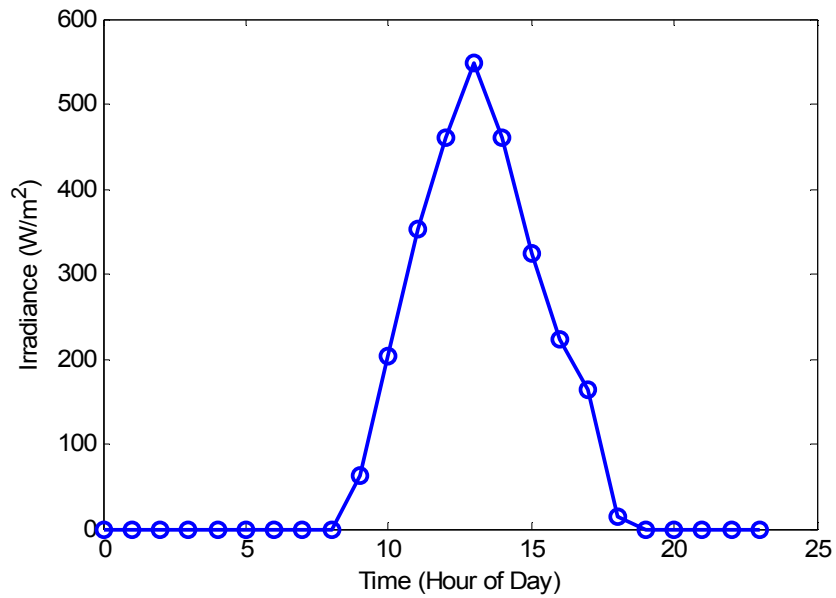


Figure 7.39. Solar irradiance data for the simulation study with continuous weather data and load demand.

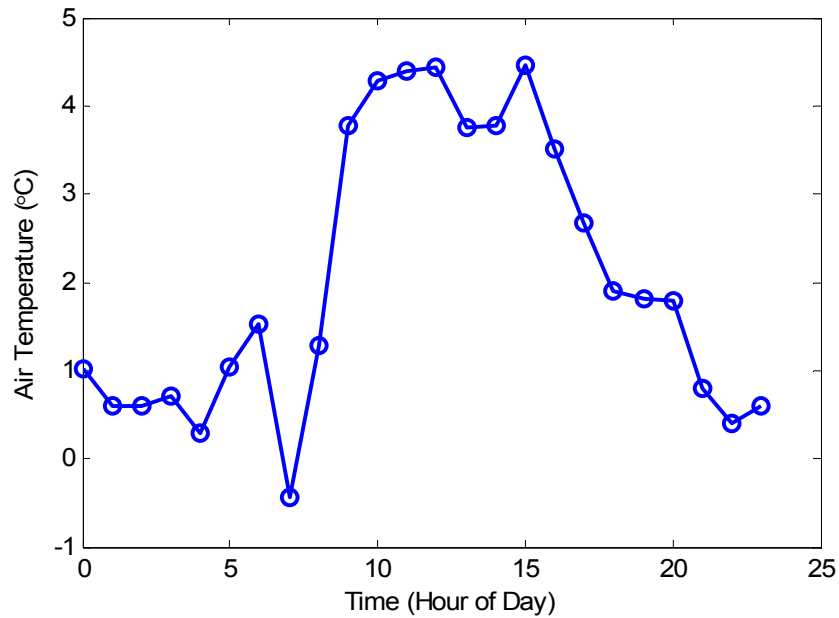


Figure 7.40. Air temperature for the simulation study with continuous weather data and load demand.

Figures 7.41 and 7.42 show the continuous wind and PV generated power, respectively. The spikes in the PV output power, shown in Figure 7.42, are due to the CMPPT control of the power electronic interfacing devices for the PV array. Figures 7.43 and 7.44 show the corresponding excess power (available for H<sub>2</sub> generation) profile and the FC output power (power shortage) profile over the simulation period.

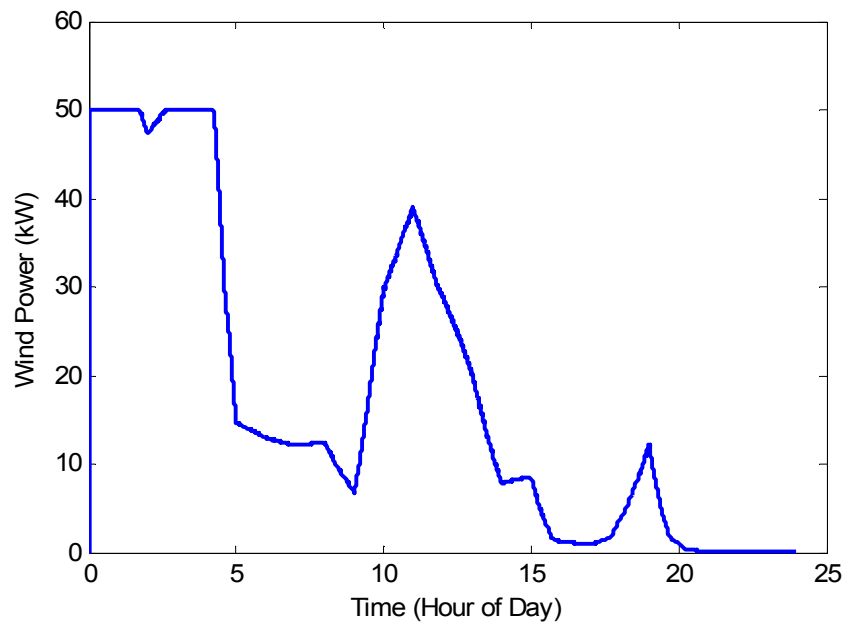


Figure 7.41. Wind power for the continuous weather data and load demand scenario.

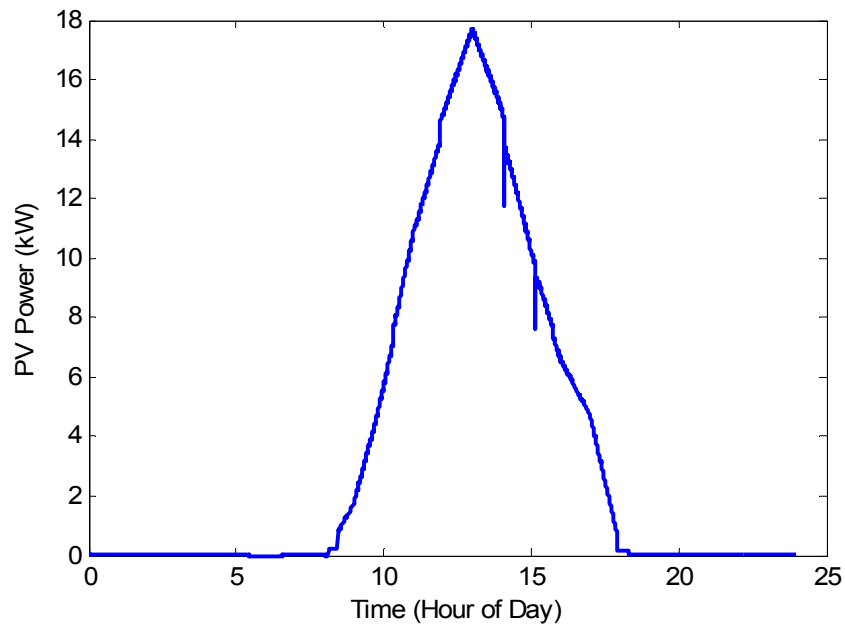


Figure 7.42. PV power for the continuous weather data and load demand scenario.

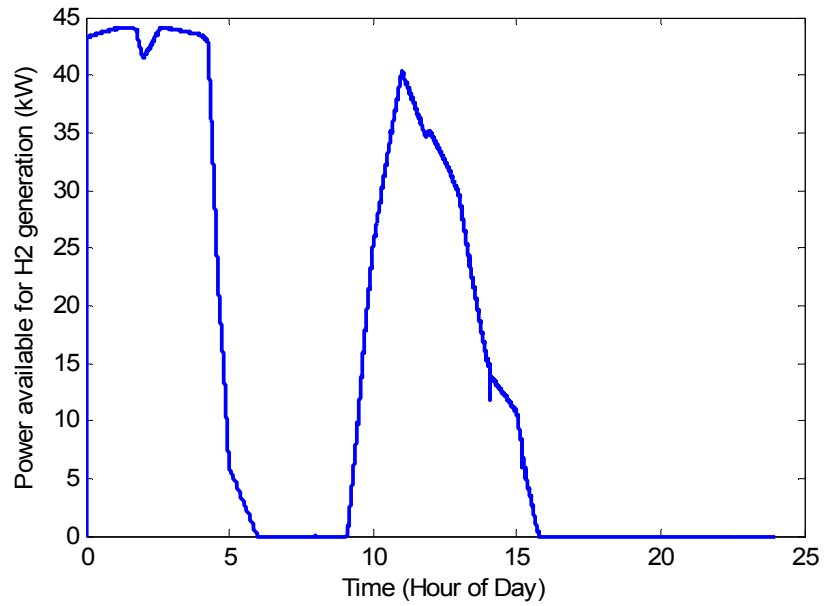


Figure 7.43. Power available for H<sub>2</sub> generation for the continuous weather data and load demand scenario.

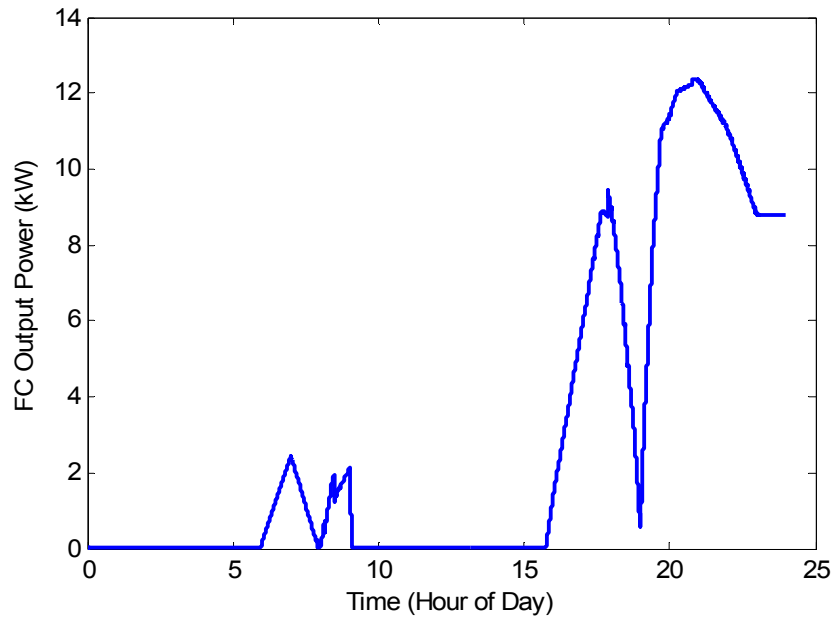


Figure 7.44. FC output power for the continuous weather data and load demand scenario.

Figure 7.45 shows the battery power profile over the 24 hour simulation period for the continuous weather data and load demand scenario. Comparing Figure 7.45 with Figures 7.22 and 7.37, it is noted that the battery spikes are much smaller in this case than the battery spikes when the discrete hourly weather and load demand data are used.

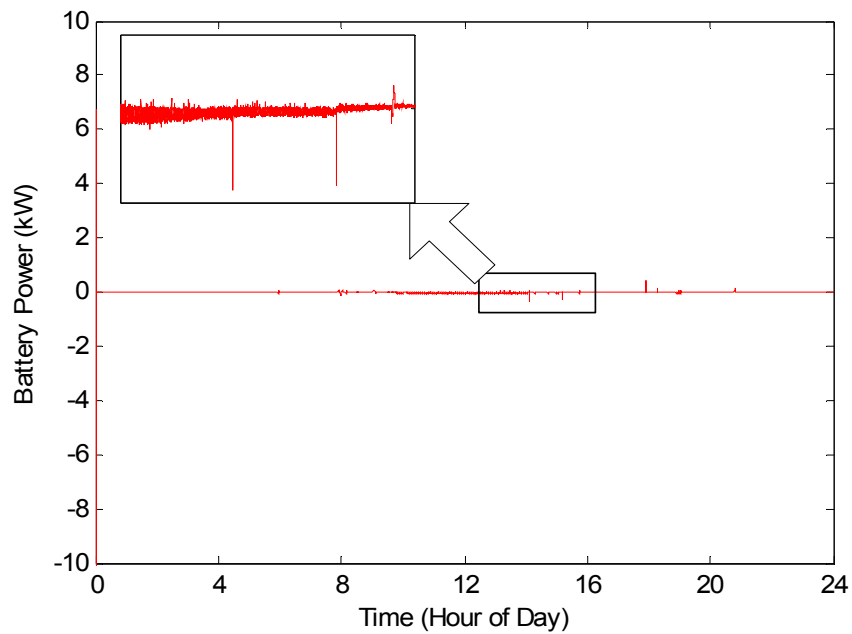


Figure 7.45. Battery power for the continuous weather data and load demand scenario.

### Summary

In this chapter, the overall control and power management strategy for the proposed hybrid energy system is presented. The wind and PV generation systems are the main power generation devices. The electrolyzer acts as a dump load using any excess power to produce H<sub>2</sub>. The FC system is the back up generation and battery picks up the fast load transients and ripples. The simulation model of the hybrid system has been developed using MATLAB/Simulink. Simulation studies have been used to verify the system performance under different scenarios using practical load profile and real weather collected at Deer Lodge, MT. The simulation results have been given and discussed for a winter and a summer scenario. The results show that the overall power management strategy is effective and the power flows among the different energy sources and the load demand is balanced successfully.

REFERENCES

- [7.1] J. Cahill, K. Ritland, W. Kelly, "Description of Electric Energy Use in Single Family Residences in the Pacific Northwest 1986-1992," Office of Energy Resources, Bonneville Power Administration, December 1992, Portland, OR.
- [7.2] Online: <http://www.usbr.gov/pn/agrimet/webaghrread.html>.
- [7.3] W.D. Kellogg, M.H. Nehrir, G. Venkataramanan, V. Gerez, "Generation unit sizing and cost analysis for stand-alone wind, photovoltaic, and hybrid wind/PV systems," *IEEE Transactions on Energy Conversion*, Vol. 13, No. 1, pp. 70 – 75, March 1998.
- [7.4] P. Gipe, *Wind power: renewable energy for home, farm, and business*, Chelsea Green Publishing Company, 2004

## CHAPTER 8

## OPTIMAL PLACEMENT OF DISTRIBUTED GENERATION

## SOURCES IN POWER SYSTEMS

Introduction

The ever-increasing need for electrical power generation, steady progress in the power deregulation and utility restructuring, and tight constraints over the construction of new transmission lines for long distance power transmission have created increased interest in distributed power generation. Distributed generation (DG) devices can be strategically placed in power systems for grid reinforcement, reducing power losses and on-peak operating costs, improving voltage profiles and load factors, deferring or eliminating system upgrades, and improving system integrity, reliability and efficiency [8.1]-[8.5].

These DG sources are normally placed close to consumption centers and are added mostly at the distribution level. They are relatively small in size (relative to the power capacity of the system in which they are placed) and modular in structure. A common strategy to find the site of DG is to minimize the power loss of the system [8.2]-[8.5]. Another method for placing DG is to apply rules that are often used in sitting shunt capacitors in distribution systems. A “2/3 rule” is presented in [8.6] to place DG on a radial feeder with uniformly distributed load, where it is suggested to install DG of approximately 2/3 capacity of the incoming generation at approximately 2/3 of the length of line. This rule is simple and easy to use, but it cannot be applied directly to a feeder

with other types of load distribution, or to a networked system. References [8.1], [8.7] present power flow algorithms to find the optimal size of DG at each load bus in a networked system assuming that every load bus can have a DG source.

In this chapter, analytical approaches for optimal placement of DG with unity power factor in power systems are presented. First, placement of DG in a radial feeder is analyzed and the theoretical optimal site (bus) for adding DG is obtained for different types of loads and DG sources. Then, a method is presented to find the optimal bus for placing DG in a networked system based on bus admittance matrix, generation information and load distribution of the system. The proposed methods are tested by a series of simulations on radial feeders, an IEEE 6-bus test system [8.1], an IEEE 30-bus test system [8.11] and a subset of it, to show the effectiveness of the proposed methods in determining the optimal bus for placing DG.

In practice, there are more constraints on the availability of DG sources, and there may be only one or a few DGs with limited output available to be added. Therefore, in this study the DG size is not considered to be optimized. The procedure to determine the optimal bus for placing DG may also need to take into account other factors, such as economic and geographic considerations. These factors are not discussed in this chapter.

### Optimal Placement of DG on a Radial Feeder

To simplify the analysis, only overhead transmission lines with uniformly distributed parameters are considered, i.e.,  $R$  and  $L$  (series resistance and inductance) per unit length are the same along the feeder while the shunt capacitance and susceptance of lines are neglected. The loads along the feeder are assumed to vary in discrete time duration; for

example, the feeder load distributions along the line for time durations  $T_i$  and  $T_{i+1}$  are shown in Figure 8.1.

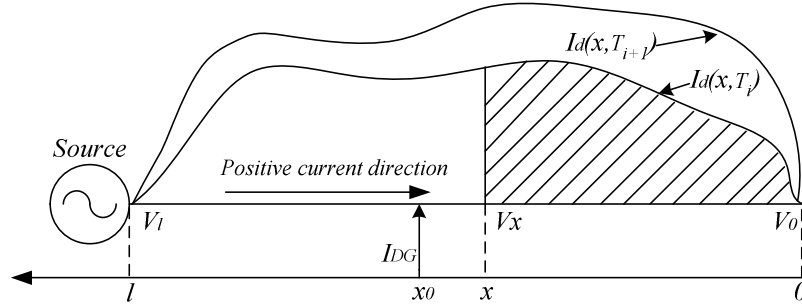


Figure 8.1. A feeder with distributed loads along the line.

### Theoretical Analysis

First consider a radial feeder without DG. During the time duration  $T_i$ , the loads are distributed along the line with the phasor current density  $I_d(x, T_i)$  as shown in Figure 8.1.

The phasor feeder current at point  $x$  is:

$$I(x, T_i) = \int_0^x I_d(x, T_i) dx \quad (8.1)$$

Assuming the impedance per unit length of the line is  $Z=R+jX$  ( $\Omega/\text{km}$ ), then the incremental power loss and phasor voltage drop at point  $x$  are:

$$dP(x, T_i) = \left( \int_0^x I_d(x, T_i) dx \right)^2 \cdot R dx \quad (8.2)$$

$$dV(x, T_i) = \left( \int_0^x I_d(x, T_i) dx \right) \cdot Z dx \quad (8.3)$$

The total power loss along the feeder within the time duration  $T_i$  is:

$$P_{loss}(T_i) = \int_0^l dP(x, T_i) = \int_0^l \left( \int_0^x I_d(x, T_i) dx \right)^2 \cdot R dx \quad (8.4)$$

The voltage drop between point  $x$  and the receiving end is:

$$V_{drop}(x, T_i) = V_x(T_i) - V_0(T_i) = \int_0^x dV(x, T_i) = \int_0^x \int_0^x I_d(x, T_i) dx \cdot Z dx \quad (8.5)$$

And the voltage at point  $x$  is:

$$V_x(T_i) = V_0(T_i) + V_{drop}(x, T_i) = V_l(T_i) - V_{drop}(l, T_i) + V_{drop}(x, T_i) \quad (8.6)$$

The total voltage drop across the feeder is:

$$V_{drop}(l, T_i) = V_l(T_i) - V_0(T_i) = \int_0^l dV(x, T_i) = \int_0^l \int_0^x I_d(x, T_i) dx \cdot Z dx \quad (8.7)$$

Now, consider a DG is added into the feeder at the location  $x_0$ , shown in Figure 8.1. In general, the load current density  $I_d(x, T_i)$  will change (normally decrease) as a result of adding DG due to improvements in the voltage profile along the line. This change in the load current density will cause the feeder current to decrease. The feeder current between the source (at  $x=l$ ) and the location of DG (at  $x = x_0$ ) will also change as a result of the injected current source  $I_{DG}(T_i)$ . However, the change in feeder current due to the change in the load current density is generally much smaller than the change in the feeder current due to the injected current  $I_{DG}(T_i)$ . For the purpose of analysis, the change in the load current density, resulted from the addition of DG, is neglected in this study. Therefore, the load current density  $I_d(x, T_i)$ , used in (1), is also used for obtaining the feeder current after adding DG. In this case, the feeder current can be written as follows:

$$I(x, T_i) = \begin{cases} \int_0^x I_d(x, T_i) dx & 0 \leq x \leq x_0 \\ \int_0^x I_d(x, T_i) dx - I_{DG}(T_i) & x_0 \leq x \leq l \end{cases} \quad (8.8)$$

The corresponding power loss and voltage drop in the feeder are:

$$P_{loss}(x_0, T_i) = \int_0^{x_0} \left( \int_0^x I_d(x, T_i) dx \right)^2 \cdot R dx + \int_{x_0}^l \left( \int_0^x I_d(x, T_i) dx - I_{DG}(T_i) \right)^2 \cdot R dx \quad (8.9)$$

$$V_{drop}(x, T_i) = \begin{cases} \int_0^x \int_0^x I_d(x, T_i) dx \cdot Z dx & 0 \leq x \leq x_0 \\ \int_0^{x_0} \int_0^x I_d(x, T_i) dx \cdot Z dx + \int_{x_0}^x \left( \int_0^x I_d(x, T_i) dx - I_{DG}(T_i) \right) \cdot Z dx & x_0 \leq x \leq l \end{cases} \quad (8.10)$$

The average power loss in a given time period  $T$  is:

$$\overline{P_{loss}}(x_0) = \frac{1}{T} \sum_{i=1}^{N_i} P_{loss}(x_0, T_i) T_i \quad (8.11)$$

where  $N_i$  is the number of time durations in the time period  $T$ .

$$T = \sum_{i=1}^{N_i} T_i \quad (8.12)$$

Equation (8.6) can still be used under this situation to calculate the voltage at point  $x$  by using  $V_{drop}(x, T_i)$  obtained from equation (8.10).

#### Procedure to Find the Optimal Location of DG on a Radial Feeder

The goal is to add DG in a location to minimize the total average power loss and assure that the voltages  $V_x$  along the feeder are in the acceptable range,  $1 \pm 0.05$  p.u., i.e.,

$$\frac{d\overline{P_{loss}}(x_0)}{dx_0} = 0 \quad (8.13)$$

The solution  $x_0$  of the above equation will give the optimal site for minimizing the power loss, but it cannot guarantee that all the voltages along the feeder are in the acceptable range. If the voltage regulation cannot be satisfied at the same time, the DG

can be placed around  $x_0$  to satisfy the voltage regulation rule while decreasing the power loss as much as possible or the DG size can be increased. The analytical procedure to determine the optimal point to place DG on a radial feeder is given as follows.

- 1) Find the distributed load  $I_d(x, T_i)$  along the feeder.
- 2) Get the output current of DG,  $I_{DG}(T_i)$ .
- 3) Use equations (8.9) and (8.11) to calculate  $\overline{P_{loss}}(x_0)$  and find the solution  $x_0$  of equation (8.13).
- 4) Use equations (8.6) and (8.10) to check whether the voltage regulation is satisfied.
- 5) If all the voltages are in the acceptable range, then the calculated  $x_0$  is the optimal spot ( $x_{op}$ ) to add DG.
- 6) If  $x_0$  doesn't meet the voltage regulation rule, then move the DG to see whether there is a point around point  $x_0$ , where all bus voltages are in the acceptable range.
- 7) If no point on the feeder can satisfy the voltage regulation rule, then increase the size of DG and repeat steps 2) to 7).
- 8) Sometimes more than one DG may be needed. Under this situation, the feeder can be divided into several segments and steps 1) to 7) can be applied to each segment.

The flow chart of the procedure is summarized in Figure 8.2.

### Case Studies with Time Invariant Loads and DGs

Table 8.1 shows the results of analyses, using the foregoing procedure, to find the optimal location for placing DG on radial feeders with three different load distributions: uniformly distributed load, centrally distributed load and uniformly increasing distributed load. In the results given in Table 8.1, it is assumed that the DG supplies all the loads on the feeder in each case, and the distribution system supplies the system losses. It is noted from the table that the DG reduces the system power losses significantly when it is located properly.

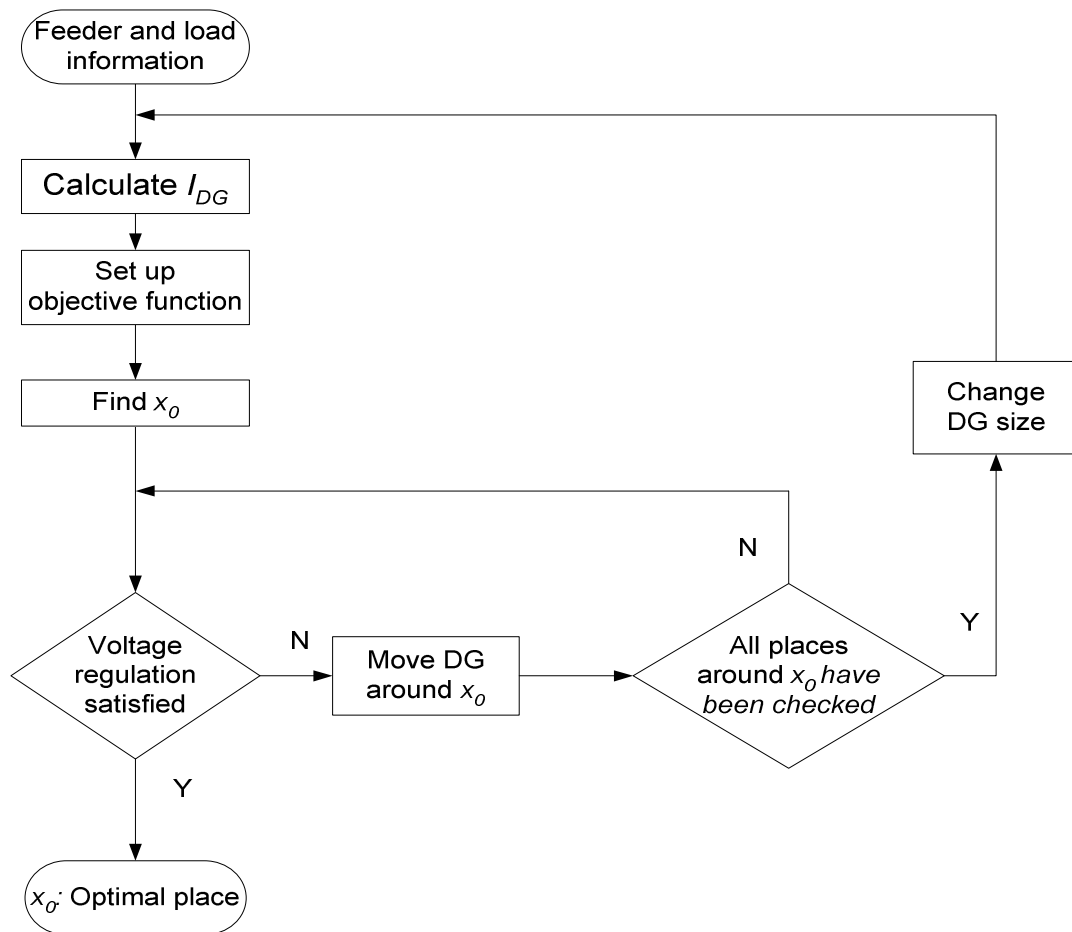
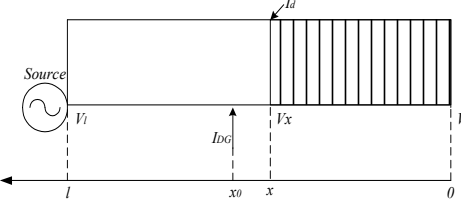
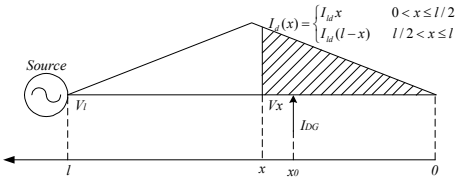
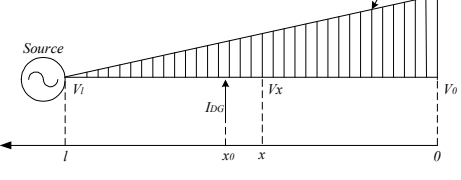


Figure 8.2. Procedure for finding optimal place for a DG source in a radial feeder.

TABLE 8.1. THEORETICAL ANALYSIS RESULTS OF CASE STUDIES WITH TIME INVARIANT LOADS AND DGs

Cases (Assuming that DG supplies all the loads in each case)	$P_{loss}^0$ (Power loss before adding DG)	$P_{loss}$ (Power loss after adding DG)	Percent of power loss reduction	Optimal place $x_0$
 <p>Uniformly distributed load</p>	$I_d^2 R l^3 / 3$	$I_d^2 R l^3 / 12$	75%	$l/2$
 <p>Centrally distributed load</p>	$\frac{23}{960} I_{ld}^2 R l^5$	$\frac{1}{320} I_{ld}^2 R l^5$	87%	$l/2$
 <p>Increasingly distributed load</p>	$0.1333 I_{ld}^2 R l^5$	$0.01555 I_{ld}^2 R l^5$	88%	$(1 - \sqrt{2})/2$

The 2/3 rule presented in [8.6] works well when the load is uniformly distributed along the feeder, but it gives inaccurate results if the load configuration is different. For a uniformly distributed load, if the DG supplies 2/3 of the total load ( $I_{DG} = I_{ld}l^2/6$ ), the optimal site is at  $x_0 = l/3$  according to equation (8.9). This result is exactly the same as that given in [8.6]. However, when the loads are centrally and increasingly distributed and the DG provides 2/3 of the total load, the optimal location for placing DG turns out to be  $l/\sqrt{6}$  and  $(1-\sqrt{2/3})l$  respectively, which differ from what the “2/3 rule” suggests in [8.6].

#### Case Study with Time Varying Load and DG

The same feeders as in the previous section (shown in Figure 8.1), but with time varying load and DG, are analyzed in this case. The analysis is given for uniformly distributed load only. The analyses for other types of loads follow similarly.

Assuming that DG is located at point  $x_0$ , then according to equation (8.9), the effective power loss is:

$$P_{loss}(x_0, T_i) = RI_d(T_i)I_{DG}(T_i)(x_0^2 - l^2) - RI_{DG}^2(T_i)(x_0 - l) + \frac{RI_d^2(T_i)l^3}{3}$$

(8.14)

where  $I_d(T_i) = I_{load}(T_i)/l$  and  $I_{load}(T_i)$  is the load current at the very sending end of the feeder. The average power loss in a given time period  $T$  is:

$$\overline{P_{loss}}(x_0) = C_1 + \frac{Rx_0^2}{T} \sum_{i=1}^{N_i} I_d(T_i)I_{DG}(T_i)T_i - \frac{Rx_0}{T} \sum_{i=1}^{N_i} I_{DG}^2(T_i)T_i \quad (8.15)$$

where  $C_1 = \frac{1}{T} \sum_{i=1}^{N_i} \left[ \frac{RI_d^2(T_i)l^3}{3} - RI_d(T_i)I_{DG}(T_i)l^2 + RI_{DG}^2(T_i)l \right] T_i$ .

Setting  $\frac{d\overline{P_{loss}}(x_0)}{dx_0} = 0$ ,  $x_0$  is obtained to be:

$$x_0 = \frac{\sum_{i=1}^{N_i} I_{DG}^2(T_i)T_i}{2 \sum_{i=1}^{N_i} I_d(T_i)I_{DG}(T_i)T_i} = \frac{l \cdot \sum_{i=1}^{N_i} I_{DG}^2(T_i)T_i}{2 \sum_{i=1}^{N_i} I_{load}(T_i)I_{DG}(T_i)T_i} \quad (8.16)$$

Assuming that all bus voltages along the feeder are in the acceptable range, equation (8.16) can be approximated as

$$x_0 \approx \frac{\sum_{i=1}^{N_i} P_{DG}^2(T_i)T_i}{2 \sum_{i=1}^{N_i} P_d(T_i)P_{DG}(T_i)T_i} = \frac{l \cdot \sum_{i=1}^{N_i} P_{DG}^2(T_i)T_i}{2 \sum_{i=1}^{N_i} P_{load}(T_i)P_{DG}(T_i)T_i} \quad (8.17)$$

where  $P_d(T_i) = P_{load}(T_i)/l$  and  $P_{load}(T_i)$  is the total load along the feeder in the time duration  $T_i$ .

### Optimal Placement of DG in Networked Systems

The theoretical analysis for placing a DG in networked systems is different and more complicated than in a radial feeder. To simplify the analysis, only one DG is considered to be added to the system.

Consider the system shown in Figure 8.3 with a DG added to the system to reinforce it. The system has  $N$  buses and loads, and the DG is located at a bus, say bus  $j$ . The main external power is injected into bus 1, which is taken as slack bus. The objective is to find the bus to install the DG so that the total system power loss is minimized and the voltage level at each bus is held in the acceptable range,  $1 \pm 0.05$  p.u.

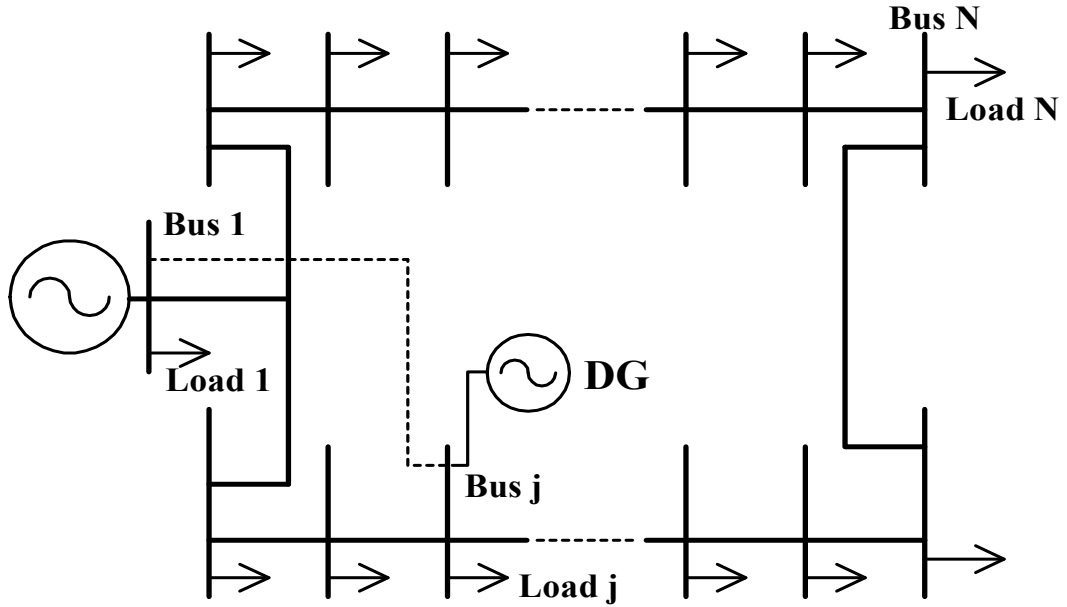


Figure 8.3. A networked power system.

Before the DG is added to the system, the bus admittance matrix is

$$Y_{bus}^0 = \begin{bmatrix} Y_{11}^0 & Y_{12}^0 & \dots & Y_{1j}^0 & \dots & Y_{1N}^0 \\ & & \dots & & \dots & \\ & & & & & \\ & & & & & \\ Y_{N1}^0 & Y_{N2}^0 & \dots & Y_{Nj}^0 & \dots & Y_{NN}^0 \end{bmatrix} \quad (8.18)$$

where superscript <sup>0</sup> denotes the original system.

Assuming that the DG is located at bus  $j$ , the system admittance matrix is changed from  $Y_{bus}^0$  to  $Y_{bus}$  by considering that bus 1 and bus  $j$  are connected together. Actually there is no line to connect those buses together, but the imaginary line will help in finding the optimal location to add DG.  $Y_{bus}$  is one dimension less than  $Y_{bus}^0$  except when the DG is located at bus 1. If the DG is at bus 1,  $Y_{bus}$  matrix will be the same as  $Y_{bus}^0$ . To obtain the new matrix  $Y_{bus}$  when the DG source is connected, we treat the system as connecting

bus 1 and  $j$  by eliminating bus  $j$  in  $Y_{bus}^0$  [8.10]. The new matrix is

$$Y_{bus} = \begin{bmatrix} Y_{11} & Y_{12} & \cdots & Y_{1k} & \cdots & Y_{1(N-1)} \\ & & & & & \\ & & & & & \\ & & & & & \\ Y_{(N-1)1} & Y_{(N-1)2} & \cdots & Y_{(N-1)k} & \cdots & Y_{(N-1)(N-1)} \end{bmatrix} \quad (8.19)$$

where

$$\begin{aligned} Y_{11} &= Y_{11}^0 + Y_{jj}^0 + 2Y_{1j}^0 & Y_{ik} &= Y_{ik}^0, 2 \leq (i, k) \leq j-1 \\ Y_{1k} &= Y_{1k}^0 + Y_{jk}^0, k = 2, \dots, j-1 & Y_{ik} &= Y_{i(k+1)}^0, 2 \leq i \leq j-1, j \leq k \leq N-1 \\ Y_{1k} &= Y_{1(k+1)}^0 + Y_{j(k+1)}^0, k = j, \dots, N-1 & Y_{ik} &= Y_{(i+1)k}^0, j \leq i \leq N-1, 2 \leq k \leq j-1 \\ Y_{k1} &= Y_{1k}, k = 2, \dots, N-1 & Y_{ik} &= Y_{(i+1)(k+1)}^0, j \leq (i, k) \leq N-1 \end{aligned}$$

The new bus impedance matrix  $Z_{bus}$  is:

$$Z_{bus} = Y_{bus}^{-1} = \begin{bmatrix} Z_{11} & Z_{12} & \cdots & Z_{1k} & \cdots & Z_{1(N-1)} \\ & & & & & \\ & & & & & \\ & & & & & \\ Z_{(N-1)1} & Z_{(N-1)2} & \cdots & Z_{(N-1)k} & \cdots & Z_{(N-1)(N-1)} \end{bmatrix} \quad (8.20)$$

Suppose the complex load and generated power of the original system are:

$$\begin{aligned} S_L^0 &= [S_{L1}^0, S_{L2}^0, \dots, S_{Li}^0, \dots, S_{LN}^0], \text{ and} \\ S_G^0 &= [S_{G1}^0, S_{G2}^0, \dots, S_{Gi}^0, \dots, S_{GN}^0], i=1, 2, \dots, N \end{aligned} \quad (8.21)$$

where  $S_{Li}^0 = P_{Li}^0 + jQ_{Li}^0$  and  $S_{Gi}^0 = P_{Gi}^0 + jQ_{Gi}^0$ .

A new load vector  $S_L$  is set up as follows:

$$S_L = [S_{L1}, S_{L2}, \dots, S_{Li}, \dots, S_{LN}] \quad (8.22)$$

where

$$S_{Li} = P_{Li} + jQ_{Li}, \text{ and,}$$

$$S_{Li} = 0, \quad \text{for } i = 1 \text{ (slack bus);}$$

$$S_{Li} = S_{Li}^0, \quad \text{for } i = \text{load buses};$$

$$S_{Li} = \begin{cases} P_{Li}^0 - P_{Gi}^0 + j0 & P_{Li} > P_{Gi} \\ 0 & P_{Li} \leq P_{Gi} \end{cases}, \quad \text{for } i = \text{P-V buses.}$$

Note that at the slack bus (bus 1)  $S_{L1} = 0$ ; it is assumed that the real and reactive power consumed by the load are supplied directly by the external generation at that bus. Also, at a voltage controlled (P-V) bus,  $Q_{Li} = 0$ ; it is assumed that the load reactive power can be supplied by the external power source at the P-V bus.

To find the optimal point to place the DG, we set up an objective function for DG at each bus  $j$  as follows:

$$f_j = \sum_{i=1}^{j-1} R_{Li}(j) |S_{Li}|^2 + \sum_{i=j+1}^N R_{Li}(j) |S_{Li}|^2, \quad j=2, \dots, N \quad (8.23)$$

where  $R_{Li}(j)$  is the equivalent resistance between bus 1 and bus  $i$  when DG is located at bus  $j, j \neq 1$ .

$$R_{Li}(j) = \begin{cases} \text{Real}(Z_{11} + Z_{ii} - 2Z_{1i}) & i < j \\ \text{Real}(Z_{11} + Z_{(i-1)(i-1)} - 2Z_{1(i-1)}) & i > j \end{cases} \quad (8.24)$$

When the DG is located at bus 1 ( $j=1$ ), the objective function will be

$$f_1 = \sum_{i=1}^N R_{Li} |S_{Li}|^2 \quad (8.25)$$

Note that in this case,  $Y_{bus}(Z_{bus})$  will be the same as  $Y_{bus}^0(Z_{bus}^0)$  and  $R_{11}=0$ .

The goal is to find the optimal bus  $m$  where the objective function reaches its minimum value.

$$f_m = \text{Min}(f_j), \quad j = 1, 2, \dots, N \quad (8.26)$$

The theoretical procedure to find the optimal bus to place DG in a networked system

can be summarized as follows:

- 1) Find the matrix  $Y_{bus}^0$  and set up the load vector  $S_L$ .
- 2) Compute  $Y_{bus}$  and the corresponding  $Z_{bus}$  for different DG locations.
- 3) Calculate the equivalent resistances according to (8.24).
- 4) Use (8.23) and (8.25) to calculate objective function values for DG at different buses and find the optimal bus  $m$ .
- 5) If all the voltages are in the acceptable range when the DG is located at bus  $m$ , then bus  $m$  is the optimal site.
- 6) If some bus voltages do not meet the voltage rule, then move the DG around bus  $m$  to satisfy the voltage rule.
- 7) If there is no bus that can satisfy the voltage regulation rule, try a different size DG and repeat steps 5) and 6).

The procedure is summarized in the flow chart shown in Figure 8.4, and the corresponding MATLAB code is given in Appendix C.

Though the discussion here is under the assumption that only one DG source is added to the system, it can be easily extended to the systems with multiple DG sources. By connecting all the DG buses and slack bus together through imaginary lines, the new  $Y_{bus}$  matrix and the corresponding objective function can be established by the method presented above.

### Simulation Results

Several simulation studies were carried out to verify the results obtained analytically for both radial and network-connected systems.

### Radial Feeder with Time Invariant Loads and DG

A radial feeder with a time invariant DG was simulated under uniformly distributed, centrally distributed and increasingly distributed loads. The simulated system for uniformly distributed loads is shown in Figure 8.5. The system architecture is the same when the loads are centrally distributed or increasingly distributed. The line parameters, DG and load sizes are listed in Table 8.2.

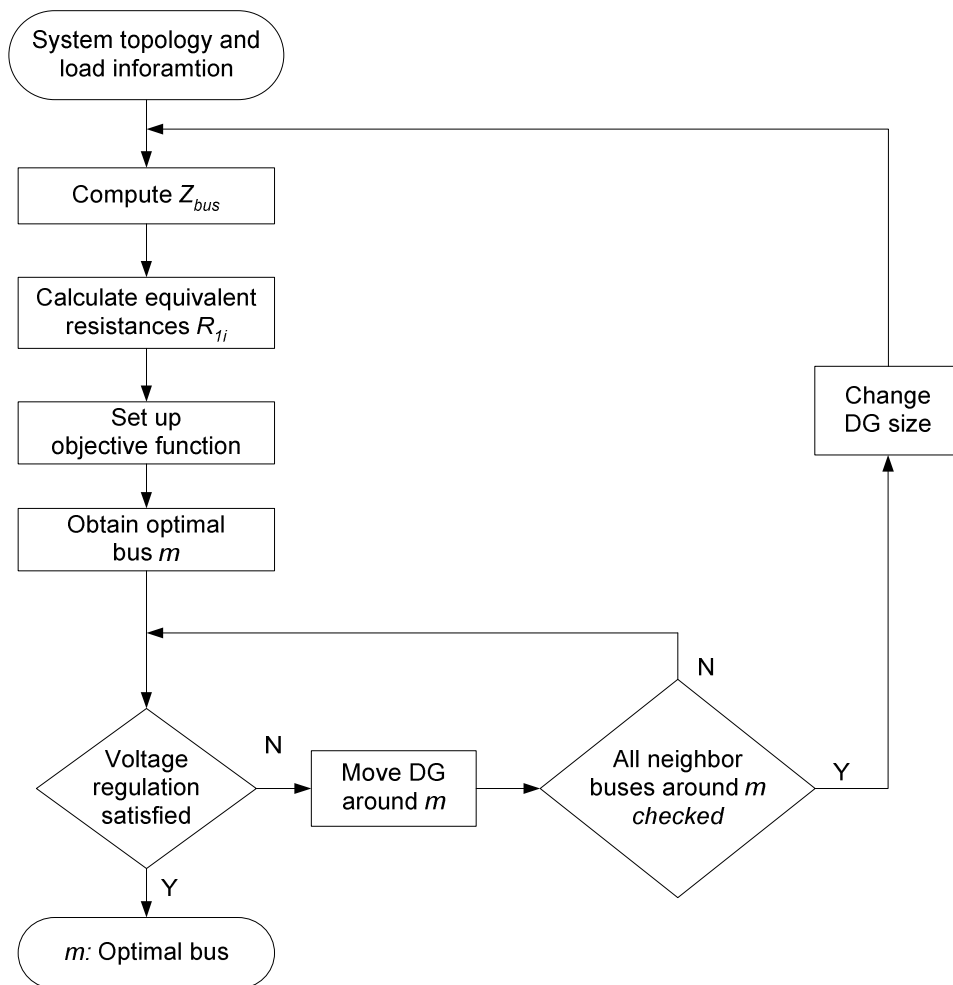


Figure 8.4. Flow chart of The theoretical procedure to find the optimal bus to place DG in a networked system.

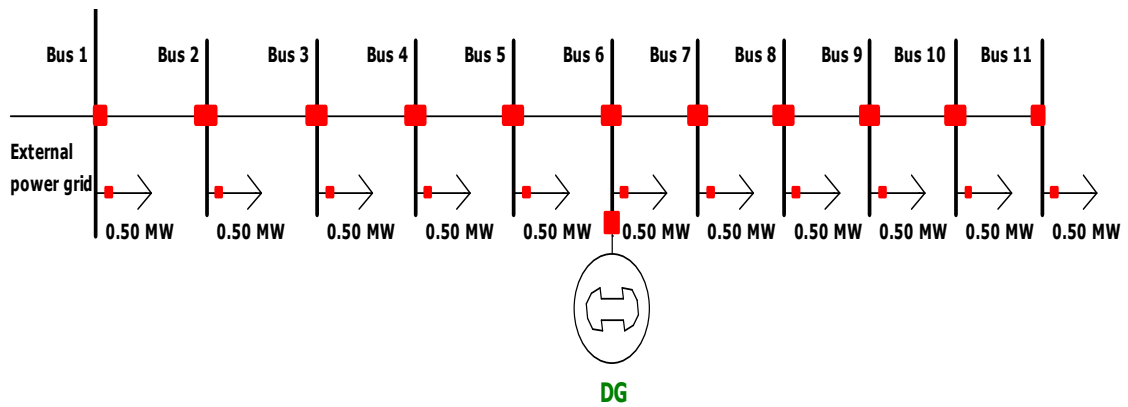


Figure 8.5. A radial feeder with uniformly distributed loads.

TABLE 8.2. PARAMETERS OF THE SYSTEM IN FIGURE 8.5

Line parameters (AWG ACSR 1/0)	Line spacing = 1.32m (equal spacing assumed) $R = 0.538\Omega$ , $X_L = 0.4626\Omega$ Bus Voltage: 12.5kV Line length between two neighboring buses: 2.5km										
Load type	Load at each bus (MW)										
	1	2	3	4	5	6	7	8	9	10	11
Uniformly distributed	0.5	0.5	0.5	0.5	0.5	0.5	0.5	0.5	0.5	0.5	0.5
Centrally distributed	0.05	0.1	0.2	0.3	0.4	0.5	0.4	0.3	0.2	0.1	0.05
Increasingly distributed	0.05	0.1	0.15	0.2	0.25	0.3	0.35	0.4	0.45	0.5	0.55
DG size (MW)	Uniformly			Centrally				Increasingly			
	5.5			2.6				3.3			

TABLE 8.3. SIMULATION RESULTS OF CASE STUDIES WITH  
TIME INVARIANT LOADS AND DG

Line Loading	Optimal Bus No. (Simulation)	Optimal Place (Theoretical)	Total Power Losses (kW)	
			Without DG	With DG
Uniform	6	6	1.7785	0.2106
Central	6	6	0.2589	0.0275
Increasing	8	8	0.8099	0.0606

In Table 8.3, the optimal bus for placing DG to minimize the total system power loss is given for each load distribution. The total system power losses are given both with and without DG. It is noted that the simulation results agree well with theoretical values. While some bus voltages fall far out of the acceptable range when there is no DG in the system, all the bus voltages are within  $1 \pm 0.05$  p.u. with the DG added.

#### Radial Feeder with Time Varying Loads and DG

This part of the study is helpful in understanding the effect of variable power DG (such as wind and photovoltaic (PV)) sources on distribution systems with time varying loads. In practice, the site of such DG sources may be mainly determined by meteorological and geographic factors. However, DG sources with predictable output power (such as fuel cells and microturbines) can be placed at any bus in the distribution system to achieve optimal result.

The feeder shown in Figure 8.5 is also used to simulate the situation with time varying uniformly distributed loads and DG. A wind-turbine generator is considered as

the time varying DG source. Actual wind data taken in a rural area in south central Montana were used to obtain the output power of a simulated (1-MW) wind turbine, as shown in Figure 8.6 [8.5], [8.8]. It shows the annual daily average output power of the turbine, which can be viewed as the filtered version of the turbine's output power. The daily average demand of a typical house in the northwestern United States, shown in Figure 8.7 [8.9], is used here as one unit of the time varying loads. The loads are assumed to be uniformly distributed along the feeder with 100 houses at each bus.

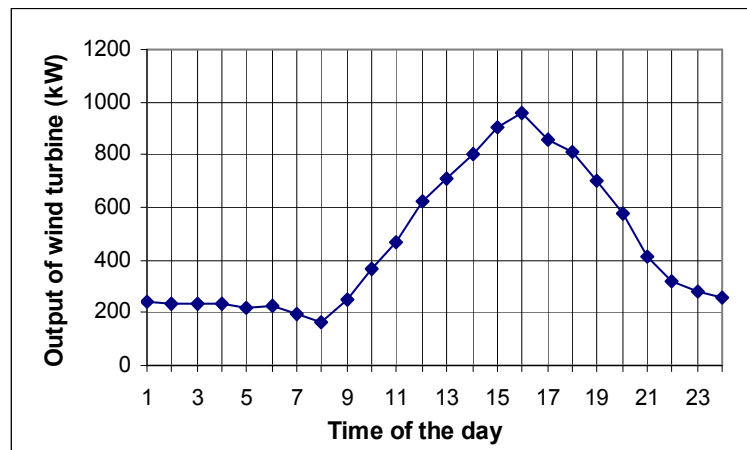


Figure 8.6. Annual daily average output power profile of a 1-MW wind-DG.

The simulated wind-DG was installed at different buses and the total system power loss was obtained in each case, shown in Figure 8.8. It is noticed from this figure that total feeder power loss reaches a minimum value when the wind-DG is placed at bus 10 in Figure 8.5. The theoretical optimal position to place the wind-DG is obtained (using equation (8.17) and the generation and demand data shown in Figures 8.6 and 8.7) to be  $x_0 \approx 0.14l$ . The position with this distance from the end of feeder in Figure 8.5 is between bus 9 and 10, but closer to bus 10, which is the same bus obtained from the simulation results shown in Figure 8.8.

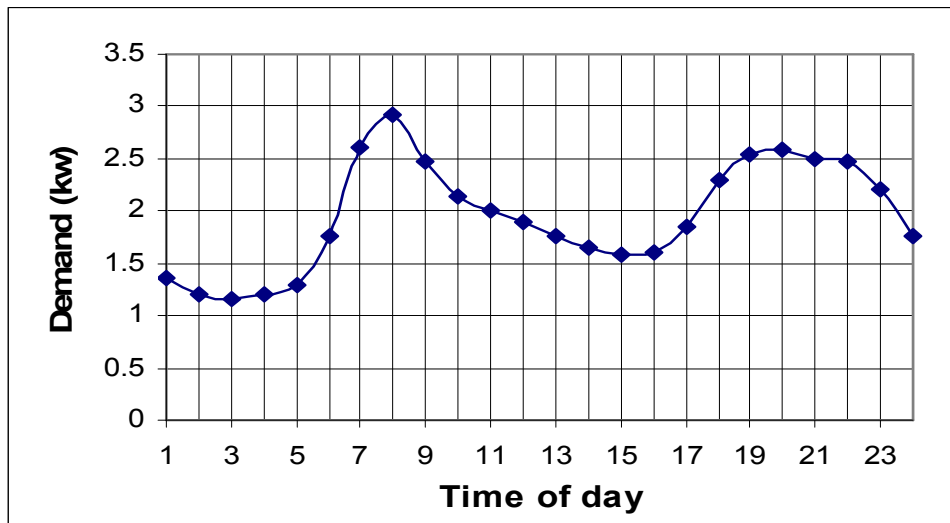


Figure 8.7. Daily average demand of a typical house.

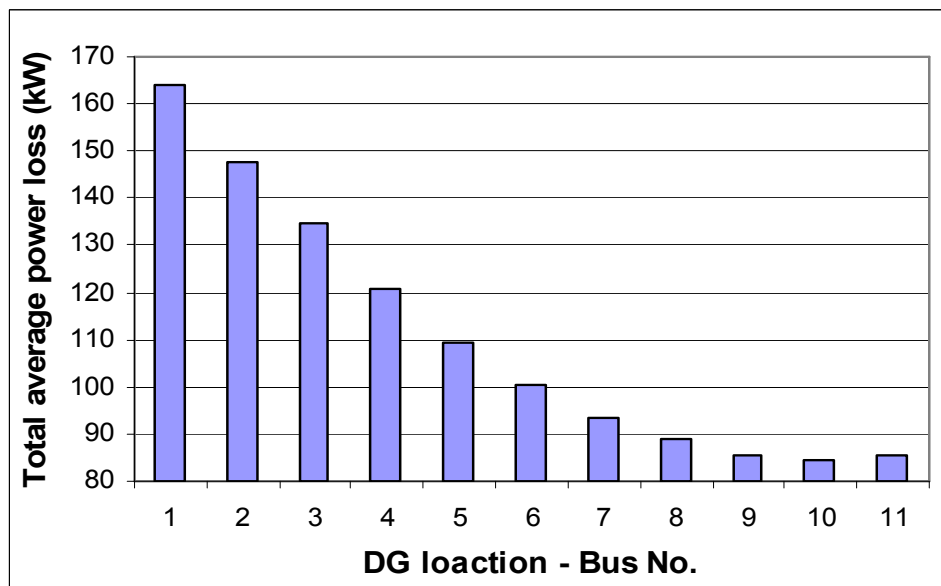


Figure 8.8. Power losses of the radial feeder with the wind-DG at different buses.

### Networked Systems

The 25 kV IEEE 6-bus system shown in Figure 8.9 [8.1], which can be considered as a sub-transmission/distribution system, was used to verify the method presented in the previous section. The parameters of this system are given in Table 8.4. A 5-MW DG was added to reinforce the system. Total system power loss was obtained from the results of power flow studies when DG was placed at different buses (Figure 8.10). It is noted from this figure that minimum power loss is achieved when DG is placed at bus 3. The values of the objective function for the system were obtained by applying the proposed analytical approach when the DG was placed at different buses. These values are shown in the bar chart of Figure 8.11. It is noted from this figure that the objective function is also at its minimum when the DG is placed at bus 3, indicating that the result obtained from the proposed analytical method is the same as the simulation result.

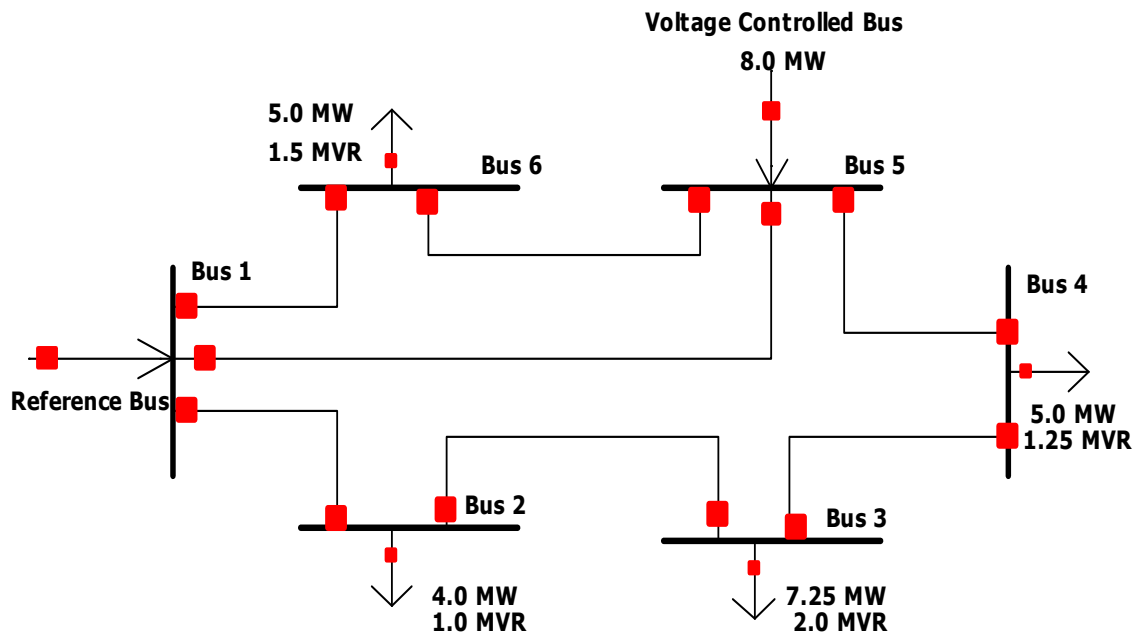


Figure 8.9. 6-bus networked power system studied.

TABLE 8.4. PARAMETERS OF THE SYSTEM IN FIGURE 8.9 [8.1]

Bus No.	Voltage (p.u.)	Bus Power (MVA)	
1	1.0+j0.0	Slack bus	
2	—	-4.0 -j1.00	
3	—	-7.25-j2.00	
4	—	-5.00-j1.25	
5	$ V_s =1.0$	8.00	
6	—	-5.00-j1.50	
Line Data			
From	To	$Z_{serial}$ (p.u.)	$Y_{shunt}$ (p.u.)
1	2	0.2238+j0.5090	j0.0012
2	3	0.2238+j0.5090	j0.0012
3	4	0.2238+j0.5090	j0.0012
4	5	0.2238+j0.5090	j0.0012
5	6	0.2238+j0.5090	j0.0012
6	1	0.2276+j0.2961	j0.0025
1	5	0.2603+j0.7382	j0.0008

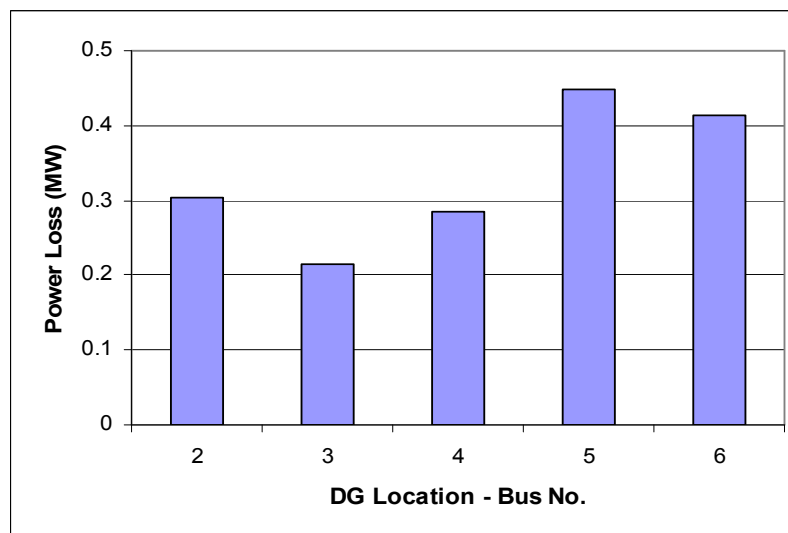


Figure 8.10. Power losses of the system in Figure. 8.9 with a 5MW DG.

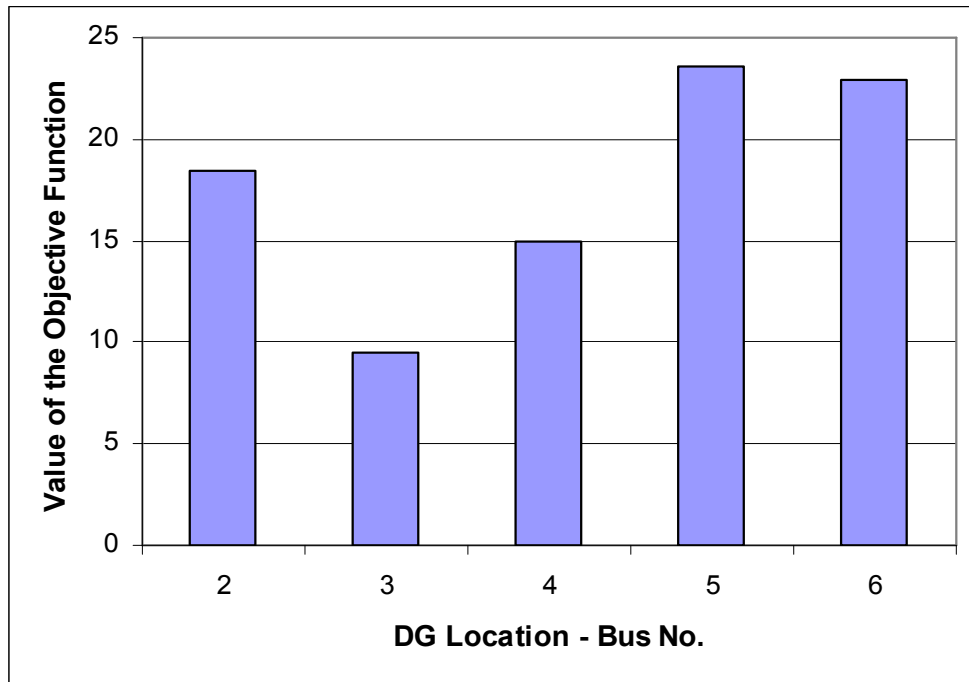


Figure 8.11. Values of the objective function of the system in Figure. 8.9.

The proposed method was also tested on the IEEE 30-bus test system shown in Figure 8.12, which can be considered as a meshed transmission/subtransmission system [8.11]. The system has 30 buses (mainly 132kV and 33kV buses) and 41 lines. The system bus data is given in Table 8.5. A 15 MW DG (about 5% of the total system load of  $283 + j126.2$  MVA) is considered to be added to reinforce the system. The total power loss of the system reaches a minimum value when DG is located at bus 5, as shown in Figure 8.13. The optimal bus determined by the method proposed in this study is also bus 5, as given in Figure. 8.14.

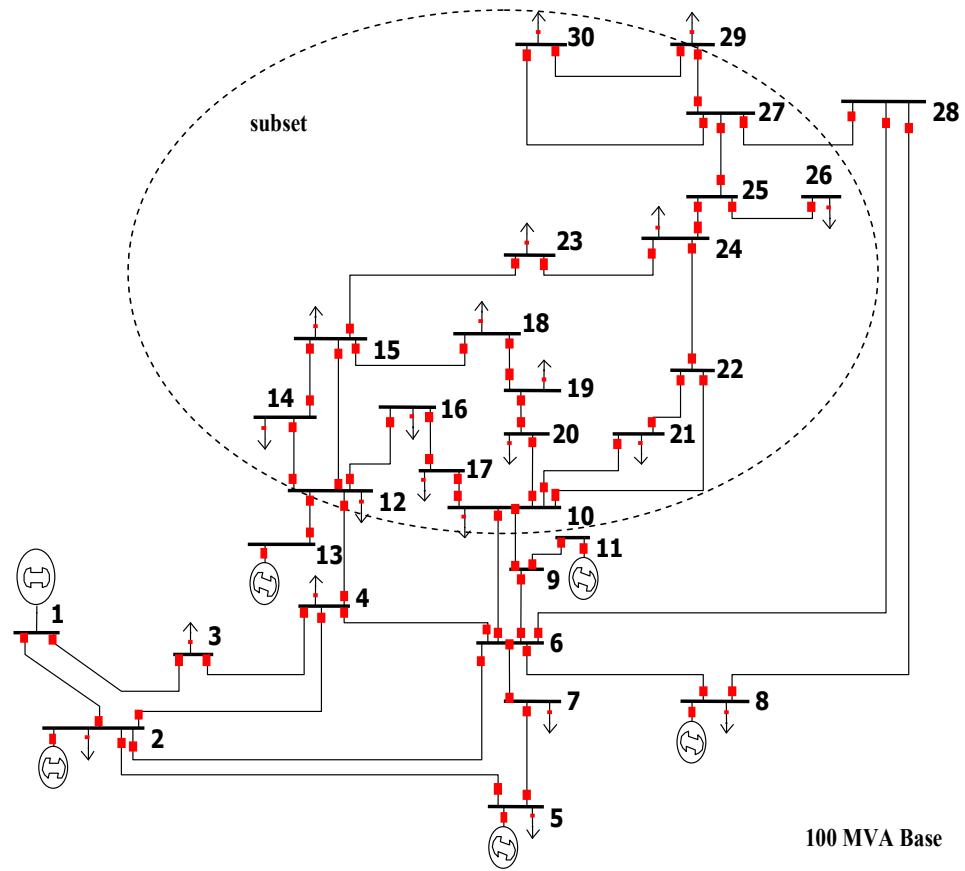


Figure 8.12. IEEE 30-bus test system.

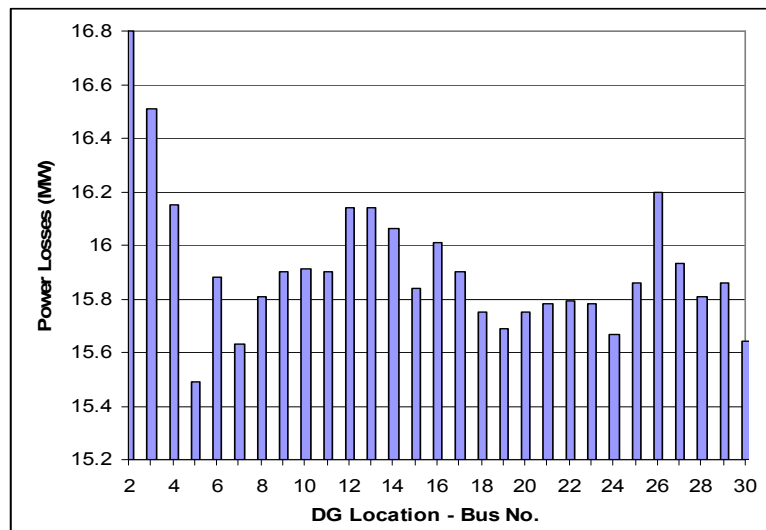


Figure 8.13. Power losses of the IEEE 30-bus test system with a 15MW DG.

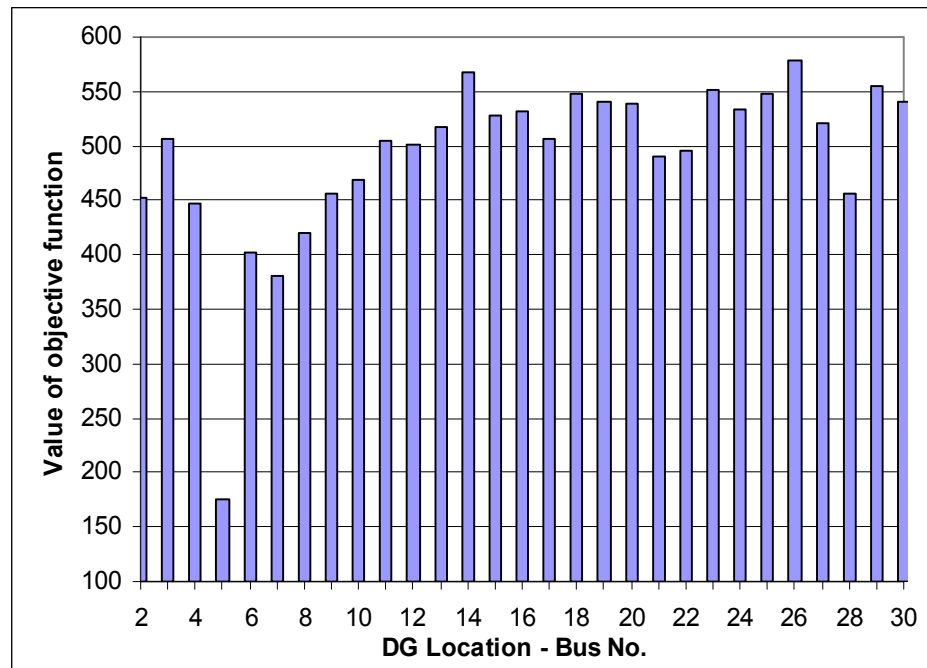


Figure 8.14. Values of the objective function of the IEEE 30-bus system.

A DG source may not be connected directly to a 132kV bus (bus 5 in Figure 8.12) as determined by the proposed method. For this reason, a subset of the 30-bus test system with lower voltage level (33kV), as indicated in Figure 8.12, was also chosen to test the proposed method. The new system has 18 buses, 22 lines and a total load of  $104.7+j50.8$  MVA. A 5MW DG (about 5% of the total load of the subset) was added to the system. Simulation results for this system are given in Figure 8.15. It is noted that the total system loss reaches a minimum value when the DG is located at bus 30. The optimal bus suggested by the proposed method is also bus 30, as shown in Figure 8.16.

All the power flow simulation studies in this chapter were carried out using PowerWorld<sup>®</sup> Simulator [8.12].

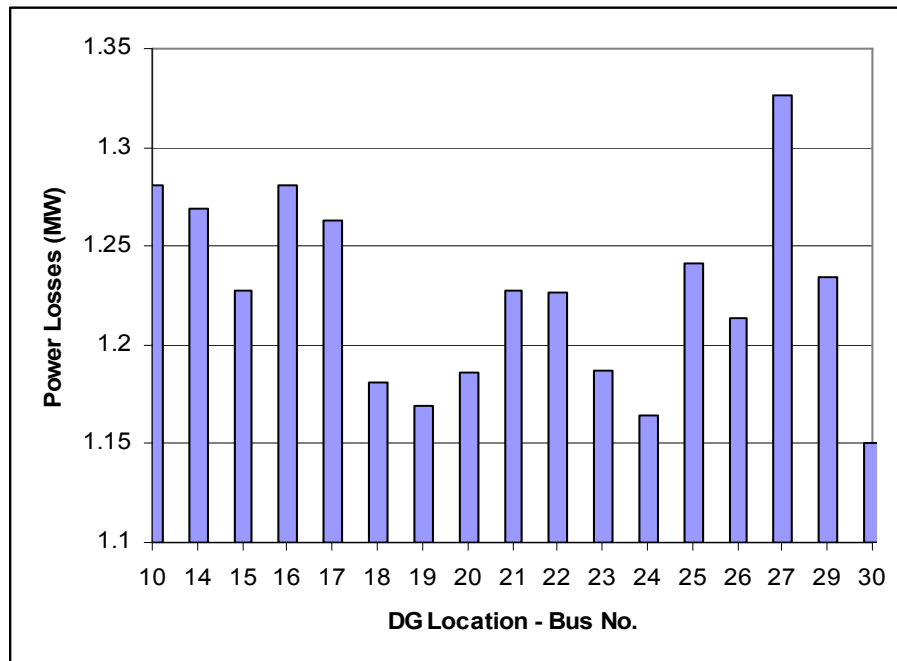


Figure 8.15. Power losses of the subset system in Figure 8.12 with a 5MW DG.

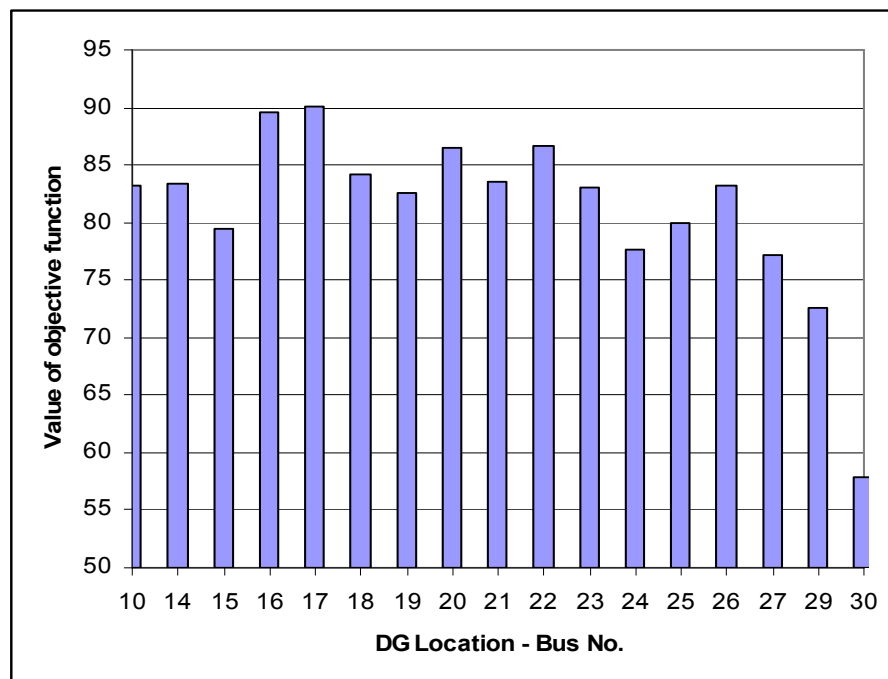


Figure 8.16. Values of the objective function of the subset system in Figure 8.12.

TABLE 8.5. BUS DATA OF THE IEEE 30-BUS TEST SYSTEM [8.11]

Bus No.	Type	Load (p.u.)	Rated Bus Voltage (kV)	Bus Voltage (p.u.)
1	Swing	0.0	132	1.060
2	P-V	0.217+j0.127	132	1.043
3	P-Q	0.024+j0.012	132	—
4	P-Q	0.076+j0.016	132	—
5	P-V	0.942+j0.19	132	1.010
6	P-Q	0.0	132	—
7	P-Q	0.228+j0.109	132	—
8	P-V	0.3+j0.3	132	1.010
9	P-Q	0.0	69.0	—
10	P-Q	0.058+j0.02	33.0	—
11	P-V	0.0	11.0	1.082
12	P-Q	0.112+j0.075	33.0	—
13	P-V	0.0	11.0	1.071
14	P-Q	0.062+j0.016	33.0	—
15	P-Q	0.082+j0.025	33.0	—
16	P-Q	0.035+j0.018	33.0	—
17	P-Q	0.09+j0.058	33.0	—
18	P-Q	0.032+j0.009	33.0	—
19	P-Q	0.095+j0.034	33.0	—
20	P-Q	0.022+j0.007	33.0	—
21	P-Q	0.175+j0.112	33.0	—
22	P-Q	0.0	33.0	—
23	P-Q	0.032+j0.016	33.0	—
24	P-Q	0.087+j0.067	33.0	—
25	P-Q	0.0	33.0	—
26	P-Q	0.035+j0.023	33.0	—
27	P-Q	0.0	33.0	—
28	P-Q	0.0	33.0	—
29	P-Q	0.024+j0.009	33.0	—
30	P-Q	0.106+j0.019	33.0	—

(100 MVA Base)

### Summary

Analytical approaches are presented in this chapter to determine the optimal location for placing DG in both radial and networked systems to minimize power losses. The proposed approaches are not iterative algorithms, like power flow programs. Therefore, there is no convergence problems involved, and results could be obtained very quickly. A series of simulation studies were also conducted to verify the validity of the proposed approaches, and results show that the proposed methods work well.

In practice, there are other constraints which may affect the DG placement. Nevertheless, methodologies presented in this chapter can be effective, instructive and helpful to system designers in selecting proper sites to place DGs.

REFERENCES

- [8.1] Narayan S. Rau, Yih-heui Wan, "Optimum Location of Resources in Distributed Planning," *IEEE Transactions on Power Systems*, Vol. 9, No. 4, pp. 2014-2020, November, 1994.
- [8.2] Kyu-Ho Kim, Yu-Jeong Lee, Sang-Bong Rhee, Sang-Kuen Lee and Seok-Ku You, "Dispersed Generator Placement using Fuzzy-GA in Distribution Systems," *Proceedings, 2002 IEEE Power Engineering Society Summer Meeting*, Vol. 3, pp. 1148-1153, July 2002, Chicago, IL.
- [8.3] N. Hadjsaid, J.F. Canard, F. Dumas, "Dispersed Generation Impact on Distribution Networks," *IEEE Computer Applications in Power*, Vol. 12, No. 2, pp. 22-28, April 1999.
- [8.4] T. Griffin, K. Tomsovic, D. Secrest, A. Law, "Placement of Dispersed Generation Systems for Reduced Losses," *Proceedings, the 33rd Annual Hawaii International Conference on Systems Sciences*, 2000.
- [8.5] M.H. Nehrir, C. Wang, and V. Gerez, "Impact of Wind Power Distributed Generation on Distribution Systems," *Proceedings, 17th International Conference on Electricity Distribution (CIRED)*, May 2003, Barcelona, Spain.
- [8.6] H. L. Willis, "Analytical Methods and Rules of Thumb for Modeling DG-Distribution Interaction," *Proceedings, 2000 IEEE Power Engineering Society Summer Meeting*, Vol. 3, pp. 1643-1644, July 2000, Seattle, WA.
- [8.7] J.O. Kim, S.W. Nam, S.K. Park, C. Singh, "Dispersed Generation Planning Using Improved Hereford Ranch Algorithm," *Electric Power Systems Research, Elsevier*, Vol. 47, No. 1, pp.47-55, Oct. 1998.
- [8.8] W. Kellogg, M.H. Nehrir, G. Venkataramanan., and V. Gerez., "Generation Unit Sizing and Cost Analysis for Stand-Alone Wind, Photovoltaic, and Hybrid Wind/PV Systems," *IEEE Transactions on Energy Conversion*, Vol.13, No. 1, pp. 70-75, March 1998.
- [8.9] J. Cahill, K. Ritland, and W. Kelly, "Description of Electric Energy Use in Single Family Residences in the Pacific Northwest, 1986-1992," *Office of Energy Resources, Bonneville Power Administration*, Portland, OR, December 1992.
- [8.10] J. Duncan Glover, Mulukutla S. Sarma, "Power System Analysis and Design, 3rd Edition," *Brooks/Cole, Thomson Learning, Inc.*, 2001.

- [8.11] R. Yokoyama, S.H. Bae T. Morita, and H. Sasaki, "Multiobjective Optimal Generation Dispatch Based on Probability Security Criteria," *IEEE Transactions on Power Systems*, pp. 317-324, Vol. 3, No. 1, Feb 1988.
- [8.12] Online, <http://www.powerworld.com>.

## CHAPTER 9

## CONCLUSIONS

This dissertation is on modeling and control of a hybrid wind/PV/FC alternative energy system. The main part of the dissertation focuses on the modeling of different energy systems and the corresponding control scheme development. Special emphasis is put on the modeling and control of fuel cell systems.

DG system modeling and control are two other aspects of the research presented in the dissertation. A hybrid alternative energy system has great potential for use as a DG source. Analytical methods for optimal placement of DG sources in power systems are given in the dissertation.

The conclusions of the research work reported in this dissertation are summarized below.

(1) Environmentally friendly and sustainable alternative energy systems will play more important roles in the future electricity supply.

(2) Dynamic models have been developed for the following: fuel cells (PEMFCs and SOFCs), variable speed wind energy conversion systems, photovoltaic power generation systems, electrolyzers, power electronic interfacing devices, battery banks and accessories including gas compressor, high-pressure hydrogen storage tank, and gas pressure regulator. These dynamic models are suitable for both detailed fast transient and large time scale performance evaluation studies. They can be used to expedite research processes in related alternative energy areas, such as system control and performance optimization studies.

(3) Control of grid-connected FC (PEMFC and SOFC) DG systems is investigated. Controller designs for the DC/DC converter and 3-phase inverter are given using linearized small-signal converter/inverter models. A  $dq$  transformed two-loop current control scheme is used on the inverter to control the real and reactive power delivered from the fuel cell system to the utility grid. The validity of the proposed control schemes over a large operating range was verified through simulations on switched nonlinear converter/inverter models. Simulation results of the case studies show that the real and reactive power delivered from the fuel cell system to the utility grid can be controlled as desired while the DC bus voltage is maintained well within its prescribed range. The results also show that the fuel cell system is capable of load-following and can remain stable under the occurrence of severe electrical faults. It is noticed that a two-loop inverter control scheme has advantage over a voltage only control scheme for the inverter on fault protection and system stability.

(4) A load transient mitigation control strategy is proposed for stand-alone fuel cell-battery power generation systems. The control strategy consists of a current controller for the DC/DC converter and a battery charging/discharging controller to keep the battery voltage within a desired range. During load transients, the fuel cell is controlled (by the proposed transient mitigation technique) to supply the steady-state power to the load while the battery will supply the transient power to the load. Simulation studies under different load transients have been carried for both the PEMFC system and the SOFC system. These studies show that the fuel cell current can be controlled as desired and the battery voltage can be held in the prescribed range. The results show that the proposed load transient mitigation technique works well for both types of fuel cell

systems (PEMFC and SOFC) studied.

(5) A hybrid wind/PV/FC DG system is proposed in this dissertation. Wind and PV are the primary power sources of the system, and the combination of FC and electrolyzer is used as a backup and long term storage unit. The different energy sources in the system are integrated through an AC link bus. The system can be used as test-bed system for other related studies on hybrid alternative energy systems.

(6) Based on the dynamic component models, a simulation model for the proposed hybrid wind/PV/FC energy system has been developed successfully using MATLAB/Simulink. The overall power management strategy for coordinating the power flows among the different energy sources is presented in the dissertation. Simulation studies have been carried out to verify the system performance under different scenarios using practical load profile and real weather data. The results show that the overall power management strategy is effective and the power flows among the different energy sources and the load demand is balanced successfully.

(7) Analytical approaches are presented to determine the optimal location for placing DG in both radial and networked systems to minimize power losses. The proposed approaches are not iterative algorithms, like power flow programs. Therefore, there is no convergence problem involved, and results could be obtained very quickly. A series of simulation studies were also conducted to verify the validity of the proposed approaches. The results show that the proposed methods work well.

APPENDICES

APPENDIX A

*abc-dq0* TRANSFORMATION

### abc-dq0 Transformation

The *abc-dq0* transformation transfers 3-phase variables in *abc* stationary frame to a rotating *dq0* frame. As explained in [4.62], the transformation can be expressed as:

$$V_{dq0} = T_{abc/dq0} V_{abc} \quad (\text{A.1})$$

Where:

$$V_{dq0} = \begin{bmatrix} V_d \\ V_q \\ V_0 \end{bmatrix}, \quad V_{abc} = \begin{bmatrix} V_a \\ V_b \\ V_c \end{bmatrix}, \quad T_{abc/dq0} = \frac{2}{3} \begin{bmatrix} \sin(\theta) & \sin\left(\theta - \frac{2\pi}{3}\right) & \sin\left(\theta + \frac{2\pi}{3}\right) \\ \cos(\theta) & \cos\left(\theta - \frac{2\pi}{3}\right) & \cos\left(\theta + \frac{2\pi}{3}\right) \\ \frac{1}{2} & \frac{1}{2} & \frac{1}{2} \end{bmatrix}, \quad \theta = \int_0^t \omega(\xi) d\xi + \theta(0);$$

$\theta$  is the angular position,  $\omega$  is the angular speed and  $\xi$  is the dummy variable of integration. For *abc* variables with constant frequency at 60 Hz and zero initial phase,  $\theta$  can be written as  $\theta = 120\pi t$ .

In (A.1),  $V$  can represent voltage, current, flux linkage, or electric charge. For balanced 3-phase AC variables in *abc* frame, the corresponding *dq0* components are DC variables with zero value for 0 component. Therefore, an *abc-dq* transformation, given in (A.2), can be used in this case.

$$T_{abc/dq} = \frac{2}{3} \begin{bmatrix} \sin(\theta) & \sin\left(\theta - \frac{2\pi}{3}\right) & \sin\left(\theta + \frac{2\pi}{3}\right) \\ \cos(\theta) & \cos\left(\theta - \frac{2\pi}{3}\right) & \cos\left(\theta + \frac{2\pi}{3}\right) \end{bmatrix} \quad (\text{A.2})$$

*dq0-abc* Transformation

The inverses *dq0-abc* transformation can be expressed as:

$$T_{dq0/abc} = (T_{abc/dq0})^{-1} = \begin{bmatrix} \sin(\theta) & \cos(\theta) & 1 \\ \sin\left(\theta - \frac{2\pi}{3}\right) & \cos\left(\theta - \frac{2\pi}{3}\right) & 1 \\ \sin\left(\theta + \frac{2\pi}{3}\right) & \cos\left(\theta + \frac{2\pi}{3}\right) & 1 \end{bmatrix} \quad (\text{A.3})$$

The corresponding inverses *dq-abc* transformation is

$$T_{dq/abc} = \begin{bmatrix} \sin(\theta) & \cos(\theta) \\ \sin\left(\theta - \frac{2\pi}{3}\right) & \cos\left(\theta - \frac{2\pi}{3}\right) \\ \sin\left(\theta + \frac{2\pi}{3}\right) & \cos\left(\theta + \frac{2\pi}{3}\right) \end{bmatrix} \quad (\text{A.4})$$

APPENDIX B

SIMULATION DIAGRAMS OF THE HYBRID ENERGY SYSTEM



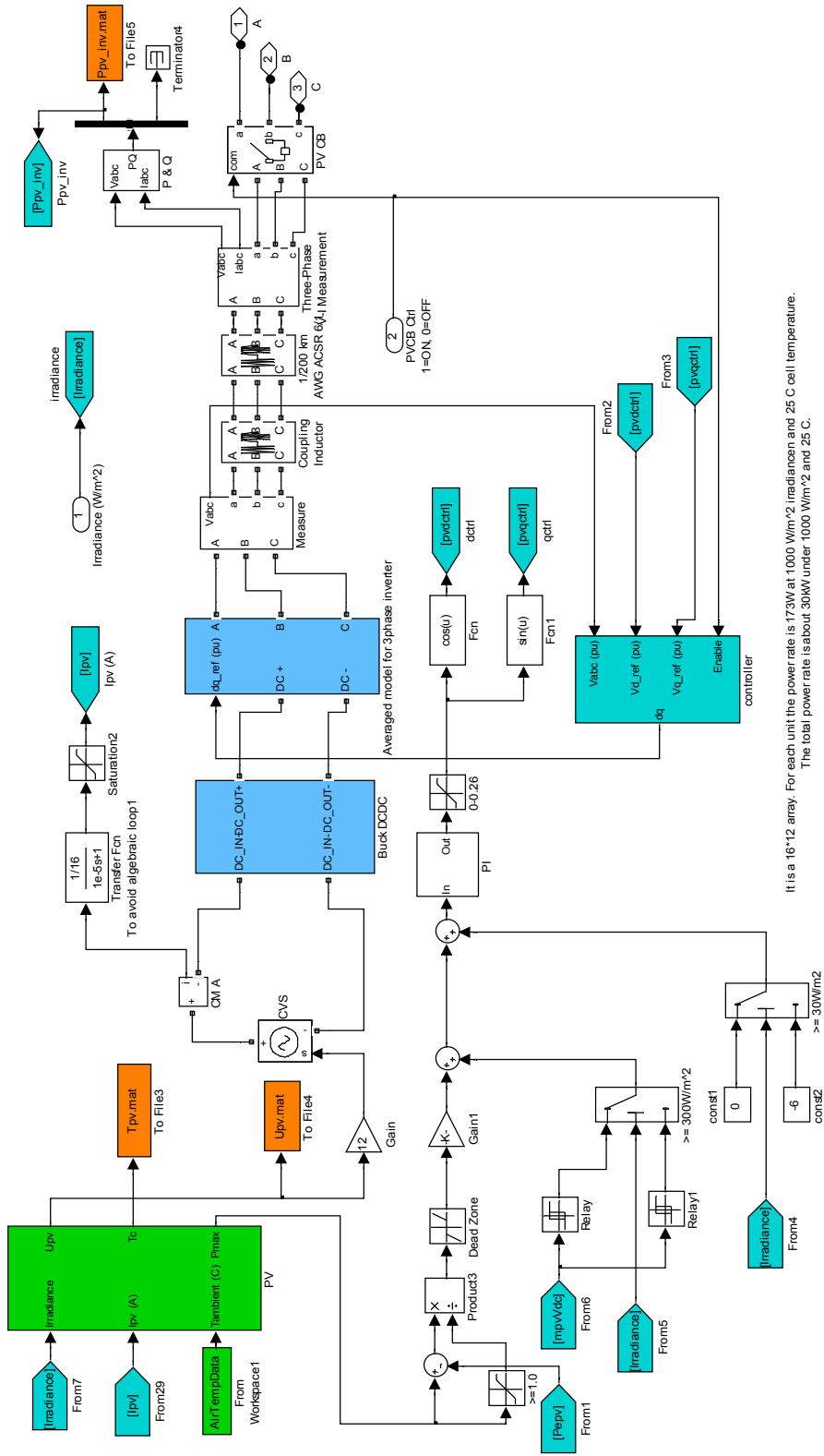


Figure B.2. Simulink model for the solar energy conversion system.



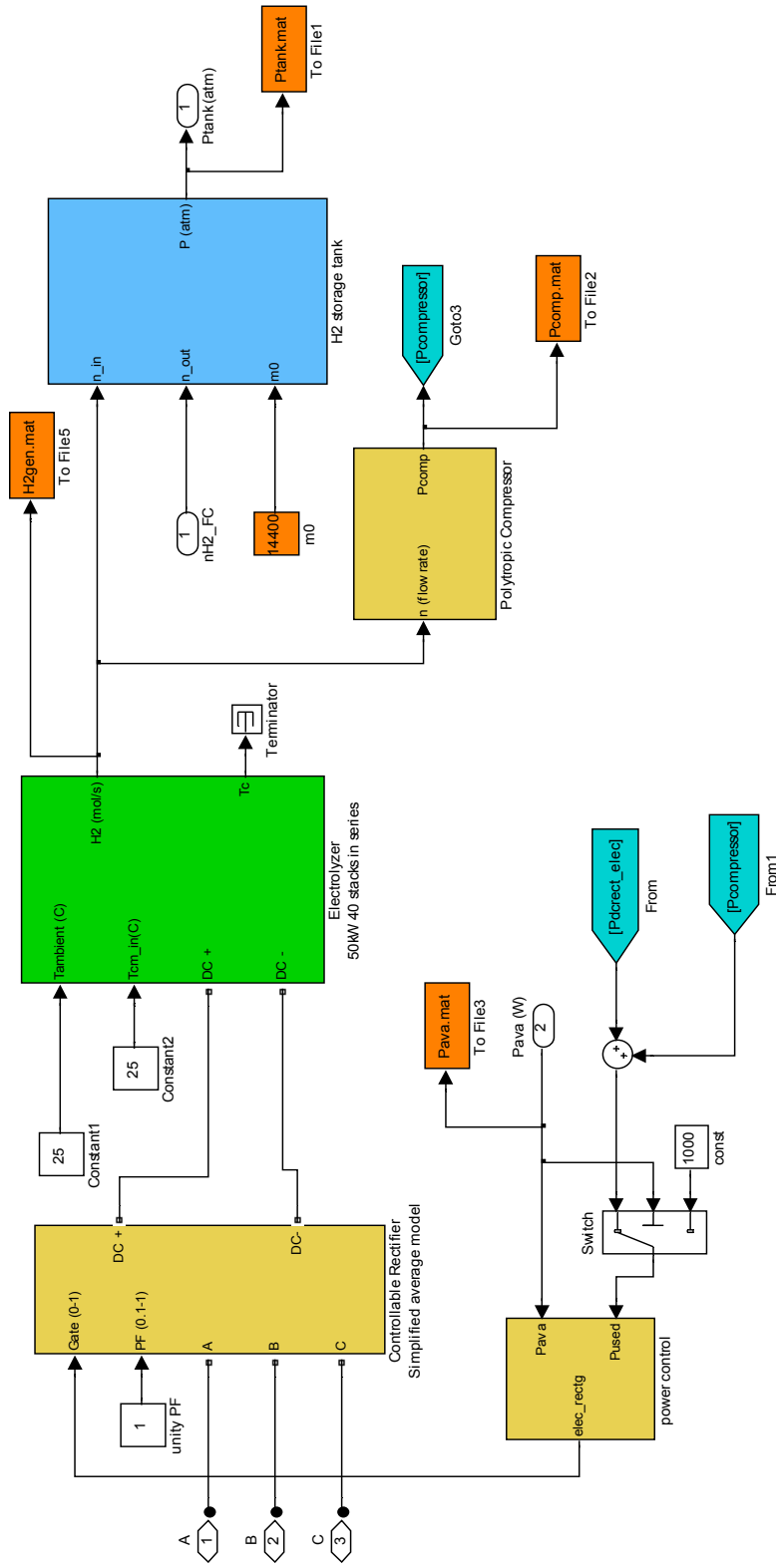


Figure B.4. Simulink model for the electrolyzer and the gas compression system.

APPENDIX C

MATLAB PROGRAMS FOR DG OPTIMAL PLACEMENT

DG Optimal Program for the IEEE 6-Bus system.

```

%Y matrix of the system
%      1          2          3  4          5          6
Y = [ 2.78-4.97j+0.005-1j -0.72+1.65j  0  0 -0.42+1.2j -1.63+2.12j;
      -0.72+1.65j          1.45-3.29j -0.72+1.65j  0  0          0;
      0          -0.72+1.65j  1.45-3.29j -0.72+1.65j  0          0;
      0          0          -0.72+1.65j  1.45-3.29j -0.72+1.65j  0;
      -0.42+1.2j  0  0 -0.72+1.65j  1.87-4.50j+0.005-1j -0.72+1.65j;
      -1.63+2.12j  0  0          0          -0.72+1.65j  2.36-3.77j;]

% Assume Xd and R of the Generator is R +jX = 0.005+j1.
%Load data in the system corresponding to different buses.
Demand = [0, 4+1.0i, 7.25+2.0i, 5+1.25i, 0, 5+1.5i] %MVA
Demand = abs(Demand);

% f(i) = Sum(Li*Pi^2): objective function
% or f(i) = Sum(Li*Si^2): objective function
% Li is the equivalent length from the DG location to load Pi or Si.
% 'i' is the bus number, i=1,2, ..., N.
% Target find the i which yields the minimum value of f(i).

BUSNO=6;

fobj = zeros(BUSNO, 1);
for busno=1:BUSNO
    Z = GetEqImpedance(Y, 1, busno);
    Req = real(Z);
    fobj(1) = fobj(1) + Req*Demand(busno)^2;
end
for dg=2:BUSNO, %move dg to different buses
    Y1 = changeYmatrix(Y,dg); %connect the bus dg with bus 1
    for busno=1:BUSNO
% if the dg location bus no is the same as the load bus no, then line
% power loss can be set to 0.
        if busno == dg
            Z = 0;
        elseif busno < dg
            Z = GetEqImpedance(Y1, 1, busno);
        else
            Z = GetEqImpedance(Y1, 1, busno-1);
        end
        Req = real(Z);
        fobj(dg) = fobj(dg) + Req*Demand(busno)^2;
    end
end
end
fobj

```

DG Optimal Program for the IEEE 30-Bus system.

```

% Assume Yg =1/(0.005+j1.1) for Synchronous Generator,
% Yc = 1/(0.008+j1.8)
% for Synchronous Condenser (Refer to Glover's Book)

% Generating Y matrix (imported from PowerWorld)
j = sqrt(-1);

Yg = 1/(0.005+j*1.1);
Yc = 1/(0.008+j*1.8);

Ybus = zeros(30,30);
Ybus( 1, 1) = 6.7655+ j*( -21.2316) + Yg;
Ybus( 1, 2) = -5.2246+ j*( 15.6467);
Ybus( 1, 3) = -1.5409+ j*( 5.6317);
Ybus( 2, 1) = -5.2246+ j*( 15.6467);
Ybus( 2, 2) = 9.7523+ j*( -30.6487) + Yg;
Ybus( 2, 4) = -1.7055+ j*( 5.1974);
Ybus( 2, 5) = -1.1360+ j*( 4.7725);
Ybus( 2, 6) = -1.6861+ j*( 5.1165);
Ybus( 3, 1) = -1.5409+ j*( 5.6317);
Ybus( 3, 3) = 9.7363+ j*( -29.1379);
Ybus( 3, 4) = -8.1954+ j*( 23.5309);
Ybus( 4, 2) = -1.7055+ j*( 5.1974);
Ybus( 4, 3) = -8.1954+ j*( 23.5309);
Ybus( 4, 4) = 16.3141+ j*( -54.9186);
Ybus( 4, 6) = -6.4131+ j*( 22.3112);
Ybus( 4, 12) = -0.0000+ j*( 3.9062);
Ybus( 5, 2) = -1.1360+ j*( 4.7725);
Ybus( 5, 5) = 4.0900+ j*( -12.1906) + Yc;
Ybus( 5, 7) = -2.9540+ j*( 7.4493);
Ybus( 6, 2) = -1.6861+ j*( 5.1165);
Ybus( 6, 4) = -6.4131+ j*( 22.3112);
Ybus( 6, 6) = 22.3416+ j*( -82.4934);
Ybus( 6, 7) = -3.5902+ j*( 11.0261);
Ybus( 6, 8) = -6.2893+ j*( 22.0126);
Ybus( 6, 9) = -0.0000+ j*( 4.8077);
Ybus( 6, 10) = -0.0000+ j*( 1.7986);
Ybus( 6, 28) = -4.3628+ j*( 15.4636);
Ybus( 7, 5) = -2.9540+ j*( 7.4493);
Ybus( 7, 6) = -3.5902+ j*( 11.0261);
Ybus( 7, 7) = 6.5442+ j*( -18.4567);
Ybus( 8, 6) = -6.2893+ j*( 22.0126);
Ybus( 8, 8) = 7.7333+ j*( -26.5275) + Yc;
Ybus( 8, 28) = -1.4440+ j*( 4.5408);
Ybus( 9, 6) = -0.0000+ j*( 4.8077);
Ybus( 9, 9) = 0.0000+ j*( -18.7063);
Ybus( 9, 10) = -0.0000+ j*( 9.0909);
Ybus( 9, 11) = -0.0000+ j*( 4.8077);
Ybus( 10, 6) = -0.0000+ j*( 1.7986);
Ybus( 10, 9) = -0.0000+ j*( 9.0909);
Ybus( 10, 10) = 13.4621+ j*( -41.5738);

```

```

Ybus ( 10, 17) = -3.9560+ j*( 10.3174);
Ybus ( 10, 20) = -1.7848+ j*( 3.9854);
Ybus ( 10, 21) = -5.1019+ j*( 10.9807);
Ybus ( 10, 22) = -2.6193+ j*( 5.4008);
Ybus ( 11, 9) = -0.0000+ j*( 4.8077);
Ybus ( 11, 11) = 0.0000+ j*( -4.8077) + Yc;
Ybus ( 12, 4) = -0.0000+ j*( 3.9062);
Ybus ( 12, 12) = 6.5740+ j*( -24.4242);
Ybus ( 12, 13) = -0.0000+ j*( 7.1429);
Ybus ( 12, 14) = -1.5266+ j*( 3.1734);
Ybus ( 12, 15) = -3.0954+ j*( 6.0973);
Ybus ( 12, 16) = -1.9520+ j*( 4.1044);
Ybus ( 13, 12) = -0.0000+ j*( 7.1429);
Ybus ( 13, 13) = 0.0000+ j*( -7.1429) + Yc;
Ybus ( 14, 12) = -1.5266+ j*( 3.1734);
Ybus ( 14, 14) = 4.0175+ j*( -5.4243);
Ybus ( 14, 15) = -2.4910+ j*( 2.2509);
Ybus ( 15, 12) = -3.0954+ j*( 6.0973);
Ybus ( 15, 14) = -2.4910+ j*( 2.2509);
Ybus ( 15, 15) = 9.3655+ j*( -16.0116);
Ybus ( 15, 18) = -1.8108+ j*( 3.6874);
Ybus ( 15, 23) = -1.9683+ j*( 3.9761);
Ybus ( 16, 12) = -1.9520+ j*( 4.1044);
Ybus ( 16, 16) = 3.2596+ j*( -8.9257);
Ybus ( 16, 17) = -1.3076+ j*( 4.8213);
Ybus ( 17, 10) = -3.9560+ j*( 10.3174);
Ybus ( 17, 16) = -1.3076+ j*( 4.8213);
Ybus ( 17, 17) = 5.2637+ j*( -15.1388);
Ybus ( 18, 15) = -1.8108+ j*( 3.6874);
Ybus ( 18, 18) = 4.8865+ j*( -9.9062);
Ybus ( 18, 19) = -3.0757+ j*( 6.2188);
Ybus ( 19, 18) = -3.0757+ j*( 6.2188);
Ybus ( 19, 19) = 8.9580+ j*( -17.9835);
Ybus ( 19, 20) = -5.8824+ j*( 11.7647);
Ybus ( 20, 10) = -1.7848+ j*( 3.9854);
Ybus ( 20, 19) = -5.8824+ j*( 11.7647);
Ybus ( 20, 20) = 7.6672+ j*( -15.7501);
Ybus ( 21, 10) = -5.1019+ j*( 10.9807);
Ybus ( 21, 21) = 21.8765+ j*( -45.1084);
Ybus ( 21, 22) = -16.7746+ j*( 34.1277);
Ybus ( 22, 10) = -2.6193+ j*( 5.4008);
Ybus ( 22, 21) = -16.7746+ j*( 34.1277);
Ybus ( 22, 22) = 21.9345+ j*( -43.4829);
Ybus ( 22, 24) = -2.5405+ j*( 3.9544);
Ybus ( 23, 15) = -1.9683+ j*( 3.9761);
Ybus ( 23, 23) = 3.4298+ j*( -6.9653);
Ybus ( 23, 24) = -1.4614+ j*( 2.9892);
Ybus ( 24, 22) = -2.5405+ j*( 3.9544);
Ybus ( 24, 23) = -1.4614+ j*( 2.9892);
Ybus ( 24, 24) = 5.3118+ j*( -9.2313);
Ybus ( 24, 25) = -1.3099+ j*( 2.2876);
Ybus ( 25, 24) = -1.3099+ j*( 2.2876);
Ybus ( 25, 25) = 4.4957+ j*( -7.8650);
Ybus ( 25, 26) = -1.2165+ j*( 1.8171);
Ybus ( 25, 27) = -1.9693+ j*( 3.7602);

```

```

Ybus ( 26, 25) = -1.2165+ j*( 1.8171);
Ybus ( 26, 26) = 1.2165+ j*( -1.8171);
Ybus ( 27, 25) = -1.9693+ j*( 3.7602);
Ybus ( 27, 27) = 3.6523+ j*( -9.4604);
Ybus ( 27, 28) = -0.0000+ j*( 2.5253);
Ybus ( 27, 29) = -0.9955+ j*( 1.8810);
Ybus ( 27, 30) = -0.6875+ j*( 1.2940);
Ybus ( 28, 6) = -4.3628+ j*( 15.4636);
Ybus ( 28, 8) = -1.4440+ j*( 4.5408);
Ybus ( 28, 27) = -0.0000+ j*( 2.5253);
Ybus ( 28, 28) = 5.8068+ j*( -22.5016);
Ybus ( 29, 27) = -0.9955+ j*( 1.8810);
Ybus ( 29, 29) = 1.9076+ j*( -3.6044);
Ybus ( 29, 30) = -0.9121+ j*( 1.7234);
Ybus ( 30, 27) = -0.6875+ j*( 1.2940);
Ybus ( 30, 29) = -0.9121+ j*( 1.7234);
Ybus ( 30, 30) = 1.5995+ j*( -3.0173);

```

```
BUSNO=30;
```

```
%Load data in the system corresponding to different buses.
```

```

Demand = zeros(1,BUSNO); %MVA
Demand(1)= 0.0;
Demand(2)= 0.0;
Demand(3)= 2.4 + j*1.2;
Demand(4)= 7.6 + j*1.6;
Demand(5)= 94.2 + j*19.0;
Demand(6)= 0.0;
Demand(7)= 22.8 + j*10.9;
Demand(8)= 30.0 + j*30.0;
Demand(9)= 0.0;
Demand(10)= 5.8 + j*2.0;
Demand(11)= 0.0;
Demand(12)= 11.2 + j*7.5;
Demand(13)= 0.0;
Demand(14)= 6.2 + j*1.6;
Demand(15)= 8.2 + j*2.5;
Demand(16)= 3.5 + j*1.8;
Demand(17)= 9.0 + j*5.8;
Demand(18)= 3.2 + j*0.9;
Demand(19)= 9.5 + j*3.4;
Demand(20)= 2.2 + j*0.7;
Demand(21)= 17.5 + j*11.2;
Demand(22)= 0.0;
Demand(23)= 3.2 + j*1.6;
Demand(24)= 8.7 + j*6.7;
Demand(25)= 0.0;
Demand(26)= 3.5 + j*2.3;
Demand(27)= 0.0;
Demand(28)= 0.0;
Demand(29)= 2.4 + j*0.9;
Demand(30)= 10.6 + j*1.9;

```

```

Demand = abs(Demand); %MVA

Demand = Demand/10;

% f(i) = Sum(Li*Pi^2): objective function
% or f(i) = Sum(Li*Si^2): objective function
% Li is the equivalent length from the DG location to load Pi or Si.
% 'i' is the bus number, i=1,2, ..., N.
% Target find the i which yields the minimum value of f(i).

BUSNO=30;

fobj = zeros(BUSNO, 1);
for busno=1:BUSNO
    Z = GetEqImpedance(Ybus, 1, busno);
    Req = real(Z);
    fobj(1) = fobj(1) + Req*Demand(busno)^2;
end
for dg=2:BUSNO, %move dg to different buses
    Y1 = changeYmatrix(Ybus,dg); %connect the bus dg with bus 1
    for busno=1:BUSNO
        if busno == dg
            % if the dg location bus no is the same as the load bus no, then line
            % power loss can be set to 0.
            Z = 0;
        elseif busno < dg
            Z = GetEqImpedance(Y1, 1, busno);
        else
            Z = GetEqImpedance(Y1, 1, busno-1);
        end
        Req = real(Z);
        fobj(dg) = fobj(dg) + Req*Demand(busno)^2;
    end
end
fobj

```